THÈSE

En vue de l'obtention du

DOCTORAT DE L'UNIVERSITÉ DE TOULOUSE

Délivré par : *l'Université Toulouse 3 Paul Sabatier (UT3 Paul Sabatier)*

Présentée et soutenue le *22 septembre 2015* **par :**

HUGAU MIZZON

The magmatic crust of Vesta.

JURY

RAPPORTEUR	M. Jean-Luc Starck	DR, CosmoStat, CEA-Saclay
RAPPORTEUR	M. Pierre Beck	MCF, IPAG, Grenoble
EXAMINATRICE	M^{me} Chloé Michaut	MCF, IPGP, Paris
EXAMINATEUR	M. Yannick Deville	Pr., IRAP, Toulouse
EXAMINATEUR	M. Tom Prettyman	Senior Sc., PSI, Albuquerque
DIRECTEUR	M. Olivier Forni	DR, IRAP, Toulouse
DIRECTEUR	M. Michael Toplis	DR, IRAP, Toulouse
ENCADRANT	M. Marc Monnereau	CR, IRAP, Toulouse

École doctorale et spécialité :

SDU2E : Astrophysique, Sciences de l'Espace, Planétologie

Unité de Recherche :

Institut de Recherche en Astrophysique et Planétologie (UMR 5277)

Contents

List of Figures

List of Tables

Aknowledgments

I would like to thank everybody who participated to the construction of this thesis, and helped me during the path that led to it. No need to tell that this represents a lot of people and that I am very grateful to you, who I forgot to mention below.

This thesis was realized within the Institute of Research in Astrophysics and Planetology (IRAP), including interactions with members of three groups of research, the DIP (Planetary Interior dynamic), PEPS (Planetary surface exploration) and SISU (Signal Image processing). This thesis started during the arrival of the Dawn spacecraft in orbit around asteroid 4-Vesta, at the occasion of the involment of my phD advisors in this space program.

First of all I would like to thank Olivier Forni and Michael Toplis for introducing me in the framework of the Dawn mission, which has been a rare privilege to work within. I hereby especially thank Michael Toplis, for stimulating discussions, for his will to make me have interactions with the investigators of the Dawn mission and for the strong support he provided me through the difficulties that I have encountered.

The first part of this thesis concerns the application of independent component analysis to gamma ray spectra of Vesta, which did not entirely fullfilled some expectations. A member of the Image and signal processing group (SISU), Yannick Deville, have significantly contributed to valorize my work and proposed the idea of working on gamma ray synthetics, to give more sense to my analyses. I am very grateful for the time Yannick allowed me to discuss with him and to follow some of his classes. It is a pleasure to have him as president of the judging panel.

I must thank Thomas Prettyman, PI of the Gamma Ray and Neutron detector onboard Dawn spacecraft, with whom I worked in Albuquerque, who have been always welcoming and of great help to make the blind source separation study progress.

I have a special thank to address to Marc Monnereau, for his constant support and more specifically for the important input he provided for implementing a code of compaction, which is the basis of the differentiation models of Vesta presented in this thesis.

I thank David Baratoux notably for his encouragement to follow a summer school in Japan and Key Kurita to have welcomed me in his lab at this occasion. I thank Jean-Alix Barrat for the precious advises and clues he provided me when I started my phD. I have to thank Doris Breuer and Wladimir Neumann, who have welcomed me in their institute, for fruitful discussions about the differentiation of Vesta.

I have to thank the members of the Dawn team for the beautiful material they provided, but also for their support, their welcome during conferences and advises, especially Christopher Russell, Carol Raymond and Harry McSween.

I would like to thank the staff members of the IRAP institute and from the OMP for their cheerful attitude and their help, more specifically Loic Jahan, Carole Gaiti, Jean-Louis Lefort, Marie-Claude Cathala, Josette Garcia, but also researchers Marie Calvet, Ludovic Margerin, Henri Samuel, Micha Bystricky, Frédéric Paletou, Hervé Carfantan, Laurent Koechlin, not to forget former and present students Lewis Schardong, Jessie Mayor, William Rapin, Delphine Hypolite, Lisa Million-Picaillon, Aurélie Michelle, Cori Pegliasco, Audrey Souchon and Yo Nishimura, with whom I had great moments.

Finally I would like to thank professors with whom I had the pleasure to be a teaching assistant in the GET laboratory Carine Lézin, Martin Roddaz, Sébastien Fabre, Bernard Andreu, Markus Aretz and Stéphane Brusset.

Je remercie ma famille, mes proches et Hélène qui n'ont pas cessé de m'encourager et de me soutenir.

Avant-propos

Le 27 septembre 2007, la sonde spatiale Dawn a quitté la Terre pour visiter deux des plus gros objets de la ceinture d'astéroïdes, Vesta qu'elle a atteint le 16 juillet 2011 et qu'elle a analysé pendant 14 mois avant de repartir pour Cérès autour de laquelle elle est en orbite depuis mars 2015. C'est dans le cadre de cette mission spatiale, qui a permis de recueillir des données tout-à-fait originales sur Vesta, que ce travail de thèse s'est déroulé.

L'intérêt d'étudier ces deux astéroïdes est que ce sont des corps très primitifs du système solaire. Ils ont été reconnu comme des vestiges de la période de formation des planètes, qui normalement auraient dû terminer leur existence à l'intérieur de l'une d'entre elles au lieu d'orbiter autour du soleil entre Mars et Jupiter. C'est aussi de la ceinture d'astéroïde que proviennent la majorité des météorites que l'on récolte sur Terre et qui sont de précieux témoins de l'état précoce du système. Pourtant, la préservation de ce réservoir n'est pas une évidence, au point qu'on pourrait se demander quelle aurait été notre connaissance, entre autres, sur la composition du manteau terrestre, sur l'âge de la Terre, s'il n'existait pas.

C'est sans doute à l'instabilité des orbites des planètes gazeuses et à leur masse qu'on doit sa formation [Walsh *et al.* , 2011, 2012]. Juste après l'effondrement du nuage stellaire en un disque d'accrétion autour du jeune soleil, les planètes gazeuses grossissent très vite, peut-être en quelques milliers d'années seulement si le mécanisme est l'effondrement local du disque. Freinées par le gaz encore présent, elles se rapprochent du soleil. Puis, l'interaction gravitationnelle avec tous les corps qui deviennent de plus en plus massifs, déstabilise leur orbite et les en éloignent. Des simulations numériques de cette dynamique montrent ainsi comment un probable aller-retour des orbites de Jupiter et de Saturne a vidé le disque planétaire de tous les petits corps à l'exception d'une zone stable à proximité de l'orbite de Jupiter, où se retrouvent piégés des corps à différents stades de leur évolution, mais aussi de composition très variables, silicatées ou carbonées, puisque ils proviennent de régions très différentes du disque, notamment en deçà et au delà de la ligne des glaces.

D'ailleurs, Vesta et Cérès n'ont pas été choisies comme objectif de la mission Dawn uniquement à cause de leur taille, mais aussi pour leur différence puisque Vesta est un des représentants des corps silicatés alors que Cérès, qualifiée de planète naine au vu de ses 476 km de rayon, appartient au cortège des corps glacés. Vesta présente aussi un intérêt tout particulier, dans la mesure où, dès les années 70, des observations spectroscopiques de sa surface ont établi une parenté avec une classe de météorites, les HED (Howardites, Eucrites et Diogénites) [McCord *et al.* , 1970; McFadden *et al.* , 1977] (voire la Figure 1**b**). Assez succinctement, les eucrites sont des basaltes ou des gabbros, les diogénites des orthopyroxénites cumulatives et les howardites, un mélange clastiques des deux premiers, de sorte que les HED apparaissent comme des fragments de la croûte d'un corps parent différencié (voire la Figure 1**d** et **f**). Ce lien fut renforcé par des observations du télescope spatial Hubble, qui permirent d'établir des cartes de la lithologie de la surface de Vesta. Ces cartes révélaient la présences de pyroxénites exposées dans le grand bassin d'impact de Rheasilvia centré sur le pole sud de Vesta [Binzel *et al.* , 1997; Zellner *et al.* , 2005]. Dans l'hypothèse où les HED proviennent bien de Vesta, l'âge de ces météorites montre

que Vesta a connu une activité magmatique importante durant les 10 à 20 premiers millions d'années du système solaire [Zhou *et al.* , 2013]. Ainsi, l'intérêt pour Vesta se trouve renforcé par la possibilité de combiner l'étude morphologique et spectrale de sa surface, les mesures globales comme sa forme, sa masse et son champ de pesanteur avec la multitude d'analyses minéralogiques et isotopiques d'échantillon des HED recueillis sur Terre. Une telle complémentarité de données n'existe que pour la lune — et bien sûr la Terre — pour laquelle on dispose d'une grande quantité d'échantillons. Ainsi, Vesta offre une fenêtre, non seulement sur un objet primitif du système solaire, mais aussi sur les processus de différenciation dont les traces ont été dispersées sur les planètes par la longue histoire dynamique qui a suivi leur formation.

Plan du manuscrit

Au cours de cette thèse, deux aspects assez distincts, mais complémentaires seront abordés. Le premier concerne l'analyse des données de spectroscopie nucléaire en vu de cartographier la distribution de certains éléments majeurs de la surface de Vesta. Un second volet présentera la modélisation de la différenciation de l'astéroïde pour comprendre et tenter de contraindre ses conditions de formation à travers la confrontation avec la lithologie des HED.

L'analyse des données gamma de la mission Dawn

Après un premier chapitre introductif, un second chapitre sera consacré à l'analyse de spectres gamma de Vesta par des méthodes de séparation aveugle de source. Cette ligne de recherche a été motivée par le succès de l'analyse en composantes indépendantes (ICA) de spectres gamma enregistrés par un détecteur au germanium (HPGe) placé à bord de la sonde lunaire Kaguya (2007-2009). Cette analyse a permis de séparer les apports élémentaires de Fe, Th et K [Forni *et al.* , 2009]. Malheureusement, l'utilisation de l'ICA dans le contexte de Vesta ne s'est pas couronnée du même succès. La principale raison tient à la nature différente des capteurs embarqués sur Kaguya et sur Dawn, un capteur HPGe ayant une bien meilleure résolution spectrale qu'un capteur BGO comme celui de Dawn. Aussi, ce chapitre vise-t-il plus à déchiffrer les facteurs clés qui font de la séparation aveugle de source un outil utile ou pas pour l'analyse de spectres BGO. Pour cela, il est apparu pertinent de reprendre l'analyse des données du capteur BGO de Lunar Prospector, très similaire à celui de Dawn afin de comparer la capacité de ces méthodes statistiques à extraire de l'information sur des objets assez différents, mais observés de la même façon. Par ailleurs, l'intérêt pour les données de Lunar Prospector est qu'elles ont déjà fait l'objet d'une interprétation poussée, à travers une procédure de démixage basée sur des spectres élémentaires synthétiques [Prettyman *et al.* , 2006].

Ce chapitre donc commencera par une brève description du principe de la spectroscopie gamma appliquée aux sciences planétaires largement inspirée par l'article de Prettyman [2006]. Puis, il exposera le fonctionnement des algorithmes de séparation aveugle de source, en se concentrant sur l'analyse en composante indépendante (ICA) et la factorisation en matrices positives (NMF). Suivront différents tests pour mesurer l'incidence de l'écart que les données réelles présentent toujours avec le cadre optimal de travail de ces méthodes statistiques, à savoir qu'elles s'appuient sur l'hypothèse d'un mélange linéaire de sources. On présentera aussi deux aspects importants dans ce type de traitement de données qui résident d'une part dans l'impact du signal de fond "*background*" sur la restitution de sources et d'autre part celui de la variabilité des abondances chimiques, modélisé avec des spectres artificiels de type lunaire. Enfin, seront exposés les résultats de ces algorithmes de séparation appliqués aux spectres gammas réels de la Lune et de Vesta.

La modélisation de la différenciation de Vesta

Le second aspect décrit dans le chapitre 3 de cette thèse s'articule autour d'un modèle de migration de magma pour étudier le magmatisme de Vesta et comprendre la nature de sa croûte. Dans la mesure où les résultats de la mission Dawn sont venus confirmer le lien entre Vesta et les HED, on dispose d'une grande quantité de données minéralogiques et géochimiques qu'il est pertinent de replacer dans le cadre des caractéristiques physiques et morphologiques de l'astéroïde déterminées par la sonde. C'est précisément le cas du grand bassin d'impact de Rheasilvia, dont certains modèles hydrodynamiques de collision suggèrent qu'il offre une coupe géologique de la croûte sur près de 80 km d'épaisseur (voir la Figure 1**e**). Mais bien avant, il convient de répondre à certaines questions relevant de la genèse des HED. Les nombreuses hypothèses formulées depuis longtemps naviguent globalement entre le paradigme de la fusion partielle du corps parent [Stolper, 1975] et celui de sa cristallisation progressive après une fusion totale [Ruzicka *et al.* , 1997]. La mission Dawn a suscité un regain d'intérêt pour ces questions et quelques études se sont attachées récemment à comprendre dans le détail la différenciation de Vesta. En particulier, elles montrent que cette fusion totale est impossible dans la mesure où la principale source de chaleur au cœur du processus de différenciation, l'^{26}Al, est extraite très vite vers la surface par la migration des premières fractions de liquide silicaté produites [Moskovitz & Gaidos, 2011], l'aluminium étant essentiellement contenu dans le minéral le plus fusible du matériel chondritique : le plagioclase.

Toutefois, ces études se basent sur des modèles simplifiés de migration des magmas comme les modèles en boîtes développés par [Neumann *et al.* , 2014]. Un formalisme d'équations homogénéisées pour la description d'écoulement bi-phasique, développé depuis de nombreuses années [Drew, 1971; McKenzie, 1984; Drew & Passman, 1999] est couramment utilisé pour l'étude de la migration des magmas sous les dorsales océaniques. Ce cadre théorique, tout-à-fait adapté à la modélisation de la différenciation de Vesta, a d'ailleurs été utilisé pour modéliser la différenciation métal-silicate dans les embryons planétaires [Šrámek *et al.* , 2012]. Néanmoins, l'utilisation simple de ce type de formalisme n'est pas suffisent pour rendre compte de la nature minéralogique des HED. Aussi, pour la première fois, ce type de modèle a été adossé à un modèle thermodynamique simplifié permettant de suivre l'évolution de la composition minéralogique (Anorthite-Pyroxène-Olivine) des liquides et des solides.

Ce troisième chapitre, présentera en premier lieu le formalisme des équations de la compaction, puis le modèle développé en géométrie sphérique réduite à une dimension (le rayon) et les tests réalisés dans le cadre simple du drainage du liquide contenu dans un corps sphérique. Il décrira ensuite l'effet de la mobilité des sources de chaleur due à la grande fusibilité du minéral porteur et précisera le taux global de fusion d'un corps comme Vesta en fonction de sa date d'accrétion — la quantité d'^{26}Al dont la demie vie est de 700 000 ans est d'autant plus importante que le corps se forme tôt. Enfin seront présentés des modèles d'évolution de Vesta tant sur le plan thermique et minéralogique, mais aussi sur celui de la composition en éléments traces. Ces modèles seront finalement discutés sur la base de nos connaissances des HED et des apports récents de la mission Dawn.

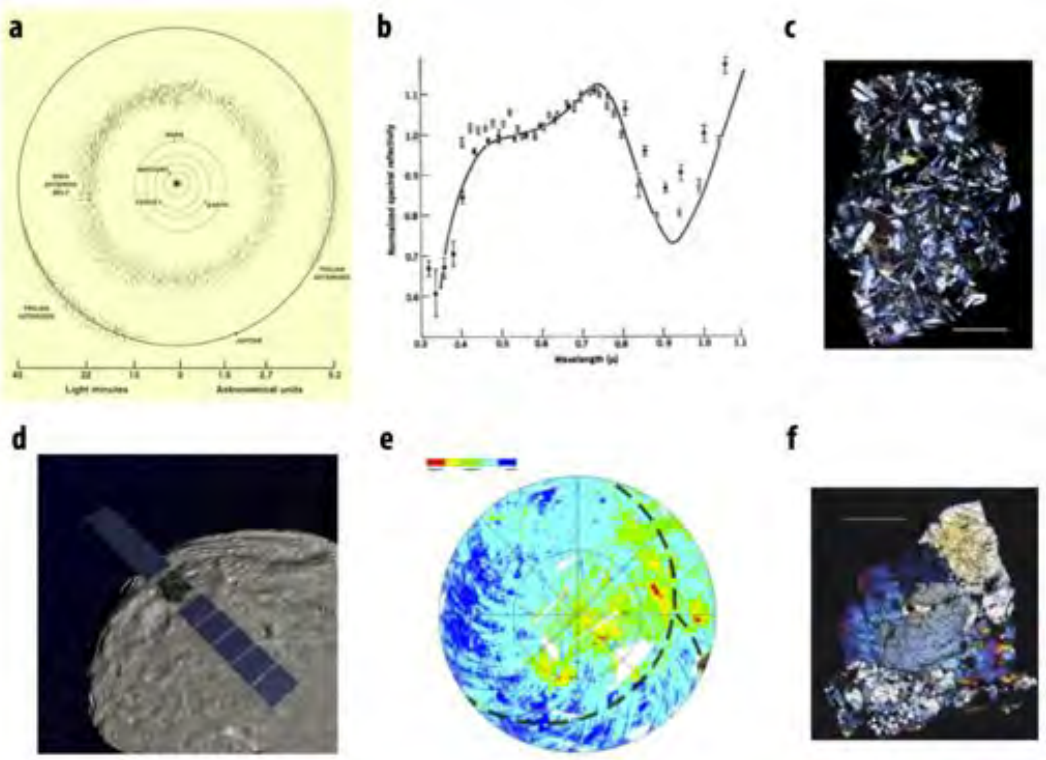

Figure 1: **a** Le système solaire interne et la ceinture d'astéroïde, vestige de la formation des planètes telluriques. Vesta appartient à la partie interne de la ceinture d'astéroïde. **b** Spectres de réflectance visibles infrarouge de Vesta (rond noirs et blancs) et d'une eucrite basaltique (ligne noire), premiers indices du lien de parenté entre Vesta et les météorites HED, tiré de McCord *et al.* [1970]. **c** Lame mince d'une eucrite basaltique vue en lumière transmise, polarisée-analysée, probable échantillon de la croûte supérieure de Vesta, d'après McSween *et al.* [2010], l'échelle donnée par le trait blanc est de 2.5 mm. **d** Vue d'artiste de la sonde Dawn, superposée à une photographie de Vesta par cette dernière prise en 2011 — crédits NASA/JPL. Grâce à cette sonde, une cartographie morphologique, minéralogique et chimique précise de la surface de Vesta a été produite, au moyen de deux caméras à prise de vue, un spectromètre visible infrarouge et un détecteur de rayons gamma et de neutrons. Le suivi de la position de la sonde a également permis de mesurer le champ de pesanteur de Vesta. **e** Carte synthétique des observations visible-infrarouge de la sonde Dawn du pôle sud de Vesta, avec le contour du bassin de Rheasilvia en pointillés noirs, fenêtre sur la croûte inférieure de Vesta [McSween *et al.* , 2013]. La couleur rouge indique une forte proportion de diogénites tendis que le bleu correspond à une plus forte teneur en eucrites. **f** Vue microscopique, en lumière polarisée-analysée d'une diogénite à olivine, roche provenant sans doute de la partie profonde de la croûte de Vesta. L'échelle donnée par le trait blanc est de 2 mm — crédits NASA/JPL-Caltech/Hap McSween (University of Tennessee), Andrew Beck et Tim McCoy (Smithsonian Institution).

Chapter 1

Introduction

Contents

Vesta and Ceres are the two largest bodies of the main asteroid belt located between Mars and Jupiter. These two bodies have been aknowledged under the status of "surviving planetary embryos", which motivated the Dawn NASA's space mission, within which this thesis was realized, including analysis of gamma ray spectra and a modelling study of the differentiation of Vesta. This asteroid is the largest silicate body of the asteroid belt and, based on visible-infrared spectroscopy, has been considered for about forty years, as the parent body of the HED meteorites, a family of extraterrestrial rocks representing about 5 % of the collected falls. This introduction aims at recalling the main lines of early solar system formation, what is the main asteroid belt, the interest of the bodies that populates it, the importancy of the study of meteorites, the unique status of asteroid 4-Vesta, and within this framework, the purposes and outline of this thesis.

1.1 Early solar system - The asteroid belt

Three centuries ago, Swedenborg [1734] imagined that the Sun and the planets could result from the gravitational collapse of a nebula of gas and dust that tends to flatten as it rotates, thus forming an accretion disk. Today, many low mass stars from our galaxy are observed and display accretion disks around them, illustrating different stages of the formation of planetary systems [Carrasco-González *et al.* , 2009; Williams & Cieza, 2011]. The gravitational collapse of the gas and dust cloud may be facilitated by the explosion of a supernova which is also supported by the traces of short lived radioactive elements in meteorite samples [Gounelle *et al.* , 2009]. At the center of the nebula, when a critical mass is reached, thermonuclear reactions ignite forming a primitive star which radiates energetic particles outward.

As the accretion disk cools down, solids such as silicates can condense. The most volatile materials, such as water and CO_2 ice are only able to solidify far from the star

because of the action of the outward stellar wind and of the radial thermal gradient. This results in the first and most obvious compositional gradient that a accretionnary disk can display, but both the organisation of solar system bodies and the textures of meteorites show that reality is not this simple.

The process by which the first microscopic solid particles were converted into rocks and boulders is a complex issue, which involves gas & dust interactions. The accretion of small bodies of radius $R \sim$1 - 100 km, can be numerically simulated by a hierarchical collisional process which takes place on relatively short time scales ($\sim 10^4 yr$) [Weidenschilling, 2011].

While the accretion process seems to have been completed in the inner solar system, it appears to have been perturbed in the region occupied by the main asteroid belt [Petit *et al.* , 2001]. Instead of finding a planet between Mars and Jupiter, ten asteroids with R $>$ 100 km were discovered during the first half of the 18^{th} century. Ceres (R = 476 km, 1802, Giuseppe Pazzi), Pallas (R= 273 km, 1802, Heinrich Olbers), Hygiea (R = 204 km, 1849, Annibale de Gasparis) and Vesta (R = 262 km, 1807, Heinrich Olbers) representing half of the mass of the asteroid belt. Today it has been estimated that this region, located between 2.5 and 3 AU from the Sun, probably contains a million rocky bodies larger than one kilometer. Two hundred of them are known to be larger than one hundred kilometers [de Elia & Brunini, 2007].

Asteroids can be classified based on the spectral characteristics of their surface. Although these spectral types may not always be directly associated to a specific surface composition [Bus & Binzel, 2002], the two most common types of asteroids (C and S) are broadly consistent with the two most abundant families of meteorites, carbonaceous and ordinary chondrites respectively [DeMeo *et al.* , 2015]. The most important difference between these two types is the lower albedo of C type asteroids, with evidence of hydrated minerals, while S type appear brighter, drier silicate dominated bodies. The general color gradient of the asteroids' surface across the main belt used to be interpreted as a gradient in composition where wetter bodies (C) are further from the Sun than drier bodies (S). This was thought to represent the thermal gradient in the primordial solar nebula [Gradie & Tedesco, 1982]. More recently, the refinement and the increase in the number of telescopic observations have given access to the spectral types of asteroids as small as 5 km. The compilation of these data show that spectral types are in fact well mixed across the main belt [DeMeo & Carry, 2014], as illustrated in Figure 1.1.

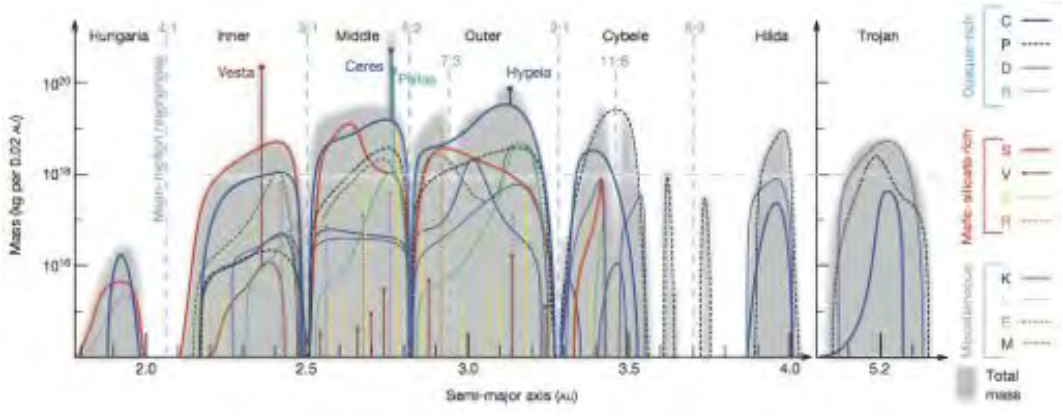

Figure 1.1: Figure 3 from [DeMeo & Carry, 2014]:"The compositional mass distribution throughout the asteroid belt out to the Trojans. The grey background is the total mass within each 0.02-AU bin. Each colour representes a unique spectral class of asteroid, denoted by a letter in the key. The horizontal line at 10^{18} kg is the limit of the work from the 1980s. The upper portion of the plot remains consistent with that work, but immense detail is now revealed at the lower range."

On the other hand, an important outcome from the dynamical models of planetary accretion, is that the giant gaseous planets probably underwent an inward and then an outward migration of their orbits during their formation, due to friction with the gas & dust of the primitive nebula and gravitational interactions with growing protoplanets. This model, illustrated in Figure 1.2, is able to explain the presence of an asteroid belt between the orbits of Mars and Jupiter, the compositional diversity of this region with radial mixing of dry and hydrous bodies, and last but not least, the small size of Mars, a feature that could not be explain by previous dynamical models [Walsh *et al.* , 2011, 2012].

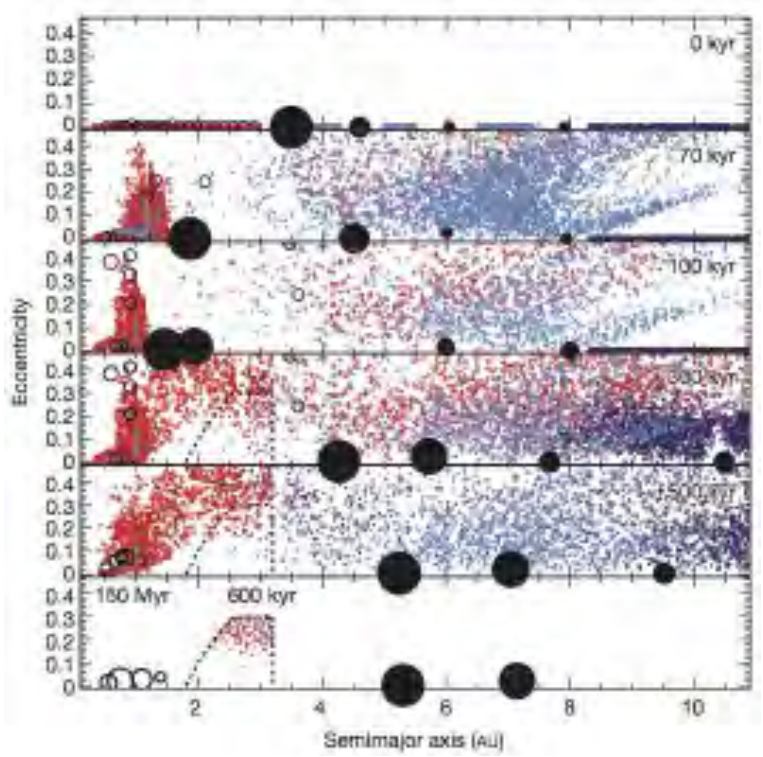

Figure 1.2: [Walsh *et al.* , 2011] "The evolution of the small-body populations during the growth and migration of the giant planets. Jupiter, Saturn, Uranus and Neptune are represented by large black filled circles with evident inward-then-outward migration, and evident growth of Saturn, Uranus and Neptune. S-type planetesimals are represented by red dots, initially located between 0.3 and 3.0 AU. Planetary embryos are represented by large open circles scaled by 1/3 of the mass (but not in scale relative to the giant planets). The C-type planetesimals starting between the giant planets are shown as light blue dots, and the outer-disk planetesimals as dark blue dots, initially between 8.0 and 13.0 AU. For all planetesimals, filled dots are used if they are inside the main asteroid belt and smaller open dots otherwise. The approximate boundaries of the main belt are drawn with dashed curves. The bottom panel combines the end state of the giant planet migration simulation (including only those planetesimals that finish in the asteroid belt) with the results of simulations of inner disk material (semimajor axis a < 2) evolved for 150 Myr, reproducing successful terrestrial planet simulations."

The formation of the asteroid belt took place at a time at which small solid bodies were in the process of accretion and/or differentiation. As a result, the asteroid belt contains undifferentiated bodies, differentiatied bodies and fragment of differentiated bodies. More importantly, the asteroids did not experience accretion into large bodies and thus, they are witnesses of early stages of the differentiation process that have been erased on large terrestrial planets. In this framework, the purpose of the space mission Dawn (NASA) was to explore the two largest bodies of this "fossilized" region, Ceres and Vesta. The

dwarf planet Ceres appears as a hydrated proto-planetary body which may or may not be differentiated [Zolotov, 2009], while the asteroid Vesta is broadly considered today as a surviving example of an early differentiated silicate body. One notable feature of Vesta, as discussed further below, is that it has been proven to be the parent body of a family of meteorites: the howardite - eucrite - diogenite clan (HED) [McSween *et al.* , 2010]. Meteorites and asteroids are intimately related as first suggested by visible and near infrared spectroscopy. The study of these rock samples is fundamental and provides information on the evolution of the early solar system that could not be unraveled from telescopic/space exploration alone.

1.2 Early solar system - Meteorites

Many pieces information can be extracted from the study of the composition and texture of rock samples. It can be determined whether a sample experienced heating and melting, what the pressure, temperature and oxidation conditions were. Furthermore, a number of isotopic systems, based on the decay of radioactive elements, can be used to constrain their thermal history. Samples coming from various locations of the solar system are constantly delivered to the Earth in the form of meteorites [Farinella *et al.* , 1994]. Sometimes, these rocks can be related to a parent body: as for lunar and martian meteorites. However, the link between a meteorite sample or a group of meteorites and a parent body that can be observed is not always established.

For this reason, meteorites are classified as a function of their mineralogy, compositional and textural characteristics. This classification, thoroughly reviewed by Krot *et al.* [2014] (Figure 1.3), divides meteorites into two main categories: chondrites and achondrites. Chondrites show silicate spherules called chondrules, refractory inclusions and a matrix that contains both metal and silicates. Most of these features are thought to be acquired within the solar nebula before being incorporated into planetary embryos. On the other hand, the textures of achondrites indicate that they have undergone heating, melting and segregation of metal and silicates within small ($R \sim 30-100$ km) bodies, although not all these rocks have undergone complete differentiation. This is also the general scheme within which the fact that rocky planets have an inner structure consisting of a metallic core, a silicate mantle and a crust is understood [Solomon, 1980]. Both chondrites and achondrites can show characteristics aquired in the primitive solar nebula, before being incorporated into planetary embryos, and features acquired afterwards. For example, H - chondrites show evidence of an important thermal metamorphism that requires a parent body with $R \sim$100 km. Most of the time, nebular features are erased in the rocks that have undergone differentiation, but remnants of chondrules, that are most likely nebular features, are present within some primitive achondrites. Also, meteorites can be viewed as samples of: (1) the primitive solids condensed in the solar nebula (2) various depths from within ancient disrupted rocky bodies (3) samples of rocky bodies that illustrate different stages of the planetary differentiation process (4) as many examples of planetary bodies that have not had the same differentiation history.

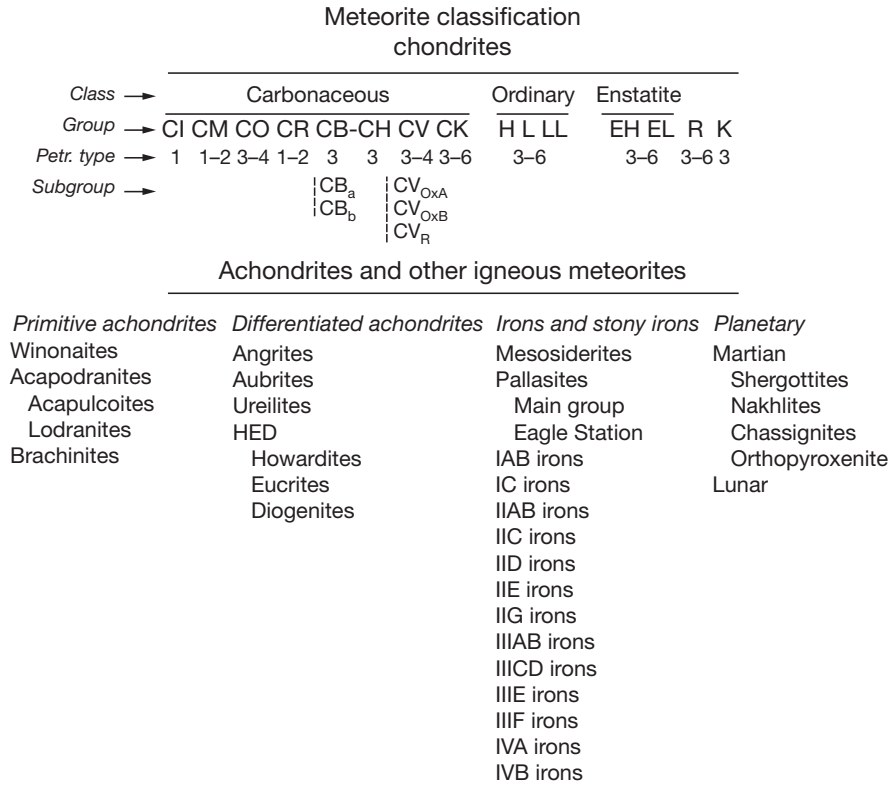

Figure 1.3: "Classification of meteorites excluding ungrouped meteorites" from Krot *et al.* [2014]. Meteorites form two main categories: chondrites and achondrites. Chondrites are subdivided into three main classes, carbonecous, ordinary and enstatite chondrites. Achondrites include four main categories. Primitive achondrites shows traces of melting but have not undergone complete segregation between metal and silicate. Stony and stony iron meteorites show evidences of partial or total segregation of metal and silicates. Other meteorites exhibiting igneous lithologies have been established to come from the Moon and Mars.

Chondrites

Chondrites get their name from chondrules they contain, which are glassy beads that can be entirely vitreous, but that can also contain grains of olivine, pyroxene, metal and sulfide. Chondrules are cemented by a matrix that includes grains of metal, sulfide, refractory inclusions and sometimes hydrated minerals (Figure 1.4). Refractory inclusions called CAI, which stands for Calcium-Aluminum rich inclusions are the oldest known solids of the solar system [Amelin & Ireland, 2013]. As the collected samples display an important compositional diversity, several chondritic clans and groups can be defined [e.g. Wasson & Kallemeyn, 1988] (Figure 1.3). There are three main compositional groups, ordinary chondrites the most abundant, carbonaceous chondrites that contain hydrated minerals and an organic matrix and enstatite chondrites named after their important content in Mg-rich pyroxenes.

The origin of the chondritic components is uncertain. Chondrules appear to have formed in dust rich environments as droplets of molten silicates during heating events lasting a few hours or days, 1 - 3 Myr after the formation of refractory inclusions [DeMeo *et al.* , 2015]. There are two families of models according to Krot *et al.* [2009]. (1) "CAI, chondrules and most of the matrix materials formed in the inner (1-4 AU) disk as a result of multiple transient heating events caused by shock waves that thermally processed presolar dust that was initially mostly amorphous" (2) or CAI and chondrules were formed in the

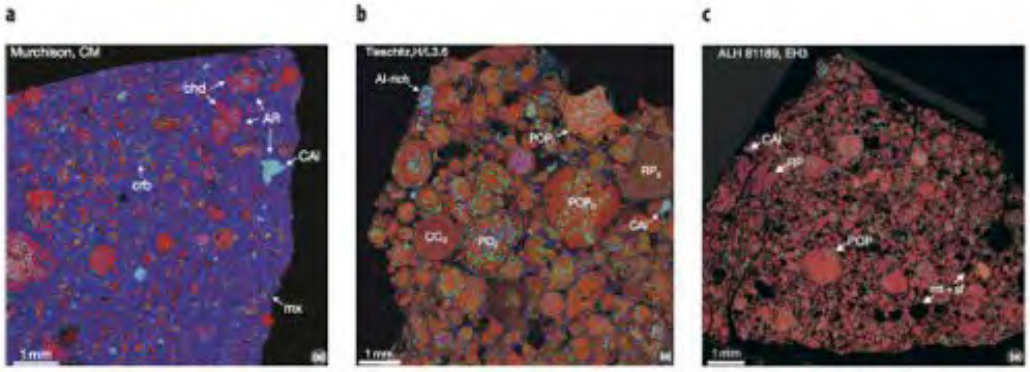

Figure 1.4: Microscopic elemental maps of thin section of the three main classes of chondrites from Krot *et al.* [2014] "**a** Combined elemental map (Mg in red, Ca in green, Al in blue) of the CM carbonaceous chondrite Murchison. Murchison contains abundant magnesian chondrules (red) with porphyritic textures, CAIs (bluish), and heavily hydrated matrix (purple) containing relatively rare grains of carbonate (green). Most chondrules and CAIs are surrounded by fine-grained accretionary rims. AR accretionary rim, CAI = Ca-Al rich inclusions, chd = chondrule, crb = carbonates. **b** Combined elemental map and (b) Mg Ka X-ray elemental map of the H/L3.6 ordinary chondrite Tieschitz. It contains abundant type I and type II chondrules of porphyritic olivine (PO) porphyritic olivine - pyroxene (POP), porphyritic pyroxene (PP), radial pyroxene (RP), and cryptocrystalline (CC) textures; Al-rich chondrules and CAIs are rare. Most chondrules are surrounded by Al-rich (bluish) fine-grained material composed of a nepheline-like phase resulted from in situ aqueous alteration. **c**. Combined elemental maps of the EH3 enstatite chondrite ALH 81189. The EH3 chondrite ALH 81189 is composed of enstatite-rich grains (red) and metal - sulfide nodules, chondrules are rare, CAIs are very rare, matrix material is very minor (difficult to recognize)."

framework of the X-wind model where the magnetic field of the young star interacts with the magnetic field of the circumstellar disk to produce a gap between the star and disk and inward and outward winds.

Achondrites

Achondrites are divided into (1) primitive achondrites that exhibit metamorphic textures, as well as relatively low degrees of partial melting and melt extraction. They have compositions that are geochemically moderately fractionated from chondritic compositions. (2) differentiated achondrites that underwent extensive melting and differentiation exhibit igneous textures and are highly fractionated with respect to the nebular material [Mittlefehldt, 2005]. The differentiated meteorites are further divided on the basis of their metal contents into stony, stony-iron, and iron meteorites. Primitive achondrites, such as the acapulcoites, lodranites, brachinites and ureilites, are roughly similar in composition to chondrites but they show of evidence of recrystallization and partial melting [Rubin, 2007; McCoy *et al.* , 1996]. Acapulcoites exhibit traces of partial melting but with limited silicate melt migration. Whether brachinites, which are olivine-rich achondrites, are residues of low degree of partial melting or magmatic cumulates is still a matter of debate [Krot *et al.* , 2014]. Other rocks seem more representative of the solid residue that was left behind by the migration of liquid silicates. Lodranites might thus have experienced 0 to 15% percent of partial melting, the ureilite parent body may have reached at least a melting degree of 15% [Taylor *et al.* , 1993]. A few examples of primitive achondrites are shown in Figure 1.5.

Iron meteorites, dominated by metallic iron-nickel alloys and iron-nickel sufides pro-

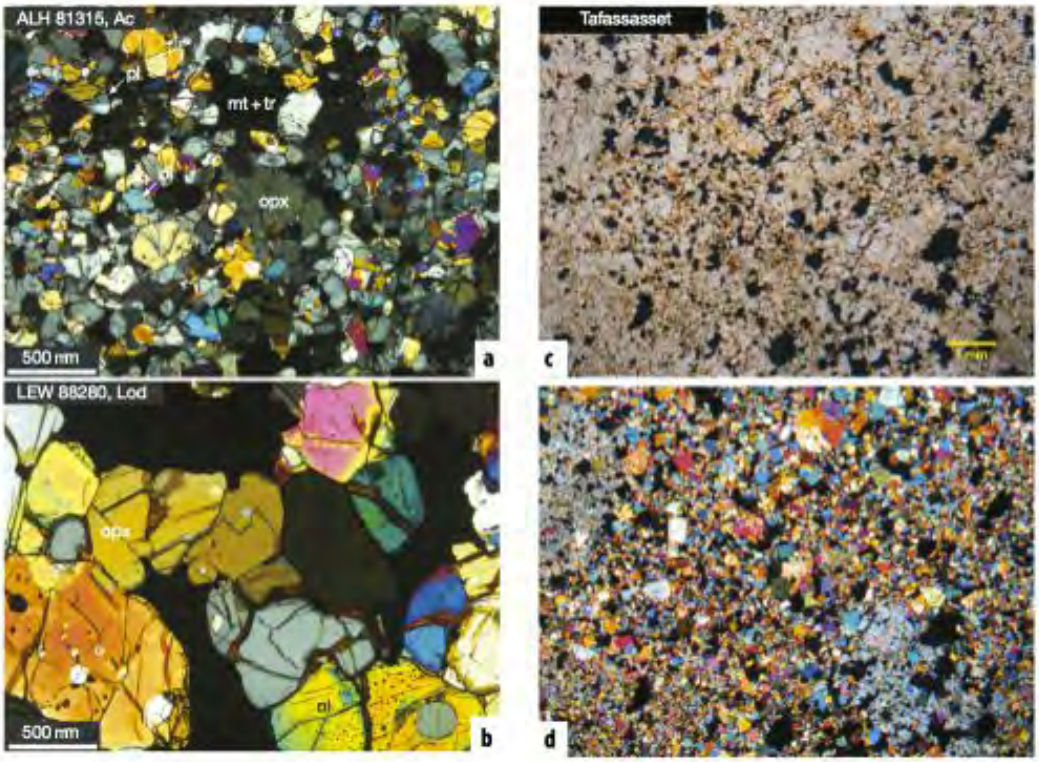

Figure 1.5: Photomicrographs of primitive achondrites from [Krot *et al.* , 2014] "**a** Acapulcoite ALH 81315 and **b** lodranite LEW 88280 have similar mineralogy (mostly orthopyroxene, olivine, Cr-diopside, Na-plagioclase, FeNi-metal, and troilite), but different grain size. Photograph courtesy of G. Benedix. **c** Plane-polarized and **d** cross-polarized light micrographs showing the general texture of Tafassasset. Tafassasset is dominated by olivine (70 vol%) with minor pyroxene and plagioclase. Opaque areas are dominantly FeNi-metal, which makes up 7% of the meteorite. Sulfide is minor ($< 2\%$)."

vide evidence of complete metal segregation. This family of meteorites, which comprises 14 chemical groups, likely represent the cores of fifty different small bodies [Goldstein *et al.* , 2009]. Mesosiderites have a FeNi metallic component intimately mixed with a stony, basaltic component, possibly formed during the collision of a differentiated body with an iron asteroid [Lorenz *et al.* , 2010]. Pallasites are mixtures of metal, sulfide and large olivine grains. They might originate from the core mantle boundaries of small bodies [Yang *et al.* , 2010].

Whether it takes place during the late stage of the crystallization of an ancient magma ocean of a given rocky planet [Elkins-Tanton, 2012], or from the partial melting of the mantle [McKenzie, 1984], the upward migration of liquid silicates is responsible for the formation of differentiated crustal material, which is less refractory than the underlying mantle. Stony achondrites seem to account for this silicate differentiation. They include three main families: aubrites, angrites and the howardite - eucrite - diogenite clan.

The aubrites are breccias made of almost pure enstatite (Mg-rich pyroxene) with lesser amounts of albitic plagioclase, nearly pure diopside (Mg-Ca rich pyroxene) and forsterite (Mg-rich olivine). Despite their brecciated texture their pyroxenitic clasts are clearly of igneous origin [Krot *et al.* , 2014].

Angrites have basaltic compositions, mainly consisting in Ca-Al-Ti-rich pyroxene, Ca-rich olivine and plagioclase. They are divided into slowly cooled plutonic angrites with homogeneous mineral compositions and quenched volcanic angrites with highly zoned minerals. Jambon *et al.* [2005] suggest that the presence of $CaCO_3$, although rare in

these meteorites [Krot *et al.* , 2014], might be the key to generate angrite-like melts because "melting in the presence of carbonate generates low SiO_2 melts with superchondritic CaO/Al_2O_3 ratios at moderate fractions of melting" which is an important specific feature of this group of meteorites.

The howardite - eucrite - diogenite clan form a cogenetic family of meteorites that are most likely from asteroid 4-Vesta. They include pigeonite-plagioclase basalts and gabbro and cumulate of orthopyroxenes. Their main petrological and geochemical features are most extensively reviewed in the next section based on McSween *et al.* [2010].

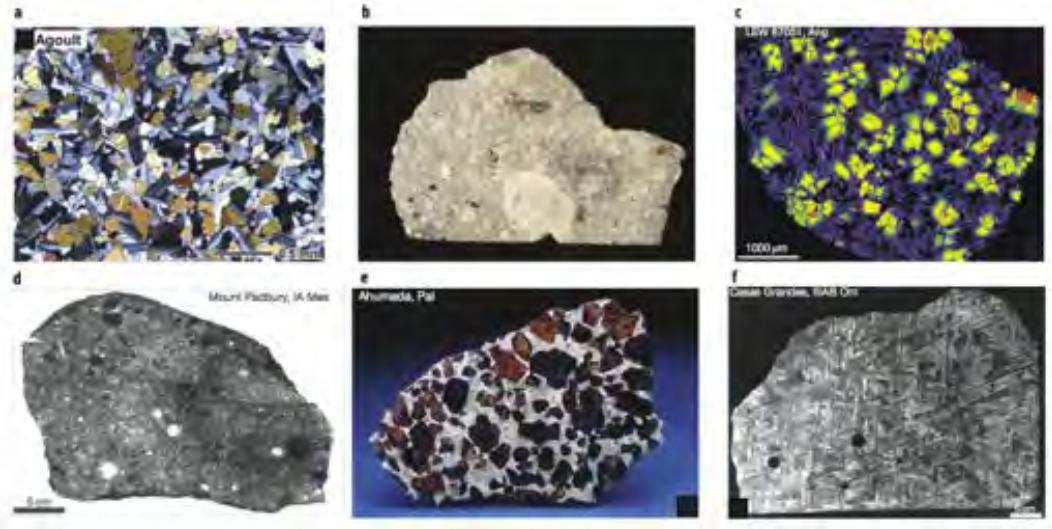

Figure 1.6: **a** Microscopic view in cross-polarized light of eucrite meteorite Agout from [Yamaguchi *et al.* , 2009] "The granulitic eucrite Agoult has a remnant subophitic textures consisting of anhedral pyroxene and elongated plagioclase." **b-e** Compilation of a few examples of differentiated achondrites from Krot *et al.* [2014]: "**b** Hand-specimen photograph of the Bustee aubrite showing the brecciated texture of the rock (9 cm in horizontal dimension). Photograph courtesy of the Smithsonian Institution. **c** Elemental maps in Mg Ka X-rays of angrite LEW 8705. This ophitic-textured rocks contain large, subhedral to euhedral grains of magnesian olivine (yellow and red) set in an ophitic textured groundmass of euhedral laths of anorthite (black) intergrown with euhedral to subhedral, highly zoned Al-Ti-diopside (purple) and ferroan olivine (blue and green). Photograph courtesy of G. McKay. **d** The type 1A mesosiderite Mount Padbury having numerous centimeter-sized silicate and metal clasts dispersed in a finely divided metal - silicate matrix **e** The pallasite meteorite Ahumada (15 cm in horizontal dimension) contains angular and subangular olivine grains in metal. **f** Polished and etched slabs of iron meteorite of the medium octahedrite IIIAB iron Casas Grandes."

Although chondrites appear more primitive from a compositional point of view, their cooling history does not always preceed that of differentiated meteorites. H-chondrites are the most oxidized group of the ordinary clan, showing various grades of metamorphism. Thermochronological data avalaible for these meteorites can be used to place constraints on the accretion history of their parent body in the framework of thermal models [Monnereau *et al.* , 2013]. Elkins-Tanton *et al.* [2011] proposed that certain chondrite groups may originate from the external region of a partially differentiated parent body. Figure 1.8 shows the cooling history of important groups of chondrites and achondrites based on radiochronological ages compiled by Elkins-Tanton *et al.* [2011]. This illustrates the fact that chondrite ages can be younger than those of achondrites.

1.3 Heat sources

Nebular chondritic material has not always been processed by differentiation within planetary embryos. This raises the question of what the potential heat sources were that allowed some planetary embryos to differentiate while others did not. Releasing of gravitational potential energy by collisions can cause important melting degrees for bodies as large as the Earth, but this is not possible for bodies whose size is lower than $\sim$ 1000 km [e.g. Moskovitz, 2009], as illustrated in figure 1.7. Despite this fact, differentiated achondrites are inferred to come from relatively small bodies (R $\sim$ 30 - 100 km). The study of ^{26}Mg content of meteorites has led to the conclusion that a part of ^{26}Mg is the daughter element of radioactive ^{26}Al, which is extinct today [Lee *et al.* , 1977]. An initial ratio ^{26}Al/^{27}Al of the solar nebula can be inferred to be $\sim 5 \times 10^{-5}$ from the study of CAIs [MacPherson *et al.* , 1995]. As aluminum is a major element in silicates, ^{26}Al which decays with a half-life of $\sim$ 0.7 Myr was able to significantly melt planetary embryos if they accreted early enough. Another potential heat source is ^{60}Fe which has a comparable decay energy, but the life time of this radioactive element is four times longer than that of ^{26}Al [Castillo-Rogez *et al.* , 2009]. In addition, Quitté *et al.* [2010] show that there probably were important heterogeneities of iron isotopes in the early solar nebula and that the initial $^{60}Fe/^{56}Fe$ ratio of the reservoir from which angrites and eucrites originated could be as low as 2×10^{-8}, which is three orders of magnitude lower than the initial ^{26}Al/^{27}Al ratio.

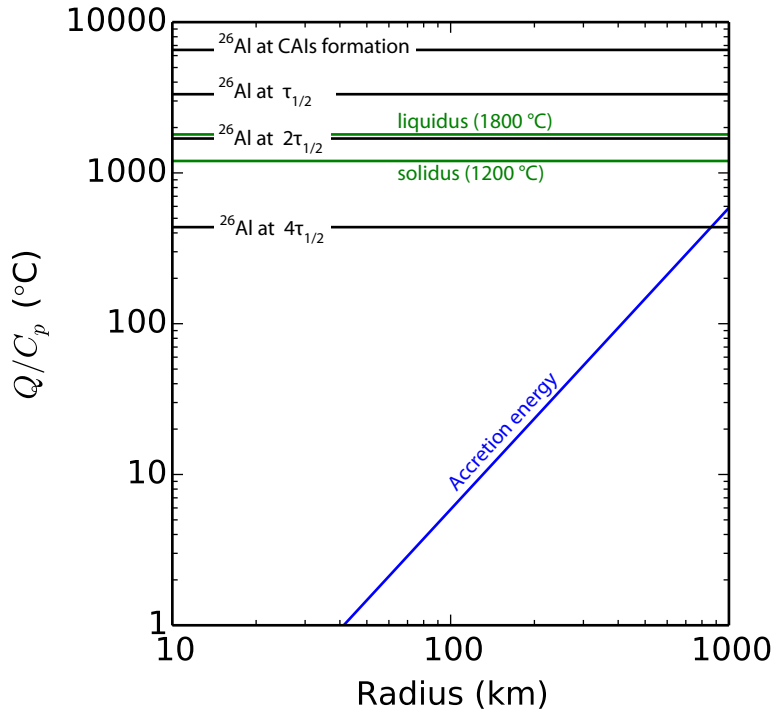

Figure 1.7: Potential temperature increase resulting from accretion energy (blue line), corresponding to the conversion of gravitational energy into heat, it is given by $4\pi G\rho R^2/5$. The potential temperature stemming from ^{26}Al decay is overplotted in black, $\tau_{1/2}$ = 0.7 Myr. ^{26}Al decay is able to cause melting in early solar system bodies with R $<$ 1000 km because the onset of silicate melting is near 1000 - 1300 °C. A body with the size of Vesta would increase in temperature by only a few tens of degrees from the accretion energy. The density is taken as ρ = 3500 kg/m^3, the specific heat used is C_p = 1000 J/Kg/K.

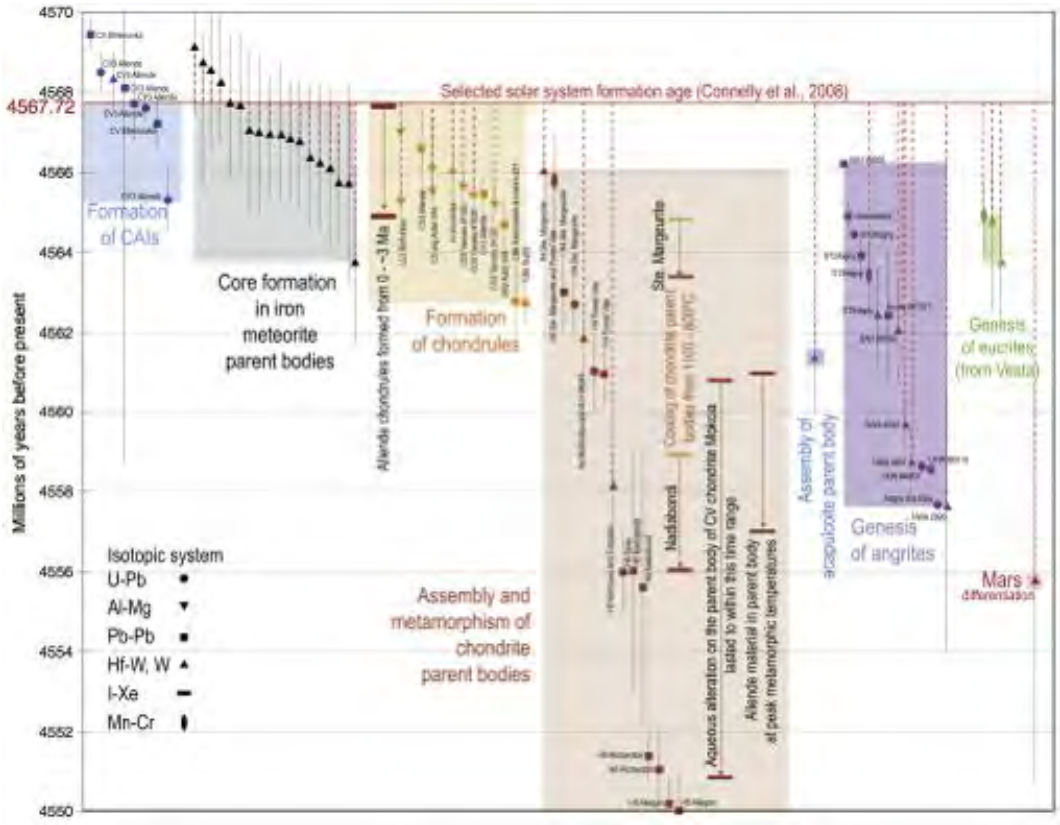

Figure 1.8: Figure 7 from Elkins-Tanton *et al.* [2011]:"Age constraints on meteorites and parent body evolution. Red dashed lines indicate ages calculated relative to the selected oldest age of CAI. The early ages of CV chondrules and CV meteorites evidence for relatively protracted thermal metamorphism indicate an early accretion age for the CV parent body."

1.4 HED meteorites

Howardites, eucrites and diogenites represent about 5% of the extraterrestrial rocks collected on the surface of the Earth. They are broadly considered as samples of Vesta although they may not necessarilly all come from this asteroid [Mittlefehldt, 2005; McSween *et al.* , 2010; Mittlefehldt *et al.* , 2015]. Although eucrites and diogenites are magmatic rocks, they are mostly delivered to Earth as impact breccias. These breccias are qualified as monomict if all clasts are petrologically similar, and polymict if several clasts are disimilar mineralogically, chemically or texturally. Howardites are polymict breccias that typically include 2/3 of eucrite clasts and 1/3 of diogenite clasts. In addition, howardites can contain minor proportions of clasts of various nature, whose origin is mostly related to impact melting processes or exogenic contamination. Although the remainder of this chapter may refer to HED meteorites that are breccias, it mainly concentrates on the magmatic history of eucrites and diogenites, before they underwent impact gardening at the surface of Vesta. The description of eucrites and diogenites developped further below, concentrates on their magmatic features, while those related to the impact history are not extensively treated.

1.4.1 Petrology

Eucrites

As presented by McSween *et al.* [2010], eucrites are basaltic and gabbroic rocks. Basaltic eucrites have a fined to medium-grained, ophitic to subophitic texture, some-

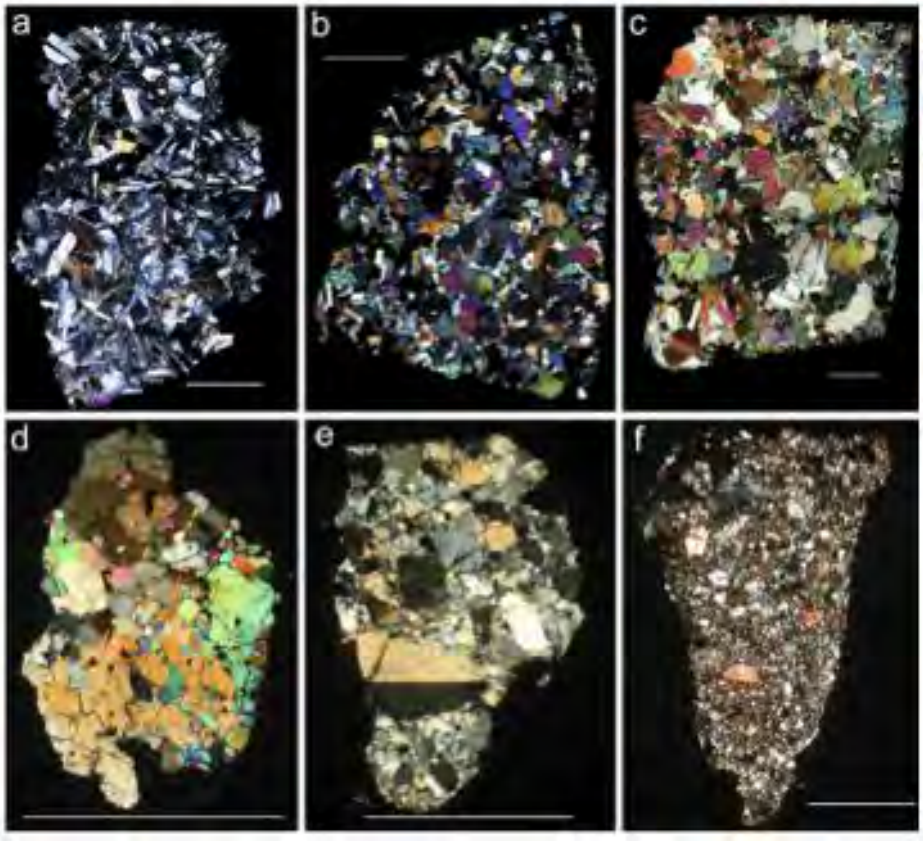

Figure 1.9: Microscopic views of HED meteorites seen in cross-polarized light from McSween *et al.* [2010]: " **a** QUE 97053 basaltic eucrite, with subophitic texture of plagioclase grains (gray laths) partly enclosed by pyroxene; **b** metamorphosed EET 90020 basaltic eucrite, with recrystallized texture; **c** Moore County cumulate eucrite; **d** GRA 98108 olivine diogenite; **e** QUE 99050 diogenite, with brecciated texture; **f** PCA 02019 howardite, a breccia composed of eucrite and diogenite clasts. all scale bars are 2.5 mm."

times even vitrophyric [Delaney *et al.* , 1984], which reflects a rapid cooling at or near the surface. These rocks are dominated by iron rich pyroxenes, pigeonite, augite, sometimes orthopyroxene and calcic plagioclase. There can be lesser amounts of metal, troilite, chromite, ilmenite and silica. Gabbroic eucrites, also known as cumulate eucrites, have coarser grains but a mineralogy very similar to basaltic eucrites. Their pyroxenes are more Mg rich and there tends to be less augite than in basaltic eucrites. Compositional variations in plagioclase (An_{90-96}), ilmenite and chromite are much lower than in basaltic eucrites. Some basaltic eucrites display Mg - zoned pyroxenes, but in most of the other samples, pyroxenes appear as unzoned low Ca pigeonite with finely exsolved augite lamellae [Mittlefehldt *et al.* , 1998], indicating thermal reequilibration. Other eucrites may have undergone further metamorphic recrystallization as can be seen in their granoblastic texture (EET90020, LEW85305). Some eucrites, which show recrystallization, exhibit interstitial tubular silica grains, which indicate that they have experienced remelting. The fact that silica grains sometimes appear in unmetamorphized eucrites suggests a different mode of formation [Mayne *et al.* , 2009]. However, Stannern trend eucrites form a possible evidence for remelting of the first basalts formed at the surface of Vesta as discussed below.

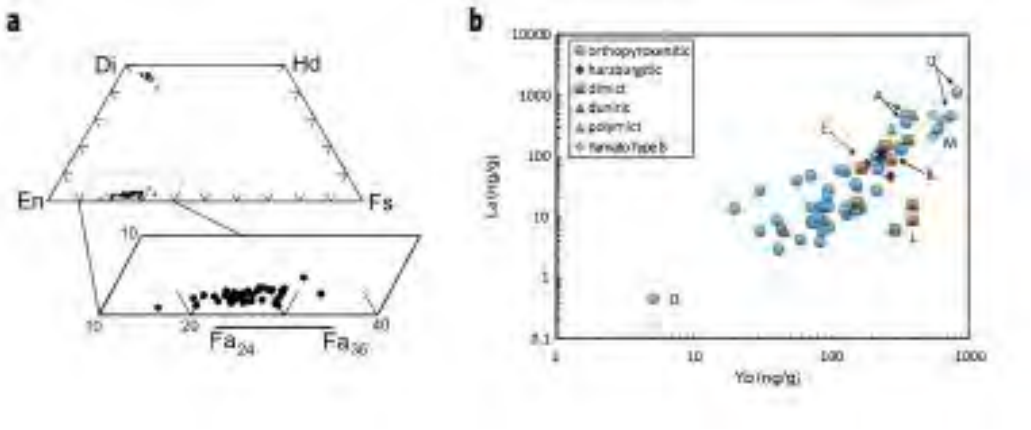

Figure 1.10: The variability of incompatible trace elements is strongly decoupled from that of the mineralogy in diogenites. **a** Compilation of pyroxene and olivine compositions from [McSween *et al.* , 2010] and references therein. **b** Compilation of trace element concentrations (La vs Yb) measured in diogenites from [Mittlefehldt *et al.* , 2011] and references therein. Most data points (blue dots) correspond to orthopyroxenitic lithologies. Dimict and polymict (brown rectangles and green triangles) are breccias where two or more petrological types of diogenites are mixed. Harzburgite here reffers to diogenites including significant fractions of olivine ($\sim$ 30%). One dunite (90% Ol, orange triangle) sample is known in the HED collection.

Diogenites

Diogenites are coarse grained rocks principally made of orthopyroxenes (87 - 99%). The major element chemistry of diogenites varies by only a few percent. Diopside can occur as exsolution lamellae in pyroxenes. Chromite and olivine appear in amounts lower than 10%, and minor phases such as troilite, plagioclase, diopside, silica and metal can be found. A number of diogenites contain significant amounts of olivine (up to 35%) [Sack *et al.* , 1991]. Olivine contained in diogenites generally has a limited range in Mg# (Fo_{70-73}). Harzburgite (Mg-rich orthopyroxene and olivine) clasts have been found [Beck & McSween, 2010], and have been proposed to form by fractional crystallization in small magma chambers. A dunite meteorite MIL 03443 appearing as genetically related to the HED is believed to represent a partial melt residue or crustal cumulate [Mittlefehldt, 2008]. The narrow range in major element composition is usually interpreted as post crystallization equilibrium and not as igneous fractionation [Mittlefehldt, 1994; Fowler *et al.* , 1995]. Several clusters in the Mg# of diogenites suggest separate equibrium source regions [Harriott & Hewins, 1984; Mittlefehldt, 1994]. Cumulate eucrites [Domeneghetti *et al.* , 1995] may have cooled faster than diogenites [Zema *et al.* , 1997], which supports the idea of a deeper origin of the latter. However, the most singular characteristic of diogenites is the impressive range observed in concentrations of incompatible trace elements from one meteorite to another. For example, despite the narrow range in Mg# (Figure 1.10**a**), La varies by 3 orders of magnitude (Figure 1.10**b**).

1.4.2 Petrogenetical models

Vesta's magmatic products show great complexity and there is no consensus on their mode of formation [Mittlefehldt *et al.* , 2011]. Interesting aspects of these meteorites can be put forward by comparing their FeO/MgO ratios to their incompatible element trace (ITE) contents, as illustrated in Figure 1.11. Basaltic eucrites from the "Main Group" have intermediate FeO/MgO ratios and ITE content. Two trends start from the Main Group. The Stannern trend has a limited range of FeO/MgO ratio along with variable and higher

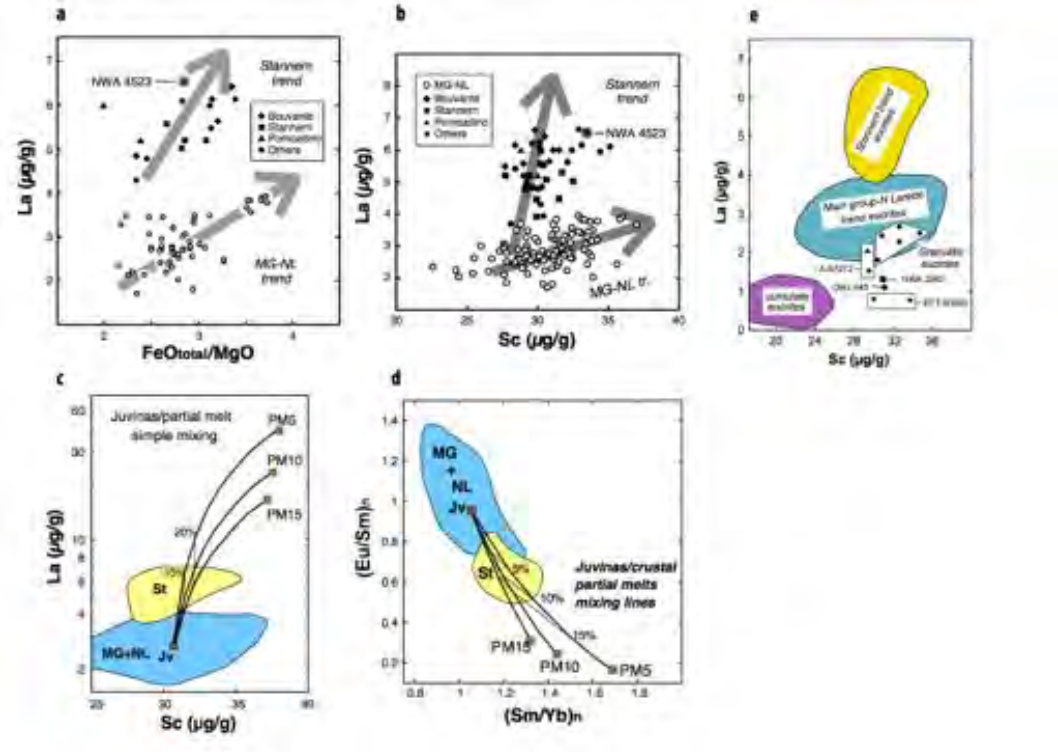

Figure 1.11: **a** - **d** are fom Barrat *et al.* [2010] **e** is taken from [Yamaguchi *et al.* , 2009]. **a** La versus FeO/MgO ratio in basaltic eucrites. Two trends can be seen the Stannern trend in black filled symbols and the Main-Group - Nuevo Laredo trend in open symbols. **b** Sc vs La concentrations in basaltic with the Main Group — Nuevo Laredo and Stannern trensd eucrites. **c** & **d** Mixing model proposed by Barrat *et al.* [2007] to explain the origin of the Stannern trend. **e** Cumulate eucrites exhibit lower La and Sc contents than basaltic eucrites Yamaguchi *et al.* [2009].

ITE contents than those of the Main Group. The Nuevo Laredo trend is less variable in ITE while its FeO/MgO ratio ranges from about 2.2 to 3.7. It is petrologically ambiguous to determine whether eucrites represent the liquid obtained by 15-20 % of partial melting of a chondritic source [Stolper, 1977] or if they correspond to the residual liquid obtained after 80 % of equilibrum crystallization of a global magma ocean [Ruzicka *et al.* , 1997]. These two extreme endmember scenarios are consistent with the mean FeO/MgO ratio and ITE content of the Main Group eucrites. It is important to note that a range of intermediate scenarios consisting of combinations of initial degree of partial melting and equilibrium and fractional crystllization might also be possible as proposed by [Mandler & Elkins-Tanton, 2013].

Stolper [1977] preferred the partial melting scenario because it allowed interpreting the Stannern trend eucrites as the products of small degrees of partial melting. The most incompatible rich eucrites could then stem from the lowest degrees of partial melting. On the other hand the FeO/MgO ratio of a given batch of partial melt that undergoes fractional crystallization, rapidly evolves because Mg-rich minerals that tend to precepitate first are removed from the solid. Again, according to Stolper [1977] the Nuevo Laredo trend of eucrites may correspond to various degrees of fractional crystallization. However, the recovery of more eucrites and a greater number of analyses revealed that more than one crystallization trend is required to explain the Nuevo Laredo trend and that the Stannern trend cannot be interpreted as representing different low degrees of partial melting [McSween *et al.* , 2010].

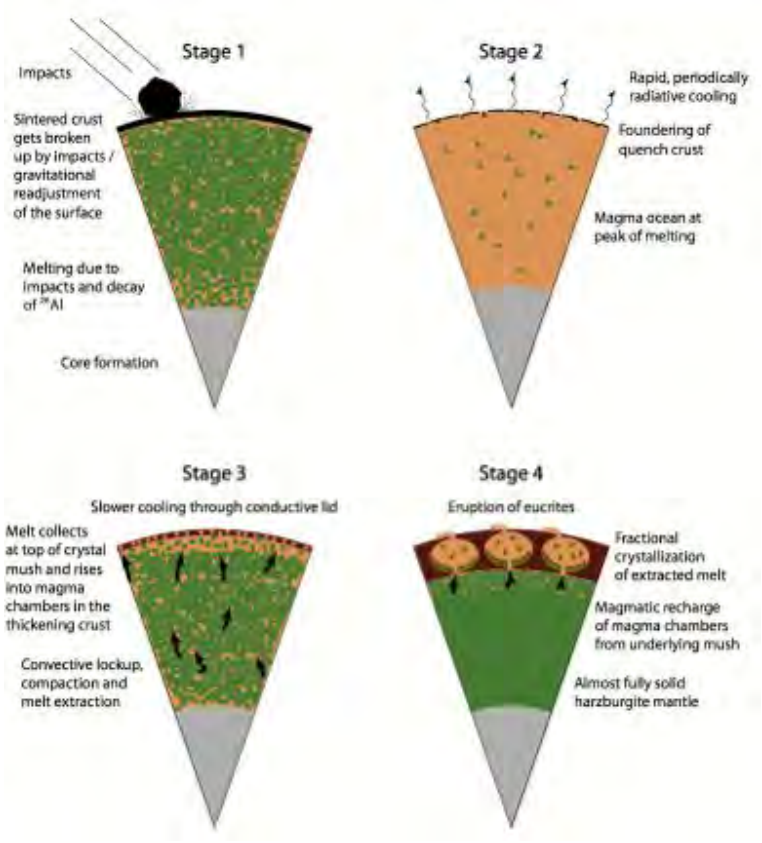

Figure 1.12: Four staged differentiation of Vesta proposed by Mandler & Elkins-Tanton [2013].

Barrat *et al.* [2007] have modeled the Stannern trend as hybrid melts. Those authors demonstrate that mixing primitive eucritic melts with eucrites of earlier generation that partially remelt from 5 to 15 % reproduces the characteristics of incompatible trace element patterns of Stannern trend eucrites (Figure 1.11 **c** and **d**). The following scenario is proposed: Magmas that are similar to the main group eucrites cause partial melting as they ascend into the hot crust which has a Main - Group - Nuevo Laredo composition of earlier generation. This ascending magma mixes with melts corresponding to small degrees of partial melting of former eucrites to obtain various degrees of ITE enrichments depending on the percentage of assimilation of the additional melt.

The partial melting scenario of [Stolper, 1977] lost favor due to the homogeneity in oxygen isotopes in the HED clan, interpreted as evidence of a global magma ocea [Greenwood *et al.* , 2005]. However, the physics of melt migration seems to preclude the existence of a global magma ocean, assuming that ^{26}Al is the only heat source capable of extensively producing melt in early small bodies. This is because plagioclase is one of the first phases to melt, thus early formed liquids are Al-rich. Rapid migration of such liquids redistributes ^{26}Al, limiting melt production where liquid has been lost [Moskovitz & Gaidos, 2011; Wilson & Keil, 2012; Neumann *et al.* , 2014].

The diversity of the patterns formed by the concentrations of Rare Earth Elements and their impressive range have been one of the most puzzling features to explain [Barrat *et al.* , 2008; Mittlefehldt *et al.* , 2011]. The Sc content can be modelled by fractional crystallization [Ruzicka *et al.* , 1997] but Sm contents of diogenites are higher than what can be predicted from a model of fractional crystallization. Several other explanations have been proposed. Diogenites may have been contaminated or contain trapped melt, but their origin has not unambiguously been provided. This geochemical diversity could reflect the

existence of multiple magma chambers [Fowler *et al.* , 1995; Mittlefehldt, 1994; Mittlefehldt *et al.* , 2011; Barrat *et al.* , 2008]. The existence of diogenite plutons could explain the various degrees of equilibration observed in eucrites through contact metamorphism [Yamaguchi *et al.* , 1997]. In the same vein as the remelting scenario proposed to explain the Stannern trend, Barrat *et al.* [2010] modelled diogenites in the following way: Orthopyroxene cumulates would result from the remelting of harzburgitic magma ocean cumulates. The partial melts obtained would then have been contaminated with minute amounts of melt from the base of the eucritic crust. This contamination would account for the diversity of trace elements observed in diogenites. [Mandler & Elkins-Tanton, 2013] suggest a combination of serial replenishment of shallow magma chambers by melts from a magma ocean and evolution of Rare Earth Element partition coefficients between orthopyroxene and basaltic liquid during crystallization to explain the REE range observed in diogenites. However, [Barrat & Yamaguchi, 2014] show that the variability of partition coefficients is not great enough to reproduce the observed range in REE using the mechanism proposed by [Mandler & Elkins-Tanton, 2013].

1.4.3 Chronology

A number of radiochronometers can be used to date eucrites and diogenites. They are based on the fact that radioactive to stable elemental ratios will be a function of time once atomic diffusion in a particular mineral stops in response to cooling. This "closure temperature" of an isotopic system depends on the effect of temperature on the diffusion coefficients, which will depend on the mineral studied, the crystal size and on the elements involved by the radiochronometer [e.g. Ganguly *et al.* , 2007].

Early onset of differentiation

The strongest evidence of very early magmatism on Vesta is the trace of short-lived radioactive elements at the time of eucrite crystallization. Excess ^{26}Mg formed by the decay of ^{26}Al (0.7 Myr half-life) is observed in eucrite plagioclase [e.g. Srinivasan *et al.* , 1999]. In addition, there is evidence for the former presence of ^{60}Fe (2.6 Myr half-life) [Shukolyukov & Lugmair, 1993] and ^{53}Mn (3.7 Myr half-life) in basaltic eucrites [Trinquier *et al.* , 2008].

Based on the ^{53}Mn - ^{53}Cr system, the global silicate differentiation age of the HED parent body occured 2.1 $\pm$ 1.3 Ma after CAI formation [Trinquier *et al.* , 2008], a system which based on studies of the diffusion of Cr in olivine and pyroxene has a closure temperature $\sim$ 900 - 1000 °C [Ito & Ganguly, 2006; Ganguly *et al.* , 2007]. Hf - W whole rock isochrons of basaltic eucrites indicate that the differentiation took place 3 $\pm$ 6 Myr after CAIs formation [Kleine *et al.* , 2009].

Rapid core formation

Hf - W data can be extrapolated to infer the initial ^{182}W/^{184}W ratio of a system, which can be used to date metal silicate separation. Using this method, Touboul *et al.* [2015] shows that core formation took place within 1 Ma after CAIs formation. Short-lived radionuclides in HEDs also support rapid core separation $\sim$ 1 Myr before crust formation [Kleine *et al.* , 2004]. La - W systematics are consistent with the fact that the eucrite source region was metal-free [Righter & Drake, 1997] but Th - W data show that some metal was present in the eucrite source(s) [Touboul *et al.* , 2015].

Basaltic eucrite ages

The ^{147}Sm-^{143}Nd ages of some basaltic eucrites indicate ancient magmatic activity close to $\sim$7 Ma after CAI formation [e.g. Wadhwa & Lugmair, 1995]. Whole - rock ^{87}Rb-

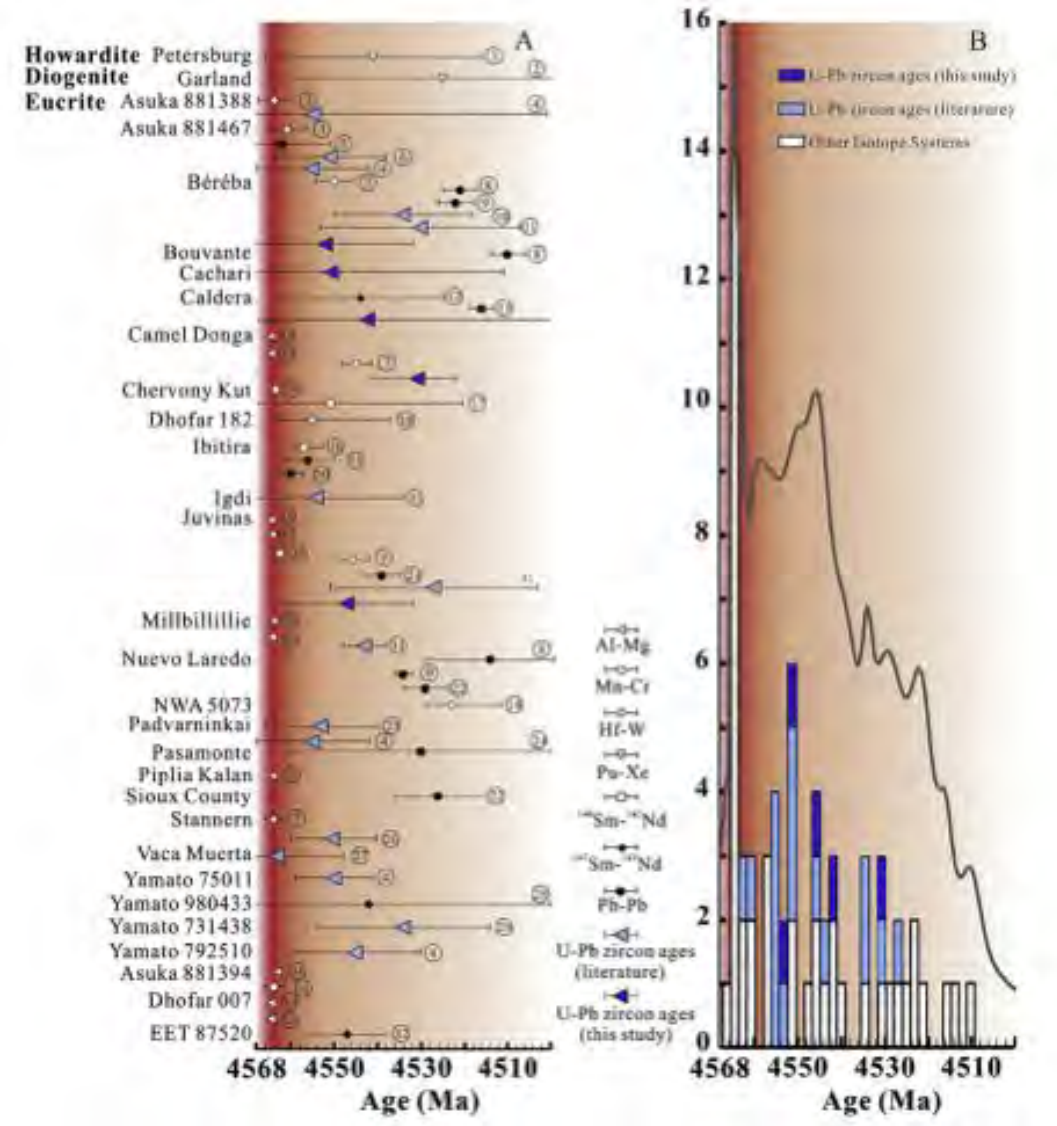

Figure 1.13: Chronology of magmatic activity of the HED parent body from Zhou *et al.* [2013] and references therein. "The chronological records of the first 50 Ma on Vesta based on radiometric age summary of HED meteorites, including one howardite (Petersburg), one diogenite (Garland) and 28 eucrites. Only high quality data with age uncertainty of less than 50 Ma are included. One of the two zircon grains found in a eucritic clast in Vaca Muerta (mesosiderite) is also included. Shown in dark blue, solid horizontal triangles are U-Pb ages of zircons from this study. Light blue horizontal triangles are U-Pb zircon ages from literature. Open (white) symbols of various shapes are based on short-lived chronometers, whereas solid symbols of various shapes are based on long-lived chronometers. (b) Histogram and the probability density curve of the same age data shown in panel a, showing the intensities and diminishing magmatic activities on Vesta during the first 50 Ma. Red backgrounds symbolize the evolving intensities of magmatic activities on Vesta, as revealed by the available chronological data."

^{87}Sr isochron yields an age of 11 - 23 Ma after CAIs formation for the basaltic eucrites [Smoliar, 1993]. These younger age are consistent with the lower closure temperature (650 - 800 °C) of the Rb-Sr system for whole rock [Harland *et al.* , 1989].

Zhou *et al.* [2013] have dated crystallization ages of zircons in a series of basaltic eucrites using the Pb-Pb and U-Pb systems. A synthesis of their data with other radiochro-

logical ages lead them to conlude that core-mantle separation occured within 3 $\pm$ 2 Myr after CAI, the peak of vestan magmatism took place at 15 $\pm$ 7 Myr, diminishing over the next 50 Myr, as illustrated in Figure 1.13. Iizuka *et al.* [2015] dated cooling ages of large zircons grains in the Agout granulitic eucrite. The eucrite zircon Hf - W isochron dates are generally consistent with the eucrite zircon ^{207}Pb/^{206}Pb ages of either 12 Ma or 37 Ma after CAIs formation. The Ti contents in Agoult zircon indicate the crystallization temperatures of $\sim$900 °C, similar to the equilibration temperatures of pyroxenes from most basaltic eucrites [Yamaguchi *et al.* , 1996]. Most eucrites yield identical zircon ^{207}Pb/^{206}Pb dates to Agoult zircon within uncertainty, i.e. 12 Ma after CAIs formation.

Iizuka *et al.* [2015] support the idea that this age reflects the timing of the metamorphic zircon growth and pyroxene exsolution during the prolonged widespread crustal metamorphism on Vesta. This interpretation can reconcile the discrepancy between the zircon ^{207}Pb/^{206}Pb age (4544 $\pm$ 15 Ma, after [Zhou *et al.* , 2013]), the much older igneous crystallization of eucrite Juvinas (4 Ma after CAIs formation), based on Mn - Cr systematics. Lugmair & Shukolyukov [1998] and the early silicate differentiation discussed above. The younger ^{207}Pb/^{206}Pb date as exemplified by Camel Donga zircon [Zhou *et al.* , 2013] ($\sim$37 Myr after CAI) might reflect the age of a subsequent short-term thermal event causing partial melting (as seen in Agoult granulitic eucrite [Yamaguchi *et al.* , 2009]), given that U - Pb system of the plagioclase was preferentially reset.

Cumulate eucrites ages

Cumulates eucrites are younger than basaltic eucrites, as supported by Hf-W data Touboul *et al.* [2015] and self-consistent ^{146}Sm-^{142}Nd isochrons for the cumulate eucrites Binda, Moama and Moore County, for which Boyet *et al.* [2010] obtained initial ^{146}Sm/^{144}Sm ratios correspond to ages of 19 $\pm$ 15 Ma, 50 $\pm$ 18 Ma and 34 $\pm$ 30 Ma after CAI formation.

Eucrite metamorphism

The global metamorphism, as depicted by the ordinary equilibrated eucrites, might have been produced by meteoroid impact at or near the floor/wall of a crater [Nyquist *et al.* , 1986]. Alternatively, the first basaltic eucrites formed at or near the surface were buried under successive lava flows and metamorphosed by heating from the hot interior Yamaguchi *et al.* [1996, 2001, 2009]. In addition, the fact that non-brecciated but highly metamorphosed basaltic eucrites and cumulate eucrites have Ar - Ar ages (90 Ma after CAIs formation, with T_c $\sim$200 °C for plagioclase), are much older than brecciated eucrites (470 Ma - 1 Ga after CAIs formation), support the fact that they acquire their metamorphic texture by burial rather than by subsequent impacts.

Diogenite ages.

Diogenite are more difficult to date because of their relatively low incompatible element content with respect ot eucrites. The ^{87}Rb-^{87}Sr system gives an age of 117 Ma after CAI for Johnston diogenite (Rb-Sr muscovite 300 - 500 °C, Rb - Sr biotite 300°C) [Takahashi & Masudat, 1990]. Late ages of cumulate eucrites and diogenites are consistent with their formation in deep plutons. Schiller *et al.* [2011] show that, based on the ^{26}Mg* composition of diogenites ($\mu^{26}Mg^* = ((^{26}Mg/^{24}Mg)_{sample}/(^{26}Mg/^{24}Mg)_{standard} - 1) \times 10^6$]) the onset of the magma ocean crystallization should have started within 0.2 - 1.1 Ma of solar system formation and based on a model of magma ocean crystallization, deduce that crystallization might have been complete whithin the next 2 - 3 Myr.

Overall, there is thus evidence for early magmatism on Vesta, beginning less than a few Ma after CAIs formation, continuing for several 10's of Ma and thermal metamorphism

(T $\sim$ 800 °C) lasting for $\sim$ 100 Myr.

The ages obtained for the differentiation of the eucrite parent body are consistent with results from numerical simulations for the thermal evolution of planetesimals heated by decay of ^{26}Al and ^{60}Fe. These simulations show that on bodies that accreted within the first 2 - 3 Myr of CAI formation magmatism began within the first 4 Myr after CAIs formation and that the last melting occurred before 10 Myr after CAI formation [Sahijpal *et al.* , 2007].

The thermal model of [Ghosh & McSween, 1998], based on short-lived radionuclide heating and constrained by the properties of HEDs, divided Vesta's evolution into stages: (1) radiogenic heating of a homogeneous asteroid until metal-sulfide eutectic melting and core separation; (2) further heating of the mantle until silicate partial melting and crust formation; and (3) subsequent heating and cooling of the differentiated body. Thermal calculations for Vesta are complicated due to the migration of heat sources during the simulation (^{60}Fe is incorporated into the core and ^{26}Al into the crust). The model produced a reverse geothermal gradient, which minimized heat loss from the asteroid's interior for $\sim$ 100 Myr.

1.4.4 Bulk composition of Vesta

Comparing the composition of eucrites, diogenites and howardites with those of chondrites allows the bulk composition of their parent body, i.e. Vesta [e.g. Consolmagno & Drake, 1977; Dreibus & Wänke, 1980; Mittlefehldt, 1987] to be inferred.

HED have a content in refractory lithophile elements that is consistent with chondritic compositions but they are highly depleted in alkali elements. For instance Na is depleted by a factor of ten with respect to chondrites. Angrites are also severely depleted in moderately volatile elements. Depletion in moderately volatile and highly volatile elements also appears characteristic of many other differentiated asteroids [McSween *et al.* , 2010]. Moreover, melting experiments [Jurewicz *et al.* , 1993, 1995] and numerical simulations [Toplis *et al.* , 2013] based on the thermodynamic calculator MELTS [e.g. Ghiorso & Sack, 1995; Asimow & Ghiorso, 1998; Ghiorso, 2013] reveal that an initial Na depletion is a necessary condition to obtain eucrite-like melt from a chondritic source.

Since Fe^{2+} and Mn^{2+} can easily be interchanged in crystal networks, these two cations undergo minor fractionation during igneous processes. Therefore, the average FeO/MnO ratio of the HED parent body is expected to be close to its derived products, e.g. eucrites [Dreibus & Wänke, 1980]. Although iron condensed as metal in the solar nebula, reactions with the cooling gas converted some of the metal to FeS and the FeO component of silicates, depending on the oxygen fugacity [Lodders, 2003]. For this reason, the FeO/MnO ratio of eucrites can be used to infer the initial oxidation state of the nebular condensates from which Vesta was accreted. This allows placing the oxidation condition of Vesta near the iron-wüstite buffer (IW-1). As many chemical characterisitcs appear to match eucrites, except the volatile content, it has been put forward that these elements may have been lost during a magma ocean stage [e.g. Ikeda & Takeda, 1985]. Based on O isotopes Boesenberg & Delaney [1997] infer that the bulk composition of Vesta should be well representated by a 3/4 - 1/4 mixture of H and CM chondrites.

Toplis *et al.* [2013], compiled various geochemical contraints, including the Fe-Mn systematics, the oxygen isotopes, the mineralogy of the HEDs, and combined this information with a geochemical model for the internal structure of Vesta that can be compared to Dawn gravity data [Russell *et al.* , 2012]. The complete publication is provided in appendix C. The model for internal structure of Vesta uses knowledge of the ratio of the partition coefficients (i.e. Kd) of FeO and MgO for molten silicates. The Kd, defined as the molar $(Mg/Fe^{2+})_{Liquid}$ / $(Mg/Fe^{2+})_{solid}$ is well constrained by experiments, for equilibrium between olivine and basaltic liquids and similarly for pyroxenes. These ratios are

Figure 1.14: "Collage of Vesta in comparison with other asteroids visited to date for which good images exist. This south polar view of Vesta shows the south pole mountain and the Rheasilvia impact basin surrounding this central peak" [Russell *et al.* , 2012].

shown to be constant during melting and crystallization so they can be used as reference quantities. The composition of the Main Group eucrite Juvinas is used as a proxy for the average composition of the basaltic crust. The assumption is made that this geochemical crust is at equilibrium with a silicate mantle consisting of olivine and pyroxenes. It allows the size and density of the core, mantle and crust of Vesta to be calculated. The most self-consistent results with Dawn and HED data are obtained for H and H - CM bulk compositions, as summarized in table 1.1.

	CM	CO	CV	CK	CR	CH	L	H	EL	EH	¾H+¼CM
Closest fit to Juvinas, ξ[b]	**1.1**[a]	**1.0**	3.7	1.8	**1.1**	**1.0**	1.2	**0.7**	2.5	3.4	**0.9**
Fe/Mn	68–85	87–109	107–133	101–127	76–96	99–123	50–63	**37–47**	64–81	**36–45**	**42–52**
Gravity data[c]	>−100	>−100	>−200	>−200	>−100	>200	>−200	**< −100**	>−100	>100	**< −100**
% eucrite/ (eucrite + Px)	81	84	100	100	46	**32**	**28**	**31**	**8**	**14**	**36**
Consistent with Righter	No	**Yes**	**Yes**	–	–	–	No	**Yes**	–	–	–
$\Delta^{17}O$	low	low	low	low	low	low	high	high	high	high	**OK**
Oxidation state	oxidized	**OK**	**OK**	–	reduced	reduced	reduced	reduced	reduced	reduced	**OK**

Table 1.1: From [Toplis *et al.* , 2013] (A version is provided in the appendix). Characteristics of predicted parent bodies and their agreement with constraints from the howardite - eucrite - diogenite meteorites and/or Vesta.[a] Values indicated in bold show a satisfactory fit to constraints from the HED/Vesta. Others do not. [b] ξ is the value of the best fit between the composition of Juvinas (a basaltic eucrite) and the melt composition modelled by MELT for an experiment of equlibrium melting of a chondritic source. The best fit is defined as the normalized root mean square between the model and the observation. [c] The values indicated are the minimum offset between the predicted density of the bulk-silicate mantle derived from the core size and density calculated by mass balance, and that constrained by the gravity data of the Dawn mission.

1.5 Study of asteroid 4-Vesta and insights from the Dawn mission.

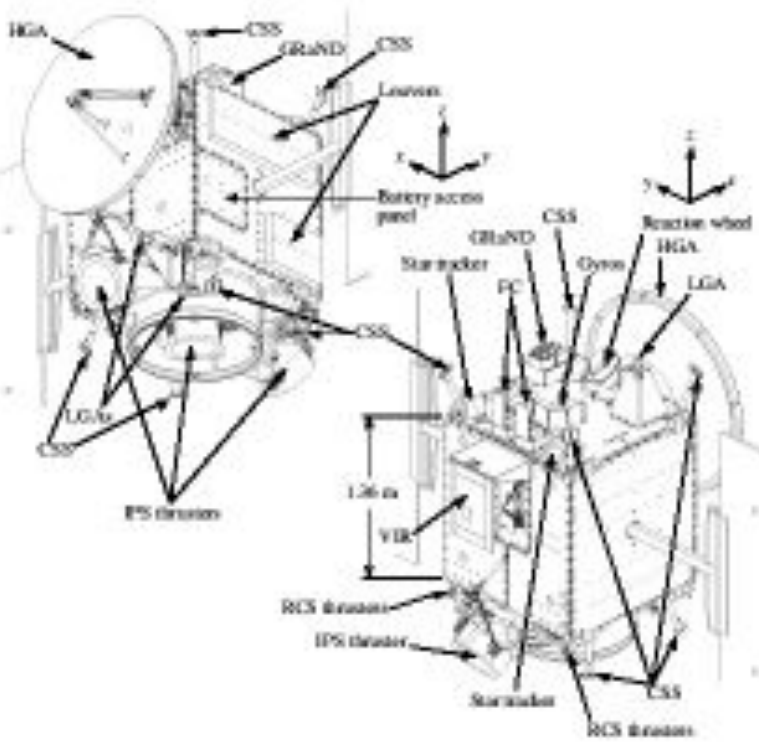

Figure 1.15: Diagram of Dawn spacecraft (from http://dawn.jpl.nasa.gov/mission/spacecraft.asp). The upper left view shows the High gain antenna (HGA) used for communicating with Earth and the three Ion Propulsion Thrusters (IPS). The Z axis corresponds to the direction pointing towards the observed object during mapping orbits. The visible-infrared spectrometer (VIR) is set on the opposite panel to the communication antenna (lower right view). The pair of framing cameras (FC) seat just above VIR on the panel which is opposite to the main thruster. The Gamma Ray and Neutron Detector (GRaND) is the set on the same panel on the upper left corner.

As alluded to above, telescopic observations of Vesta on the one hand, and the laboratory spectroscopy of HED meteorites on the other hand, have progressively confirmed a clear connection between the asteroid and the meteorites suite, mainly drawing on the characteristic absorption bands observed in reflectance spectra associated to the presence of pyroxenes [McCord *et al.* , 1970; McFadden *et al.* , 1977]. In addition, a number of other smaller bodies that orbit in the asteroid belt, called vestoids, are dynamically related to Vesta and similar in surface composition. The orbital configuration of this family of asteroids supports the possibility of delivering vestan meteorites to the Earth [Binzel & XU, 1993; Burbine *et al.* , 2001; Cochran *et al.* , 2004]. This link was further supported by the Hubble space telescope observations, which provided the first lithological maps of the surface of Vesta. These maps revealed pyroxenite exposed in a huge impact basin located at the south pole [Binzel *et al.* , 1997; Zellner *et al.* , 2005; Li *et al.* , 2010]. Comparing the physical characteristics of Vesta, obtained from telescopic observations, with the petrology of eucrites and diogenites has significantly contributed to understanding of the conditions of asteroid differentiation and volcanism Keil [2002].

However, understanding of Vesta has been revolutionized by the Dawn spacecraft that orbited Vesta in 2011 and 2012. Dawn was lauched in 2007 by a Delta-II-Heavy rocket and reached Vesta in 2011. In detail, Dawn entered Vesta's gravity field on July 16^{th} 2011

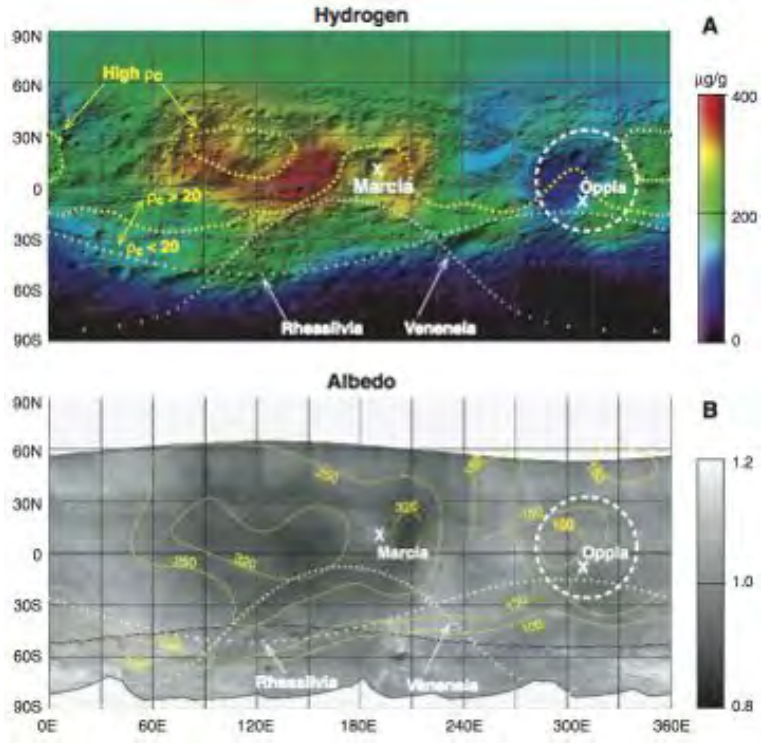

Figure 1.16: **A** Map of $[H]$ superiposed on shaded refief is compared with **B** an albedo map of Vesta (from [Prettyman *et al.* , 2012]). The dashed white lines outlines depressions, notably the two large Rheasilvia and Veneneia impact basins located at the south pole of Vesta.

and was successfully put into survey orbit (at an altitude of 2735 km) around the asteroid in August 2011 [Russell *et al.* , 2013]. Later on, Dawn got closer to Vesta during two lower altitude mapping orbits: first at an altitude of 685 km, a phase called HAMO (High altitude mapping orbit) and at 210 km from the surface of the asteroid during LAMO (Low altitude mapping orbit).

The spacecraft is equipped with three scientific instruments: a set of two framing cameras (FC), VIR a visible & infrared spectrometer and GRaND a Gamma Ray & neutron detector [Russell *et al.* , 2007]. The information provided by these instruments are compositional, mineralogical and morphological. Stereographic images provided by the FC allowed the production of a refined shape model of the asteroid [Jaumann *et al.* , 2012]. In addition, each FC is equiped with a color filter wheel, which allows characterizing Vesta in real and artificial colors using a total set of seven wavelengths. The spatial resolution of the FC is about 10 m at an altitude of 100 km. The VIR instrument records reflectance spectra from 0.95 to 5 microns [De Sanctis *et al.* , 2009]. VIR can resolve 250 m wide features at an altiude of 100 km. GRaND is able to detect neutrons ranging from 0 to $\sim$10 MeV and gamma rays ranging from 0 to 9 MeV [Prettyman *et al.* , 2011]. The spatial response of this instrument has approximately a 300 km arc length FWHM during LAMO [Prettyman *et al.* , 2013]. The radio transmission antenna used for communication between Dawn and mission control, can be considered as a fourth scientific instrument. Changes in the spacecraft velocity and position during time can be finely monitored through the analysis of the Doppler shift that affects the radio signal transmitted, to the point that it can be used to measure the gravity field of the body [Konopliv *et al.* , 2011; Ermakov *et al.* , 2014].

The shape of Vesta differs from a sphere, principally because of the presence of two large impact basins at its South pole, named Rheasilvia and Veneneia. The spiral shape features visible around its rotation poles are also witnesses of these past violent collisions.

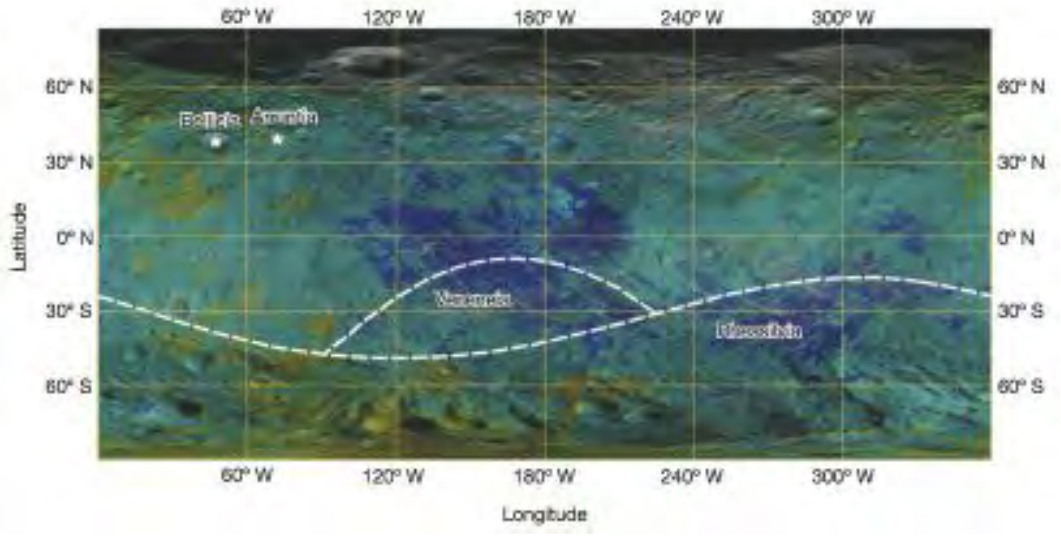

Figure 1.17: Surface mineralogy of Vesta inferred from VIR data [Ammannito *et al.* , 2013a]. Howardites are shown in cyan, eucrite rich regions are blue and diogenites rich regions are yellow and red. Belitia and Arruntia are indicated with white stars, where small olivine rich spots have been detected.

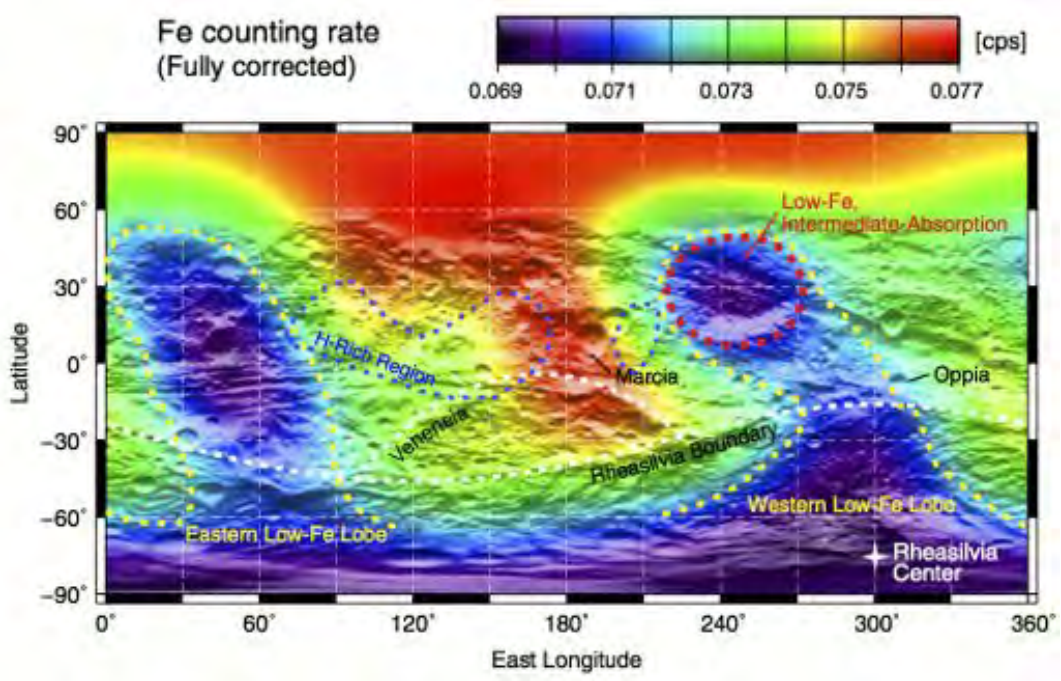

Figure 1.18: From Yamashita *et al.* [2013]. Global distribution of Fe counting rates on the surface of Vesta. The gamma-ray counts were fully corrected for variations of neutron number density and abundance of hydrogen. The map has been smoothed with a boxcar filter having a radius of 30°. The Rheasilvia and Veneneia basins are indicated by white broken curves. Eastern and western low-Fe lobes are delineated with yellow dots. H-rich regions are shown with blue dots. These approximate the 320 μg/g H contours from Prettyman *et al.* [2012]. The low-Fe, intermediate-absorption region, indicative of cumulate-eucritic materials is presented with a red broken circle. The map is drawn using a simple cylindrical projection.

Two series of equatorial troughs are structurally related to Rheasilvia and Veneneia, which

have been interpreted as the consequence of global disruption of the asteroid during these two successive impacts [Buczkowski *et al.* , 2012]. The late age of the Rheasilvia impact (1 - 2 Gyr before present, e.g. [Schenk *et al.* , 2012]), supports the vestoid origin of HED meteorites [Binzel *et al.* , 1997], as these companions would have been dispersed if they originated from a much older impact basin. Another conclusion of this work is that, the model of impact flux that is used for the Moon appears inconsistent with the sizes and distribution of craters observed at the surface of Vesta, while a model for the flux of impacts, based on the formation and migration of the giant planets, causing significant scattering and moving of material out of the asteroid belt, is much more consistent with the cratering record that is seen [Marchi *et al.* , 2012; O Brien *et al.* , 2014].

The oldest terrains on the surface of Vesta also exhibit a low albedo and contain an unexpected amount of volatiles (H) with respect to the volatile content of HED meteorites as shown in Figure 1.16. On the other hand younger terrains with high albedo are volatile free. The volatile-rich dark material is thus proposed to be exogenic and might be well represented by carbonaceous impactors [Prettyman *et al.* , 2012]. The presence of these volatiles may also be responsible for the presence of pitted terrains on several crater floors such as those of Marcia and Cornelia [Denevi *et al.* , 2012]. The characteristics of the absorption bands related to the presence of pyroxene at the surface, observed in visible infrared spectra, are consistent with an average howardite composition [De Sanctis *et al.* , 2012]. The measurement of the Fe/Si and Fe/O ratios inferred from gamma rays measured by GRaND reinforces this connection between the HED meteorites and the surface of Vesta [Prettyman *et al.* , 2012].

Furthermore, Dawn has confirmed that Vesta is a fully differentiated body, including a core, a mantle and a crust. An internal structure model composed of a one hundred kilometer iron-nickel rich core and an outer silicate envelope of average density of about 3200 kg/m^3, satisfies the gravity data [Russell *et al.* , 2012] and the preferred chondritic source material for Vesta [Toplis *et al.* , 2013].

The position of absorption bands observed in visible infrared spectra are related to the composition of pyroxenes and can be used to discriminate between eucrite-rich and diogenite-rich regions. The petrological map retrieved in this manner by Ammannito *et al.* [2013a] is provided on Figure 1.17. An equivalent GRaND petrologic map, assuming that the surface of Vesta consists in a mixture of basaltic eucrite and orthopyroxenitic diogenite, was determined from neutron absorption data [Prettyman *et al.* , 2013]. More recently, based on neutron and gamma ray data, Beck *et al.* [2015] have developed maps where basaltic and cumulate eucrites are treated as distinct petrological endmembers.

The spatial distribution of the different HED lithologies is consistent with a generally deeper origin for diogenites, as this material is more abundant in the Rheasilvia basin [Prettyman *et al.* , 2012, 2013; De Sanctis *et al.* , 2012; McSween *et al.* , 2013]. The map of Fe retrieved from the analysis of the 7.6 MeV neutron capture gamma rays (Figure 1.18) is visually self-consistent with the petrologic maps alluded to above, where Fe-poor regions overlap diogenite-rich regions [Yamashita *et al.* , 2013].

Gravity data shows heterogeneity in diogenite distribution, but the coincidence of positive Bouguer anomalies [1] with central mounds of the RheaSilvia and Veneneia impacts demonstrate that most diogenites have a deeper origin than eucrites. However, diogenites may not form a deep continuous layer, but may be organized as an ensemble of plutons. The presence of strong material in Vestalia Terra has been interpreted as the trace of a shallow diogenite pluton [Buczkowski *et al.* , 2014].

1. A positive Bouguer anomaly indicates in theory the presence of a denser material

1.6 Thesis outline

This thesis is built around two principal fields of work. The motivation of the first aspect is that independent component analysis (ICA) of gamma ray spectra obtained with a high purity Ge detector (HPGe) from the Kaguya mission around the Moon is able to separate the elemental contributions of Fe, Th and K [Forni *et al.* , 2009]. This raises the question of whether similar results can be obtained from spectra derived from a bismuth germanate (BGO) detector, notably used for the Lunar Prospector and Dawn space missions.

Unfortunately, applying ICA to the vestan gamma ray data is not as successful to extract elemental contributions. This first chapter aims at unravelling the key factors that make blind source separation successful or not when applied to BGO spectra. It starts with a short overview of the principles of gamma ray spectroscopy when applied to planetary sciences, mainly drawing upon [Prettyman, 2006]. The working of blind source separation algorithms is presented, focusing on ICA and the Non-Negative Matrix Facorization (NMF). The different artificial and real BGO datasets that are analyzed are presented along with the possible processings that can be performed before or after the application of blind separation. The results of ICA and NMF are illustrated as the degree of complexity of the data is increased. The first tests are performed on linear mixtures of library spectra and aim at measuring the performance of the separation algorithms. The following tests are used with the intent to show how real data differ from a linear mixture model. The effect of changing the chemical variability is shown through the analysis of artificial lunar data where the dynamic range of elemental abundances is progressively decreased. Ultimately, the algorithms are applied to the real Lunar Prospector and vestan gamma ray data from the Dawn mission. After having compared the compositional information extracted from Lunar Prospector data with previous analyses, the results of BSS for Vesta are discussed in the light of the results on synthetic and real lunar data.

The implications of the analyses of the BGO vestan data are mostly methodological. In parallel to the analysis of gamma ray spectra, a 1D spherical model for the magmatism of Vesta has been developped during the course of this thesis and is presented in chapter 3. Due to the presence of a large impact basin in the southern hemisphere of Vesta, olivine rich mafic material was expected in this region [Binzel *et al.* , 1997]. However, the analysis of visible and infrared data [Ammannito *et al.* , 2013a] showed that the proportion of olivine in the Rheasilvia bassin cannot be greater than 20 - 30%. As discussed above, the initial composition of asteroid Vesta has been inferred based on comparative geochemistry between the HEDs and chondritic meteorites and geophysical constraints [Toplis *et al.* , 2013]. That study shows that the preferred average compostion for Vesta is an H or 3/4H1/4CM composition. In general terms, magmatic differentiation leads to a vertical layering of less and less refractory material from bottom to top. The thickness of the crust, containing more felsic minerals, can then be determined by mass balance. For instance, if one converts the H composition proposed by [Toplis *et al.* , 2013] into equivalent volumes of olivine, pyroxene and plagioclase, one can find that pyroxene and plagioclase occupy 40% of the volume of Vesta. If one assumes that this volume represents the "crust" and that pure olivine makes up the "mantle", the crustal thickness is 40 km using the radius of Vesta proposed by [Russell *et al.* , 2012]. On the other hand, hydrodynamic modelling predicts that the excavation depth of the Rheasilvia basin can be as large as 80 km, so olivine rich average compositions for Vesta can be called into question [Clenet *et al.* , 2014].

Models of differentiation of Vesta are often presented in terms of several segmented stages [Ruzicka *et al.* , 1997], [Mandler & Elkins-Tanton, 2013] often with a global, entirely molten magma ocean. However, results from physical models of melt migration, seem to preclude the existence of global magma ocean, [Wilson & Keil, 2012], [Neumann *et al.* , 2014], [Moskovitz & Gaidos, 2011]. These latter studies favor the idea that eucrites

and diogenites stem from partial melting of a primitive mantle, as originally proposed by [Stolper, 1975, 1977]. In addition, these models suggest the importance of the continuity through time of the process of melt production, melt migration, magma ocean crystallization and crystal settling. During all these phases of differentiation, composition evolves, thus, it appears essential to consider the coupling between chemical evolution and melt migration. Such models may provide insights into the questions of the bulk composition of Vesta and the differentiation sequence that leads to the formation of eucrites and diogenites.

By trying to adopt a self-consistent geochemical and geophysical approach, a fortran code has been written, in 1D spherical geometry, to calculate the compositional evolution as a function of depth and time as melt migrates upward. This code was constructed incrementally, by first implementing a numerical solver of compaction equations, benchmarked on a previous study in cartesian geometry [Ricard *et al.* , 2001]. The calculation of melt production was then added following [Šrámek *et al.* , 2012], [Neumann *et al.* , 2014], using a solver of energy equation described in [Monnereau *et al.* , 2013]. Composition can be monitored through use of a phase diagram, as shown in [Ribe, 1985]. A binary eutectic diagram was initially implemented, including a low melting point component containing aluminum (plagioclase) and a refractory component (undifferentiated mixture of pyroxene and olivine). This choice is justified by the behaviour of plagioclase melting for an H type chondrite [Toplis *et al.* , 2013]. Although, this enables the effect of aluminum migration [Neumann *et al.* , 2014] to be accounted for, the mineralogy of eucrites, diogenites, and the issue of the absence of olivine near the surface of Vesta, requires the treatment of olivine and pyroxene as two separate components. Thus, the binary diagram was replaced by an olivine-anorthite-silica ternary diagram, adapted from [Morse, 1980]. This has been used to explore the consequences for internal structure, in particular the distributions of plagioclase, pyroxene and olivine. Finally, monitoring these minerals allows following the concentrations of Rare Earth elements using appropriate partition coefficients. This is used as an attempt to asses the enigmatic diversity of Rare Earth element patterns observed in diogenites.

Chapter 2

Blind source separation of planetary gamma ray spectra obtained with BGO detectors.

Contents

Table 2.1: Summary of notations used in the first chapter.

Symbol	Nature	Dimension	Unit
N_P	Number of pixels on a sphere	-	-
N_C	Number of channels in a gamma ray spectrum	-	-
N_S	Number of sources in a mixture of signals	-	-
p	pixel index	-	-
l	channel index	-	-
k	source index	-	-
$\boldsymbol{X}$	Set of gamma ray spectra / observed signals	$N_P \times N_C$	Counts/s
X_{pl}	Elements of $\boldsymbol{X}$	-	Counts/s
$\boldsymbol{S}$	Set of source spectra / source signal	$N_S \times N_C$	-
S_{kl}	Elements of $\boldsymbol{S}$	-	-
$\boldsymbol{M}$	Mixing coefficients	$N_P \times N_S$	-
M_{pk}	Elements of $\boldsymbol{M}$	-	-
$\boldsymbol{X}'$	Centered observed signals	$N_P \times N_C$	Counts/s
$\boldsymbol{S}'$	Centered source signals	$N_S \times N_C$	-
$\boldsymbol{C_{XX}}$	Covariance matrix	$N_P \times N_P$	-
D	Dynamic range	-	-
D'	Modified dynamic range	-	-
t	Current iteration of a separation algorithm	-	-
$E\{\}$	expectation	-	-

Acronyme	Meaning
BSS	Blind source separation
PCA	Principal component analysis
ICA	Independent component analysis
NMF	Non negative matrix factorization
BGO	Bismuth germinate
LPGRS	Lunar Prospector Gamma Ray Spectrometer
GRaND	Gamma Ray and Neutron Detector (on board Dawn)
MCNPX	Monte Carlo N particle transport code [Briesmeister, 2000]

Abstract: The procedure required to transform gamma ray spectra into geochemical maps of planetary surfaces may require the development of a complex physical model. Methods of blind source separation (BSS) assume that observed signals correspond to the superposition of a set of source signals that show a certain contrast between each other, which is lost during mixing and that an appropriate algorithm may restore. For the signals considered here, i.e. gamma ray spectra, ICA, a method based on the mutual independence and non-gaussianity of the source signals, has been proven to be useful in the case of lunar gamma ray spectra of high spectral resolution. The quality of ICA separation can be improved by combining it with NMF, an algorithm based on the positiveness of the data. This study has been constructed to determine whether ICA-NMF may be useful to the analysis of another type of gamma ray spectra of lower spectral resolution obtained with BGO detectors. Lunar synthetic spectra are used to assess the roles of the properties of the source spectra, the complexity of the mixing model, and the chemical variability of the surface on the performance of ICA-NMF. Real LPGRS data are analysed to check the principal outcomes of the analysis of synthetic spectra. Finally, the method is applied to the vestan data with consideration of a denoising procedure for this dataset acquired at higher altitude and during a shorter period than the lunar data. The results are discussed and perspective of other blind source analyses are provided as a guideline for future analyses of BGO spectra including Ceres.

2.1 Introduction

Gamma ray spectroscopy can be used to determine the chemical composition of the surface of planetary bodies as detailed in section 2.2 which draws on the review study by [e.g. Prettyman, 2006]. Gamma ray detectors have been on-board numerous space missions around the Moon, Mars, Mercury, the asteroids Eros and Vesta and soon the asteroid Ceres (see Table 2.2). From this point of view, the Moon has been a widely studied target, starting with the NaI(Tl) [1] scintillators carried in the Service Module of Apollo 15 and 16 spacecraft [Harrington *et al.* , 1974]. These instruments allowed geochemical mapping of about 10 % of the surface of the Moon, highlighting the greater Al/Si ratio of the feldspathic lunar highlands with respect to the basaltic Maria and the anticorrelation between the Al/Si and Mg/Si ratios [Trombka *et al.* , 1974]. Lunar samples collected during Apollo and Luna missions and lunar meteorites form a ground truth for calibrating measurements of the composition made remotely [e.g. Korotev *et al.* , 2003]. In addition, several other gamma ray detectors have been placed in orbit around the Moon including the Kaguya (JAXA), Chang'E-1, Chang'E-2 (CNSA) and Lunar Prospector (NASA) spacecraft. Subsequently the recorded gamma ray spectra have been analyzed to produce elemental maps of K, Th, Fe, Mg, Ca, Al, Si, O [Hasebe *et al.* , 2009; Yamashita *et al.* , 2012; Zhu *et al.* , 2010, 2013; Prettyman *et al.* , 2006].

On the one hand, the analysis of gamma ray spectra can be delicate as it may require the development of a complex physical model for extracting a maximum number of elemental contributions [Prettyman *et al.* , 2006]. On the other hand, algorithms of blind source separation (BSS), which have the general purpose of extracting source signals that are latent in the observations, can provide useful insights for the analysis of such datasets. Here, one focuses on ICA, independent component analysis, a method based on independence and non-gaussianity of the source signals, and NMF, the non-negative matrix factorization, a method based on the positiveness of the data. These two methods are presented in more detail in section 2.4.

When applied to gamma ray spectra recorded by the Kaguya HPGe spectrometer, JADE [2], an algorithm of ICA is able to separate elemental contributions from radioactive elements (K, Th, U) and iron [Forni *et al.* , 2009]. Furthermore, it is even possible to discriminate the contributions of Th and K, despite the very high spatial correlation of these two elements on the surface of the Moon [Forni *et al.* , 2010]. In addition, the combination of ICA and NMF has been shown to improve the quality of the sources extracted by ICA from hyperspectral images [Benachir *et al.* , 2013].

The purpose of this chapter consists in testing whether ICA and ICA - NMF are able to extract elemental contributions from gamma ray spectra obtained with BGO detectors, keeping in mind that the latter do not provide such a high spectral resolution as HPGe detectors. This assessment is carried out by studying the BGO spectra recorded by the Lunar Prospector Gamma Ray Spectrometer (LPGRS) [Feldman, 2004].

The interest of using these data is that they are already well-understood. They have been analyzed in the past to produce maps of Fe, Th, K [Lawrence, 2004]. Furthermore, elemental abundances of ten elements were inferred from the observed gamma ray spectra by unmixing of simulated elemental spectra [Prettyman *et al.* , 2006]. The availibity of synthetic elemental spectra and a mixing model from Prettyman *et al.* [2006] is essential in understanding the key factors that will make ICA and/or NMF work or not on a set of BGO spectra.

As initial tests, elemental spectra are used to test BSS tools in a forward modelling approach. For example, one can produce linear mixtures of elementary spectra, i.e. satisfying the model required by the considered BSS methods. This model is usually written

1. Sodium iodide crystal doped with Thallium
2. JADE: Joint Approximate Diagonalization of Eigen matrices [Cardoso & Souloumiac, 1993]

as $\mathbf{X} = \mathbf{MS}$ where $\mathbf{X}$ is the observation matrix, $\mathbf{M}$ the mixing matrix and $\mathbf{S}$ the source matrix. Such an approach is used here to quantify the performance of the BSS algorithms by comparing the input and output source signals.

This premilinary and essential test is used to select the method that best performs in reconstructing elemental contributions in order to apply it to more complex datasets. On the other hand, the statistical properties of the source signals can be quantified in order to assess whether ICA hypotheses (independence, non-gaussianity of source signals) are respected or not. That being said, further tests may be required to understand the results obtained on real data.

Prettyman *et al.* [2006] provides a physical mixing model which is mostly linear but which cannot be written exactly as $\mathbf{X} = \mathbf{MS}$ likely to be closer to real data than a simplified linear mixing model. Applying ICA-NMF to synthetic data obtained with this physical mixing model is intended to test whether the difference between the simplified linear mixtures and the physical mixtures is critical for the success of the separation algorithm.

In addition, a background component is present in each spectrum, because gamma rays are also produced during reactions that do not involve one specific element. ICA-NMF is applied to two set of synthetic spectra which follow the model of [Prettyman *et al.* , 2006]: one that includes a background and one that does not include it.

Another important key factor for the correct working of the separation algorithm is the chemical variability of the observed surface. Indeed, the methods of separation used in this study require that there are, at least, as many different observations as source signals. If the surface of a planet, as seen by the instrument, is chemically homogeneous, records will just be the repetition of a single mixture. Under these conditions ICA or NMF will not be able to separate elemental contributions from each other, even if the other prerequisites of these methods (independence of the sources for ICA, positiveness for NMF) are satisfied.

The model from [Prettyman *et al.* , 2006] also enables making gamma ray data from an artificial Moon whose surface composition is modified. Here, ten artificial datasets are constructed that take account of a composition whose variability is progressively decreased down to a tenth of the real variability observed in lunar elemental abundances. ICA-NMF is applied to these artificial data in order to assess how the decrease in chemical variability of the surface complicates extraction of elemental contributions using ICA-NMF. ICA-NMF is then applied to real lunar LPGRS data to check the outcomes obtained for synthetics.

Finally the same separation method is applied to vestan BGO data acquired by the GRaND instrument. Additional processings are considered to reduce the level of noise of the data.

The main outcomes are finally summarized, intended for providing a guideline for future blind source analysis of other BGO spectra, notably those that will be recorded at Ceres.

2.2 From planetary gamma rays to elemental abundances.

2.2.1 Nuclear interactions.

Counting gamma rays that leak from planetary bodies is an indirect measurement of the composition of their surface. The reason is that rock forming elements participate in the nuclear reactions that produce these high energy photons [Reedy, 1978; Prettyman, 2006]. There are three main reactions involved. The most direct reaction is the disintegration of radioactive elements, such as ^{40}K or ^{232}Th. In this case, gamma rays are produced in quantity proportional to the abundance of the element. Other non radioactive elements can also produce gamma rays if they are activated. This is possible when the atmosphere is fine or even absent, like in the case of the Moon and Vesta. High energy particles coming from the sun or from other stars reach the surface of the body and produce a shower of energetic particles within the regolith [Evans *et al.* , 1993]. Many of these particles are neutrons and are essentially responsible for the production of gamma rays that do not result from the desintegration of radioactive elements. Fast neutrons can collide with nucleii and continue their path losing a little kinetic energy, which is converted into a photon by energy conservation. This reaction, called non-elastic scattering, produces an amount of gamma rays which is a function of the abundance of the target element and the average atomic mass of the material. When they loose their energy through collisions, fast neutrons progressively become thermal neutrons. They can then be captured by heavy nucleii such as ^{56}Fe. The amount of gamma rays produced by this reaction is a function of the number density of thermal neutrons and the abundance of the element that capture them [Prettyman *et al.* , 2006].

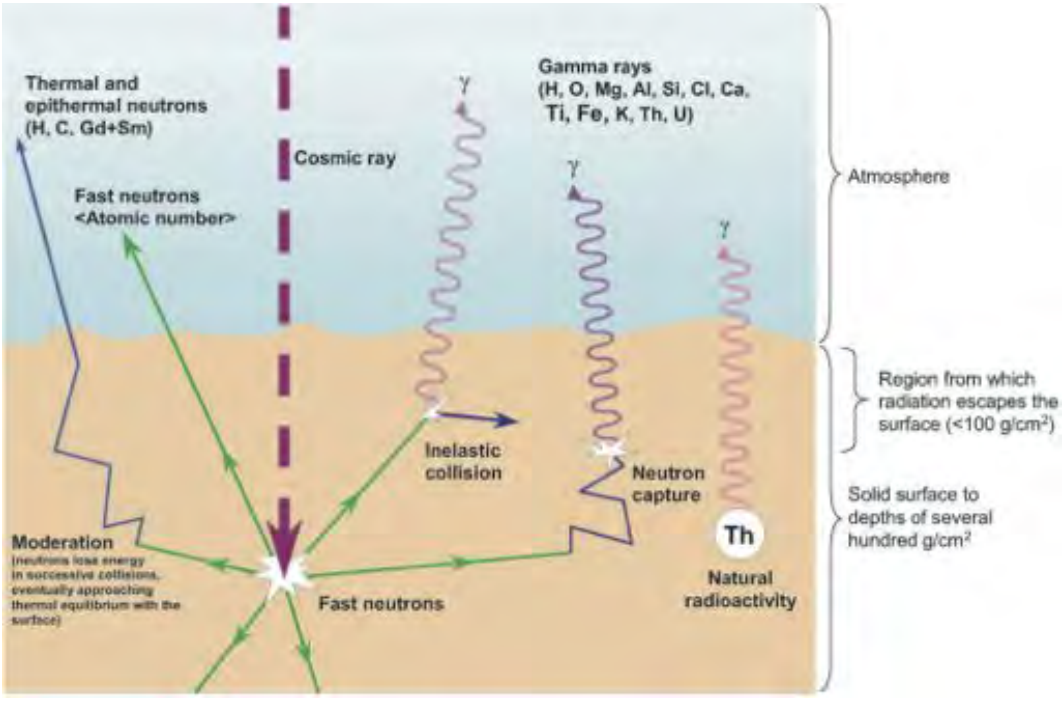

Figure 2.1: Cartoon representing nuclear interactions responsible for the production of gamma rays within a planetary regolith from Prettyman [2006].

Mission	**γ-ray detector**	**Body**	**Reference**
Apollo 15 & 16	NaI(Tl)	Moon	[Harrington *et al.* , 1974]
Kaguya	HPGe	-	[Hasebe *et al.* , 2009]
Chang'E-1	CsI(Tl)	-	[Zhu *et al.* , 2010]
Chang'E-2	$LaBr_3$	-	[Zhu *et al.* , 2013]
Lunar Prospector	BGO	-	[Feldman, 2004]
Dawn	BGO	Vesta and Ceres	[Prettyman *et al.* , 2011]
MESSENGER	HPGe	Mercury	[Peplowski *et al.* , 2012]
Mars Odyssey	HPGe	Mars	[Boynton *et al.* , 2004]
NEAR	BGO & NaI	Eros	[Evans *et al.* , 2001]
γ-ray detector	**Spectral resolution at 662 keV**		
HPGe	0.2 - 0.4 %		
NaI(Tl)	7 - 8 %		
CsI(Tl)	9 %		
$LaBr_3$	5 %		
BGO	10 - 11 %		

Table 2.2: List of spacecraft carrying gamma ray detectors. The spectral resolution of the different gamma ray detector is given in the lower part of the table in terms of the FWHM of the peak relative to the peak energy.

2.2.2 Gamma ray detection.

Two types of gamma ray detectors have been used in space missions, semiconductors and scintillators. In the first, a semiconductor dielectric material is placed between two electrodes and a high voltage is applied across the electrodes. When a gamma ray interacts with the semiconductor, it produces free electron-hole pairs. As the latter drift in the electric field, they induce charge on the electrodes, which is measured using a charge-sensitive preamplifier. The amplitude of the charge pulse, or pulse-height, is proportional to the energy deposited by the gamma ray, which is used to establish a histogram of pulse heights, known as a pulse-height spectrum [Prettyman, 2006]. Such semiconductor detectors have flown onboard the MESSENGER, Selene and Mars Odyssey missions [Peplowski *et al.* , 2012; Hasebe *et al.* , 2009; Boynton *et al.* , 2004].

On the other hand gamma rays can be detected by a scintillator. This consists in a transparent organic or inorganic crystal that can be of different composition (see Table 2.2). Such crystals produce visible light when ionized during interactions with neutrons or gamma rays. The visible photons are collected, amplified and converted to an electrical current by a photomultiplier tube, a device connected optically to the scintillator. The amplitude of the current depends on the energy deposited by the collected gamma ray, so that a gamma ray spectrum is produced similarly to the case of the semiconductor detector.

In light of the comparison between HPGe and BGO spectra provided in Figures 2.2 and 2.3, HPGe detectors appear better suited for precise gamma ray spectroscopy. However, mainly because of the low operating temperatures required by HPGe, the added cost and complexity of HPGe relative to scintillation technology, scintillators have remained competitive for some missions [Prettyman, 2006].

2.2.3 Gamma ray interactions.

Gamma rays produced during nuclear reactions can undergo further interactions within the planetary surface, within the spacecraft and within the detector via pair production, Compton scattering, and the photoelectric effect. If an incident gamma ray has an energy $E_\gamma > 1.022$ MeV it can be converted to an electron-positron pair. When the positron is annihilated by an electron, two (511 keV) gamma rays are produced. If one of the two

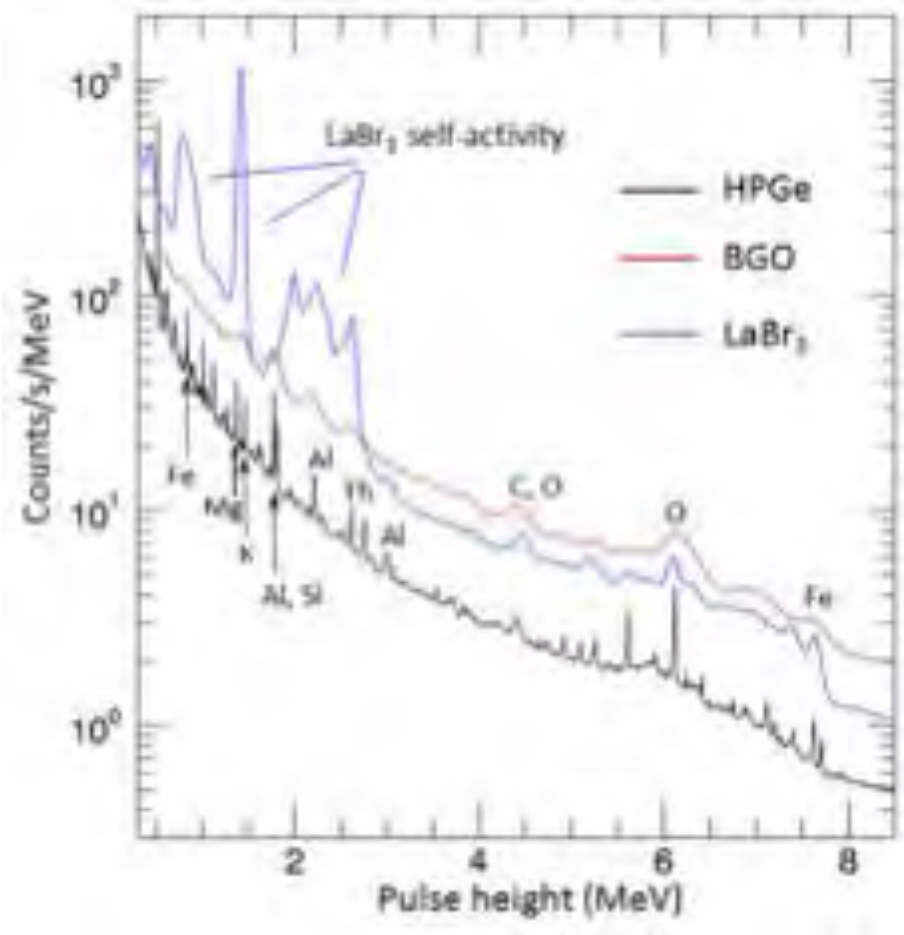

Figure 2.2: From [Prettyman, 2014]: "Comparison of whole Moon gamma ray spectra acquired by Lunar Prospector (BGO, red), Kaguya (HPGe, black), and Chang'E-2 ($LaBr_3$, blue)". The spectral resolution of BGO spectra is $\sim$ 20 times lower than HPGe and about two times lower than $LaBr_3$. $LaBr_3$ has a self activity visible below $E_\gamma \sim 3$ MeV which masks low energy features such as K and Th peaks.

511 keV photons escapes from the detector, a peak with energy equal to the initial incident gamma ray $E_\gamma -$ 511 keV will be produced while if the two 511 keV gamma rays escape, a $E_\gamma -$ 1022 keV peak will be produced. In Compton scattering, a portion of the energy of the gamma ray is transferred to an electron. The energy lost by the gamma ray depends on the scattering angle, thus each true gamma ray emitted from a nucleus exhibits a Compton continuum. Fe escape peaks are visible in Figure 2.3 along with Compton continuum.

2.2.4 Spatial resolutions

A spectrometer placed in orbit recieves radiations coming from underneath all the way out to the limb of the planet. The response of a spectrometer as a function of the distance from the sub-spacecraft point thus has a gaussian shape. The ability of the spectrometer to resolve spatial regions with different compositions depends on the FWHM of the Gaussian, which is approximately 1.5 times the orbital altitude [Prettyman *et al.* , 2006]. For GRaND at Vesta the orbital altitude during the low altitude mapping orbit was 210 km. This corresponds to a 300 km arc length FWHM or 20% of Vesta's circumference, as illustrated in Figure 2.4. Lunar Prospector data were recorded during a low altitude (30 km) and high amtitude (100 km) orbit. The corresponding spatial resolutions (FWHM) correspond then to 0.4 and 1% of the lunar circumference.

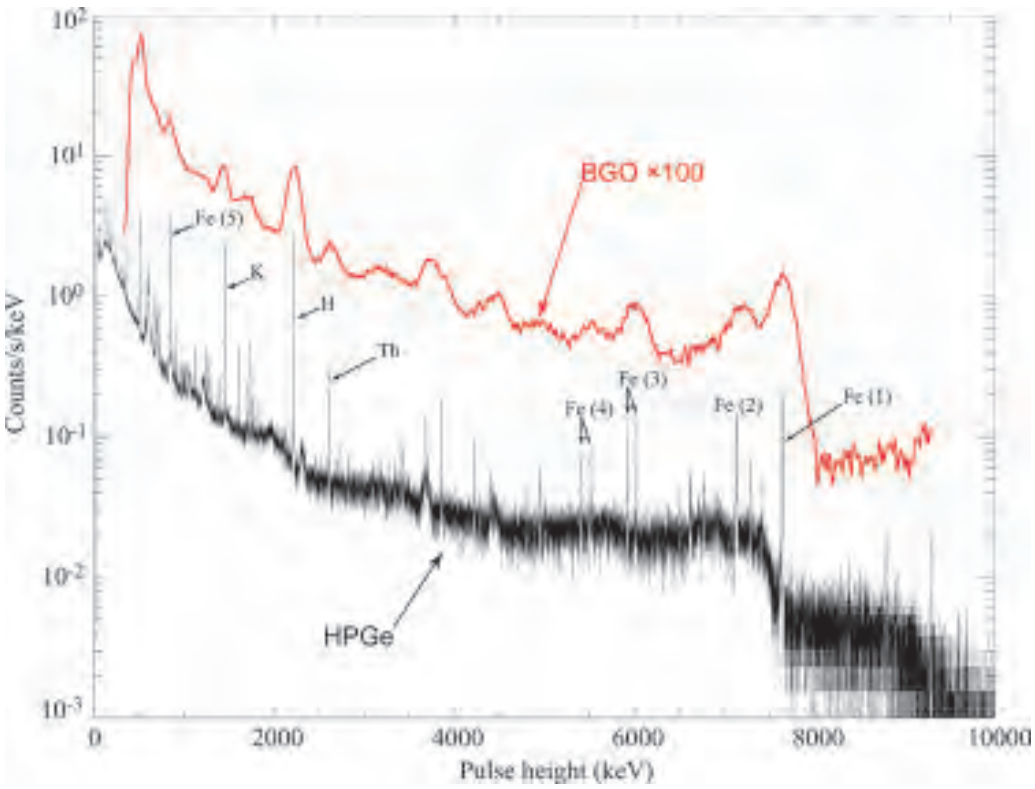

Figure 2.3: From Prettyman *et al.* [2006] A pulse height spectrum for a large volume coaxial HPGe detector (black) in comparison to BGO detector (red). "The gamma rays were produced by moderated neutrons, with an energy distribution similar to the lunar leakage spectrum, incident on an Fe slab. Well-defined peaks corresponding to neutron capture and inelastic scattering with Fe appear in the spectrum. For example, the doublet labeled Fe(1) corresponds to gamma rays (7646- and 7631-keV) produced by neutron capture with Fe. The peaks labeled Fe(2) are shifted 511 keV lower in energy and correspond to the escape of one of the 511 keV gamma rays produced by pair production in the spectrometer. The continuum that underlies the peaks is caused by external Compton scattering and the escape of gamma rays that scattered in the spectrometer. Gamma rays from neutron capture with H and the radioactive decay of K and Th are also visible."

2.2.5 LPGRS and GRaND

In this first chapter, we concentrate on the analysis of gamma ray spectra recorded around the Moon by the Lunar Prospector gamma ray spectrometer, (LPGRS) [Feldman, 2004] and around Vesta by the Gamma Ray and Neutron Detector (GRaND) [Prettyman *et al.* , 2011]. GRaND is one of the four scientific instruments on board of the Dawn spacecraft. This instrument is an ensemble of twenty-one different sensors: one BGO scintillator for gamma rays with energy lower than 9 MeV, sixteen CdZnTe semiconductors for gamma rays of less than 3 MeV, two phosphor sandwiches of Lithium-loaded Glass (LiG) and Boron-Loaded Plastic (BLP) scintillators and two Boron-Loaded Plastic (BLP) scintillators for the detection of thermal, epithermal and fast neutrons [Prettyman *et al.* , 2011]. The point of analyzing LPGRS and GRaND at Vesta datasets together, lies in the fact that the recorded signals are similar in shape, because both LPGRS and GRaND detect gamma rays using a bismuth germanate crystal that produce similar gaussian spectral response functions. In the case of LPGRS, this function has a full width at half maximum (FWHM) of 12.4% at 662 keV and 15 °C [Feldman, 2004], for the same conditions,

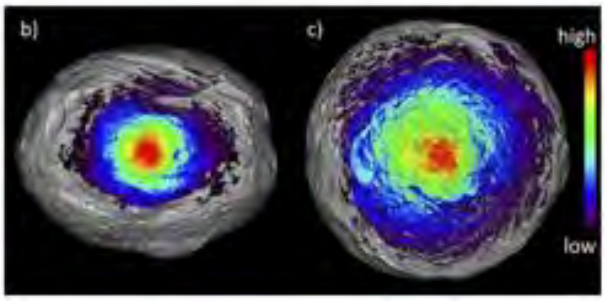

Figure 2.4: Field of view (FOV) of the GRaND instrument at Vesta from Prettyman *et al.* [2011]. "The contribution to the flux of each point of the surface within the FOV of GRaND is superimposed on orthographic projections of a shape model determined by Gaskell from FC images acquired by Dawn in Survey orbit: (b) for a subsatellite point near the equator; and (c) for a subsatellite point near the south pole. Both images are for a radial distance of 410 km and are well-representative of the instrument response function during low altitude mapping orbit.

GRaND's BGO ouput FWHM is 10.7% [Prettyman *et al.* , 2011, p46].

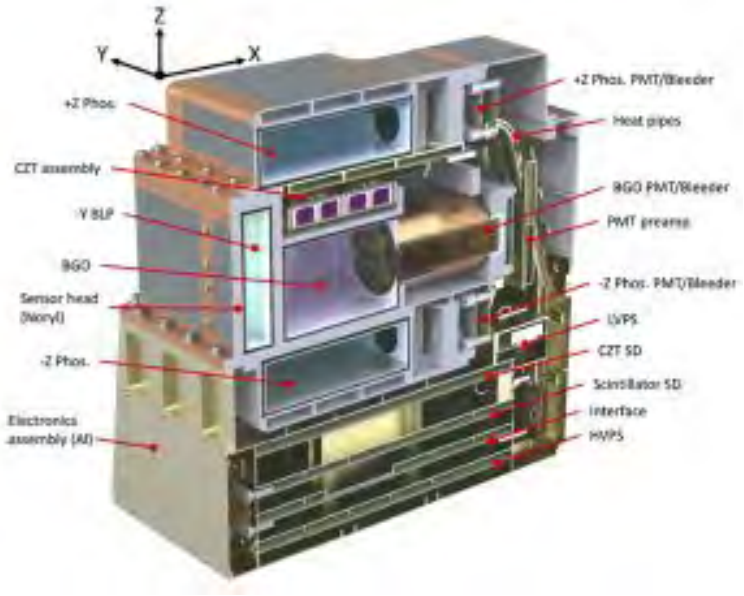

Figure 2.5: Cross section of the Gamma Ray and Neutron Detector onboard Dawn spacecraft from Prettyman *et al.* [2011]. The detection of gamma ray is enabled by the coupling of a BGO cristal (purple cube), which products visible light during interactions with gamma rays to a photomultiplier tube (PMT, orange cylinder) used to detect and amplify the light ouput from the scintillator.

The analysis of gamma rays relies upon an understanding of the physics of nuclear reactions. Generally, the first step of the analysis consists in identifying a spectral feature which is shown to stem from a particular reaction [Reedy, 1978]. For instance if a peak is identified between two channels, the integral of counting rates between these two channels can be converted into an elemental abundance. As this integrated counting rate can be affected by variations in observation conditions, or because the counting rate is not directly proportional to the element abundance, corrections are applied to the peak area, so its spatial variation can be correlated to the elemental abundance. Such an analysis is presented in [Yamashita *et al.* , 2012] to produce an iron map for Vesta (see Figure 1.18 in

the general introduction), based on 7.6 MeV gamma rays produced by neutron capture.

A given element does not typically produce only one gamma ray emission line, but a series of them. As such, one can consider using the entire energy spectrum, or, at least the region where representative peaks of the element are present, to perform the analysis. The Monte Carlo N particle transport code (MCNPX), [Briesmeister, 2000], enables modelling the gamma ray output, for instance, of a sphere of given composition, bombarded by a given flux of energetic particles. MCNPX is used in [Prettyman *et al.* , 2006] to model the gamma ray ouput of the Moon, as seen by the LPGRS, for a composition that is known from lunar samples. These model gamma ray spectra can be classified for radioactive decay, non elastic scaterring and neutron capture, element by element. The authors demonstrate that the shape of the individual elemental spectra do not depend significantly on composition. After having defined a mixing model that relates the elemental abundances to the observed gamma ray counting rates, a non negative least square inversion is used to retrieve the elemental abundances.

Blind source separation of spectral components from the bulk signal can be considered as a complementary analysis to the classical nuclear physics approach and can help understanding planetary gamma ray data. The following section introduces what blind source separation is and concentrates on two methods that are potentially useful for the analysis of the datasets considered in this study.

2.3 Synthetic gamma ray spectra

The Lunar Prospector Gamma Ray Spectrometer (LPGRS) dataset [3] is of particular interest because it is well understood and has been extensively analyzed. Inoput source signals are required to compare with the output source signals that are estimated by the separation algorithms. For this purpose we use elemental spectra simulated by the Monte Carlo N particle transport code called MCNPX as described by Prettyman *et al.* [2006].

2.3.1 Elemental spectra

For each individual chemical element, three distinct contributions to gamma-ray spectra may be identified, as discussed in [Prettyman *et al.* , 2006]. The first of these is the contribution from non-elastic scattering that is of the form:

$$n_{kl} = \frac{\tilde{n}_{kl}}{(a_k < A > +b_k) < w_k >}, \tag{2.1}$$

where $\tilde{n}_{kl}$ is the elemental pulse height spectrum per source particle of element k which results from non-elastic scattering. $< A >$ is the average atomic mass of the lunar surface material, $< w_k >$ is the average weight fraction of element k in the lunar surface. a_k and b_k are element specific constants.

The second contribution is from neutron capture:

$$c_{kl} = \frac{\tilde{c}_{kl}}{(a'_k < N > +b'_k) < w_k >}, \tag{2.2}$$

where $\tilde{c}_{kl}$ is the elemental pulse height spectrum per source particle of element k which results from neutron capture. $< N >$ is the average neutron number density of the lunar surface. a'_k and b'_k are element specific constants. Finally, there is the potential contribution of radioactive decay:

$$r_{kl} = \kappa_{rk} \frac{\tilde{r}_{kl}}{< w_k >}, \tag{2.3}$$

3. source: http://pds-geosciences.wustl.edu/missions/lunarp/reduced_grsns.html

where $\tilde{r}_{kl}$ is the elemental pulse height spectrum per source particle of element k which results from radioactive decay. κ_{rk} is an element specific scaling constant.

The MCNPX code can be used to predict a set of library spectra, n_{kl}, c_{kl} and r_{kl}, that can subsequently be used to model the observed gamma ray spectra:

$$X_{pl} = \kappa \sum_{k=0}^{6} (a_k A_p + b_k) w_{pk} n_{kl} + \kappa \sum_{k=1}^{6} (a'_k N_p + b'_k) w_{pk} c_{kl} + \sum_{k=7}^{9} w_{pk} r_{kl} + B_{pl} \quad (2.4)$$

X_{pl} is the counting rate observed at pixel p and channel l. k is the element index (k = 0, ..., 9 for O, Mg, Al, Si, Ca, Ti, Fe, K, Th, U), n_{kl} are non elastic scattering elemental spectra, c_{kl} are neutron capture elemental spectra, r_{kl} are the radioactive decay elemental spectra. The terms w_{pk} are the weight fraction of element k, A_p is the average atomic mass of pixel p, N_p is the neutron number density. κ is a common scaling constant for neutron capture and non-elastic scattering. The neutron capture contribution from O is found to be negligible in [Prettyman *et al.* , 2006], hence $1 < k < 6$ for capture contributions. B_{pl} is a background spectrum which results from the ensemble of the gamma rays that are not produced specifically by one element. One can see that the contribution of radioactive elements is a simple linear function of weight fraction. On the other hand, non-elastic scattering scales linearly with the elemental weight fraction but also with average atomic mass. In a similar way, the contribution of neutron capture scales linearly with elemental abundance but also the neutron number density.

While complete consideration of Eqn. 2.4 will be tested below, for the purposes of testing the BSS algorithms, we begin by making the simplifying assumption that average atomic mass and neutron number density are constant, such that all spectral components scale linearly with the weight fraction only. The values of $< A >$ and $< N >$ used for this purpose are those of the average composition of the lunar surface material as derived by Prettyman *et al.* [2006]. Individual elemental spectra were calculated by using:

$$S_{kl} = \kappa \left(\frac{\tilde{n}_{kl}}{(a_k < A > + b_k) < w_k >} + \frac{\tilde{c}_{kl}}{(a'_k < N > + b'_k) < w_k >} \right) \quad (2.5)$$

Multiplying these spectra by the weight fractions thus provides simplified gamma ray spectra of the Moon :

$$X_{pl} = \sum_{k=1}^{N_s} w_{pk} S_{kl}, \quad (2.6)$$

Mixtures of these spectra in proportions derived from the spatial geochemical variability proposed by Prettyman *et al.* [2006] have been used to assess to what extent BSS algorithms are capable of extracting endmember spectral components for lunar-like datasets. The library of elemental spectra and the spatial distributions of weight fraction used are illustrated in Figure2.6.

In addition, these spectra are used as references in the recognition procedure, described in section 2.4.4, which will be used in the rest of the chapter as a measure of the performance of the BSS techniques.

It is important to note that due to the configuration of the Lunar Prospector orbiter, the GRS axis was always parallel to the spin axis of the Moon. Thus the output spectra have a dependency on latitude. Here, the theoretical gamma ray spectra take account of the response function of the LPGRS instrument when it is located above the equator of the Moon. The latitude dependent response function will be considered later.

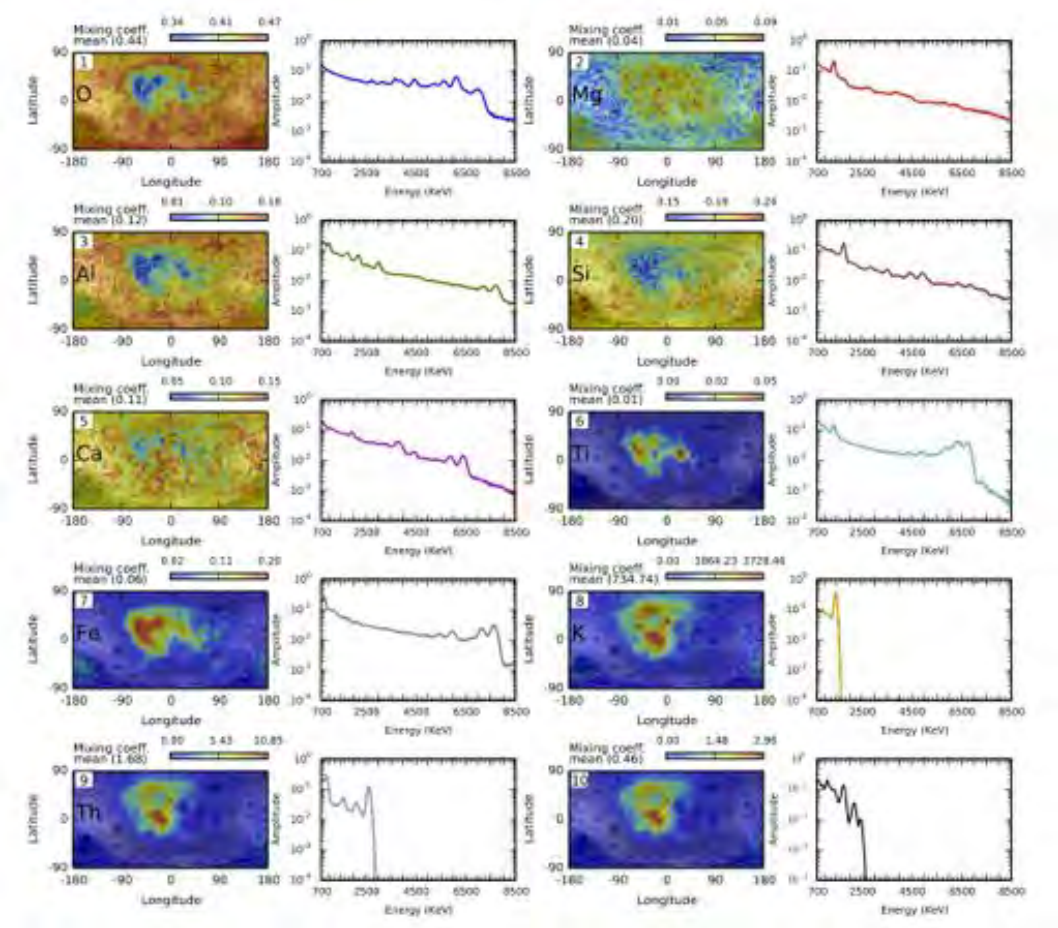

Figure 2.6: Elemental spectra of O, Mg, Al, Si, Ca, Ti, Fe, K, Th, and U simulated using the Monte Carlo N particle transport code (MCNPX) [Briesmeister, 2000]. The elemental spectrum of O take account of non-elastic scattering only, because the contribution from neutron capture was found to be negligible for this element [Prettyman *et al.* , 2006]. Elemental spectra of Mg, Al, Si, Ca, Ti, Fe take account of both non-elastic scattering and neutron capture. Contributions from K, Th and U stem from radioactive decay only. All these spectra are calculated for average lunar composition, atomic mass and neutron number density. They take account of the response function of the LPGRS instrument when it is located above the Moon's equator. The digital elevation model determined from the Lunar Orbiter Laser Altimeter is shown in transparency on each map.

2.3.2 Synthetic noise

The synthetic mixtures of gamma rays presented above do not take account of statistical noise that affects the counting rate of gamma rays at a given pixel p and channel l. Noise was thus added to these mixtures in order to respect the sampling conditions for the real LPGRS data. Lunar Prospector was in polar orbit around the Moon and gamma ray spectra were initially recorded as time series. Each gamma ray spectrum is acquired for 32 s during which time the spacecraft's position does not change significantly so it can be assumed that it corresponds to a fixed location. The spectra recorded above a pixel of given resolution, which was taken as 5°, form a bin. The counting rate X_{pl} corresponds to the average of the records contained in this bin. The uncertainty on this average can be estimated by the standard deviation of the values contained in the bin. Lawrence [2004] showed that after rejection of bad records and corrections, these values are similar to Poisson random variables, so the standard deviation of the bin is identical to the average counting rate, the

uncertainty on this average is thus given by:

$$\sigma_{pl} = \sqrt{\frac{X_{pl}}{N}} \tag{2.7}$$

where X_{pl} is the average counting rate at pixel p and channel l and N is the number of records used to calculate this average (see Figure 2.7). The derivation of this formula can be found in [Bevington & Robinson, 2003]. Therefore, for the synthetic datasets used below (produced initially by Eqn. 2.4 then by Eqn. 2.6) the noise was modelled as follows: A series of N values with an average equal to the noise-free counting rate X_{pl} is computed with the Matlab generator of Poisson random numbers. Then the average of this random series is taken as the noisy counting rate $\tilde{X}_{pl}$ and the uncertainty is taken as: $\sigma_{pl} = \sqrt{\tilde{X}_{pl}/N}$. Because the number of observations (total counting time) is variable from one pixel to another, the noise is also variable from one pixel to another (see Figure 2.7).

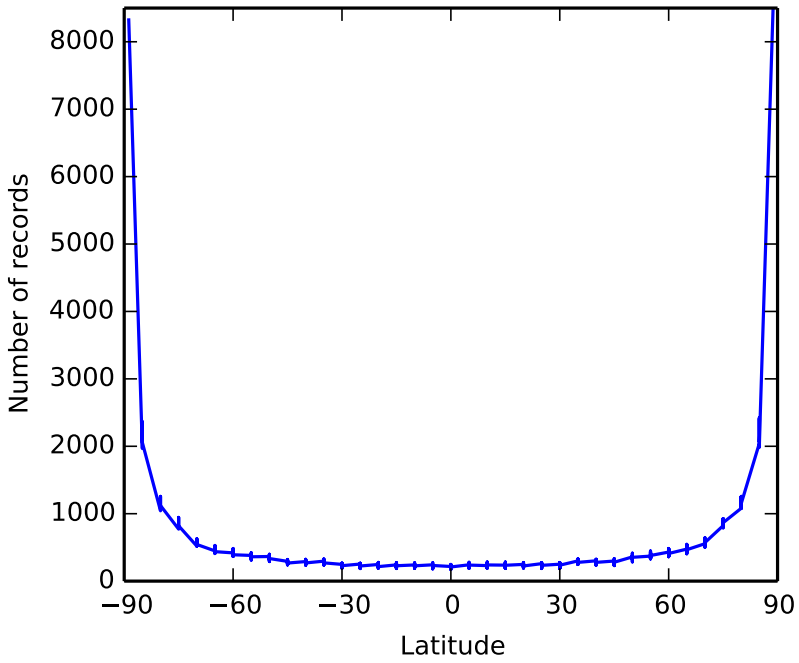

Figure 2.7: Number of spectra accumulated in each pixel as function of latitude for the 5° equal angle rebinned Lunar Prospector Gamma Ray Spectrometer (LPGRS) dataset. This sampling reflects the polar orbit of the spacecraft and manifests as a much better signal to noise ratio for spectra collected near the pole than for spectra recorded at the equator. This was taken into account to determine the level of noise to apply to synthetic spectra.

2.4 Methods of blind source separation.

2.4.1 Definition and principle

In a cocktail party, a certain number of people speak together in a room. A series of microphones are placed at different locations in the room so that each recording gives a different mixture of the speeches. Similarly the contribution of gamma rays stemming from different chemical elements present on the surface of a planet (equivalent to the speakers) vary in the spectra (equivalent to the recordings) acquired above different locations, because the composition varies from place to place. Can one extract the individual speeches from the records, or the elemental contributions from the set of measured gamma rays, with the least possible a priori information? This is what blind source separation (BSS) generally aims to do.

Deville [2011] defines BSS as "the ensemble of the methods that aim at estimating a series of unkown source signals from a series of available signals that are mixtures of the source signals that are sought, without knowledge or with a limited knowledge of the transformation of the source signals that generate their mixture". Since the term blind source separation appeared in the late 1980's, this discipline has developed significantly [Jutten & Taleb, 2000]. Speech separation [Deville & Puigt, 2007], artifact removal in electroencephalograms [Hyvärinen & Oja, 2000], mapping using hyperspectral images [Moussaoui *et al.* , 2008], are only a few examples among the wide field of applications of BSS. The analyzed signals and the strategies implemented to construct algorithms of blind source separation are various. This diversity has led to a widespread and diverse development of this field of study [Pal *et al.* , 2013].

Mixing model

An algorithm of blind source separation is based on a mixing model and a mathematical property to be used, such as the indepence, the sparcity or the positiveness, either to restore the sources and/or the mixing process. The methods used in this study are based on the following mixing model:

$$X_{pl} = \sum_{k=1}^{N_S} M_{pk} S_{kl}, \ \forall\, p \in \{1, ..., N_P\} \ and \ \forall\, l \in \{1, ..., N_C\}, \tag{2.8}$$

where p is the index of a pixel (location), l is the index of a channel (energy), k is the index of a source spectrum (e.g. one elemental contribution). N_P is the number of pixels, N_C is the number of energy channels and N_S is the number of source spectra. In other words, in this model, a gamma ray of given energy X_{pl} is considered as the linear superposition of contributions from different elemental gamma rays S_{kl}. According to the model of [Prettyman *et al.* , 2006], if X_{pl} are gamma rays stemming from radioactive decay only, S_{kl} are elemental counting rate per abundance unit, of a set of radioactive elements. In this case, then M_{pk} is the abundance of element k at pixel p. In fact, if other reactions are involved, the actual nature of gamma ray mixtures is more complicated as shown by the mixture model considered in Prettyman *et al.* [2006].

Separation algorithm

In some iterative algorithm, let t be the current iteration and $t+1$, the next one. The BSS algorithm is an iterative estimator either of the inverse of $\mathbf{M}(t+1)$, $\mathbf{M}(t+1)$ itself and/or $\mathbf{S}(t+1)$, based on manipulations of $\mathbf{X}(t)$, $\mathbf{S}(t)$ and/or $\mathbf{M}(t)$. Iterations are stopped when a separating criterion implying that the sources are restored is satisfied.

2.4.2 Properties used for separation

The signal properties used to construct such algorithms are numerous, a few examples are illustrated here.

Sparcity

Sparsity is the degree to which only a small number of entries of a signal differ significantly from zero. Zibulevsky & Pearlmutter [2001] introduced a BSS method that focuses on sparsity to distinguish the source signals. Most real-world signals are not sparse in the domain they are originally recorded in. Therefore, those authors suggest to transform the sources into a basis (also called dictionary, e.g. a wavelet basis) where the source can be sparsely representable, so that a procedure based on the maximization of sparcity allows signal separation within this basis. Finally, the sources originally sought are obtained by the inverse transform.

In the case of audio signals, a time frequency (TF) representation of the records enables locating zones where only one source signal is active. As this isolated source is recorded by different sensors, this TF zone can be used to estimate the mixing coefficients of the isolated source and to eventually reconstruct the entire mixing matrix [Deville & Puigt, 2007].

In the case of multichannel images, Bobin *et al.* [2006] develop a method where in addition to sparsity, the morphological diversity of the sources is exploited, i.e. the fact that the sources are sparse in different basis, a method generalized in [Bobin *et al.* , 2007]. Such method has been successfully applied to reflectance visible-infrared hyperspectral data from the Omega mission, allowing extraction of CO_2 and H_2O spectra [Moudden & Bobin, 2011].

Correlation

Exploring how each signal is linearly related to another one, can be performed via one estimator: the correlation [Pearson, 1901]. Let's imagine that the correlations between the observed signals (X_{pl}) stem from the fact that they are linear combinations of signals whose values are not originally correlated (S_{kl}). Looking for the basis in which, the signals show minimum correlation, is a way to separate the uncorrelated signals. This procedure is also known as principal component analysis, PCA [Hotelling, 1933]. This is usually done by finding the transformation onto which the covariance matrix of the observations $\mathbf{C_{XX}} = E\{\mathbf{X'X'}^T\}$, where $\mathbf{X'}$ are the centered signals, obtained by:

$$X'_{pl} = X_{pl} - \frac{1}{N_C}\sum_{l=1}^{N_C} X_{pl} \tag{2.9}$$

The covariance can be decomposed into eigenvalues and eigenvectors [Jolliffe, 2002].

$\mathbf{C_{XX}} = \mathbf{EDE}^T$ where $\mathbf{D}$ is a diagonal matrix containing the eigenvalues in decreasing order, $\mathbf{E}$ is an orthogonal matrix containing the eigenvectors in its columns in the same order.

Projecting the signals onto the basis where they are not correlated is done through the operation:

$$\mathbf{Z} = \mathbf{W}\,\mathbf{X'}, \tag{2.10}$$

where the matrix $\mathbf{W}$ is derived from the diagonal version of the covariance matrix: $\mathbf{W} = \mathbf{D}^{-1/2}\mathbf{E}^T$. Note that by setting the scaling $\mathbf{D}^{-1/2}$, the signals $\mathbf{Z}$ have unit variance. This decorrelation and normalization procedure is often refered to as "whitening" or sphering the observations [e.g. Hyvärinen & Oja, 2000, sec. 5.]. If $\mathbf{W} = \mathbf{D}^{-1/2}\mathbf{E}^T$, the number of

decorrelated signals $\mathbf{Z}$ is N_P. But, if they are sorted by magnitude, the first eigenvalues of the covariance matrix often account for most of the variance of the dataset. In practice, only N_S most significant eigenvalues and vectors are retained, which is a way to reduce the dimensionality of the data. The criteria that may be used to select a particular value for N_S are discussed in section 2.8.2.

Note that by replacing the mixing model into 2.10, one obtains:

$$\mathbf{Z} = \mathbf{WM}\,\mathbf{S}', \tag{2.11}$$

It is straightforward to show that $\mathbf{WM}$ is an $N_S \times N_S$ orthogonal matrix that one can note $\mathbf{U}$. If this latter equals the identity matrix:

$$\mathbf{S}' = \mathbf{Z}, \tag{2.12}$$

which is true only if the initial uncorrelation hypothesis holds. This also means that the mixing matrix is:

$$\mathbf{M} = \mathbf{W}^{-1} = \mathbf{ED}^{1/2}. \tag{2.13}$$

Correlation can be viewed as the second order of statistical independence, which is why very often, algorithms of independent component analysis, a method treated next, use the whitening procedure as an intermediate step [Comon, 1994].

Independence

In a similar approach, one can make the hypothesis that the observations are linear mixtures of signals that are not just uncorrelated but more generally are independent [Hyvärinen & Oja, 2000]. The methods of signal separation based on this hypothesis are called independent component analyses (ICA) and originate from the study of neural networks [Hérault & Ans, 1984]. More specifically, ICA requires three hypotheses [Deville, 2011]. For the gamma rays, they could be formulated as follows. (1) The fact that an elemental contribution takes the value A at a given channel is independent of the fact it takes the value B at a different channel (an elemental spectrum can be assimilated to the sampling of N_C series of independent random variables).

$$P(S_{il} = A | S_{jl} = B) = P(S_{il} = A)P(S_{jl} = B). \tag{2.14}$$

(2) The fact that, at a given channel, an elemental contribution takes the value A is independent of the fact that at this same channel, another elemental contribution takes the value B (the N_S series of random variables are mutually independent).

$$P(S_{ki} = A' | P(S_{kj} = B') = P(S_{ki} = A')P(S_{kj} = B'). \tag{2.15}$$

(3) Any separation system based on independence cannot achieve its goal if more than one of the source signals show values that have a gaussian distribution [Comon, 1994].

Several strategies can be used to restore independent signals of mixtures that can either focus on the properties of each individual independent signal or on their mutual independency [Deville, 2011].

Independence of each source

Mixing independent signals with non gaussian distributions produces observations that become dependent and have distributions that tend towards gaussian ones. This latter important and constant statistical property is formulated through the central limit theorem, e.g. [Rice, 1995]. This may be used to show that ICA can be defined as an optimization problem, which will search to minimize the non-gaussianity of each source signal [Hyvärinen & Oja, 2000].

Mutual independence

Other approaches exploit the properties of auto and cross cumulants of independent signals, such as the fact that all cross cumulants of independent variables cancel. Comon [1994] proposes to view ICA as an extension of the principal component analysis except that PCA only restores the independence of the sources to the second order, so that ICA would have to be based on the use of higher order statistics. A family of ICA aims at cancelling the fourth order cross cumulants of the signals to restore the independent sources [Cardoso & Souloumiac, 1993; Comon, 1994; Cardoso, 1999; Lacoume *et al.* , 1997]. The fourth order cumulants form a tensor, $\mathbf{C}$, of dimensions $N_S \times N_S \times N_S \times N_S$. For a series of signals $\hat{\mathbf{S}}$ that have zero mean and unit variance the elements of this tensor can be defined in terms of moment as:

$$C_{ijkl} = E\{S_i S_j S_k S_l\} - E\{S_i S_j\}E\{S_k S_l\} - E\{S_i S_k\}E\{S_j S_l\} - E\{S_i S_l\}E\{S_j S_k\}. \tag{2.16}$$

Note that:

$$C_{iiii} = E\{S_i^4\} - 3E\{S_i^2\}^2 \tag{2.17}$$

is the fourth order auto-cumulant of one signal, also known as kurtosis. Gaussian signals have a zero kurtosis, which is another expression of the fact that ICA cannot handle more than one gaussian source signal, as shown in [Comon, 1994]. One possible fourth order cumulant of a pair of signals is:

$$C_{iijj} = E\{S_i^2 S_j^2\} - E\{S_i^2\}E\{S_j^2\} - 2E\{S_i S_j\}^2. \tag{2.18}$$

JADE [Cardoso & Souloumiac, 1993] illustrates the cancelling procedure of certain cross-cumulants to restore the independent signals. More specifically, Cardoso & Souloumiac [1993] show that:

$$\phi^{JADE}(\hat{\mathbf{S}}) = \sum_{ijkl \neq iikl} (C^{\hat{\mathbf{S}}}_{ijkl})^2, \tag{2.19}$$

is a constrast function, i.e. a measure of the dependence between the signals. The interest of using ϕ^{JADE} (section 3.1.3 in [Cardoso, 1999]) is that it is also a criterion to simultaneously diagonalize a set of cumulant matrices. This algorithm is described in detail in the following section.

Joint Approximate Diagonalization of cumulant matrices

As many ICA algorithms, JADE includes a preliminary whitening step (equation 2.10). As such, the joint diagonalization problem starts with:

$$\mathbf{S} = \mathbf{U}^T \mathbf{Z}. \tag{2.20}$$

The aim of orthogonal ICA algorithms, such as JADE, consists in finding $\mathbf{U}$ that restore $\mathbf{S}$ as a set of independent source signals. Cardoso & Souloumiac [1993] use (1) ϕ^{JADE} as a criterion for optimizing independence. (2) They show that for independent sources $\mathbf{U}$ is the joint diagonalizer of a set of cumulant matrices [Cardoso & Souloumiac, 1993, 3.1]. (3) They exploit the fact that the matrix $\mathbf{U}$ can be decomposed into a product of $N = N_S(N_S - 1)/2$, 2×2 rotation matrices [Lacoume *et al.* , 1997, p252], to perform the joint diagonalization. The cumulant matrices are defined as:

$$\mathbf{Q}^{kl} = \sum_{k,l=1}^{N_S} C_{ijkl} M_{kl} \tag{2.21}$$

where $\mathbf{M}$ is chosen in [Cardoso & Souloumiac, 1993] as $\mathbf{b}_k\mathbf{b}_l^T$, where $\mathbf{b}_k$ denotes the $N_S \times 1$ vector with 1 in the kth position and 0 elsewhere. Cancelling cross cumulants then requires to simultaneously diagonalize these $N_S \times N_S$ matrices. There are N_S^2 such slices but it can be shown that considering $N_S(N_S+1)/2$ cumulant matrices is sufficient (section 4.2 Cardoso [1999] p175). Here is an example of these cumulant matrices in the case of three sources. The $N_Q = N_S(N_S+1)/2 = 6$ cumulant matrices are $\mathbf{Q}^{11}$, $\mathbf{Q}^{22}$, $\mathbf{Q}^{21}$, $\mathbf{Q}^{33}$ $\mathbf{Q}^{31}$, $\mathbf{Q}^{32}$:

$$\begin{pmatrix} C_{1111} & C_{1211} & C_{1311} \\ C_{2111} & C_{2211} & C_{2211} \\ C_{3111} & C_{3211} & C_{3311} \end{pmatrix}; \begin{pmatrix} C_{1122} & C_{1222} & C_{1322} \\ C_{2122} & C_{2222} & C_{2222} \\ C_{3122} & C_{3222} & C_{3322} \end{pmatrix}; \begin{pmatrix} C_{1133} & C_{1233} & C_{1333} \\ C_{2133} & C_{2233} & C_{2233} \\ C_{3133} & C_{3233} & C_{3333} \end{pmatrix} \quad (2.22)$$

$$\begin{pmatrix} C_{1121} & C_{1221} & C_{1321} \\ C_{2121} & C_{2221} & C_{2321} \\ C_{3121} & C_{3221} & C_{3321} \end{pmatrix}; \begin{pmatrix} C_{1131} & C_{1231} & C_{1331} \\ C_{2131} & C_{2231} & C_{2331} \\ C_{3131} & C_{3231} & C_{3331} \end{pmatrix}; \begin{pmatrix} C_{1132} & C_{1232} & C_{1332} \\ C_{2132} & C_{2232} & C_{2332} \\ C_{3132} & C_{3232} & C_{3332} \end{pmatrix} \quad (2.23)$$

The diagonalization of this set of matrices can be performed via a series of 2×2 rotations often called Givens rotations [Golub & Van Loan, 2013]:

1) For each pair (p,q) of signals the following $N_S \times N_Q$ matrix is formed:

$$\mathbf{g}^{pq} = \begin{pmatrix} Q_{pp}^s - Q_{qq}^s & \dots & Q_{pp}^{N_Q} - Q_{qq}^{N_Q} \\ Q_{pq}^s - Q_{qp}^s & \dots & Q_{pq}^{N_Q} + Q_{qp}^{N_Q} \end{pmatrix}, \quad (2.24)$$

such that:

$$(\mathbf{g}\mathbf{g}^T)^{pq} = \begin{pmatrix} \sum_{s=1}^{N_Q} (Q_{pp}^s - Q_{qq}^s)^2 & \sum_{s=1}^{N_Q} (Q_{pp}^s - Q_{qq}^s)(Q_{pq}^s + Q_{qp}^s) \\ \sum_{s=1}^{N_Q} (Q_{pp}^s - Q_{qq}^s)(Q_{pq}^s + Q_{qp}^s) & \sum_{s=1}^{N_Q} (Q_{pq}^s + Q_{qp}^s)^2 \end{pmatrix}. \quad (2.25)$$

2) Defining the rotation matrix:

$$\mathbf{G} = \begin{pmatrix} cos\theta & -sin\theta \\ sin\theta & cos\theta \end{pmatrix}, \quad (2.26)$$

where the angle θ that cancels off-diagonal terms of $(\mathbf{g}\mathbf{g}^T)$ can be computed following the method described in [Golub & Van Loan, 2013] p428, which here leads to:

$$\begin{aligned} &\theta^{pq} = arctan\left(t_{off}, t_{on} + \sqrt{t_{on}^2 + t_{off}^2}\right) \\ &\text{where} \\ &t_{on} = (gg^T)_{11}^{pq} - (gg^T)_{22}^{pq} \\ &t_{off} = (gg^T)_{12}^{pq} + (gg^T)_{21}^{pq}. \end{aligned} \quad (2.27)$$

3) The subset of $\mathbf{U}$ corresponding to the pair p,q is rotated using $\mathbf{G}$. For instance for the pair p=1,q=3 the rotated version of $\mathbf{U}$ would be:

$$\mathbf{U}' = \begin{pmatrix} cos\theta\ U_{11} - sin\theta\ U_{13} & U_{12} & sin\theta\ U_{11} + cos\theta\ U_{13} \\ cos\theta\ U_{21} - sin\theta\ U_{23} & U_{22} & sin\theta\ U_{21} + cos\theta\ U_{23} \\ cos\theta\ U_{31} - sin\theta\ U_{33} & U_{32} & sin\theta\ U_{31} + cos\theta\ U_{33} \end{pmatrix} \quad (2.28)$$

where θ is the Givens angle that diagonalizes $(\mathbf{g}\mathbf{g}^T)^{13}$. The cumulant matrices are updated accordingly. 1), 2), 3) are repeated until the Given's angle, θ becomes small, meaning

that the set of cumulant could not be more diagonal, i.e. that the mutual independence of the estimated signals has reached an optimum. The Given's angle was set to $10^{-6}/\sqrt{N_C}$ in this thesis according to [Cardoso, 1999] and the online version of JADE[4]. The final estimated independent source signals are given by:

$$\mathbf{S} = \mathbf{UWX}, \tag{2.29}$$

and the mixing matrix can be obtained by:

$$\mathbf{M} = \mathbf{W}^{-1}\mathbf{U} = \tilde{\mathbf{E}}\tilde{\mathbf{D}}^{1/2}\mathbf{U}. \tag{2.30}$$

In the present study, the sign undetermination is "corrected" after the last iteration, if the power of the positive part of the estimated source is higher than the power of the negative part, its sign is changed, it is unchanged otherwise.

An algorithm may be capable of restoring independent source signals. But, if this hypothesis is not true, similarly to the fact that PCA extracts the least correlated components of the signals, ICA restores the least dependent components of the signals based here on the contrast ϕ^{JADE}. Furthermore, the impossibility of JADE to perfectly diagonalize the set of cumulant matrices, can be the reflection of the impossibility of finding independent components [Cardoso, 1999].

The algorithm JADE as a whole works as summarized in algorithm 1, derived from [Cardoso, 1999].

1) Remove mean value from each spectrum **X**.
2) Compute the covariance matrix $\mathbf{C_{XX}} = E\{\mathbf{X'X'}^T\}$.
3) Search for N_S $E\{\mathbf{X'X'}^T\}$ eigenvalues / vectors.
4) Whiten data $\mathbf{Z} = \mathbf{WX'}$ (eqn. 2.10)
5) Form a set of $N_S(N_S+1)/2$ cumulant matrices **Q**'s.
6) Diagonalize the set of cumulant matrices $\mathbf{Q}'s$ to find the rotation matrix **U**:
while $\theta > 10^{-6}/\sqrt{N_C}$ **do**
  For each pair p,q with $p \neq q$
  Compute the 2×2 Givens rotation (eqn 2.24 to eqn 2.27)
  Rotate **U**(p,q)
  Rotate **Q**(p,q)'s.
end
7) Compute estimated source signals: $\mathbf{S} = \mathbf{U}^T\mathbf{Z}$
8) Correct sign of **S**.

Algorithm 1: The ICA algorithm JADE based on the simultaneous diagonlization of cumulant matrices [Cardoso & Souloumiac, 1993].

Positiveness

Under the constraint of positiveness of the data, an algorithm where M and S are estimated jointly and iteratively, seeks to express the observations X into the product MS, by minimizing the distance, or divergence $D(X, MS)$ [Lee & Seung, 2001], [Berry *et al.* , 2007], [Cichocki *et al.* , 2009]. Here, only algorithms based on the minimization of the euclidian distance are considered. This distance is defined as:

$$D(\boldsymbol{X}, \boldsymbol{MS}) = ||\mathbf{X} - \mathbf{MS}||^2 = \sum_{p=1}^{N_P}\sum_{l=1}^{N_C}\left(X_{pl} - \sum_{k=1}^{N_S} M_{pk}S_{kl}\right)^2 \tag{2.31}$$

4. http://perso.telecom-paristech.fr/~cardoso/Algo/Jade/jadeR.m

This cost function can be weighted to account for the fact that gamma ray counting rates are Poisson random variates, which would turn the function into:

$$D(\boldsymbol{X}, \boldsymbol{MS}) = \sum_{p=1}^{N_P} \sum_{l=1}^{N_C} \left(\frac{X_{pl} - \sum_{k=1}^{N_S} M_{pk} S_{kl}}{\sigma_{pl}} \right)^2 = \sum_{p=1}^{N_P} \sum_{l=1}^{N_C} \frac{\left(X_{pl} - \sum_{k=1}^{N_S} M_{pk} S_{kl} \right)^2 N}{X_{pl}}. \tag{2.32}$$

This optimization problem is not convex and does not guarantee convergence towards a global minimum. Defining a starting point is essential in the search for a local minimum of interest as discussed in the next paragraph "Initialization of NMF". Several approaches can be used to minimize $D(\boldsymbol{X}, \boldsymbol{MS})$. Lee & Seung [2001] have shown that applying the following update rule:

$$\begin{aligned} S_{kl}(t+1) &= S_{kl}(t) \frac{[\boldsymbol{M}^T \boldsymbol{X}]_{kl}}{[\boldsymbol{M}^T \boldsymbol{MS}(t)]_{kl}} \\ M_{pk}(t+1) &= M_{kl}(t) \frac{[\boldsymbol{S}(t+1) \boldsymbol{X}^T]_{pk}}{[\boldsymbol{MS}(t+1) \boldsymbol{S}(t+1)^T]_{pk}}, \end{aligned} \tag{2.33}$$

inevitably leads to a reduction of $D(X, MS)$ for positive $\boldsymbol{X}$, $\boldsymbol{M}$ and $\boldsymbol{S}$. They show that this update rule is equivalent to what is obtained by developing an update rule based on a gradient descent along $D(\boldsymbol{X}, \boldsymbol{MS})$. Paatero & Tapper [1994] propose a different form of NMF by alternatively solving two non-negative least square minimizations:

$$\boldsymbol{M}(t+1) = \underset{\boldsymbol{M} \in \mathbb{R}^{N_P \times N_S}}{\arg\min} \frac{1}{2} D(\boldsymbol{X}, \boldsymbol{M}(t) \boldsymbol{S}(t)), \tag{2.34}$$

subject to positive M_{pk}'s, and:

$$\boldsymbol{S}^(t+1) = \underset{\boldsymbol{S} \in \mathbb{R}^{N_S \times N_C}}{\arg\min} \frac{1}{2} D(\boldsymbol{X}, \boldsymbol{M}(t+1) \boldsymbol{S}(t)). \tag{2.35}$$

subject to positive S_{kl}'s. t correponds to the current state of matrices $\boldsymbol{M}$ or $\boldsymbol{S}$ and $t+1$ to their state after the update.

Lin [2007b]; Gong & Zhang [2012] have used a projected Newton method to solve the individual non-negative least square problems, that allows a faster convergence of NMF than with the classical multiplicative update or the gradient descent methods usually implemented. The code for this algorithm is available at: http://www.public.asu.edu/~pgong5/

Initialization of NMF

NMF algorithms are not guaranteed to converge to a unique solution when they are initialized with random matrix factors because they are based on the optimization of a non convex cost function [Lin, 2007a]. This can be resolved by modifying the optimized function, including penalty terms that will add more constraints on the form of the solution [Berry *et al.* , 2007]. On the other hand, one can initialize one of the factors with an initial solution that was obtained from another BSS method [Langville *et al.* , 2006]. Using independent components as a first guess, has been shown to significantly improve the quality of the reconstruction of source signals and mixing coefficients, in the case of terrestrial hyperspectral imaging [Benachir *et al.* , 2013]. Here we have initialized matrix $\boldsymbol{S}$ with:

$S^{JADE} - min(S_{JADE})$ and used the algorithm of Gong & Zhang [2012] to perform non matrix factorization. It is important to stress that S^{JADE} has zero mean and is estimated up to a sign. To remedy this undeterminacy, the sign of S^{JADE} is corrected such that the power of its positive part is always greater than the power of its negative part, which was found to avoid reverted gamma ray peaks.

2.4.3 Quality of signal reconstruction

As alluded to above (2.4.2), the number of estimated sources N_{Sout} to be reconstructed is specified by the user. The optimum number of output sources can be defined by setting a selection criterion. In the case of PCA and most ICA methods which include PCA as a preleminary step, selecting N_S can be done by fixing a threshold for the percentage of cumulated variance accounted by the eigenvalues of the covariance matrix retained, but choosing a particular value may lack rigour. Another approach consists in measuring the difference between the original signal and the signal reconstructed by blind source separation and compare its value against the values of N_S that are tested [e.g. Starck *et al.* , 2010, p238]. Here the reduced χ^2 goodness of fit between the observation and the reconstruction was used to take account of the uncertainty on the observation. The reduced χ^2 value should decrease as the number of sources increases until the point it becomes lower than one, in which case adding more components is not significant for the signal within the range of uncertainties. This quality criterion is written as:

$$\chi^2_p = \frac{1}{N_C - N_{Sout}} \sum_{l=1}^{N_C} \left(\frac{X_{pl} - \sum_{k=1}^{N_{Sout}} M^{BSS}_{pk} S^{BSS}_{kl}}{\sigma_{pl}} \right)^2 , \tag{2.36}$$

where χ^2_p is the quality of reconstruction of the spectrum of pixel p. N_C is the number of channels, N_{Sout} is the number of estimated sources. S^{BSS}_{kl}, M^{BSS}_{pk} are respectivelay the sources and the mixing coefficients estimated by BSS, X_{pl} are the observed gamma ray counting rates.

Ten elements contribute significantly to the LPGRS data as shown in [Prettyman *et al.* , 2006] so this number of eigenvalues could be retained. In order to avoid making an a priori choice, all datasets considered in this chapter are systematically analyzed by exploring a variable number of potential sources N_{Sout} (from 2 to 15). The value of the average quality of signal reconstruction is then compared to N_{Sout}, which provides a guide to choose a relevant value of N_{Sout}.

2.4.4 Element recognition

The signal reconstruction provided by a BSS technique might be satisfactory, but the estimated source signals might not fullfil the expectation of extracting elementary signatures. Here, a procedure is designed to assess whether a component extracted by ICA or ICA-NMF is spectrally and spatially coherent with the gamma ray signature of one element in the lunar BGO spectra. This is based on comparisons with the elementary spectra and maps presented in Figure 2.6.

ICA or ICA-NMF produce estimates of S_{kl} and M_{pk}. The similarity of these estimates with either an elemental spectrum of the library or an abundance map is measured by using two correlation matrices. Spectral correlations are stored in $\boldsymbol{Cs}$. Spatial correlations are stored in $\boldsymbol{Cm}$. The correlation of estimated source spectrum i with library spectrum j is

defined as:

$$Cs_{ij} = \rho_{S_i^{BSS}, S_j^{lib}} = \frac{cov(S_i^{BSS}, S_j^{lib})}{\sigma_{S_i^{BSS}} \sigma_{S_j^{lib}}}, \tag{2.37}$$

where, S_i^{BSS} is the BSS ouput source, S_i^{lib} is the input source from the library, $cov(A, B)$ is the covariance of the spectra A and B and σ_A the standard deviation of the spectrum A. Similarly, the correlation between the estimated map i with the library map j:

$$Cm_{ij} = \rho_{M_i^{BSS}, M_j^{lib}} = \frac{cov(M_i^{BSS}, M_j^{lib})}{\sigma_{M_i^{BSS}} \sigma_{M_j^{lib}}}. \tag{2.38}$$

Element recognition

Elemental spectra of the library and maps are stored in the same order. In this way, the estimated source i is considered as recognized from the library when it shows simultaneous maximum correlation with library spectra and maps, a condition that can be written as:

$$argmax(\boldsymbol{cs}_i) = argmax(\boldsymbol{cm}_i). \tag{2.39}$$

where $\boldsymbol{cs}_i$ is a "row" of $\mathbf{Cs}$ that contains the correlations between estimated source i and library spectra. Similarly, $\boldsymbol{cm}_i$ contains the correlations between the estimated map i and library maps.

2.5 Application of ICA-NMF to simplified mixtures.

2.5.1 Linear mixtures of Fe, Ti and K

For the sake of simplicity ICA refers to JADE [Cardoso & Souloumiac, 1993] and ICA-NMF refers to the combination of JADE with the NMF developed in [Gong & Zhang, 2012] (see section 2.4) in the rest of this chapter. As a first test, ICA and ICA-NMF are applied to linear mixtures (Eqn. 2.6) of three elemental spectra associated to Fe, Ti (non elastic scattering and neutron capture) and K (radioactive decay). Element weight fractions are taken as mixing coefficients. Noise is added accordingly to the conditions of sampling of the LPGRS instrument as detailed in section 2.3.2. This synthetic dataset is shown in Figure 2.8.

The maps of K, Ti and Fe inferred from ICA and ICA-NMF are provided in Figure 2.9 and the estimated elemental spectra are given in Figure 2.10 when the number of ouput sources N_{Sout} is set to 3. After applying NMF, the spatial distributions of iron and titanium can be discriminated whereas it is not the case for the maps estimated via ICA, that appear dominated by the spatial distribution of iron (Figure 2.9). As far as elemental spectra are concerned, JADE alone is able to separate the potassium component from the rest of the signal, as shown by the presence of the emission line at 1.45 MeV. Iron and titanium can be extracted as depicted by the reconstruction of non elastic scattering peaks at low energies (0.8 MeV for iron, 1.4 MeV for titanium) and neutron capture peaks at high energy at 7.6 MeV and 6.7 MeV for Fe and Ti respectively.

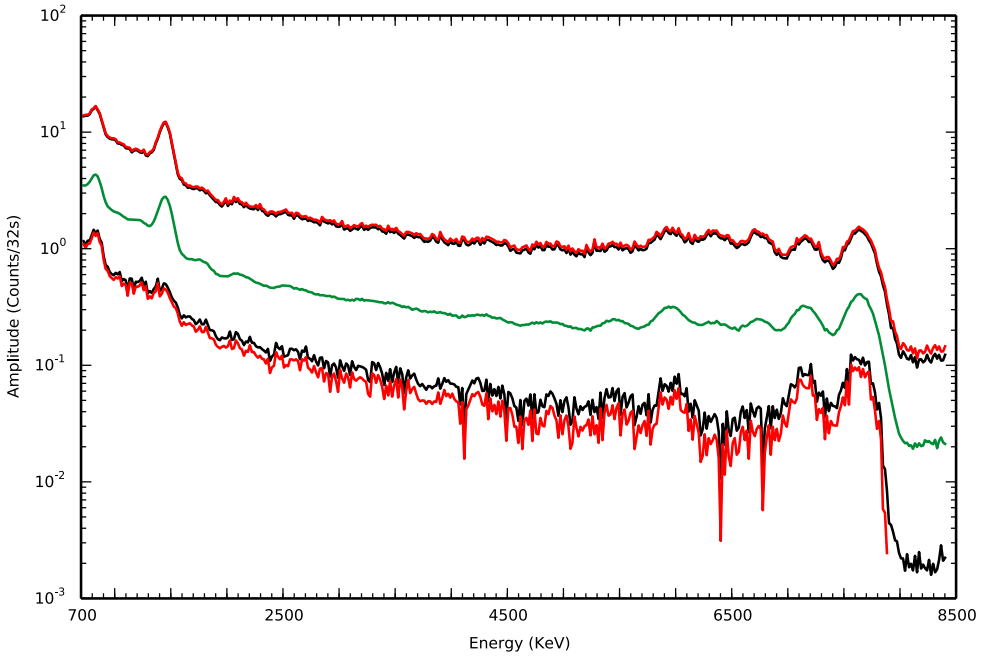

Figure 2.8: The middle spectrum corresponds to the average spectrum of mixtures of K, Fe, and Ti elemental spectra to which statistical noise was added. The upper and lower black spectra correspond to the envelope of the ensemble of these mixtures. The red envelope takes into account the uncertainties.

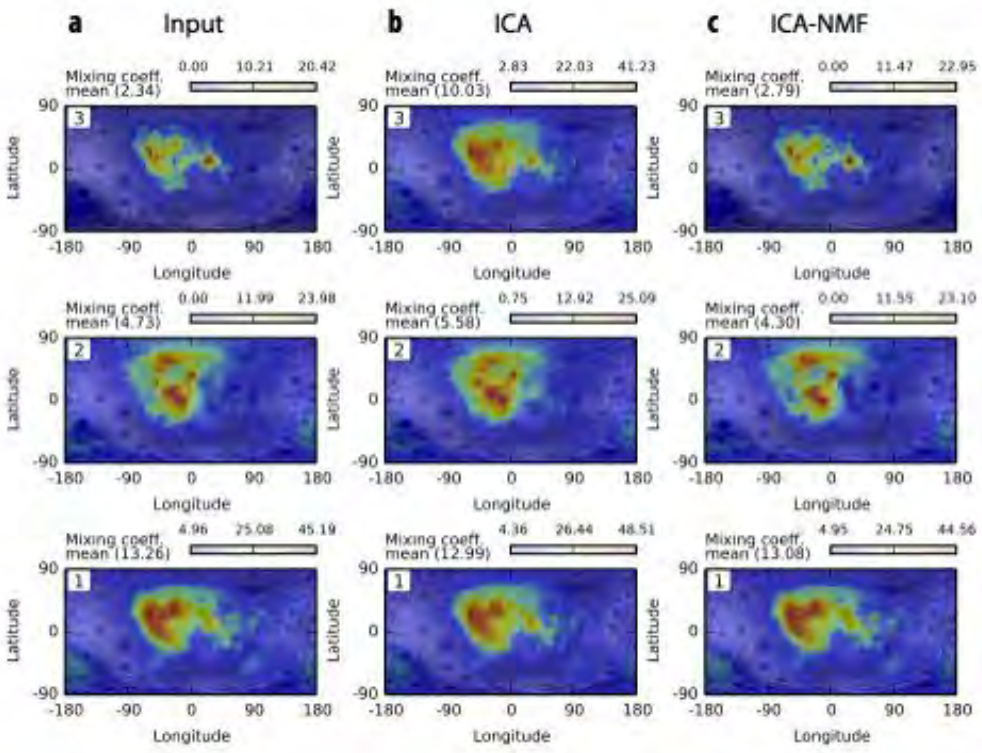

Figure 2.9: **a** Mixing coefficients used as input for producing a series of linear mixtures of elemental spectra of Fe, Ti and K. **b** Mixing coefficients estimated by JADE from these linear mixtures. **c** Mixing coefficients estimated by ICA-NMF. All mixing coefficients are normalized such that the variance of each source spectrum equals one.

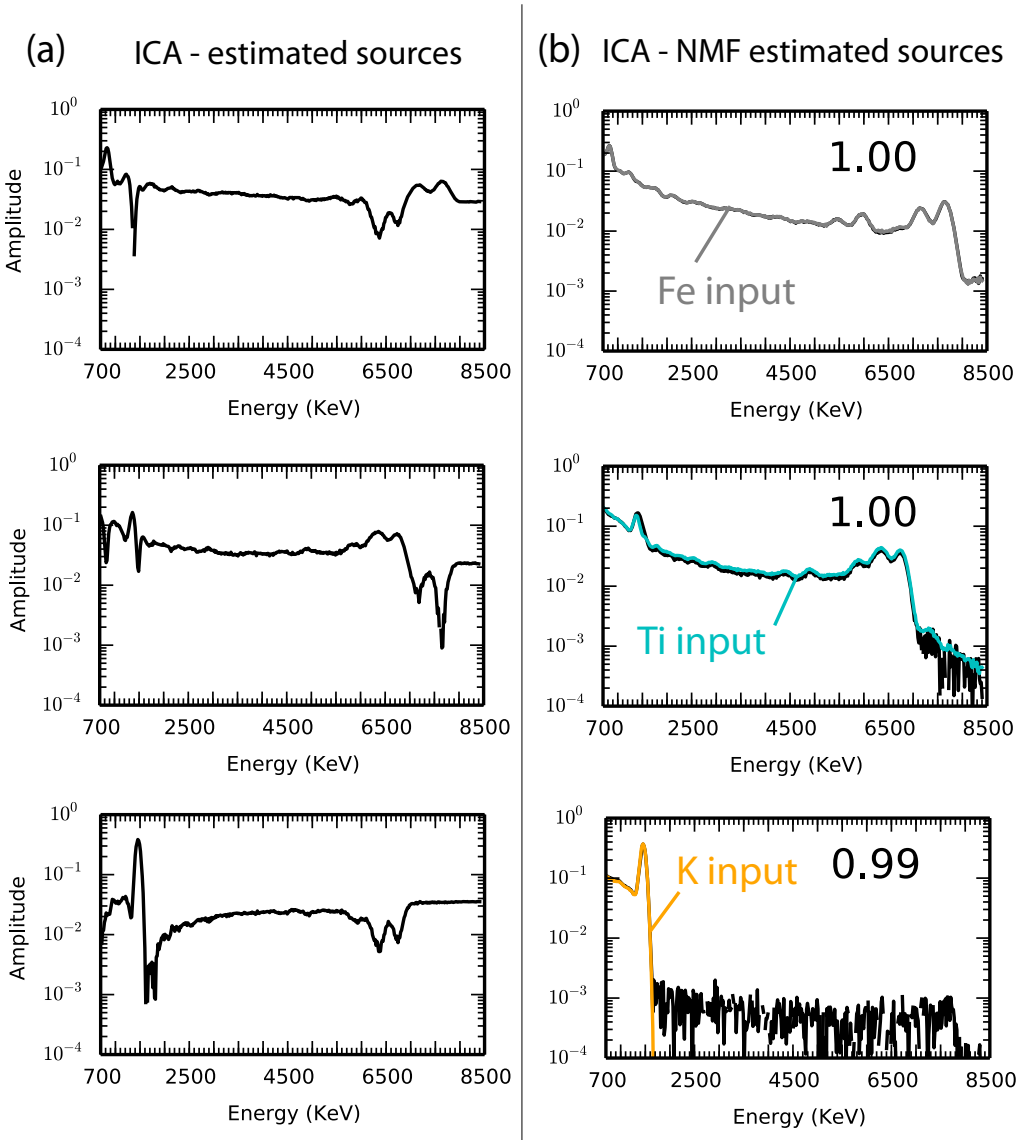

Figure 2.10: Source signals estimated by applying ICA and ICA-NMF to linear mixtures of elemental spectra for Fe, Ti and K for three output sources. All signals have unit variance by convention. (a) Source signals estimated by JADE, what is plotted is $S^{JADE} - min(S^{JADE}$ in order to compare the shape of the input spectra and ICA ouput on a logarithmic scale. (b) Source signals estimated by applying NMF to the same dataset but using the source estimated by ICA as an initial solution (ICA-NMF). The input spectra, i.e. simulated by MNCPX (see section 2.3) are overplotted in color. K is in orange, Fe in grey and Ti in light blue. The major peaks can be separated, but the spectral shapes are poorly reconstructed, as far as ICA is concerned. The first ICA component (top row) shows the double peak from neutron capture by iron near 7.6 MeV, and displays a negative double peak at the position of the double peak from neutron capture of titanium. The situation is reversed for the second ICA component that shows the capture double peak for titanium and a reverse couple of peaks at the position of the iron capture doublet. Applying NMF based on the ICA estimate signficantly improves the quality of reconstruction of the input signals.

However, it can clearly be seen that these spectral features are present with an opposite sign on both components. Figure 2.10 (b) shows the sources and mixing coefficients extracted by the NMF algorithm of Gong & Zhang [2012] initialized with the component estimated by JADE shown in Figure 2.10 (a). The separation is much better when ICA-NMF is used. The input elemental spectra are almost perfectly reconstructed. A small contribution of the iron doublet (7.6 MeV) appears in the potassium related component.

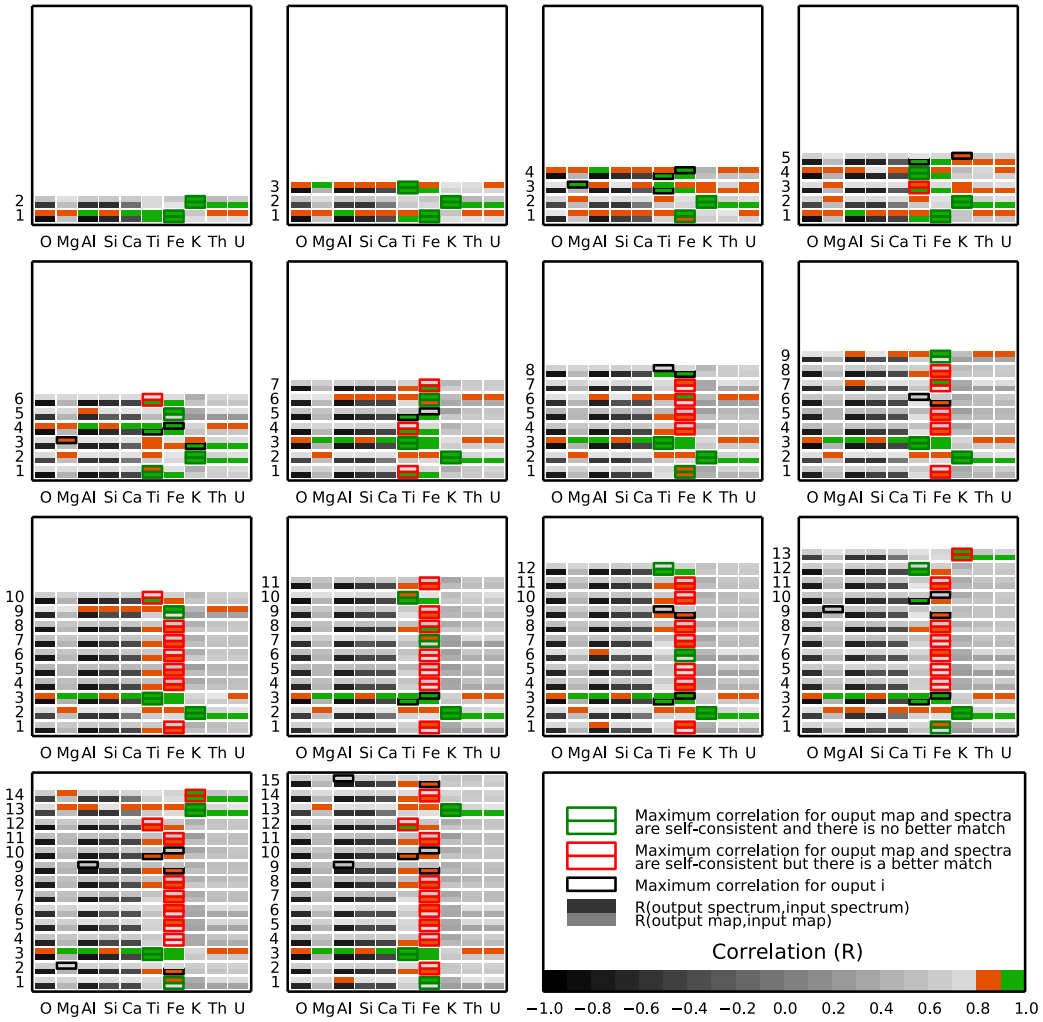

Figure 2.11: Linear mixtures of Ti, Fe, K: correlation matrices between library data (x-axis) and ICA-NMF output (y-axis). The number of ouput sources was set from 2 (upper left subfigure) to 15 (lower left subfigure next to the legend). As illustrated in the legend each comparison cell is made of a stack of two rectangles. The lower rectangle corresponds to the correlation of the spatial distribution of the source (mixing coefficient) with a map of elemental weight fraction, the upper rectangle gives the correlation between the elemental spectrum estimated by the separation and the library elemental spectrum.

Figure 2.11 provides correlation matrices for different values of the number of ouput sources tested. These correlation matrices are formed as follows.

On the one hand, the correlation between each estimated source spectrum and each library spectrum is calculated. On the other hand, the correlation between each set of mixing coefficient and each set of elemental weight fractions is also calculated. For each output the maximum correlation of an ouput (spectrum or set of mixing coefficient) with library data (spectrum or map of weight fraction) is localized.

A black rectangle indicates the occurence of maximum correlation when spectral and spatial correlations are not consistent. For instance, in the case of $N_{Sout} = 6$ (first column, second row of Figure 2.11, the source spectrum #3 has a maximum correlation with the library gamma ray spectrum of Mg but the mixing coefficients show maximum correlation with K weight fractions.

Two red or two green rectangles indicate that spatial and spectral correlations are self-consistent. In this same case ($N_{Sout} = 6$), output source #6 shows maximum spectral and spatial correlations for element Ti. The red color means that there is a better match in the same column (for the same element).

Two green rectangles indicate that there is no better match for the element considered. In this case the element is considered to be recognized. In the example case, output source #1 is thus recognized as Ti. The elements recognized in this way are plotted as a function of the number of sources in Figure 2.12 for the case of the analysis of linear mixtures of elemental spectra of Fe, Ti and K. In all figures showing the element recognized as a function of N_{Sout}, the elements are sorted from the worst to the best match (based on spatial and spectral correlation) from bottom to top.

Figure 2.12 (b) shows the quality of reconstruction of the total spectrum as a function of N_{Sout}. The quality improves importantly when the number of source equals 3 and does not evolve if N_{Sout} is increased. Fe, Ti and K are always recognized except for $N_{Sout} = 2, 4$, but the quality of reconstruction of the elemental spectra and mixing coefficients are only maximum for N_{Sout} equals 3, obviously because this is the number of input sources, but also 5 and 7.

2.5.2 Linear mixtures of ten spectra

The previous section has shown that ICA-NMF provides a satisfying source reconstruction when it is applied to a set of linear mixtures of three elemental spectra. However, more than three elemental spectra are required to account for the gamma ray spectra measured in orbit around the Moon [Prettyman *et al.* , 2006].

The next step consists in testing the method on linear mixtures of the full set of elemental spectra that have been previously considered for the analysis of the LPGRS data. This dataset is presented in Figure 2.13. The number of ouput sources is varied from 2 to 15, as previously.

The number of recognized sources, using procedure 2.4.4, is not a linear function of the number of ouput sources as can be seen in Figure 2.14. The same elements are not recognized as a function of the number of output sources. Fe and Th are recognzied more often. Nine of the ten input elemental spectra can be recognized, but six at most can be reconstructed for a given value of N_{Sout}. However, the correlation between the input and the ouput is clearly lower than in the case of a mixture of three elemental spectra only. Figure 2.15 illustrates the case where the highest number of elemental contributions is recognized (N_{Sout} = 9). Component #1 is recognized as iron, but the titanium doublet is also visible in the spectral component.

Component #2 displays the Si non elastic scattering peak near 1 MeV and near 4.5 MeV. Although the general spectral shape is respected, this component is marked by negative features that can be associated with radioactive elements, such as the K line at 1.45 MeV and the Th line at 2.6 MeV. The generally higher contribution of Si in the highlands and the South Pole Aitkin basin is well reproduced, but the negative contributions of radioactive elements clearly dominate the Mare patterns.

The spatial distribution of Th can be recognized in component #3, for which the highest amplitudes are reached above the KREEP terrains. Spectrally, the 0.8 MeV and 2.6 MeV peaks are well reproduced but the quality of fit between these two spectral features is less certain. It seems that this region is also marked by uranium peaks. This component also

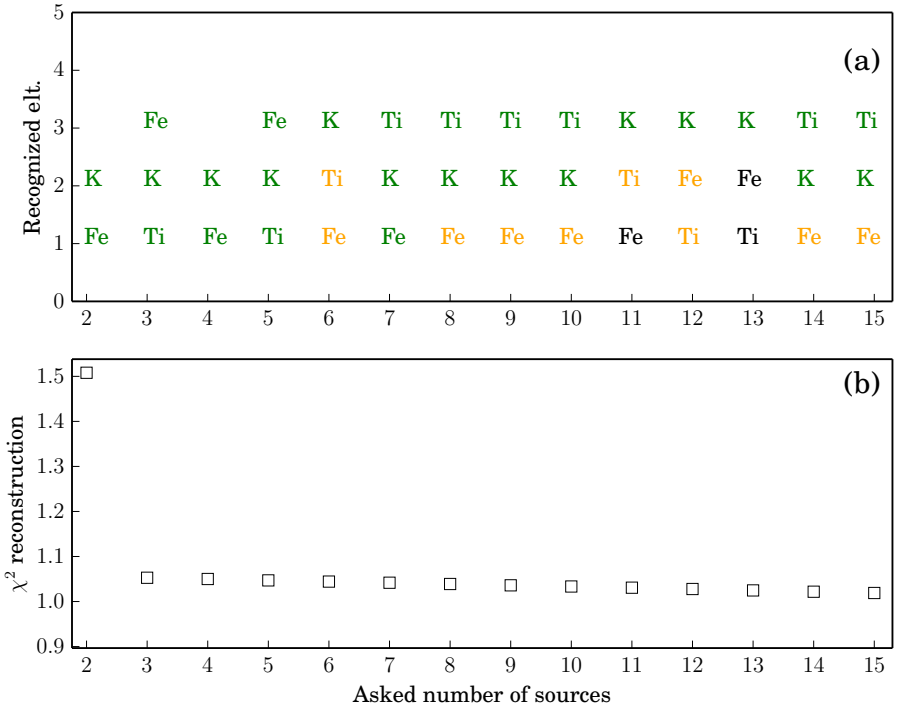

Figure 2.12: Performances of ICA-NMF applied to linear mixtures of Ti, Fe, K spectra as a function of the number of output sources. (a) Element recognized using the procedure 2.4.4. The recognized elements are ordered from the worst to the best reconstruction from top to bottom in terms of quality of reconstruction. The green color indicate a correlation higher than 0.9, yellow corresponds to the 0.8-0.9 interval, black corresponds to a correlation < 0.8. (b) Average reduced χ^2 (Equation 2.36) between observed spectra $\tilde{X}_{pl}$ and ICA-NMF reconstruction $X_{rec}^{ICA-NMF}$. Ti, Fe and K can be restored with a correlation better than 0.9 between for $N_{Sout} = 3 = N_S$ but also when N_{Sout} equals 5 and 7. The quality of signal reconstruction clearly improves from 2 to 3 and do not progress significantly if more sources are asked.

shows the contributions of neutron capture doublets produced by Fe (7.6 MeV) and Ti (6.7 MeV). Component #4 spectrally matches the K emission line at 1.45 MeV but it is still mixed with other elemental contributions. Notably, the negative contribution of Th can be seen at 2.6 MeV. On component # 5, aluminum lines are visible and its spatial distribution is self consistent. Negative contributions from radioactive elements are also visible.

Component # 6 is identified as magnesium. However the correlation of the source spectrum is nearly equal to the correlation with Ti, as can be seen in the correlation table of Figure A.1, fourth column, second row (in appendix A). Component # 7 is spatially dominated by the signature of radioactive elements. Spectrally, it displays emmision lines from K, Th, U, but also non elastic scattering lines from O. Component #8 is dominated by noise, although it displays three more prominent peaks at 1.2, 1.5 and 2.0 MeV, altough the presence of these peaks cannot be explained in terms of the input elemental spectra. Component #9 is consistent with the small patches of high Ti content on Mare surfaces, more importantly neutron capture lines near 6.7 MeV seem well reconstructed. However the non scattering emission line is not reconstructed and the higher spectral correlation with iron makes this component not recognized as Ti (see Figure A.1 in appendix A).

In contrast to the case of mixtures of only a few source spectra, reconstruction of the library spectra is not reached when a full set of chemical elements is considered. Fe and Th

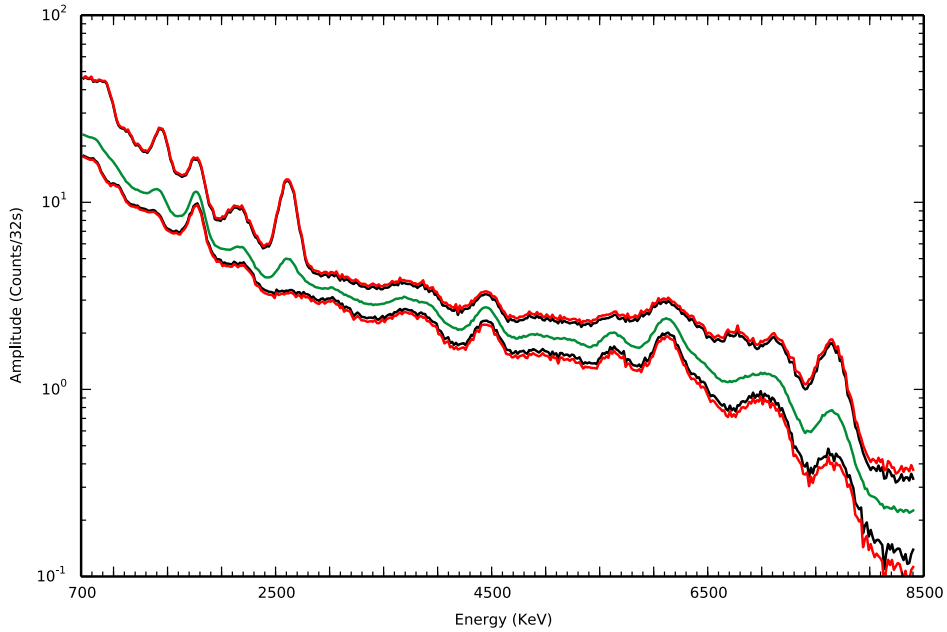

Figure 2.13: Linear mixtures of ten elemental spectra. The middle spectrum shows the average spectrum of a set of mixtures of O, Mg, Al, Si, Ca, Ti, Fe, K, Th and U elemental spectra with additive Poisson noise. The upper and lower black spectra indicate the envelope of these synthetic spectra. The red envelope takes into account the Poisson uncertainty on the counting rates.

are the best estimated sources that are consistently recognized. K, Al, Si, Mg and Ti can also be recognized, but are not always that well reconstructed. The separation of elemental spectra is always imperfect. Even for Fe and Th, contributions of other elements can be observed in their endmember sources.

In order to understand this result one may want to verify whether the hypotheses required by ICA are fulfilled. NMF uses an estimate of the input sources provided by ICA. By minimizing the distance between the observations and the reconstruction, NMF is supposed to improve the quality of source estimation. However, this is possible only if ICA provides estimates of the input sources that are not too different from the exact solution. ICA will provide a good estimate if the elemental spectra are independent enough from each other and if the mixtures show sufficient diversity. The validity of the independence of the elemental spectra is tested in the next section in order to explain why certain elements can be extracted more easily than others and why the separation is always imperfect.

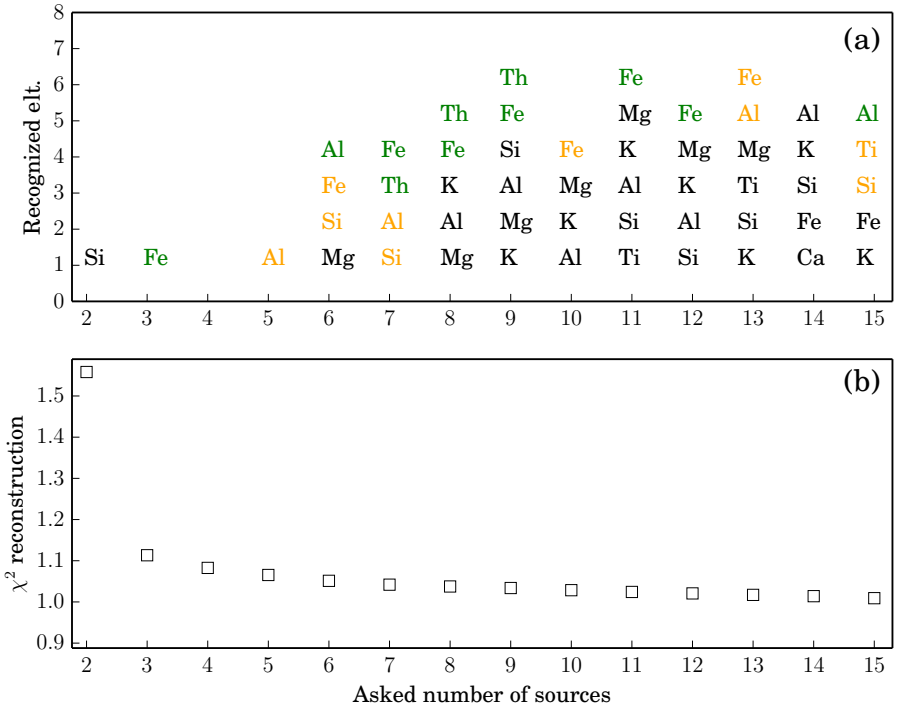

Figure 2.14: **Performance of ICA-NMF applied to linear mixtures of ten elemental spectra.** (a) Element recognized as a function of the number of ouput sources. (b) Average χ^2_{red} between observed spectra $\tilde{X}_{pl}$ and ICA-NMF reconstruction $X_{rec}^{ICA-NMF}$. Mg, Fe, K and Th can be reconstructed with a correlation better than 0.9 between the library data and the blind separation ouputs when the number of output sources equals 9 and 10. Increasing further the number of sources does not seem to allow extracting more information as the signal reconstruction is not signficantly improved.

2.5.3 Interpretation of the sources extracted from linear mixtures

According to the theorem of central limit, any linear combination of signals that have non-gaussian distributed values, leads to a signal whose values are more gaussian. If the source signals already have gaussian distributions before being mixed, the distribution of the observed values will not change, so neither will the contrast function used by JADE to unravel independent components. Secondly, JADE, like other ICA algorithms, restores the version of the signals that optimize independence between them [Cardoso, 1999]. If the values taken by the source spectra are themselves correlated, or not correlated but not independent, JADE will not restore the source signals. The cross-correlations between the elemental spectra and between the elemental maps are given in Figure 2.16.

The 4^{th} order cumulants of the spectra are given in Figure 2.17. Library spectra can show high cross-correlations, which explains why, even in the case of linear mixtures of a few spectra, JADE does not restore the input spectra, but optimized independent components, which can show positive signatures of one element but also negative features associated with other elements (Figure 2.10(a)). However, although these independent components are imperfect estimates of the input spectra, they provide a useful constraint for initializing NMF. Following this idea one can perfectly restore the input signals for mixtures of K, Ti and Fe.

The same approach does not succeed on mixtures of ten elemental spectra (Figure 2.15) because a number of the source spectra are highly correlated with each other, in-

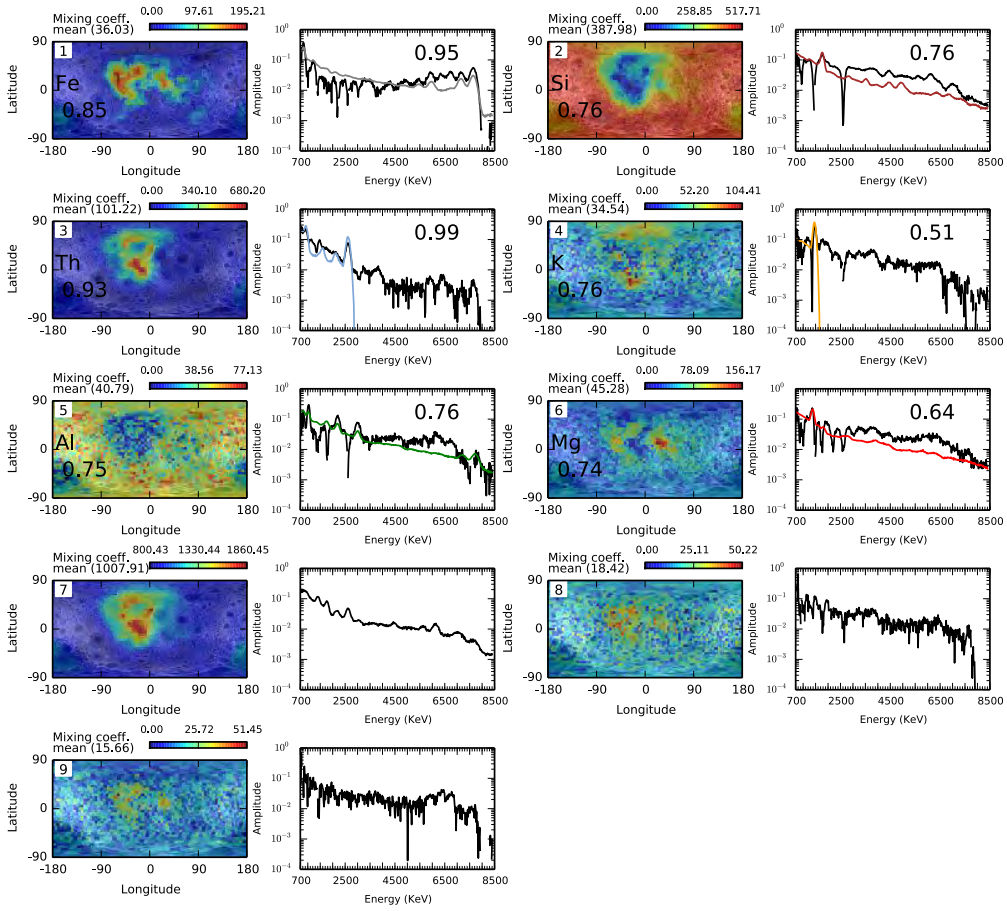

Figure 2.15: **ICA-NMF applied to linear mixtures of ten source spectra.** Each couple of plot shows the extracted sources (black spectrum on the right) and mixing coefficients (color map on the left). The elemental spectra and maps that are identified using procedure 2.4.4 are indicated by the name of the element on the map, and the library elemental spectrum overplotted on the ouput source in color. The best reconstructed elemental features are those of Th (3), Fe (1), Al (5), Si (2) Mg (6) and K (4) in order of decreasing quality. Components #8 and 9 are not recognized as a specific element.

ducing a degradation of source separation, as exemplified by the loss of Ti from the components that are extracted. In addition, in Figure 2.17, one can see that K, Th, Fe have maximum kurtosis (see Eqn. 2.16), K, Mg, Ti, Al, U, Si show intermediate values, O and Ca take values that follow a more gaussian distribution. This is coherent with the fact that Th, K and Fe are more readily extracted than other elemental contributions. This is despite the high spatial correlation between K and Th (Figure 2.16). Indeed, K has a very high 4^{th} order contrast and has relatively small cross-cumulants with the other elemental spectra. Thus, the small differences in the contributions of K and Th elemental spectra from one mixture to the other allows ICA to separate them in spite of the strong spatial correlation.

This discussion illustrates the fact that the shape of elemental spectra is a key factor influencing the ability of BSS technique such as ICA-NMF to successfully reconstruct input signals.

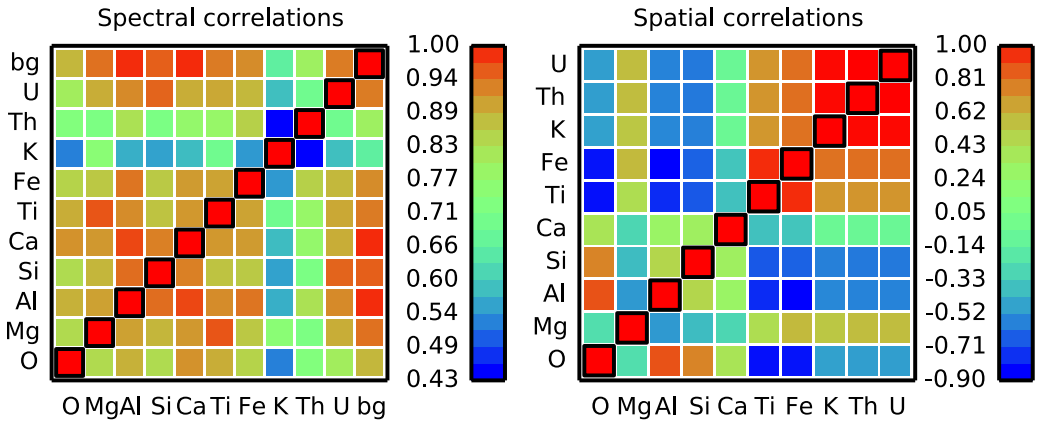

Figure 2.16: Cross-correlations between elemental and background (bg) spectra (left). Cross-correlations between 5°rebinned elemental abundances (right).

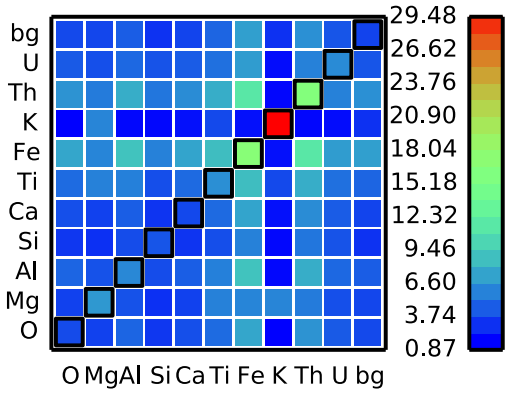

Figure 2.17: Fourth order cumulants C_{ijkl} such that i=j, k=l for the centered and reduced library spectra. The off diagonal terms give for instance Cum(O,O,Mg,Mg), diagonal terms give autocumulants. Values close to zero, indicate a near gaussian distribution. Any cross cumulant of two independent signals cancel.

2.6 Application of ICA-NMF to physical model mixtures.

In this section synthetic spectra that follow the mixing model of [Prettyman *et al.* , 2006] (Eqn. 2.4) are analyzed with ICA-NMF. In this model, unlike in the simplified mixtures analyzed previously, the contributions of non-elastic scattering and neutron capture are separated (as far as Si, Al, Ca, Ti, Mg, Fe are concerned) and the contribution of non-elastic scattering (O, Si, Al, Mg, Fe, ti, Ca are concerned) is modulated by the spatial variation of the average atomic mass, while the contribution of neutron capture (Si, Al, Ca, Ti, Mg, Fe are concerned) is modulated by the spatial variation of the neutron number density.

In addition, the orbit of Lunar Prospector was polar while the inclination of the GRS instrument was always parallel to the Moon's spin axis. Hence, gamma rays encountered the GRS with different incident angles and do not interact exactly with the same material before reaching the BGO crystal. This results in a latitude dependent gamma ray output which is taken into account in the model used to produce synthetic gamma ray spectra [Prettyman *et al.* , 2006]. Finally this physical model includes a background gamma ray spectrum, which is formed by all gamma rays that are not produced by an element-specific reaction. The shape of this background is approximatively constant, but its amplitude

changes, principally as a result of the latitude dependent response function.

Two synthetic datasets are produced by this physical model, one where the background is absent (Figure 2.18) and one where it is present (Figure 2.21).

The first purpose of this section consists in determining whether the separation of non-elastic scattering and neutron capture contributions in the mixing equation and the latitude dependent response function of the LPGRS instrument have significant effects on the components extracted by ICA-NMF with respect to the case treated previously, where the two contributions are grouped together and the instrument response function is constant. The second point concerns the effect of adding a background and is presented in section 2.6.2.

Note that, as previously, the performance of ICA-NMF is assessed based on comparison of the ouput maps and ouput source spectra with maps of element weight fractions and elementary spectra simulated by MCNPX that are calculated for average lunar composition, atomic mass and neutron number density.

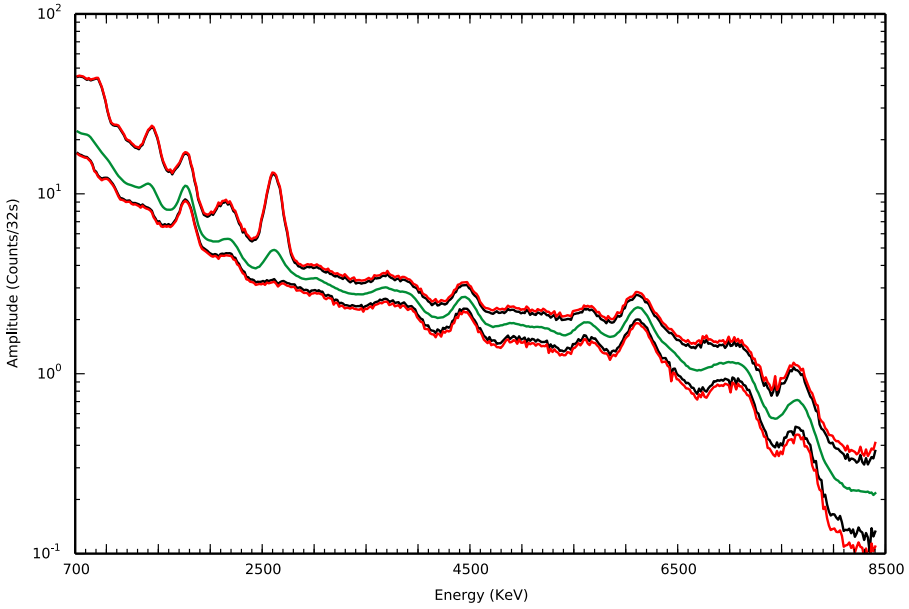

Figure 2.18: Synthetic gamma ray spectra following the physical model of [Prettyman *et al.* , 2006] without background (see section 2.3) for details). The middle green spectrum corresponds to the average spectrum. The upper and lower black spectra show the envelopes of these synthetic data. The red envelope takes account of the uncertainties.

2.6.1 In the absence of a background

At most, six elemental contributions can be recognized by the procedure described in 2.4.4, as can be seen in Figure 2.19. The spectral and spatial correlations with library data are better than 0.9 only for Fe, Th and Al. The correlation matrices used for the element recognition procedure are shown in Figure A.2 of Appendix A. The extracted component and mixing coefficients are shown in Figure 2.20 for ten ouput sources used as an illustration as it is here that the most components are recognized.

Spatially, component #1 is most correlated with thorium but spectrally it is correlated with aluminum. Component #2 appears to match silicon. Component #3 matches iron which is both spatially and spectrally well reconstructed. Component #4 is recognized as Mg but with poor correlations. Component #5 displays the K emission line at 1.45

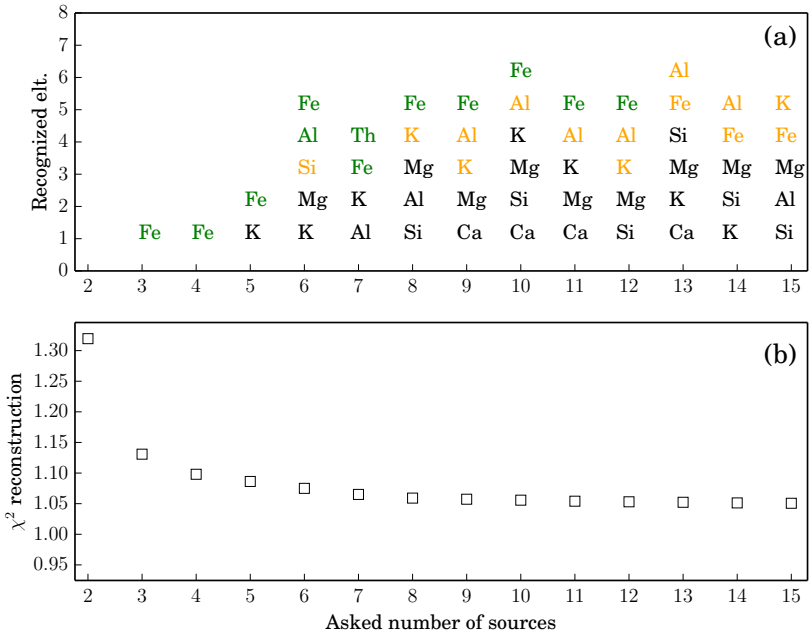

Figure 2.19: Performance of ICA-NMF applied to synthetic gamma ray spectra following the model of Prettyman *et al.* [2006] without background (Eqn. 2.4). (a) Element recognized as a function of the asked number of source. (b) Average χ^2_{red} between input mixtures and ICA-NMF reconstruction.

MeV. Both component #6 and #7 are recognized as aluminum (see Figure A.2 in App. A). Component #7 is a better match to Al, but it includes emission lines that can be attributed to O at 6.1, 5.6 and 4.45 MeV. Components # 8 and 9 do not exhibit a particuliar spectral or spatial feature specific to one element.

Component # 10 is recognized as Ca, but with a poor fit. Note that this component, as well as components #4, 5, 8 and 9 clearly display the latitude dependency included in the physical model analyzed here. The χ^2 of signal reconstruction flattens to a value of $\sim$1.05 when the number of source is greater than eight.

2.6.2 In presence of a background

The following test shows the influence of adding a background to gamma ray spectra that include elemental contributions. The synthetic gamma ray spectra analyzed, based on Eqn. 2.4, are illustrated in Figure 2.21. As previously, numbers of ouput sources ranging from 2 to 15 were tested.

As illustrated in Figure 2.22, the output sources exhibiting the highest correlations with reference spectra and maps are again Fe and Th. This is also visible in Figure 2.23, where the estimated sources and mixing coefficients are shown in the case of 11 output sources. This case corresponds to the situation where a maximum number of elements (Fe, Th and Mg) are recognized with significant correlations with theoretical elemental contributions (>0.9 for Fe and Th). Most components are affected by a latitude dependency, with the exception of component #5 that matches iron, and component #9, which corresponds to Th. Mg is recognized on component 8 with a poor quality of reconstruction. Most other components are hard to associate to specific elements, although the K peak at 1.45 MeV seems to emerge in a background dominated component (#4).

Five elements are recognized at most, but the number of elements correctly extracted never reaches more than two (Figure 2.22). A decrease in the number of recognized el-

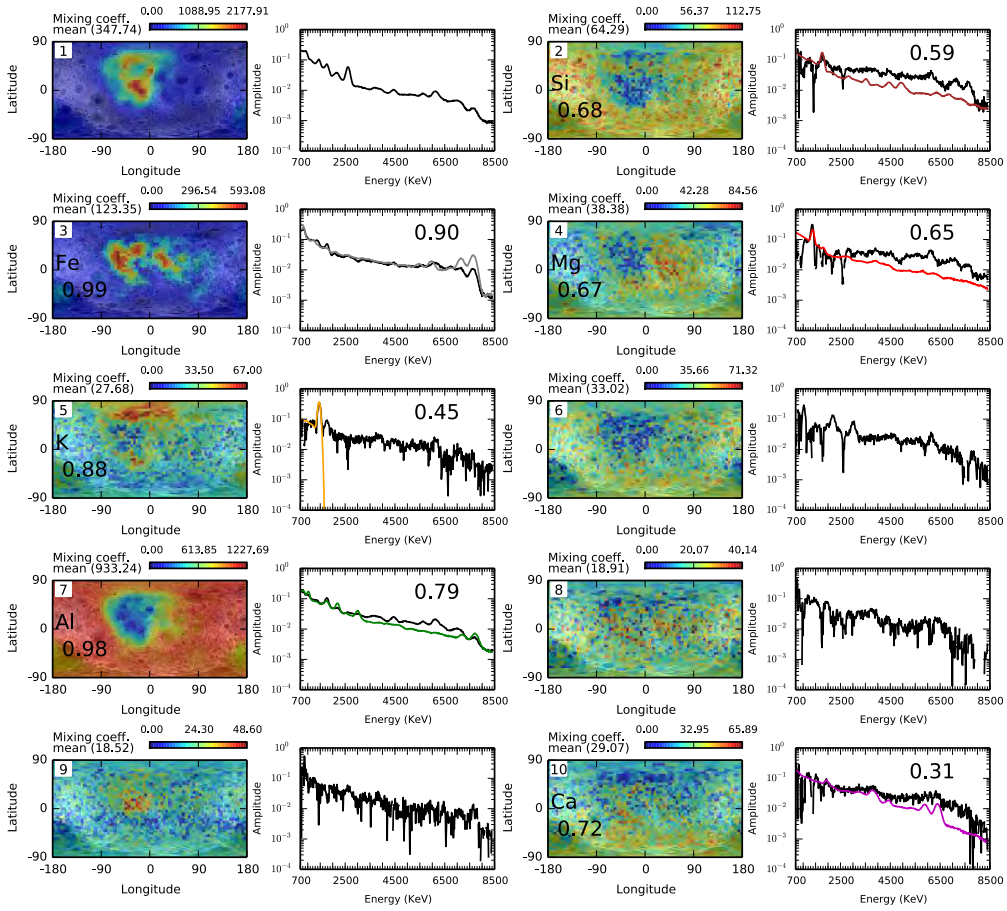

Figure 2.20: **ICA-NMF applied to synthetic gamma ray spectra following the model of Prettyman *et al.* [2006] without background.** The number of ouput sources is set to ten. Fe, Al, K, Mg, Si, Ca can be recognized. Fe and Al show the best correlations with library data, but emission lines associated with oxygen are present on the Al component at 6.1, 5.6 and 4.45 MeV.

ements is observed with respect to analysis of datasets that are background free (Figure 2.19). The correlation matrices used for the procedure of element recognition are given in Figure A.3 of Appendix A.

The results obained in the case of linear mixtures of ten elemental spectra and in the case of the physical model are not significantly different in the absence of background. Output sources that can be correctly recognized as elemental contributions are Fe and Th. Al is recognized more often in the case of the physical model. The spectral contribution of K can be separated in both cases. The difficulties related to the statistical properties highlighted in section 2.5.3 ICA are not changed and their effect is not surprisingly still observed: the most kurtic sources K, Th and Fe are more readily reconstructed than the other elemental spectra. However, the addition of a background signficantly worsens the results. This is probably due to the high correlations of this spectral component with the other elemental spectra as can be seen in Figures 2.16 and 2.17.

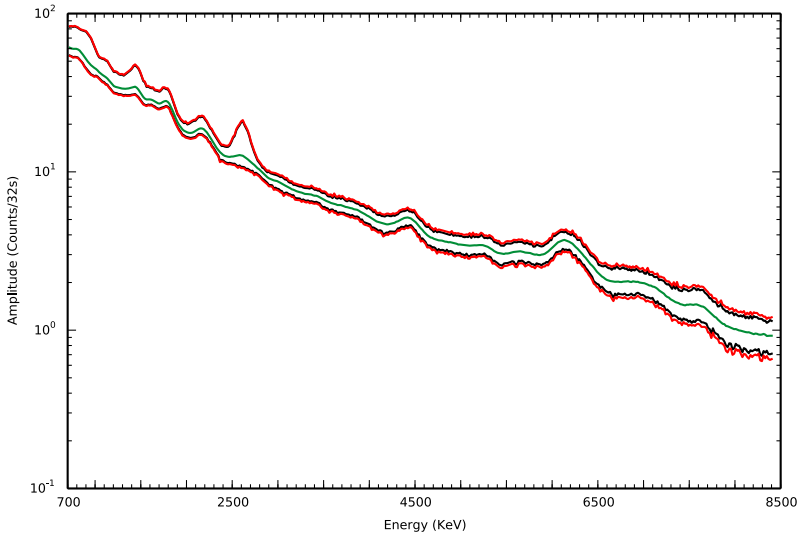

Figure 2.21: Gamma ray spectra following the mixing model (Eqn. 2.4) of Prettyman *et al.* [2006] with a background. (see section2.3 for details). The average spectrum is shown in green. The upper and lower black spectra give the envelope of this series of spectra. The red envelope takes account of the uncertainties.

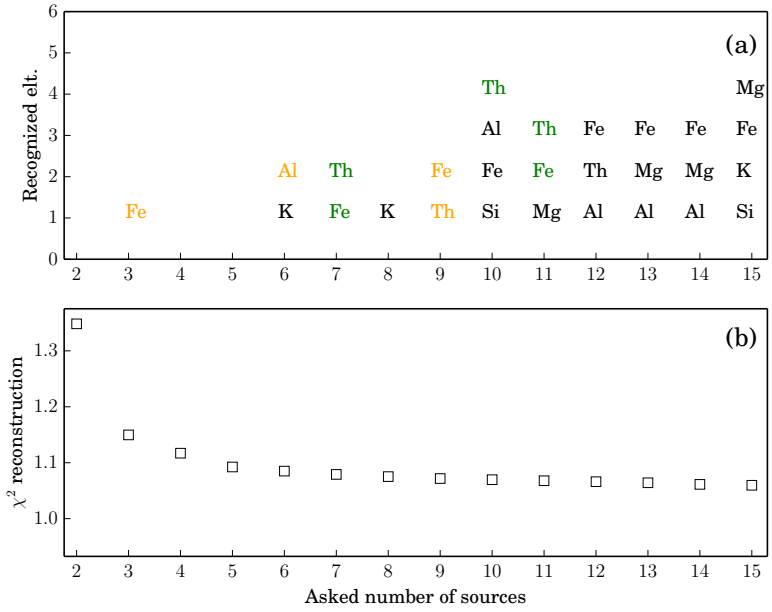

Figure 2.22: Performance of ICA-NMF applied to synthetic gamma ray spectra following the model of Prettyman *et al.* [2006] in the presence of a background. Less elements can be recognized compared to the case without a background.

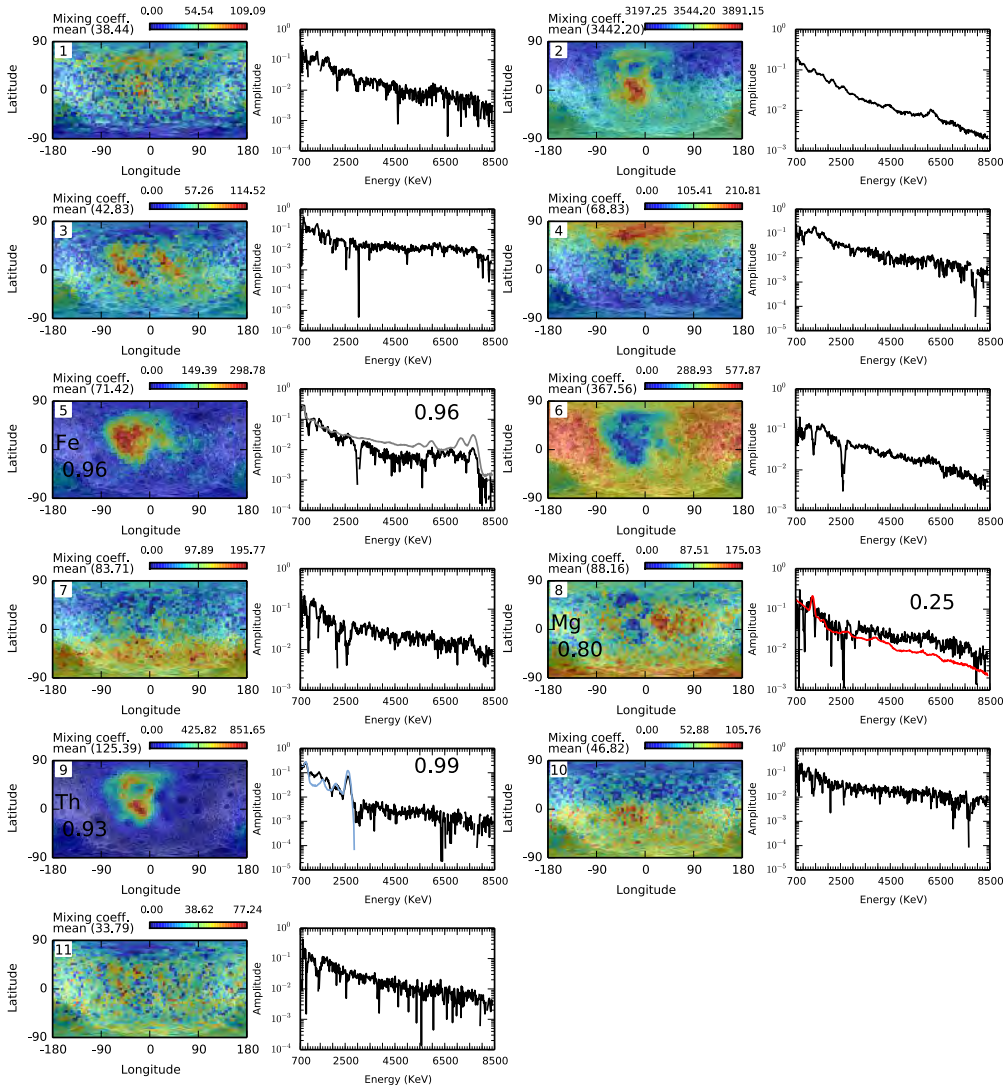

Figure 2.23: ICA-NMF applied to synthetic gamma ray spectra following the model of Prettyman *et al.* [2006] in the presence of a background. The number of ouput sources was set to 11. This case is shown because it corresponds to the situation where a maximum of elements can be recognized with a significant degree of correlation with theoretical elemental contributions. Each pair of plots shows the output sources (right) and mixing coefficients (left). Fe, Th and Mg are assigned by the element recognition procedure described in section 2.4.4.

2.7 Impact of the variability of elemental abundances

The analyses carried out previously have shown that Fe and Th are most readily extracted spectral components. K can be discriminated from Th although the quality of reconstruction of this contribution is not as good as for Fe and Th. More marginally the contributions of Al, Mg, Si and Ca can be extracted. The differences between the ideal linear mixtures (Equation 2.8), and the physical mixing model of equation 2.4 does not significantly alter ICA-NMF outputs. However, the addition of a background component has a dramatic effect, reducing the number of recognized elements and the quality of their reconstruction.

Another important key factor for the correct application of the separation algorithm is the chemical variability. Indeed, the methods of separation used in this study require that there are at least as many different observations as source signals. If the surface of a planet, as seen by the instrument, is chemically homogeneous, records will just be the repetition of a single mixture. Under these conditions ICA or NMF will not be able to separate elemental contributions from each other, even if the other prerequisites are satisfied.

Another advantage of using synthetic data is the possibility of producing mixtures where the variability of the element abundances can be controlled. A method for reducing chemical variability is presented here.

The dynamic range of weight fractions used to generate synthetic spectra can be modified to test the sensitivity of the separation method to the chemical variability. The dynamic range of element weight fractions is defined by:

$$D = \frac{w_{max} - w_{min}}{\overline{w}}, \tag{2.40}$$

where w_{min}, w_{max} are the minimum and maximum weight fractions, $\overline{w}$ is the average weight fraction. Table 2.3 gives the lunar values from [Prettyman *et al.* , 2006] for each element. The modified weight fraction is given by:

$$w'_p = \alpha w_p + (1-\alpha)\overline{w} \qquad \forall \ p \in \{1, ..., N_P\}. \tag{2.41}$$

This expression allows conserving the average:

$$\overline{w'} = \frac{1}{N_P}\sum_{p=1}^{N_P} w'_p = \alpha\frac{1}{N_P}\sum_{p=1}^{N_P} w_p + (1-\alpha)\overline{w} = \frac{1}{N_P}\sum_{p=1}^{N_P} w_p = \overline{w}. \tag{2.42}$$

The new dynamic range is given by:

$$D' = \frac{w'_{max} - w'_{min}}{\overline{w'}}. \tag{2.43}$$

Replacing w'_{max}, w'_{min} and $\overline{w'}$ by their expressions following equation 2.41, leads to:

$$D' = D\alpha. \tag{2.44}$$

Synthetic datasets, following equation 2.4 were produced for $D'/D = 0.1, 0.2..., 0.9$. One can compare the larger extent of the data envelope for the real chemical variability and that produced by a ten times lower variability in Figure 2.24. Counting rates were simulated for intermediate dynamic ranges D'/D between 0.9 and 0.1 with a step of 0.1.

ICA-NMF was applied to the nine datasets of reduced chemical variability, the number of ouput sources was set, as previously, from 2 to 15.

Elements	Average	Minimum	Maximum	Dynamic
O (wt%)	43.55	34.48	46.99	0.29
Mg (wt%)	4.35	0.53	9.44	2.05
Al (wt%)	12.34	0.71	18.33	1.43
Si (wt%)	20.30	14.86	24.00	0.45
Ca (wt%)	11.29	4.60	14.87	0.91
Ti (wt%)	0.56	0.00	4.90	8.71
Fe (wt%)	5.94	2.22	20.25	3.03
K (ppm)	734.74	0.00	3728.46	5.07
Th (ppm)	1.68	0.00	10.85	6.46
U (ppm)	0.46	0.00	2.96	6.47

Table 2.3: Lunar elemental abundances from [Prettyman *et al.* , 2006], units are weight % for O, Mg, Al, Si, Ca, Ti and Fe and ppm for K, Th and U.

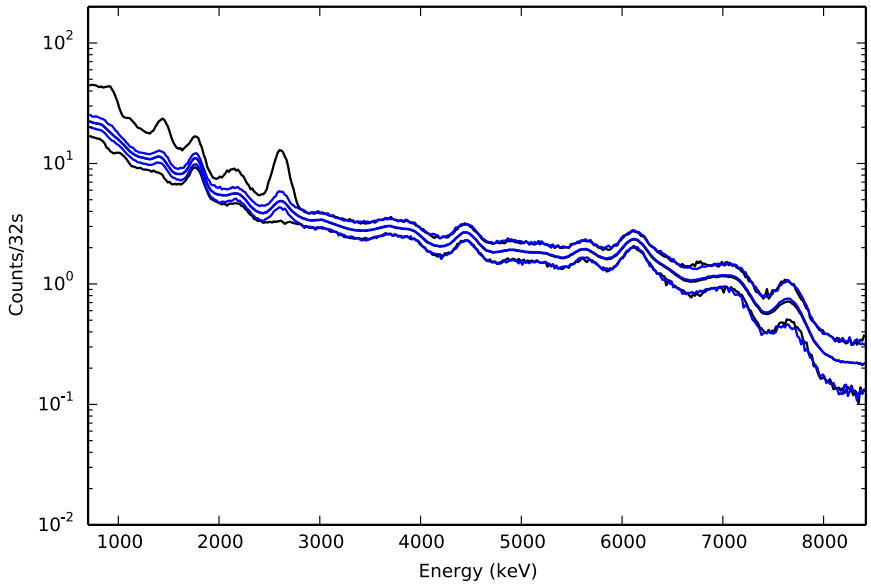

Figure 2.24: Synthetic gamma ray specta following the physical model (Eqn. 2.4). The black envelope corresponds to gamma rays when the real chemical variability is used to simulate the data. In blue the weight fractions were modified through equation 2.41 such that the chemical variablity is ten times lower than the real one ($D'/D = 0.1$). The middle spectrum corresponds to the average spectrum.

2.7.1 In the absence of a background

The ability of ICA-NMF to separate elemental contributions decreases when the dynamic range of elemental abundances is reduced. This is illustrated in Figure 2.25, where the number of recognized elements is plotted as a function of the number of output sources N_{Sout} and the dynamic range of the elemental weight fractions D'/D. There is certainly a tendency to identify less elements and to obtain worse matches with the library data when D'/D decreases, but this tendency is not linear. To first order, Fe, Al and Th can be identified and well reconstructed when $D'/D \geq 0.8$. Below this value, only Fe can be reconstructed with a correlation with the library data better than 0.9. Even Fe cannot be well reconstructed below $D'/D = 0.4$. However, at $D'/D = 0.6$, Al can be identified with a good match with library for $N_{Sout} = 11, 13, 14$. Similarly, Th can be identified even when $D'/D = 0.4$.

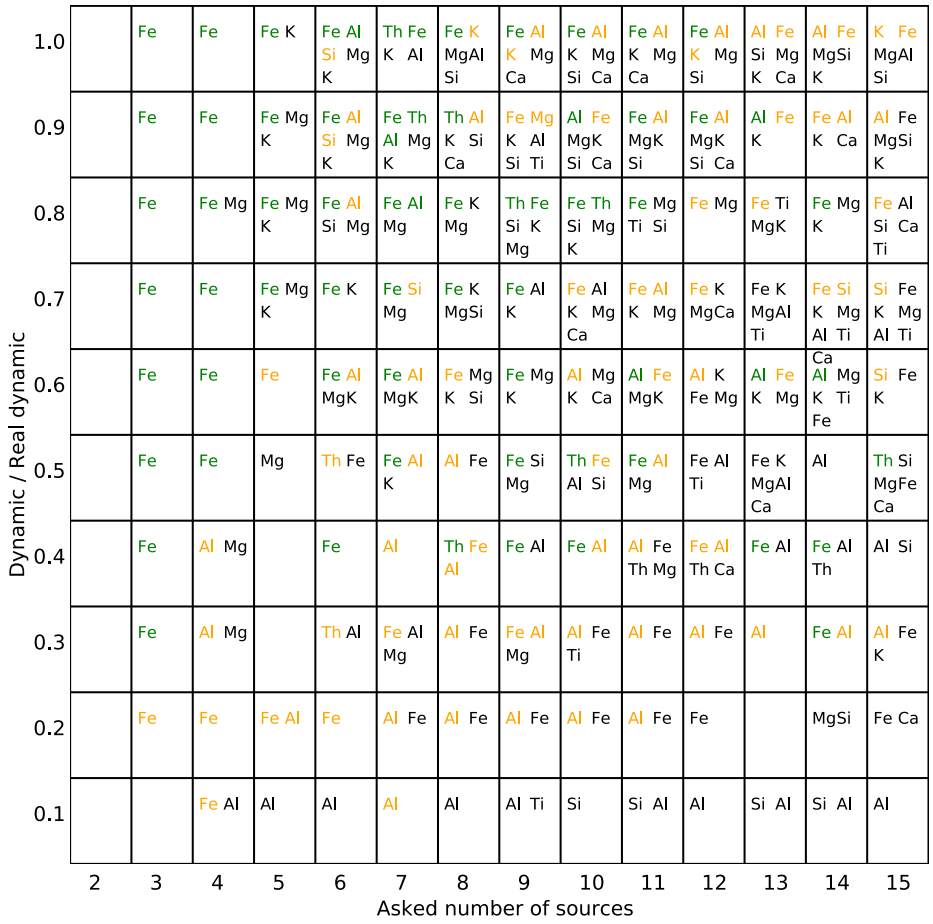

Figure 2.25: Quality of separation as a function of the dynamic range of elemental abundance. Note that the first row of this figure corresponds to Figure 2.19. An element is recognized when the maxima of spectral and spatial correlation between library and extracted sources are coherent (Procedure 2.4.4) as exemplified by Figure A.2. In each box, the reconstructed elements are sorted by decreasing correlation with library data from left to right and top to bottom. Going down the rows, the chemical variability was decreased, using equation 2.41. Globally, the quality of the reconstruction of elemental spectra and abundance decrease with the dynamic of elemental abundances. Potassium and thorium are rapidly lost while iron can be well reconstructed for D'/D as low as 0.3.

2.7.2 In the presence of a background

Results obtained in section 2.6 demonstrated that fewer elements can be recognized in the presence of a background (Figure 2.23) than in the case of background-free data (Figure 2.20) even for the full lunar chemical variability. Figure 2.26 gives the elements recognized after application of ICA-NMF to synthetic datasets which include the background, as a function of the number of output sources and of the dynamic range of the elemental weight fractions. Another consequence of the presence of background gamma rays is a deterioration of element recognition that is much more severe when the dynamic range of elemental abundances D'/D decreases. For example, Fe and Th can be jointly reconstructed with $R > 0.9$ only if D'/D is greater than 0.7.

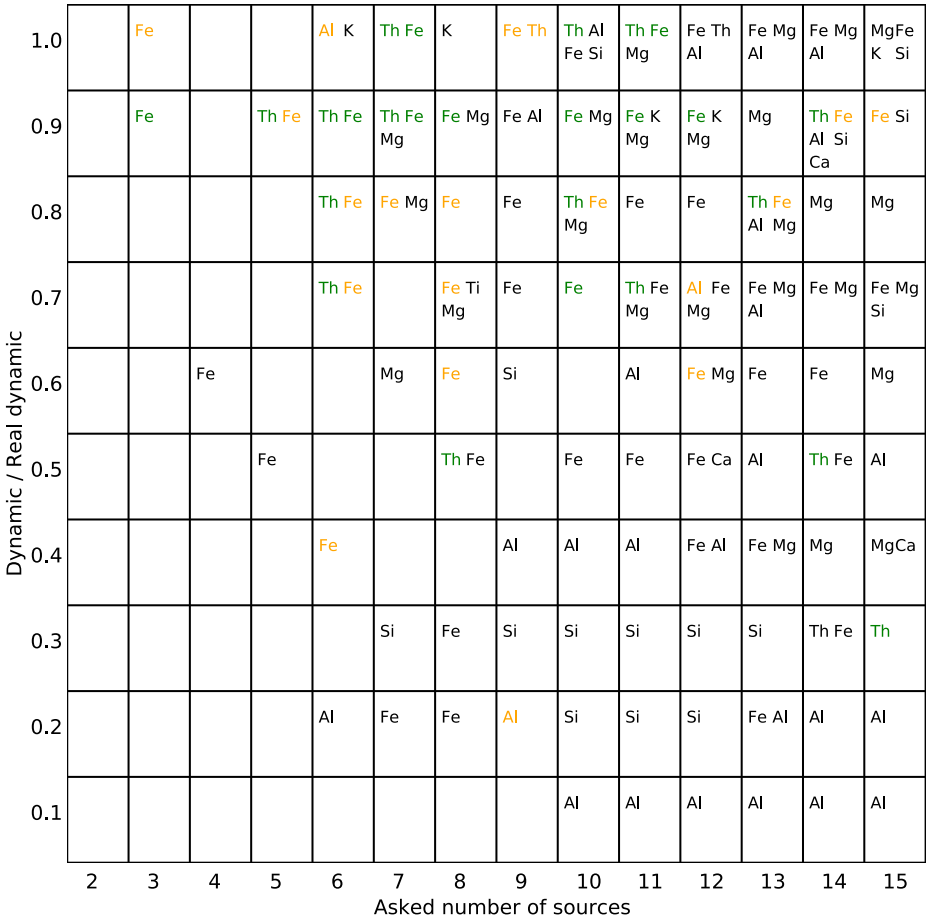

Figure 2.26: Quality of separation as a function of the dynamic range of elemental abundance. This table show the elements recognized by applying ICA-NMF to mixtures of gamma rays based on equation 2.4 that include background gamma rays. Fewer elements can be recognized than in the absence of a background. Th and Fe are mostly lost for D'/D <0.7.

2.8 Real data

2.8.1 Generalities

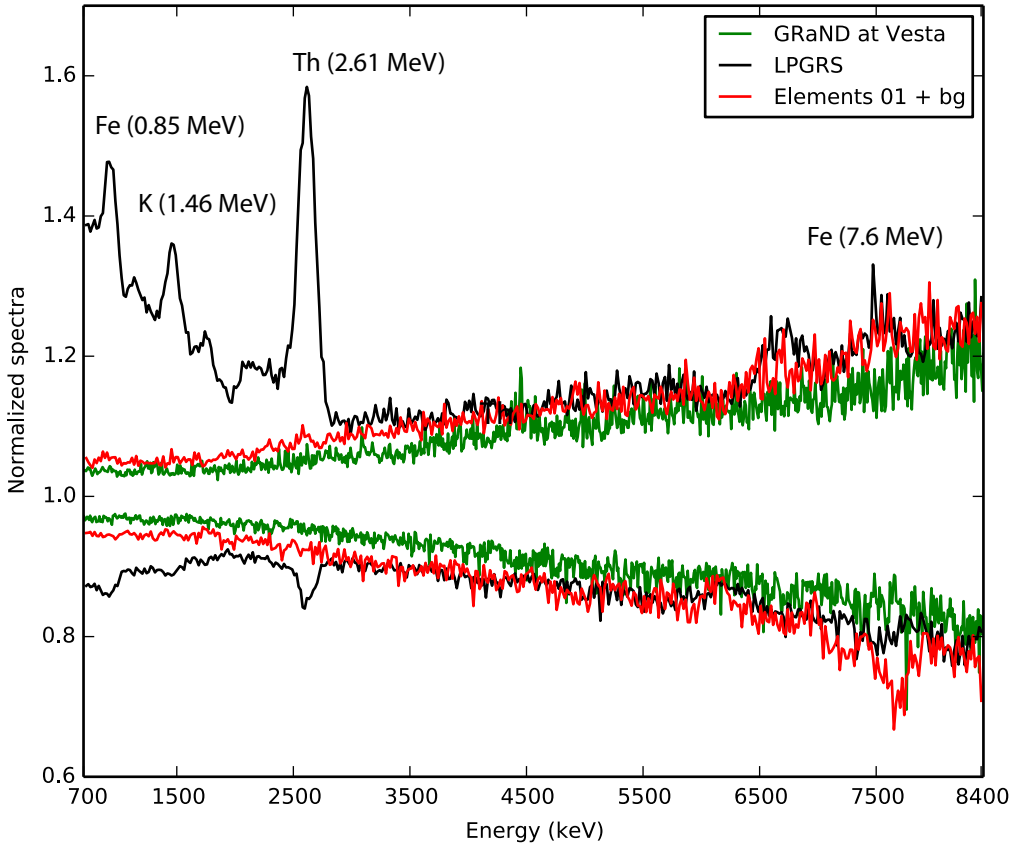

Figure 2.27: Envelopes of gamma ray datasets divided by their respective average spectrum. Vestan (GRaND) data are shown in green, Lunar data are shown in black (LPGRS). The red envelope corresponds to an artificial lunar dataset for which the range of elemental abundances was reduced by a factor ten. The variability of the radioactive elements at low energy and that of iron and titanium at high energy can clearly be observed on the LPGRS envelopes. The lunar spectra clearly show Th lines at 2.6 MeV and K line at 1.46 MeV.

Figure 2.27 presents the envelope of three sets of spectra normalized by the spectrum formed by the average of each channel in order to compare their relative variability. This comparison includes the LPGRS BGO spectra, artificial lunar BGO spectra based on the physical mixture model for which the chemical variability was reduced by a factor of ten with respect to reality (see section 2.7), and the BGO spectra from Vesta. Lunar gamma ray counting rates are strongly variable, especially the counting rates of gamma rays produced by the decay of radioactive elements: K, Th and U. Of particular note is the fact that the lunar synthetic dataset that has the least chemical variability (D'/D=0.1, see section 2.7), has nevertheless more variability than the gamma ray spectra recorded around Vesta.

In this section, ICA-NMF is applied to real lunar and vestan data. It was shown previously that the presence of a background limits the possibility of extracting elemental contributions. Fewer elements can be recognized spectrally and spatially and the quality of the reconstruction of these elemental contributions is poorer than if background gamma rays are not added to the mixtures, based on comparison with library data. Since a model of background gamma rays is available for the LPGRS data, tests are performed also on

LPGRS spectra from which these background gamma rays were substracted.

An alternative approach is to divide each observed spectrum by an average spectrum because this is possibly a way to reduce the statistical dependence between the sources that appears to be an essential factor for the working of ICA (section 2.5.3). Finally, as the signal is much weaker in the vestan case, the noise level is stronger, so that a wavelet filter may be applied to reduce the noise level and consequently optimize the performance of ICA-NMF [Forni *et al.* , 2009].

2.8.2 Lunar prospector.

The Lunar Prospector dataset consists of a 5° rebinned series of gamma ray spectra. As mentionned in section 2.3.2 for the purpose of modelling noise, before being organized as a $N_P \times N_C$ data cube, planetary nuclear data are stored as time series.

Note that these time series have undergone a series of selections and corrections prior to the binning procedure that can be found in Lawrence [2004]. Corrections include coverage of several potential sources of bias, such as the changes in energy gains (shifting of peaks due to variation in voltage), the variation of the flux of galactic cosmic rays and the changes in the solid angle of view subtended by the Moon and the spacecraft.

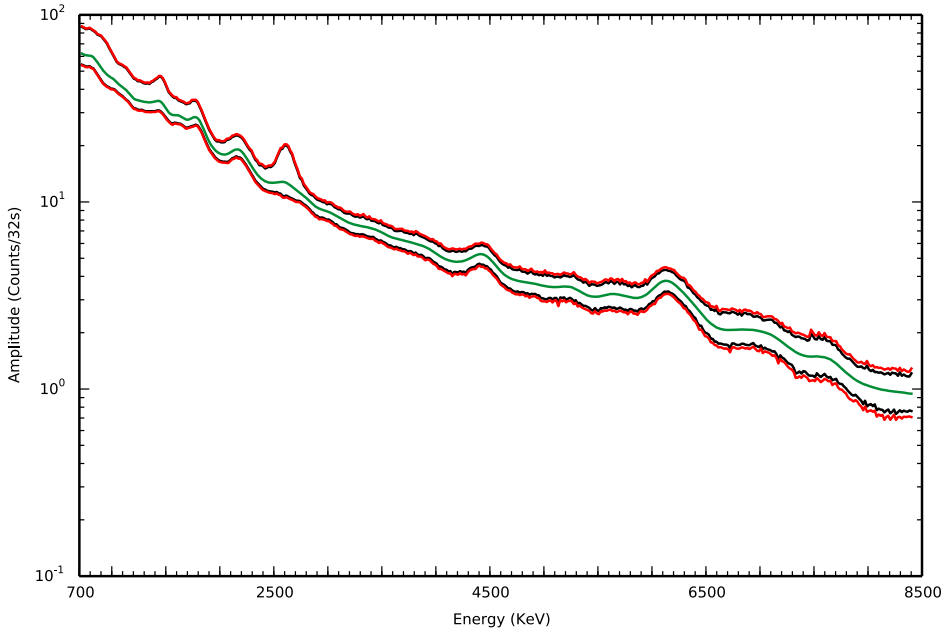

Figure 2.28: LPGRS dataset. The average spectrum is represented in green, the envelope that contains all spectra is shown in black, the red envelope take account of the uncertainties.

No pretreatment.

ICA-NMF is applied to the lunar prospector dataset presented in Figure 2.21. The elements recognized and the quality of signal reconstruction are given in Figure 2.34 as a function of the number of potential sources. Fe, Th, Mg, Si and K can be recognized by procedure 2.4.4. The correlation tables used for the recognition procedure are given in Figure A.4 of Appendix A. Generally, the number of elements recognized is two but it can increase up to four when the number of ouput sources is 14. However, the correlations of the estimated sources and the maps of the mixing coefficients with the spectra and the

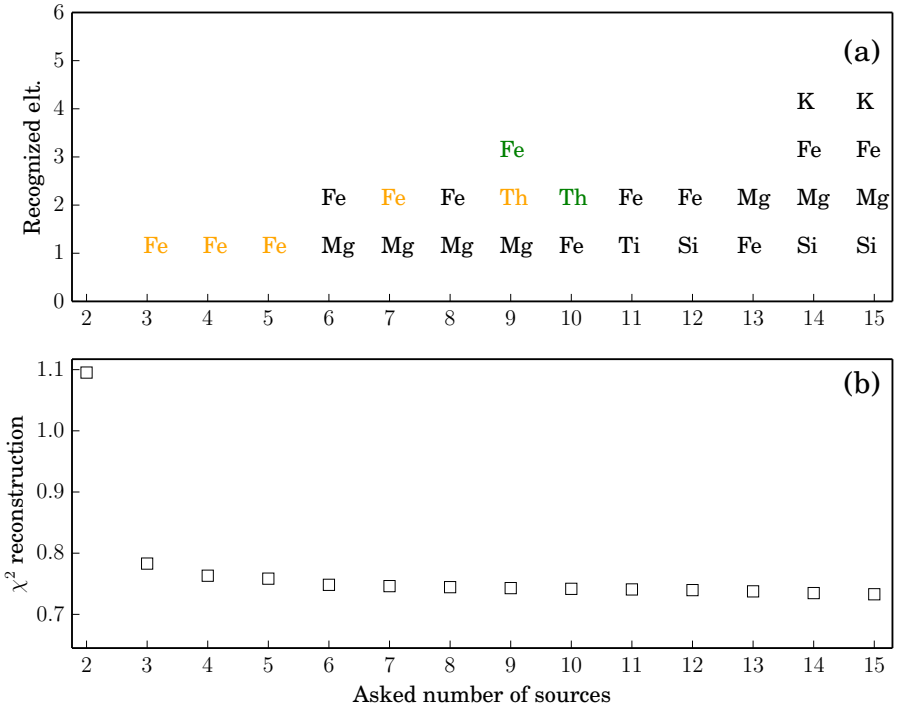

Figure 2.29: Performances of ICA-NMF applied to the LPGRS dataset: (a) Elements recognized by the correlation method 2.4.4 as a function of the number of ouput sources. (b) Average chi-square of reconstructed spectra as function of the number of output sources.

maps of the library, are lower in this case. As for the tests carried out on synthetics, the spectral and spatial signatures of Fe are recovered most often.

Figure 2.30 displays the reconstructed maps and source spectra when the number of ouput sources equals nine. Component #1's mixing coefficients are higher in Mare regions and spectrally this component displays a peak at 0.8 MeV, the bumpy region between 6 and 8 MeV could indicate the contribution of neutron capture of Fe and Ti in this component. This could be consistent with the spatial distribution of the mixing coefficients. Component # 2 cannot be associated to one specific element. Component #3 displays emission lines associated with Th at 2.6 MeV. Component #4 is recognized as Th mainly because of the match with 950 KeV emission line, and consistency with the spatial distribution of mixing coefficients and Th abundance. It is otherwise a bad fit. An emission line is visible at 1.3 MeV in component #5 that could correspond to the non-elastic scattering contribution of Ti, but this is the only feature that can clearly be identified. Component #7 is recognized as Mg. Component #9 matches iron but it remains unseparated from Th as one can see the 2.6 MeV line. There are no specific features on components #6 or 8.

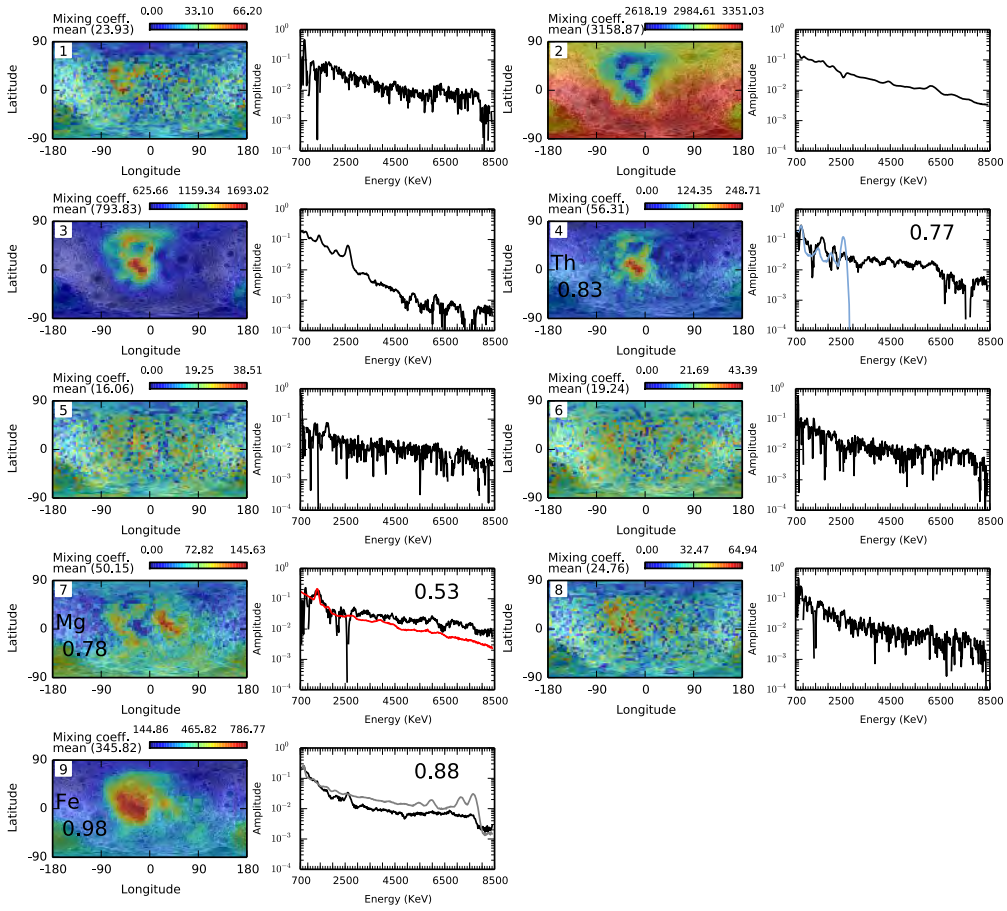

Figure 2.30: Estimated sources and mixing coefficients estimated by ICA-NMF applied to LPGRS data in the case of 9 output sources. Fe(9), Mg(7) and Th(4) can be recognized.

Background removal.

As shown in section 2.7.2 the addition of a background to the elemental gamma rays degrades the quality of separation of elemental contributions, which motivates substracting the background gamma rays from the real LPGRS data. More components can be recognized in this case and the correlations with library data are better than without background substraction (Figure 2.34). Figure 2.32 shows the estimated sources and mixing coefficients when the number of output sources is 14. This number is chosen because a maximum of output sources are recognized with significant correlations with reference spectra and maps (section 2.3). K, Th and Fe, Si and Mg can be recognized. Negative iron features can be observed on the K component (#10). Other extracted components can be either redundant with Fe (#3, #4, #7), Th (#1) or Mg (#13, #14). The nature of the other components is less clear.

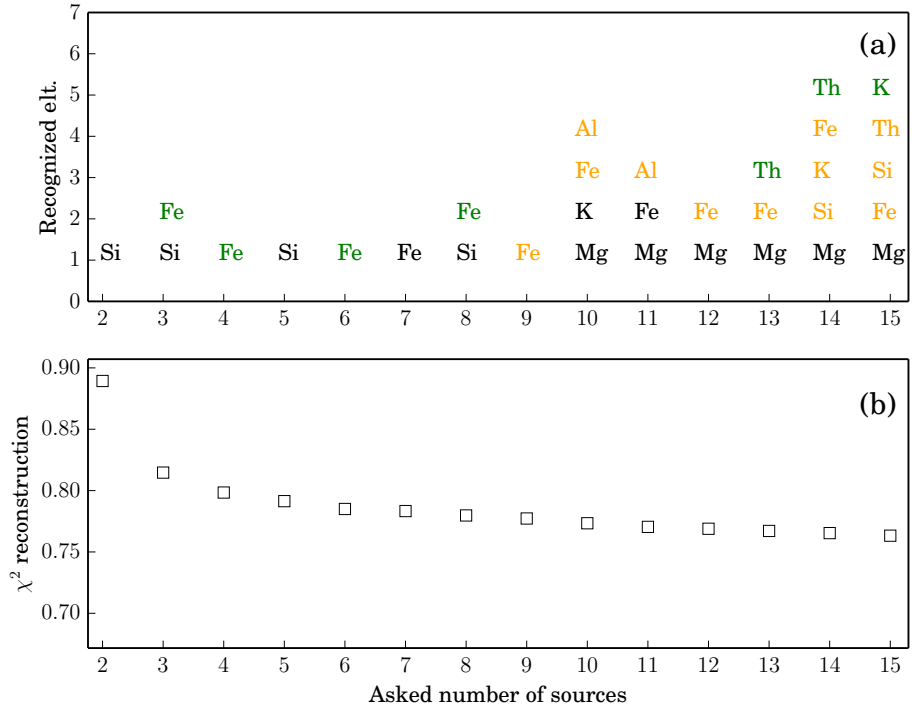

Figure 2.31: Element recognized (a) and quality of LPGRS signal reconstruction (b) by ICA-NMF as a function of the number of output sources, after removing the simulated background gamma rays.

Dividing by an average spectrum

As shown in Figure 2.16, the elemental spectra of the library display important correlations between each other. This is related to the fact that each gamma ray line produced by a nuclear reaction is scattered (Compton scattering) which produces a continuum whose amplitude decreases while the energy increases. The consequence is that the shape of the elemental spectra can be very similar from one element to another. A way to enhance the contrast between the source spectra is to divide each of them by some function, that would attenuate their cross correlations. It is proposed here to take this function as the spectrum formed by the average of each channel because it is simple to calculate and accessible from the data set X_{pl} only:

$$\overline{x}_l = \frac{1}{N_P} \sum_{p=1}^{N_P} x_{pl}, \tag{2.45}$$

whose associated propagated uncertainty is:

$$\sigma_{\overline{x}_l} = \frac{1}{N_P} \sqrt{\sum_{p=1}^{N_P} (x_{pl}\sigma_{pl})^2}. \tag{2.46}$$

The transformed spectra and the propagated uncertainty are:

$$\tilde{x}_{pl} = \frac{x_{pl}}{\overline{x}_l} \text{ and } \tilde{\sigma}_{pl} = \frac{\sigma_{pl}}{\overline{x}_l} + \frac{x_{pl}\sigma_{\overline{x}_l}}{\overline{x}_l^2}. \tag{2.47}$$

ICA-NMF was applied to the LPGRS data devided by an average spectrum and the quality of blind source separation was assessed as previously by comparing the quality of signal

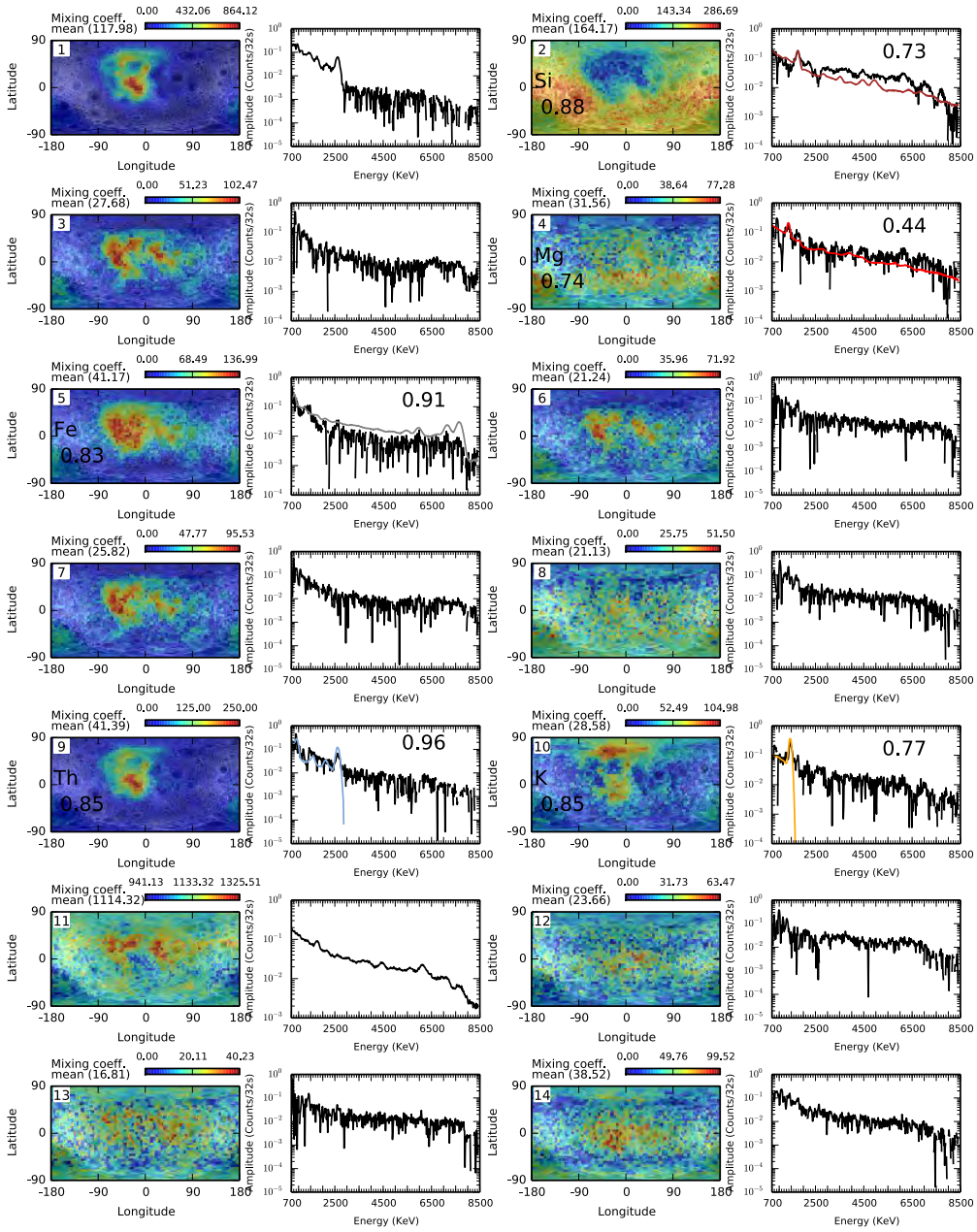

Figure 2.32: Sources and map reconstructed by ICA-NMF from the LPGRS dataset after substraction of the simulated background. Contributions of Fe (5), Th(9), K(10), Si(2) and Mg(4) can be recognized. The elemental spectra of the library are overplotted in color for comparison.

reconstruction (see section 2.8.2) to the number of ouput sources. The quality of signal reconstructions flattens off when N_{Sout} >5 (Figure 2.33 (a)). Th, Fe, Ti are systematically recognized but the quality of reconstruction is good only for Th. Note here that the library spectra where divided by a normalized average spectrum to enable using the element recognition procedure (see section 2.4.4). The case of N_{Sout} = 4 is selected for illustration (Figure 2.33) because increasing the number of sources neither significantly improves signal reconstruction nor the quality of match between output sources/mixing coefficients with library spectra and maps. One can see that the Th and K peaks appear on component #1. Component #2 displays Fe neutron capture peak (7.6 MeV) along with the associated single escape peak (7.1 MeV) and 0.8 MeV Fe non-elastic scaterring peak. Most other low

energy peaks do not seem to be associated to Fe. Component #3 is hard to associated with one element. Component #4 is recognized as Ti. Although the neutron capture peak at 6.7 MeV can be recognized, the single escape peak (6.2 MeV) and the low energy non-elastic scattering peak (1.4 MeV) are not reconstructed and the 0.8 MeV non-elastic scattering of Fe is present .

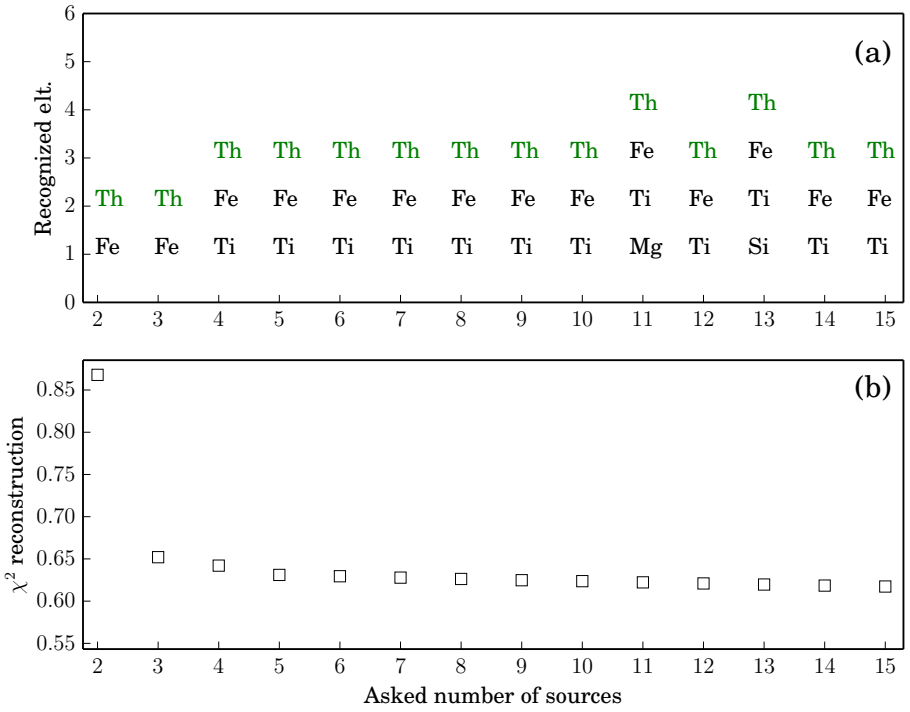

Figure 2.33: Element recognized and quality of signal reconstruction as a function of the number of output sources, after applying ICA to LPGRS spectra that are first divided by the average spectrum.

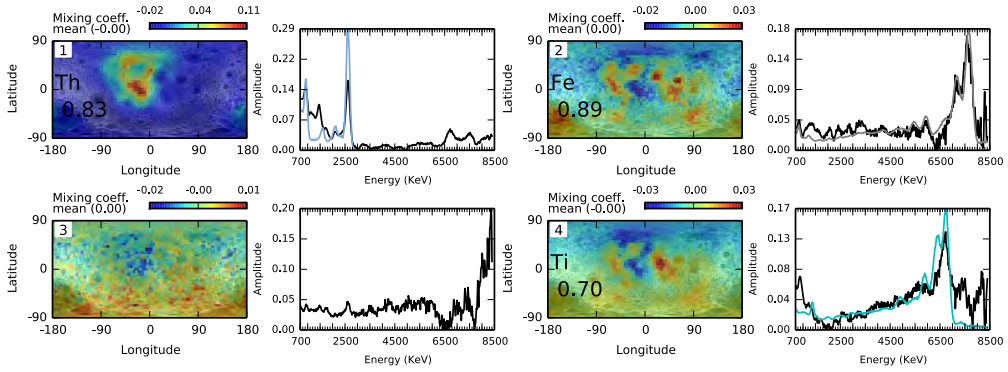

Figure 2.34: Sources and map reconstructed by ICA from LPGRS data divided by the average spectrum. The number of output sources is set to 4. Component (1) is associated to radioactive elements. Component (2) can be recognized as Fe. Component (3) cannot be associated to one specific element. Component (4) corresponds to Ti.

2.8.3 GRaND vestan dataset.

The dataset provided by the GRaND instrument consists in a time series of BGO spectra corrected for gain and artifacts induced by analog to digital conversion [Yamashita *et al.* , 2012]. The spectra were recorded as Dawn was orbiting Vesta at low altitute (210 km, i.e. LAMO = Low Altitude Mapping Orbit) between December the 8^{th} 2011 and April the 27^{th} 2012 [Russell *et al.* , 2013]. Figure 2.35 shows the counts of the simultaneous activation of at least three sensors inside GRaND during LAMO. These events were shown to vary in proportion to the flux of galactic cosmic rays (GCR) independently as measured by the Mc Murdo base in Antarctica [Prettyman *et al.* , 2012]. The flux of GCR is modulated by solar activity and it can be seen that two solar particle events occured while Dawn was in LAMO, increasing the flux of energetic particles up to 4 times the average flux of the recording period. Since gamma rays and neutrons produced in Vesta's regolith and in the spacecraft vary with the flux of galactic cosmic rays (GCR), it is preferable to exclude data recorded during the solar particle events. Datasets were generated by accumulating these time series on a 192 pixels healpix sphere [Gorski *et al.* , 2005]. The average counting rate of pixel p channel l is obtained by:

$$X_{pl} = \frac{1}{N}\sum_{i=1}^{N} x_{il}, \tag{2.48}$$

where N is the number of measurements recorded above pixel p. x_{il} are the time ordered counting rates corresponding to pixel p. The uncertainty on the average counting rate is estimated fom the standard deviation of the counting rates accumulated in pixel p ([Bevington & Robinson, 2003] p54):

$$\sigma_{pl} = \sqrt{\frac{\frac{1}{N-1}\sum\limits_{i=1}^{N}(x_{il} - X_{pl})^2}{N}}. \tag{2.49}$$

Figure 2.36 shows the sampling conditions of GRaND using the 192 pixel healpix projection. The topography of Vesta is also shown in this Figure by transparency: it is dominated by two large impact basins that are displayed by black solid lines. As for the Moon, basins are shown in darker color than highlands.

Although, as far as nuclear spectroscopy is concerned a spherical approximation of the Moon's shape is sufficient, the same is not true for the very irregular shape of Vesta that exhibits important variations in solid angle (Figure 2.40).

Furthermore, unlike for the Moon where there is an important contrast between the composition of the highlands and that of the Mare, such an important chemical variability is not apparent on the surface of Vesta [De Sanctis *et al.* , 2012; Prettyman *et al.* , 2012; Yamashita *et al.* , 2012]. BGO spectra of Vesta have been used to derive a map of iron [Yamashita *et al.* , 2012] and global elemental ratios of Fe/Si and Fe/O have been derived [Prettyman *et al.* , 2012]. These data demonstrate that within a 3σ detection limit of the instrument, the K content of the surface of Vesta is below 1000 ppm although more recent analysis implies an average global value of $\sim$ 600 ppm [Prettyman *et al.* , 2015a]. Here ICA-NMF is applied to BGO spectra of Vesta to test whether it is possible to extract elemental contributions like in the lunar case.

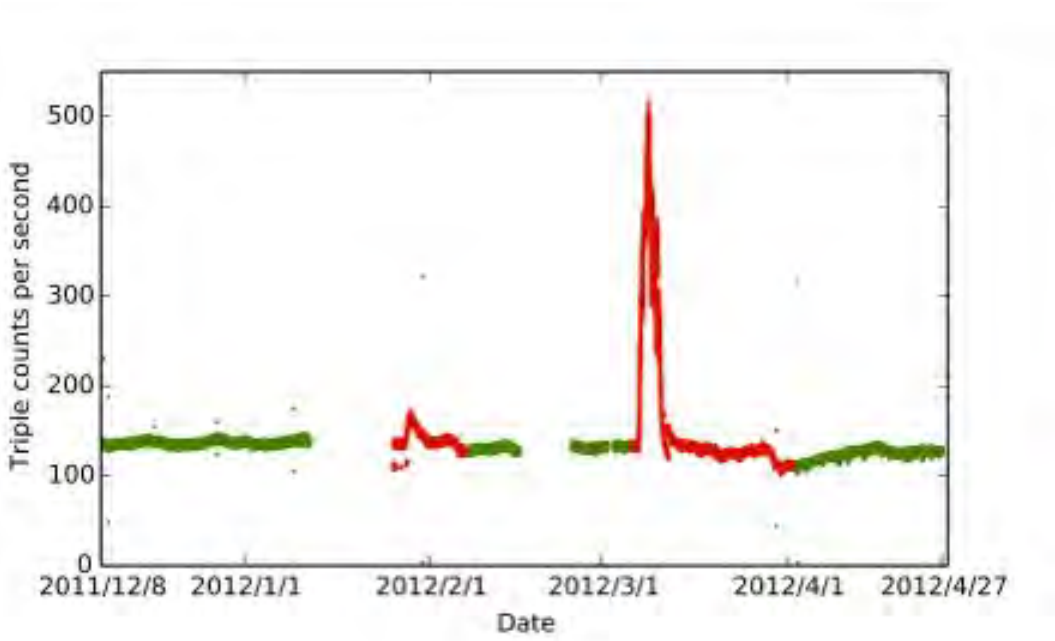

Figure 2.35: Triples (i.e. simultaneous activation of at least three sensors in GRaND) counting rate while the Dawn spacecraft was in Low Altitude Mapping Orbit around Vesta. Red colored periods indicate the occurence of energetic solar particle events.

Epochs	Beginning	End
IA	8 Dec 2011 (2455904)	14 Jan 2012 (2455941)
IIA	7 Feb 2012 (2455965)	22 Feb 2012 (2455980)
IB	24 Feb 2012 (2455982)	6 Mar 2012 (2455993)
IIB	2 Apr 2012 (2456020)	27 Apr 2012 (2455679)

Table 2.4: Recording periods during Low altitude mapping orbit of Dawn around Vesta. These periods corresponds to the quiet solar activity periods that are plotted in green in Figure 2.35. Value in parenthesis correspond to Julian days.

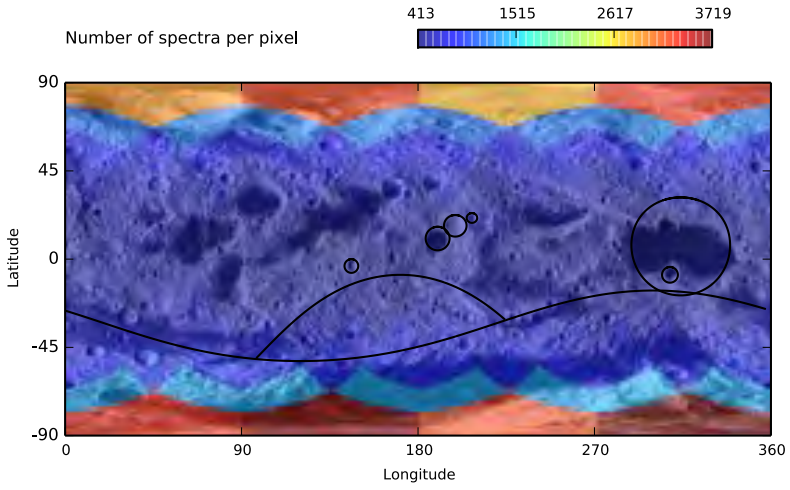

Figure 2.36: Number of spectra accumulated in each pixel for a $N_P = 192$ healpix sphere. The contours of the main impacts basins and craters are shown in solid black lines.

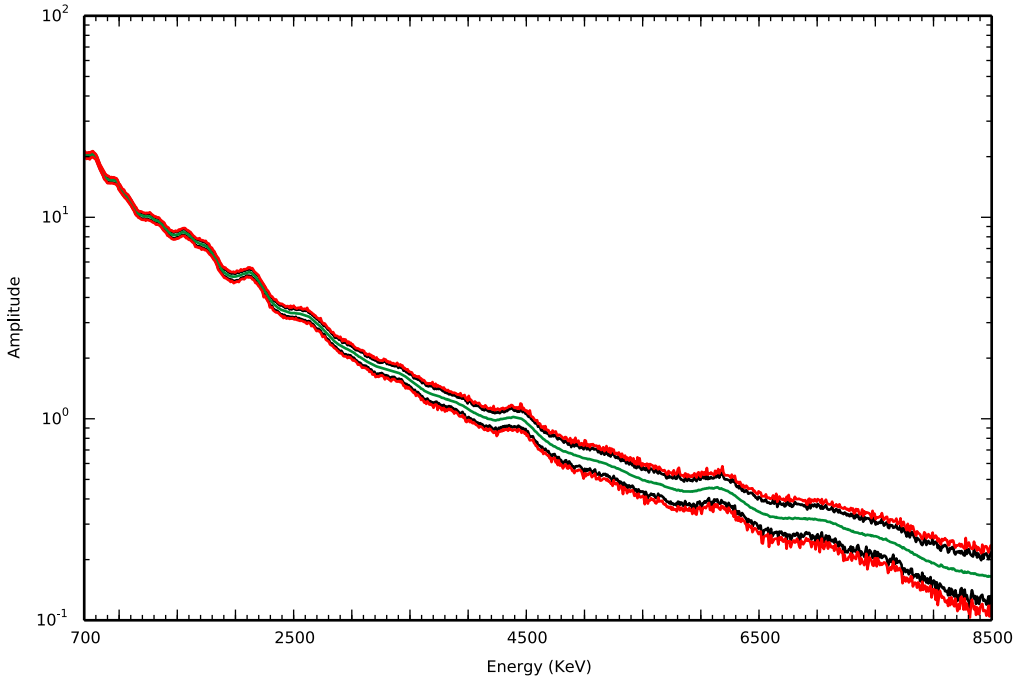

Figure 2.37: Envelope of BGO spectra recorded during the low altitude mapping orbit around Vesta. Spectra were accumulated on a 192 pixel healpix sphere. The average spectrum is shown in green. The envelope of data is shown in black. The red envelope takes account of the uncertainties. The amplitude of the gamma ray counting rate is given in Counts/32s.

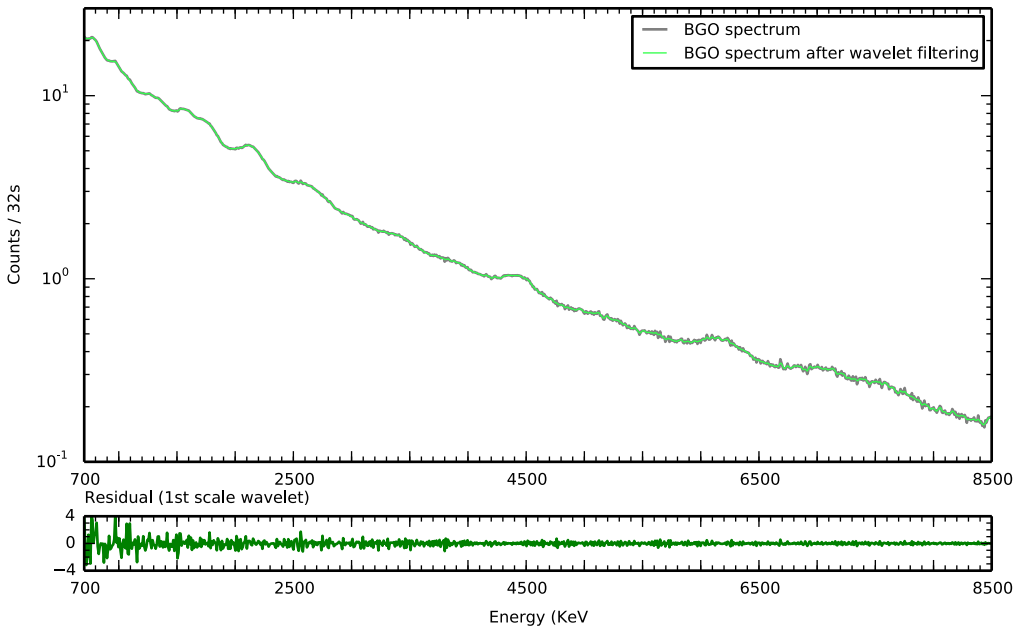

Figure 2.38: Comparison of one BGO spectrum of Vesta (#1 at the North pole of Vesta) before (thick grey line) and after wavelet denoising (thin light green line). The first wavelet component of the BGO spectrum is plotted at the bottom in green. It corresponds to the difference between the original and the denoised spectrum.

Reduction of noise by wavelet filtering

Because of a higher relative altitude during mapping (210 km), the gamma ray signal recorded at Vesta is much weaker for Vesta than for the Moon (100 km). Before any analysis, a filter can be applied to attenuate the level of statistical noise. A method to discriminate noise from the desired signal consists in filtering the components of the signal that vary at lower scales than the instrument's response function, which, for GRaND's BGO scintillator, is a gaussian function with a full width at half maximum (FWHM) of $\sim 10\%$ of the channel's energy [Prettyman *et al.* , 2011]. The wavelet transform is performed with the "a trous" algorithm using a cubic spline function as scaling function [Starck & Murtagh, 2006] was used here to decompose each gamma ray spectrum. The noise is considered to correspond to the component that varies at the smallest scale. This component is then substracted from the signal to attenuate noise. Figure 2.38 illustrates the denoising procedure using the first wavelet component of BGO spectra.

Background correction

Similarly to the lunar case, gamma ray spectra recorded around Vesta include a background, which, in this case, is essentially formed by gamma rays produced within the spacecraft by interactions with galactic cosmic rays [Prettyman *et al.* , 2012]. It can be assumed that the spacecraft records the sum of a vestan and a background contributions which are modulated by the flux of galactic cosmic rays and the solid angle of Vesta from the spacecraft point of view:

$$X(t,E) = \left[X_v(t,E)\frac{\Omega(t)}{\Omega_{ref}} + \left(1 - \frac{\Omega(t)}{4\pi}\right) B(E) \right] \frac{GCR(t)}{GCR_{ref}}, \tag{2.50}$$

where X_v are gamma rays produced within the surface of Vesta, Ω is the solid angle of Vesta from the spacecraft point of view, Ω_{ref} is any reference value. B is the background, GCR is the flux of galactic cosmic rays, and GCR_{ref} is a reference flux. Note that the background component contributes as much as Vesta does not obstruct GCRs. Based on this hypothetical model and following Prettyman *et al.* [2012], the background removal takes the form:

$$X_v(t,E) = \left[X(t)CFCR(t) - \left(1 - \frac{\Omega(t)}{4\pi}\right) X_{survey}(t,E) \right] \frac{\overline{\Omega}}{\Omega(t)} \tag{2.51}$$

where X_{survey} is the average gamma ray spectrum recorded during the survey orbit around Vesta (at an altitude of $\sim$2700 km), which is used as an estimate of the background spectrum. Ω_{ref} is taken as the average solid angle value during LAMO orbit $\overline{\Omega} = 1.07sr$. CFCR is the galactic cosmic ray correction factor, which is defined as:

$$\begin{aligned} &CFCR(t) = \frac{\overline{CMS^*(t)}}{G(CMS^*(t))} \\ &\text{where} \\ &CMS^*(t) = \frac{4\pi C1}{C1(4\pi - \Omega(t)) + C2)} CMS(t) \end{aligned} \tag{2.52}$$

where CMS is the counting rate of coincidence events (illustrated in Figure 2.35), which can be used as a proxy for the flux of GCR. $CMS^*(t)$ is the theoretical value of CMS far from the observed object, which blocks a part of the isotropic GCR flux. The coefficients C1 and C2, measured during Mars gravitational assist, were found to be respectively equal to 14.5, 5.95 (T.H. Prettyman personal communication). $\overline{CMS^*}$ corresponds to the average value during the recording period. $G(CMS^*(t))$ indicates a smoothing by a gaussian

filter with a FWHM of 400 measurements (∼8h). This smoothing is applied to reduce the variance introduced by the correction [Prettyman *et al.* , 2012]. This correction procedure is illustrated on Figure 2.39 by comparing the corrected and uncorrected BGO spectra of Vesta.

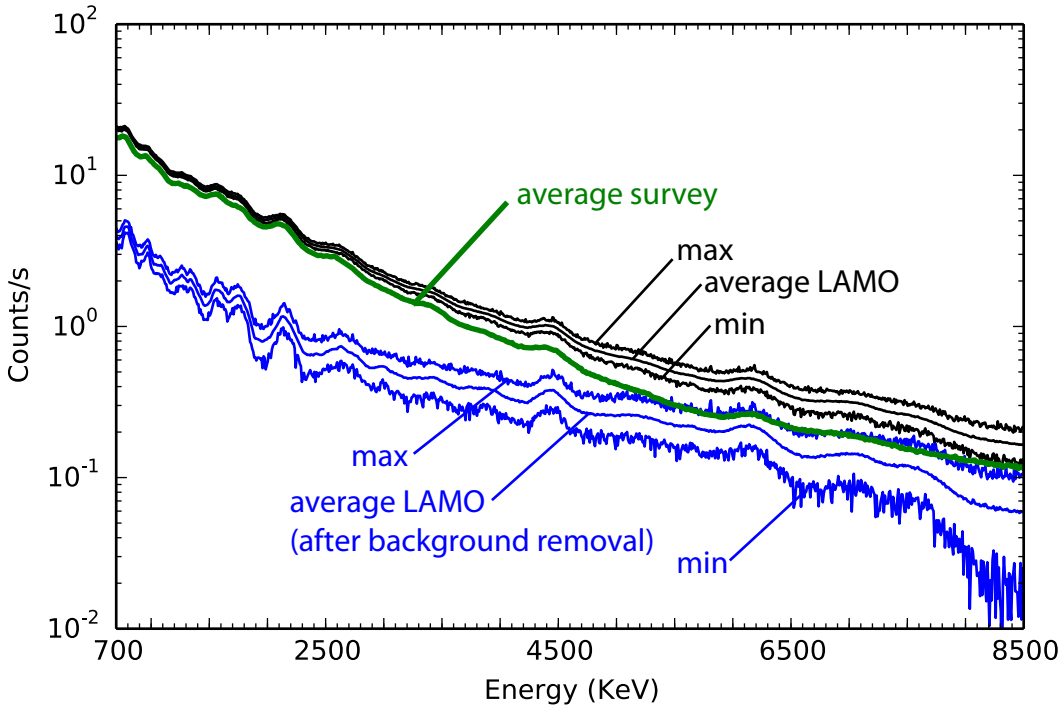

Figure 2.39: Enveloppe of BGO spectra recorded during LAMO at Vesta rebinned on 192 pixels (black). Average BGO spectrum during survey orbit (altitude of 2700 km) used as a proxy for the background (green). BGO spectra after background removal rebinned on 192 pixels (blue). The background removal procedure takes account of the variations of the flux of galactic cosmic rays and that of the solid angle of Vesta from the spacecraft point of view.

Results

ICA-NMF is applied to the gamma rays recorded by GRaND at Vesta presented in Figure 2.37. The quality of signal reconstruction is given as a function of the number of ouput sources in Figure 2.41. The number of output sources was set from 2 to 15 as for the analysis of lunar data, because it is assumed that the same number of potential sources can be expected. The reduced χ^2 decreases below one for a number of output sources equal to four. In this case, the sources and mixing coefficients estimated by ICA-NMF are shown in Figure 2.41. Components #3 and #4 look like the average spectrum of Vesta, which is shown in Figure 2.37. The spatial distribution of these components appears correlated to the solid angle of Vesta, which is shown in Figure 2.40. Figure 2.42 shows similar ICA-NMF outputs, but for spectra that were filtered for their first wavelet component prior to the analysis. Again, one component looks like an average spectrum of Vesta and its spatial distribution is dominated by the influence of the solid angle. Two components remain very noisy. It is difficult to identify element specific peaks. One component shows a peak at 0.8 MeV and a bump at 7.5 MeV, these two features potentially corresponding respectively to the non-elastic scattering and neutron capture contributions from iron. The 0.8 MeV has a higher amplitude than the 7.6 MeV neutron capture peak and thus dominates this

spectral component. Since non-elastic scattering is not affected by variation in neutron number density, if the fact that component 4 reflects contribution of iron is correct, it can be directly compared to a Fe counting rate map, without considering the effect of neutron number density. The spatial distribution is, to first order, consistent with the distribution of iron derived by [Yamashita *et al.* , 2012] (Figure 1.18). The northern hemisphere is richer in iron than the southern hemisphere and two tongue shaped areas of low iron content are visible. These two areas start from the southern hemisphere and reach the equator at a longitude of $\sim$0 and $\sim$180 respectively (Figure 2.43).

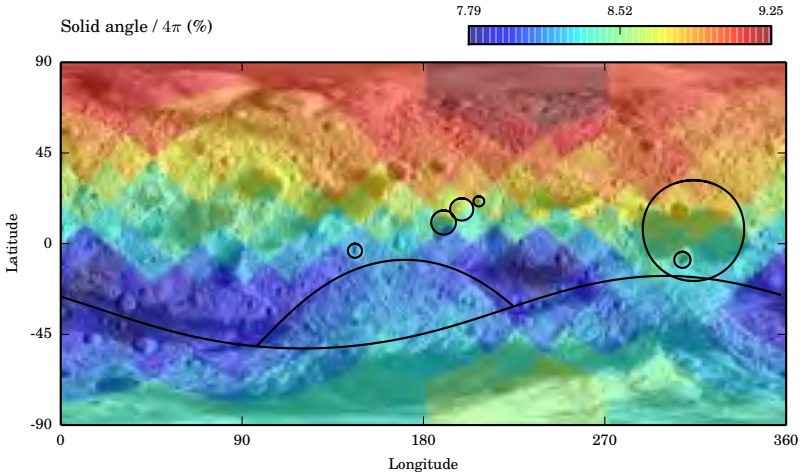

Figure 2.40: Portion of the sky occupied by Vesta (solid angle / 4π expressed in percent), as seen by Dawn during Low Altitude Mapping orbit, as function of the location of the surface of Vesta towards which the spacecraft points at.

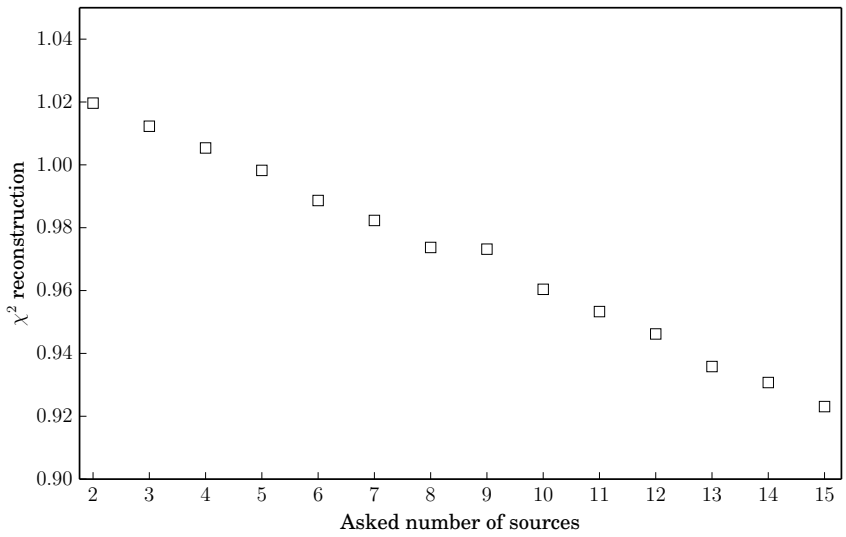

Figure 2.41: χ^2 versus number of sources asked for ICA-NMF applied to vestan BGO spectra. Spectra were recorded during LAMO orbit, when the solar activity was quiet. Spectra were rebinned on a 192 pixels healpix sphere.

The removal of a background improves ICA-NMF performances in the case of the analysis of the LPGRS dataset. This encouraging result motivated the application of a

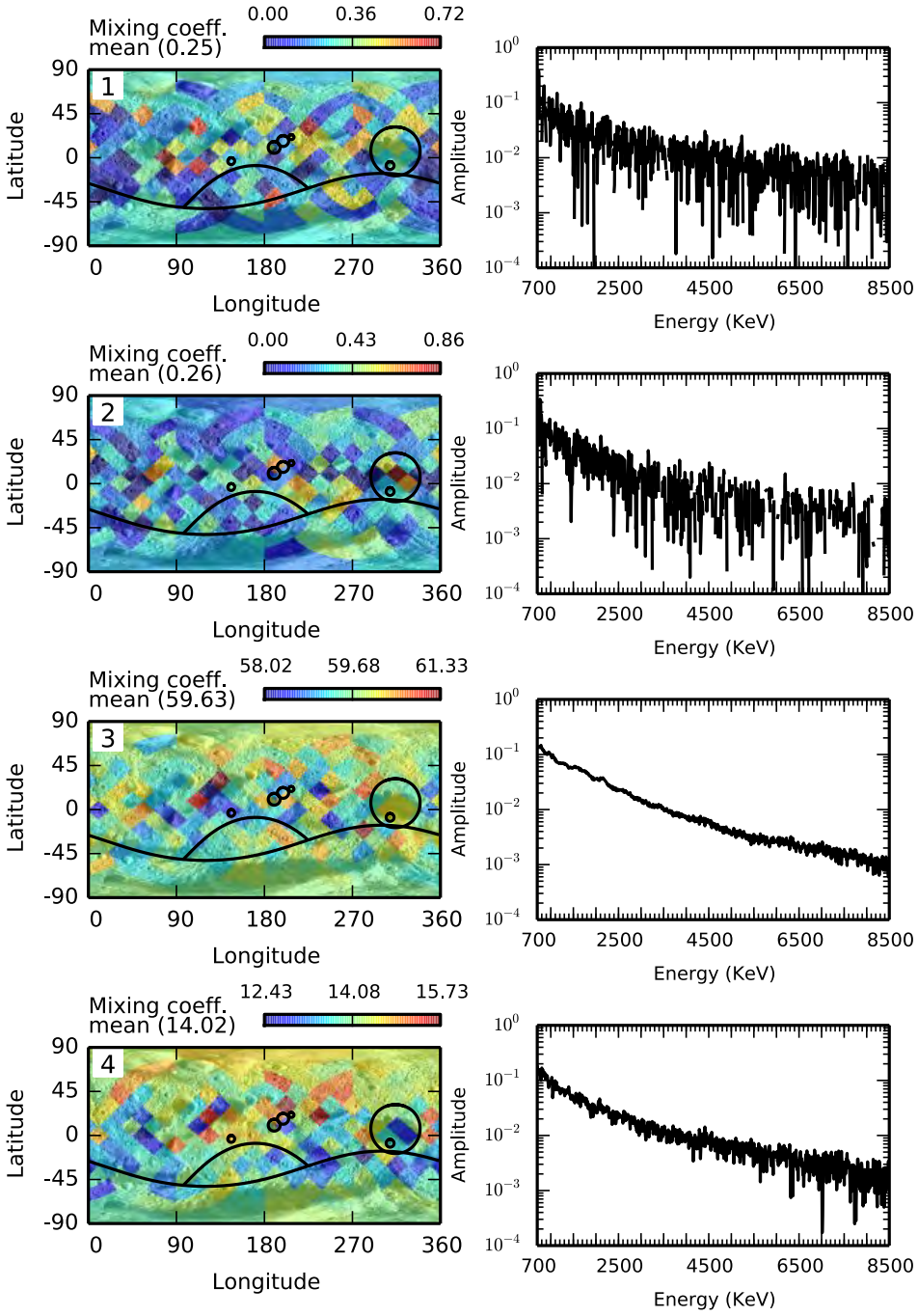

Figure 2.42: Source spectra extracted from the 192 pixel accumulated dataset. Only data recorded during quiet solar activity were included. Two components (3,4) look like an average spectrum of Vesta, while components 1 and 2 appear dominated by noise. The spatial distribution of component 4 is partially correlated with Vesta's solid angle with a linear Pearson correlation coefficient of ρ=0.47.

similar procedure in the case of Vesta. The background removal procedure, described in section 2.8.3, is adapted here to take account of the change of GCR and solid angle, the latter introducing an important observational bias. The sources extracted by ICA-NMF from the corrected series are shown on Figure 2.44. As previously four sources are asked to be reconstructed. The correction, expected to enhance the ability of ICA-

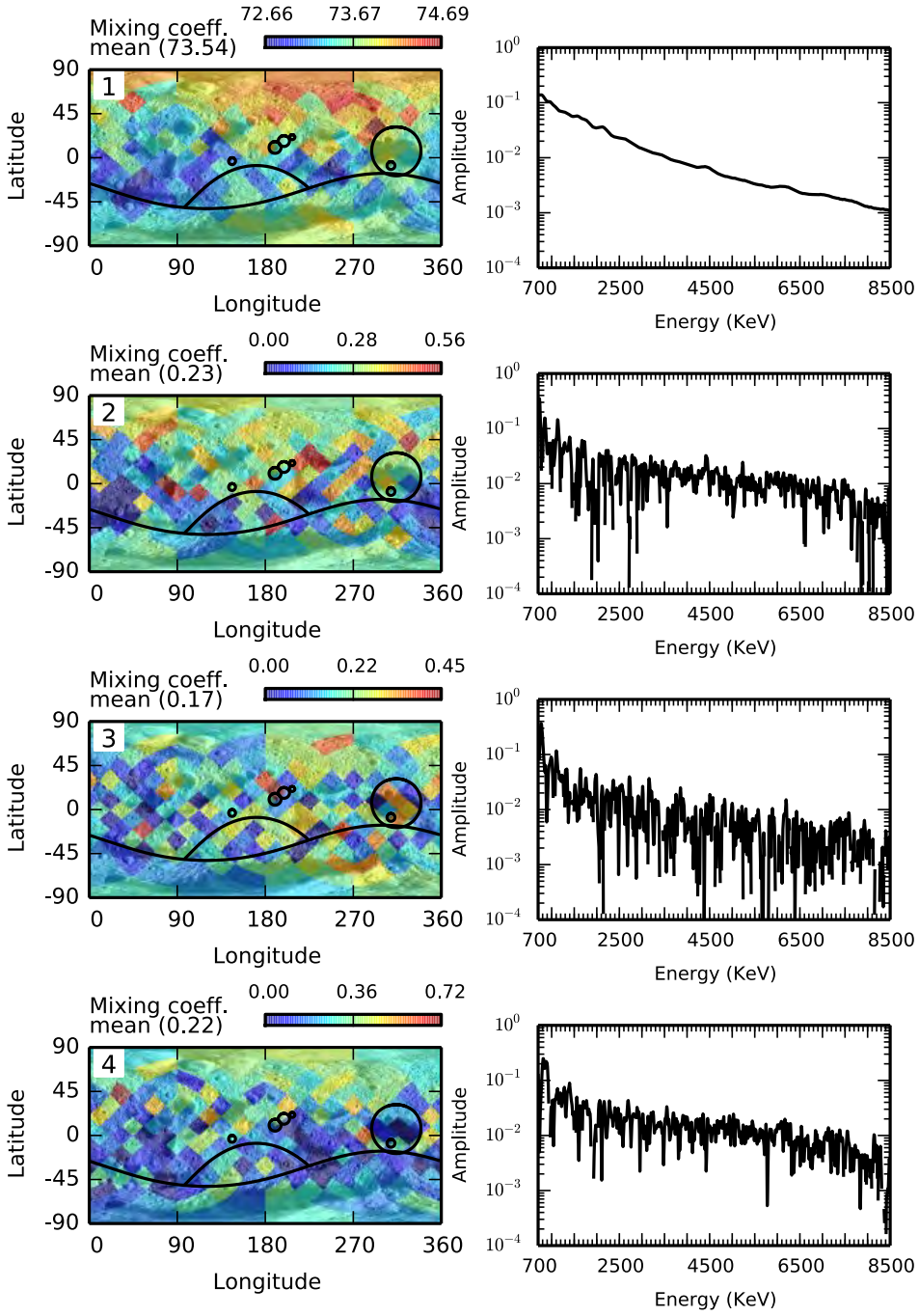

Figure 2.43: Source spectra extracted from the 192 pixel accumulated dataset. Only spectra recorded during quiet solar activity were included. The first wavelet was filtered out prior to analysis. Component 1 looks like an average spectrum of Vesta. Its spatial distribution is clearly dominated by the influence of the solid angle of Vesta (with a correlation coefficient of ρ=0.77). It seems hard to recognize specific peaks on components 2 and 4 which are very noisy. Component 4 shows a peak at 0.8 MeV and a wide bump near 7.5 MeV which could be attributed to iron. The spatial distributions of this component is discussed in more detailed in the text.

NMF to extraction elemental contribution, does not allow any relevant reconstruction of an elemental signal, including an iron signal, which marginalizes the result obtained in the

case of the uncorrected series.

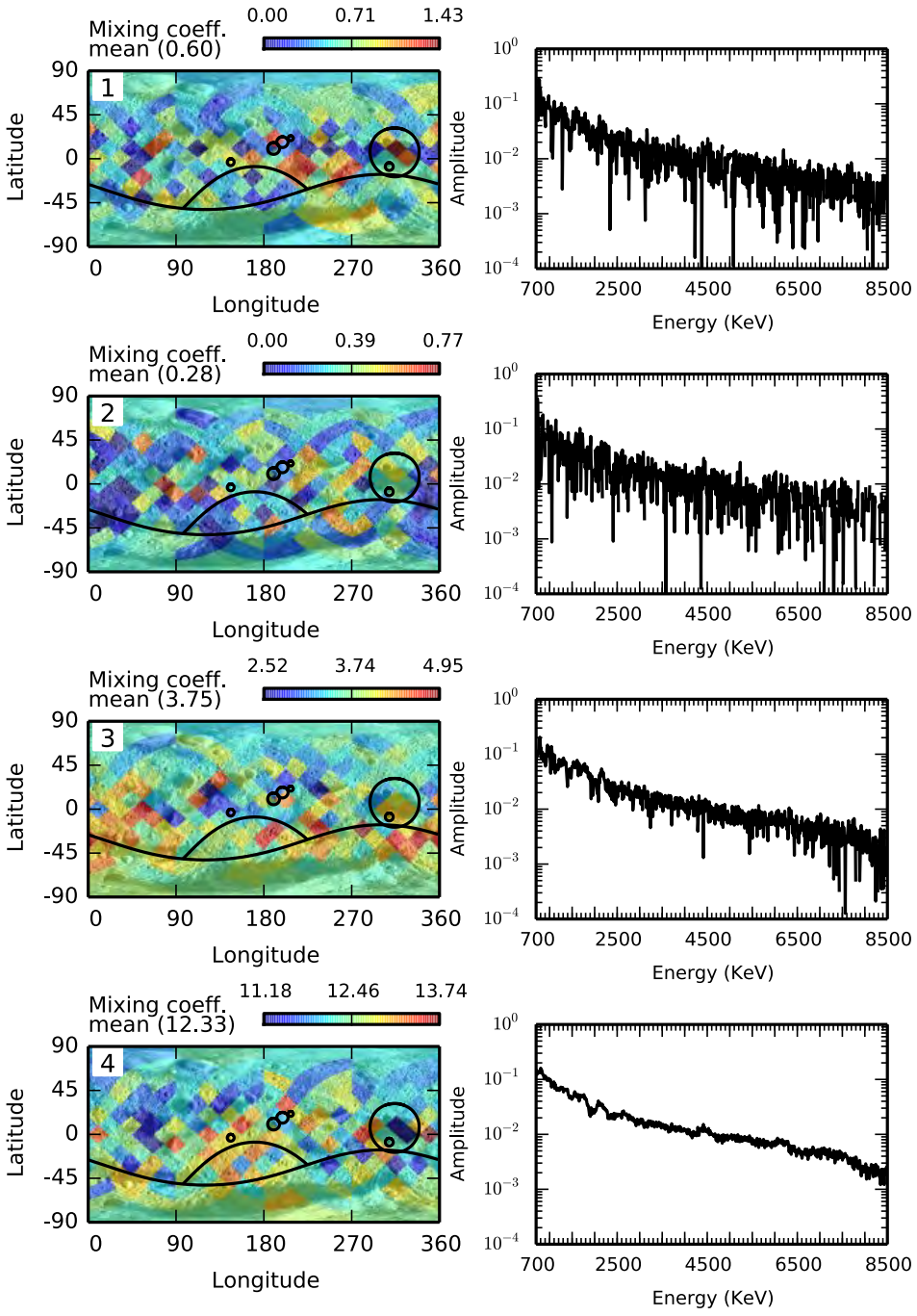

Figure 2.44: Components extracted by ICA-NMF from BGO spectra of Vesta after background removal. The number of asked sources was set to four. The background correction, which takes account of the observational bias introduced by changes in the apparent solid angle of Vesta and in the flux of galactic cosmic rays, does not improve the ability for ICA-NMF to recover any element specific contribution from the vestan gamma ray spectra.

2.8.4 Summary of analyzed datasets

Synthetic datasets (for the Moon only)

Mixture	Elements	Spatial response	Background	D'/D	Bins	E (MeV)
2.6	K, Ti, Fe	constant	absent	1	1790	1 - 8.42
2.6	all	constant	absent	1	1790	1 - 8.42
2.4	all	latitude dependent	absent	0.1 - 1	1790	1 - 8.42
2.4	all	latitude dependent	present	0.1 - 1	1790	1 - 8.42

Real datasets (Moon and Vesta)

Mission	Body	Comment	Bins	Energy (MeV)
LPGRS	Moon	5 °rebinned	1790	1 - 8.42
GRaND	Vesta	all records	192	1 - 8.5
GRaND	Vesta	quiet solar activity	192	1 - 8.5

Table 2.5: Analyzed datasets. In column "elements", all = O, Mg, Al, Si, Ca, Ti, Fe, K, Th and U. D'/D is the ratio of the dynamic range of the abundances applied to the mixtures / the real dynamic range.

2.9 Discussion.

ICA-NMF was implemented in this study to reconstruct elemental spectra and, by projecting their contribution to the observed spectra on the sphere, reveal elemental maps. However, even for linear mixtures of elemental spectra this method is not able to perfectly reach the expected objective. ICA can work if the sources are independent, if their values have non-gaussian distributions and if there are at least as many different linear combinations of the source signals as there are source signals. A corrolary to this last condition is the fact that two components whose mixing coefficients are perfectly correlated cannot be separated (e.g. $M_{p1} = \alpha M_{p2}$).

In the case of mixtures of ten elemental spectra, ICA-NMF is only able to separate the contributions of Th, K, Fe with a satisfactory quality of reconstruction and still there are contributions of other elements associated to these components. This is mainly because elemental spectra present high cross-correlations. The tendency to extract Th, K and Fe is related to their important 4^{th} order contrast which allows ICA to separate them.

Despite the differences between the physical mixtures (Eqn. 2.4) and linear mixtures (Eqn. 2.8), the results of elemental signal separation do not significantly change between these two models. However, the addition of a background significantly worsens the results because several elemental spectra are importantly correlated with the background, and the distributions of its values are nearly gaussian.

Spatial variations of the components extracted are coherent with elemental maps reconstructed by other analyses. For instance, maps of iron and radioactive elements are consistent with those based upon the inversion of model 2.4 in [Prettyman *et al.* , 2006], and the maps of Th determined from peak area analysis from the LPGRS data [Lawrence, 2004] as well as other gamma ray datasets such as that from the Chang-E mission [Zhu *et al.* , 2013].

The contributions of U and Th do not seem possible to separate because their abundances are perfectly correlated [Prettyman *et al.* , 2006]. These two elements are also extracted together in the same independent component when JADE is applied to the Kaguya gamma ray spectra [Forni *et al.* , 2010], which supports this strong association. However, the very high correlation between the abundances of K and that of Th does not stop ICA from separating the two elemental contributions. This may be because the spectral 2^{nd}

and 4^{th} order correlations between Th and U are lower than correlations between K and Th (Figure 2.16 and 2.17). However, this easier separation seems more importantly related to the fact that the kurtosis of the source spectrum of K, which has the narrowest energy range of any element, is significantly higher than for the other sources and that its cross-cumulants with other elements are always low.

For the case of Vesta, the study of the HED meteorites allowed to predict the mineralogical and geochemical nature of the surface of this asteroid before Dawn reached its target [Usui & McSween, 2007; Prettyman *et al.* , 2011]. Marginal lithologies observed in the HED generated high expectations, such as the possibility of finding potassium rich terrains [Usui *et al.* , 2010; Barrat *et al.* , 2009]. However, K signal is barely visible in GRaND data such that only the average K content of Vesta can be determined relevantly [Prettyman *et al.* , 2015a]. Th and U were not detected.

Spectral components extracted from the BGO spectra of Vesta using ICANMF are not easy to associate to a specific element, although Fe, K and Th signals from Vesta have been detected [Yamashita *et al.* , 2013; Prettyman *et al.* , 2015b]. The signal variations seem to be dominated by the variation in solid angle of view under which the spacecraft observed Vesta and a background removal adapted to correct the changes in solid angle does not allow to retrieve more elemental contribution. Yet the scintillator used to record these data is similar to that used at the Moon. The change in composition from place to place, the variations of the solid angle subtented between the spacecraft and the surface of the planet, the contribution of the spacecraft and/or the instrument itself differ between the two datasets. Determining which factor influences more the contrast between the two results is a complex question.

Extraction of elemental contributions is more difficult when the chemical variability is decreased as demonstrated with lunar synthetic spectra. Indeed the elemental contributions for Vesta might not be exactly the same as the elemental components for the Moon, and the nature of the background gamma rays might differ from that of LPGRS observational conditions. Rigourously the tests that were carried out here for the Moon should be implemented for Vesta, i.e. generating synthetic spectra of Vesta with an increasing variability, in order to prove that the lack of chemical variability on Vesta is the reason for the difficulty of extracting elemental contributions. To first order, the same elements O, Si, Mg, Fe, Ca, Al present on the surface of the Moon are also present on the surface of Vesta and the BGO spectra of the Moon and Vesta have comparable shapes. The vestan dataset is less variable than the least variable lunar synthetic dataset (Figure 2.27). Besides, the dynamic range of iron content between pure diogenites and basaltic eucrites considered here can reach 30%. But if the dynamic range of known howardite samples is considered, one obtains about 10%. This is more consistent with the iron counting rate map obtained by [Yamashita *et al.* , 2012]. This map, obtained from the analysis of the area of the 7.6 MeV neutron capture peak, has a dynamic range also on the order of 10% after corrections. The dynamic range of iron on the moon, as inferred in [Prettyman *et al.* , 2006] is 300%, so the least variable lunar dataset presented in this study has a dynamic range of 30%, which is more variable than howarditic compositions. According to Figure 2.22 it is not possible to extract the contribution of iron for the least variable lunar dataset in the presence of a background. The suggestion made in this study is that ICA-NMF is only marginally able to extract the contribution of iron from the BGO spectra of Vesta.

The low chemical variability of howardites could suffice to explain the lack of extraction of elementary signal in the case of Vesta. In this matter, it is important to stress that the sampling of the instrument can reduce the apparent chemical variability of a dataset, because the petrological endmembers present in geological units smaller than the spatial response function of the instrument will appear mixed in the same sample.

The Dawn spacecraft is currently in orbit at Ceres, providing BGO spectra of this asteroid with a spatial resolution of $\sim 20\%$ of the dwarf planet circumference similarly to

Vesta. Given the petrological endmembers expected at the surface of Ceres, as illustrated in Figure 2.45, BGO spectra are likely to be more variable. If these petrological endmembers form as many geological units that can be resolved by GRaND as there are relevant elemental contributions to be extracted, ICA-NMF could be a relevant tool to consider. More specifically, hydrogen, which shows a prominent sharp peak at 2.2 MeV is present in much higher concentrations than on Vesta. The elementary spectrum of H probably has a significant kurtosis because, similarly to K , it displays a single low energy emission line. This makes the contribution of H, a spectral component that should be readily extracted by ICA-NMF from the Ceres dataset.

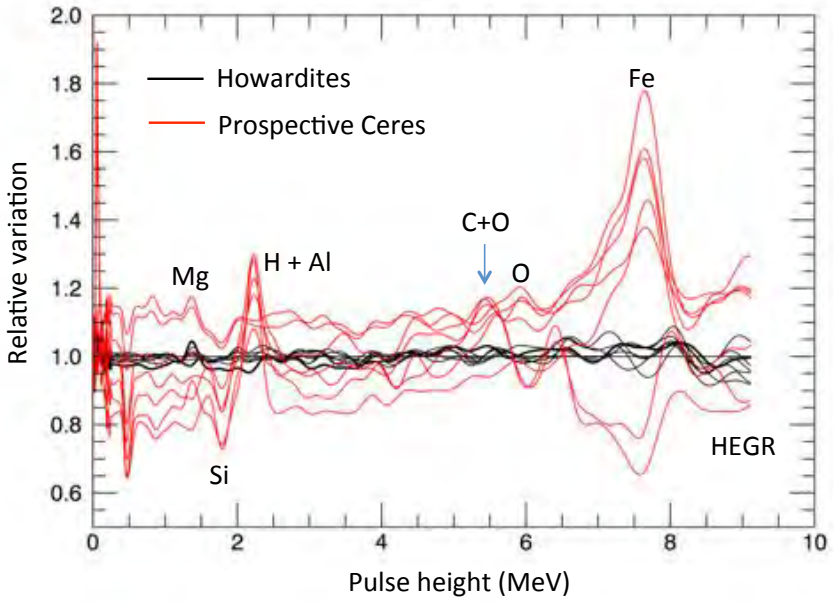

Figure 2.45: MCNPX simulated BGO spectra of Vesta, based on howarditic compositions (black) including 10 to 90 % of eucritic material (black). Simulated BGO spectra for Ceres (red), based on lithological endmembers inferred from telescopic VIR spectrometry (see [Prettyman *et al.* , 2011] and references therein). These are expected to be alteration products including saponite, carbonates, iron-rich clays, brucite, salts, salt hydrates, ammonia ice and water ice. Each gamma ray spectrum is divided by an average spectrum to emphasize spectral variability (T.H. Prettyman, personal communication).

2.10 Conclusions.

In this study, we measured the performance of two BSS methods in reconstructing elemental spectral shapes and elemental spatial distributions using BGO gamma ray data. The association of ICA-NMF manages much better spectral and spatial reconstructions than ICA alone. The separation performance is clearly lower when a large number of spectra are mixed together because they are not all perfectly independent. However some of these sources have an important enough 4^{th} order "contrast" that enable their separation. This allows explaining the separation of K, Th and Fe contributions from the lunar data. In particular K and Th can be separated despite important spatial correlations of the abundances of these two elements.

The addition of a background spectrum, which results from nuclear reactions that are not element specific, significantly worsens the performances of ICA-NMF, a number of

elementary spectra being importantly correlated to this spectral component because of the presence of a continuum rather than prominent peaks.

The linear approximation, which appears not entirely justified when compared to a physical model of gamma ray mixtures is a minor problem compared to the aforementionned issues concerning the properties of the sources.

The viewing geometry, although affecting the spatial distribution of elemental signatures, does not appear to control their extraction because the elements recognized are the same whether the latitude dependent response function of the LPGRS instrument is taken into account or not.

However, the inherent (chemical) variability plays a crucial role as extraction of Th and Fe is shown to be clearly degraded if the dynamic range of element weight fraction is artificially reduced.

Inferences made from the study of artificial lunar data with reduced chemical variability support the idea that the lack of sufficient chemical variability (probably $\sim$30% for iron) can explain the marginal extraction of an iron signal in the case of vestan BGO spectra.

Given the prospective lithological endmembers present at the surface of Ceres, ICA-NMF might be successful on BGO spectra of this asteroid due to the potential presence of prominent H and Fe peaks.

Chapter 3

A coupled chemical melt migration model of Vesta, eucrites and diogenites.

Contents

Abstract: A numerical method is implemented to solve mass and momentum equations, developped to describe two phase-flows in the Earth and planetary sciences, more specifically in this case, the migration of silicate melt. This enables computing the fractions of liquid and solid in space and time in 1D spherical geometry. The two phase flow equations are coupled to the heat equation, where the heat is supplied by the decay of ^{26}Al, which is considered to be dominant in the heat budget of small bodies formed early in the solar system. A binary phase diagram is used to implement the melting law for the silicates. This approach allows the mobility of the heat source ^{26}Al to be taken into account, an important aspect of early planetary differentiation as highlighted by recent numerical studies. Finally, the binary system is replaced by an anorthite-olivine-silica phase diagram, considered to be a good proxy for describing the petrology of the HED meteorites. In this way, the mineralogy of the final rocks, once crystallization has taken place, can be predicted. In addition, trace element concentrations can be computed using appropriate mineral - melt partition coefficients.

Table 3.1: If not indicated otherwise, the physical and chemical properties used in the numerical simulations presented in this chapter are given in this table. The references are numbered as follows: 1 = [Russell *et al.* , 2012], 2 = webmineral.com, 3 = [Dingwell *et al.* , 2004], 4 = [Hirth & Kohlstedt, 2003], 5 = [Krot *et al.* , 2014], 6 = [Šrámek *et al.* , 2012], 7 = [Monnereau *et al.* , 2013], 8 = [Neumann *et al.* , 2014], 9 = [Castillo-Rogez *et al.* , 2009], 10 = [MacPherson *et al.* , 1995], 11 = [Morse, 1980], 12 = [Buono & Walker, 2011], 13 = [Toplis *et al.* , 2013],

Symbol	Property	Value	Unit	Source
R_s	Vesta radius	262	km	1
ρ_{an}	Anorthite density	2700	kg/m^3	2
ρ_{en}	Enstatite density	3200	kg/m^3	2
ρ_{fs}	Ferrosilite density	3950	kg/m^3	2
ρ_{di}	Diopside density	3400	kg/m^3	2
ρ_{fo}	Forsterite density	3270	kg/m^3	2
ρ_{fa}	Fayalite density	4390	kg/m^3	2
ρ_{Fe}	Iron density	7874	kg/m^3	2
ρ_{Ni}	Nickel density	8900	kg/m^3	2
ρ_{FeS}	Iron suldie density	4840	kg/m^3	2
ρ_{NiS}	Nickel sufide density	5300	kg/m^3	2
μ_f	Liquid silicate viscosity	0.1 - 10	Pas	3
μ_m	Matrix viscosity	10^{18}	Pas	4
a_0	Grain size	0.001	m	5
Cp_{sil}	Silicate specific heat	1000	J/kg/K	6
Cp_{met}	Metal specific heat	440	J/kg/K	6
L_{sil}	Silicate latent heat	500000	J/kg	6
L_{met}	Metal latent heat	247000	J/kg	6
k	Thermal conductivity	4	W/m/K	7
$Text$	Surface temperature	292	K	7
α	Thermal expansivity	2×10^{-5}	1/K	8
M_{Al}	Aluminium molar mass	0.027	kg/mol	-
M_{An}	Anorthite molar mass	0.277	kg/mol	-
$M26$	^{26}Al molar mass	0.026	kg/mol	-
^{26}Al/^{27}Al	Initial isotopic ratio	5×10^{-5}	Natom/Natom	9
λ_{Al26}	Decay constant	3.063×10^{-14}	1/s	10
Ed	^{26}Al decay energy	5×10^{-13}	J/atom	10
A	Avogadro's number	6.0221415×10^{23}	Natom/mol	-
T_{eut}^{sil}	Silicate eutectic T	1543	K	11
T_{px}	Pyroxene melting	1830	K	11
T_{ol}	Olivine melting	2163	K	11
T_{Fe}	Iron melting	1811	K	11
T_{eut}^{met}	Fe-FeS eutectic T	1261	K	12
X_{eut}^{sil}	Silicate eutectic	An0.58Px0.42Ol0	kg/kg	11
X_{eut}^{met}	Metal eutectic	Fe0.15FeS0.85	kg/kg	12
X_{Vesta}	Bulk composition	Fe | FeS | An | Px | Ol 4.8 | 4.2 | 8.1 | 31.4 | 51.5	vol %	13
H_{lid}	Critical lid thickness	3	km	-
MO_{thres}	Magma ocean threshold	0.6	kg/kg	-
nr	Number of radial levels	1000	-	-

3.1 Introduction

Based upon chemical, mineralogical and isotopic study it is established that the howardite, eucrite and diogenite meteorites (HED) represent a single family of rock-types from a relatively small differentiated body that accreted sufficiently early in the history of the solar system that live ^{26}Al was still present in significant amounts [McSween *et al.* , 2010]. Furthermore, telescopic observations suggest that the HEDs may originate from the asteroid 4-Vesta [McCord *et al.* , 1970], a hypothesis strengthened by data from the Hubble space-telescope and recently confirmed by the results of the NASA Dawn mission [Russell *et al.* , 2012]).

Two alternative scenarios are usually considered for obtaining eucritic liquids. They could either result from about 15 - 20% of equilibrium melting of a chondritic source [Stolper, 1975] or could be the residual liquid after 80-85% of equilibrium crystallization of a 100% molten source [Righter & Drake, 1997], i.e. the symmetric scenario from a thermodynamic point of view [McSween *et al.* , 2010]. However, maintaining equilibrium crystallization in a convective magma ocean up to such a high fraction of crystals seems unlikely and Mandler & Elkins-Tanton [2013] propose an intermediate scenario where the melt is extracted into shallow magma chambers after 60 - 70% of equilibrum crystallization of a magma ocean. Fractional crystallization takes place in these magma chambers that are periodically recharged by the underlying compacting crystal mush. This scenario produces the main petrological characteristics of the HED suite.

As detailed in the general introduction (Section 1.4.4), the bulk composition of the HED parent body can be determined from comparisons between chondritic groups and the HED meteorites, and from geochemical models of the internal structure of Vesta. For the chondritic compositions that are considered, a $\sim$ 40 km thick crust consisting of eucrites and diogenites atop an olivine rich mantle is usually predicted [e.g. Ruzicka *et al.* , 1997; Toplis *et al.* , 2013; Mandler & Elkins-Tanton, 2013]. However, the hydrodynamic modelling of two successive head-on impacts at the South pole of Vesta, infers that material as deep as 80 km might be present in the Rheasilvia basin [Jutzi *et al.* , 2013]. On the other hand, olivine concentrations measured in this region from Visible-Infrared spectroscopy, are lower than or equal to 30 vol% at least at the spatial scales characterized by the VIR instrument ($>$200 m) [Ammannito *et al.* , 2013b]. Olivine can be present in important proportions ($>$90%) in local spots a few hundreds of meters across [Ammannito *et al.* , 2013a]. The absence of olivine rich material in the Rheasilvia basin may call into question the chondritic nature of Vesta [Clenet *et al.* , 2014; Consolmagno *et al.* , 2015].

Numerical models of the thermal evolution of a Vesta sized object constitute an alternative source of information and such studies have provided important insights into the timing of differentiation [Gupta & Sahijpal, 2010]. However, it is only recently that attempts have been made to combine modelling of the thermal and physical evolution with notions of chemistry. Indeed, consideration of chemistry is an essential aspect to take into account, in particular for bodies for which ^{26}Al is an important heat-source. This is because aluminium is concentrated in the liquid silicate during melting. As such, rapid melt migration acts against complete melting, because the principal heat source is removed from the interior [Neumann *et al.* , 2014]. The construction of a model of melt production and migration for small bodies can draw on the two-phase flow equations developped in the Earth sciences [e.g. Bercovici *et al.* , 2001] as illustrated by the modelling of Šrámek *et al.* [2012] for the segregation and formation of metallic cores. A similar formalism can be implemented, this time to focus on the migration and fate of liquid silicates. In light of the current knowledge of the differentiation of Vesta, such models may require combining the aspects of two-phase flow dynamics with a self-consistent thermodynamical model because the mineralogical composition of the HEDs and of the surface of Vesta are the main observational constraints available.

Description of the relative motion between a partial melt and its solid silicate matrix is essential for a better understanding of magmatic differentiation and the compositional evolution of this dynamical system. This phenomenon is complicated to describe as it includes both dynamic and thermodynamic aspects. The rate of ascent of a silicate melt depends on the permeability of the medium and on the viscosity of the fluid, but the viscosity of the matrix, which has to deform to enable the expulsion of the melt, is an important controlling factor as well [McKenzie, 1984]. Based on the general theory of two-phase flow developped by Drew [1971], McKenzie [1984] proposed a formalism that became a reference to quantify the dynamics of melt extraction. It can be used to measure the impact of the compositional diversity of terrestrial magmatic liquids on their ability to migrate towards the surface [McKenzie, 1985]. Spiegelman [1993] showed that the development of porosity waves is a fundamental feature of these two phase flow equations. More recently, these two-phase flow equations were reformulated in a framework that includes the effects of surface tension and damage [Bercovici *et al.* , 2001].

Another important aspect of silicate migration is that during the separation of liquid and solid phases, they continue to interact chemically. In this respect, it is generally assumed that chemical equilibrium is instantaneous when compared to the rate of migration. On the other hand, chemical equilibrium may in fact be only partial if the characteristic time for chemical equilibrium is not negligible compared to characteristic time scale of melt migration [Rudge *et al.* , 2010]. If equilibrium can be assumed, this enables exploiting the geometric relationship between the composition and the equilibrium temperature provided by an equilibrum phase diagram. The liquid fraction and the compositions of solid and liquid can be calculated as a function of the bulk composition and of the available energy. This method was developped in the framework of melt ascent below oceanic ridges [Ribe, 1985; Katz, 2008]. The effect of compositional evolution appears essential for small bodies that differentiated early in solar system history. Indeed their heat budget is dominated by the radioactive decay of ^{26}Al, hence the process of differentiation will be affected by the spatial distribution of Al inside the planetary embryo. Al is a moderately incompatible element and it is not distributed uniformly between the minerals which make up the silicates. Incidentally, melting will significantly change the concentration of this element in the liquid and in the solid residue. Moskovitz & Gaidos [2011] compared the average melt production in a body where the heat source is homogeneously distributed, to the case where this element preferentially enters the liquid. They find that the migration of Al dampens the maximum temperature and melting degree reached in the body.

Undifferentiated planetary embryos consist in mixtures of silicate and metal such that within a body internally heated to the point of melting both liquid silicates and metal are potentially mobile. Neumann *et al.* [2012, 2014] use a modified Darcy's law and assume that the matrix is immobile so that they can use the analytical expression of the separation velocity to model the downward percolation of liquid metal and the upward migration of liquid silicates simultaneously. More recently, three-phase flow equations were derived from a formalism similar to [Bercovici *et al.* , 2001], allowing to model the percolations of the two fluids without neglecting the important impact of the deformation of the matrix [Nishimura & Monnereau, 2015]. Neumann *et al.* [2014] use a partition coefficient to monitor the migration of ^{26}Al and come to the conclusion that only a shallow magma ocean could have existed on a Vesta sized body. Šrámek *et al.* [2012] use the formalism of Bercovici *et al.* [2001] and Bercovici & Ricard [2003] to compute metal segregation in planetary embryos. As they use two-phase flow equations, those authors consider solid and liquid silicates and solid iron to be the matrix phase, liquid iron being the mobile fluid phase. The present study uses a similar formalism but makes the opposite choice: it is assumed that liquid iron remains attached to the matrix along with solid iron and solid silicates, and that the mobile fluid phase is the liquid silicate. As long as one considers that metal and silicates have limited chemical interactions and that the heat sources contained

in metal are negligible, the consequences of the upward migration of liquid silicates on the composition should not be affected by the fact that metal segregates or not.

The work presented in this chapter aims to quantify the impact of melt migration on the composition and mineralogy of the rocks that finally crystallize. First, the set of equations used to describe melt migration is recalled. The details of the numerical methods used to solve these equations may be found in Appendix B.1.1. The solution of the velocity equation is compared to an analytical solution. The transport of liquid is compared to draining experiments from [Ricard *et al.* , 2001]. The numerical model of liquid migration is used to assess the impact of the ratio of the size of the body to the compaction length. The heat equation is presented in section 3.4 and its numerical solution is given in appendix B.1.3. The coupling between the dynamics and thermodynamics is illustrated through use of an equilibrium phase diagram. Results are shown for bodies with the size of Vesta composed of a binary mixture of anorthite and a more refractory component.

The effect of ^{26}Al migration demonstrated by former studies is reproduced. However, the equations considered are not suited to describe the homogeneization and cooling of the shallow magma ocean obtained. A method is proposed to account for these effects. In parallel, the binary system is replaced by an olivine-anorthite-silica ternary phase diagram as a potential analogue for the HED based on previous experimental melting studies. A method based on mineral-melt partition coefficients is proposed to predict the Rare Earth Element (REE) concentrations of the modelled rocks. Simulations are presented as a function of the accretion time, the initial composition and melt/solid viscosities. The stability of the model is tested by changing the spatial resolution and the finite difference scheme. The impact of the parameters used for the cooling of the magma ocean are discussed. In light of these results, the implications of the model are discussed for the scenario of differentiation of Vesta and its internal structure.

3.2 Melt migration - Compaction equations

Various approaches exist to model multicomponent flow. For instance, phase field methods, interface capture or tracking methods aim to describe fluid flow at the mixture scale, where the various phases remain spatially discernible. Such approaches cannot be used to describe multi-phase flow inside systems whose characteristic size (typically $\sim$km in Earth and planetary sciences) is several orders of magnitude larger than the grain/pore size (μm - cm). An alternative approach is based on the averaging of the classical conservation equations [Drew & Passman, 1999]. Instead of locating each parcel of the phase, all the quantities are averaged over a control volume. The control volume must be large enough to contain a sufficient number of grains or pores but small enough to solve gradients and not violate the continuum limit δV [Drew & Passman, 1999]. The properties of phase i are averaged using the function θ_i, a distribution function which is 1 inside the phase i and 0 elsewhere. The volume fraction of each phase can thus be defined as:

$$\phi_i = \frac{1}{V}\int_{\delta V} \theta_i dV \tag{3.1}$$

where δV is the total volume of an element of mixture. An immediate consequence is that the sum of the volume fractions ϕ_i has to be equal to 1, as no void spaces are allowed ($\sum \phi_i = 1$). The velocity of phase i averaged over its volume is $\mathbf{v}_i$, is defined such that:

$$\phi_i \mathbf{v}_i = \frac{1}{V}\int_{\delta V} \tilde{\mathbf{v}}_i \theta_i dV. \tag{3.2}$$

Under the assumption of incompressibility, the true velocity $\tilde{\mathbf{v}}_i$ is solenoidal ($\boldsymbol{\nabla} \cdot \tilde{\mathbf{v}}_i = 0$). However, this is not true for the average velocity $\mathbf{v}_i$ since it has been averaged over pore

or grain volumes, which are variable in space and time. Note that $\mathbf{v}_i$ is the interstitial velocity, while $\phi_i \mathbf{v}_i$ may be seen as the filtration velocity.

Following this theoretical framework, Bercovici *et al.* [2001] and Bercovici & Ricard [2003] proposed a set of equations for a two-phase mixture. The model is based on the following assumptions that i) each phase is incompressible, ii) inertia and acceleration are neglected, i.e. forces are always in balance, iii) the two-phase mixture remains isotropic, i.e. pores and grains do not collectively elongate in a preferred orientation. The separation between fluid and matrix can be computed by combining a set of two advection equations, which satisfy mass conservation and two equations describing the interaction between the fluid and the matrix, which satisfy the conservation of momentum.

The conservation of mass can be written as:

$$\frac{\partial \phi_i}{\partial t} + \boldsymbol{\nabla} \cdot (\phi_i \mathbf{v}_i) = \frac{\Gamma_i}{\rho_i}, \tag{3.3}$$

where Γ is the melting/crystallization rate, ρ_i is the density, subscripts i respectively refers either to the fluid (f) or matrix (m). Liquid silicate components belong to the fluid phase, while solid silicates, metal and sulfide, whether solid or liquid belong to the matrix. The following chemical components: olivine (ol) , pyroxene (px), anorthite (an), metal (met), sulfide (sulf), and a set of Rare Earth Elements (REE) will be considered in the final coupled form of the model. Note that the right hand side of this equation corresponds to the production/consumption of a volume fraction of one of the phases per unit time. Here we neglect the density contrast between the solid and liquid phases, to avoid changes in volume. The density contrast between solid and liquid is only taken into account in the source term of the velocity equation.

Similarly, the conservation of momentum of each dynamic phase (either fluid or matrix) can be written as:

$$-\boldsymbol{\nabla}[\phi_i P_i] + \boldsymbol{\nabla} \cdot \phi_i \boldsymbol{\tau}_i - \rho_i \phi_i \mathbf{g} + \mathbf{h}_i = 0 \tag{3.4}$$

where $\mathbf{g}$ is the gravitational acceleration, P is the volume averaged pressure, and $\boldsymbol{\tau}$ is the volume averaged viscous stress tensor. $\mathbf{h}_i$ is the interaction force between the phases, which for the fluid and matrix are written as:

$$\mathbf{h}_f = c\Delta v + P^* \boldsymbol{\nabla}\phi + \boldsymbol{\nabla}(\sigma\alpha) \quad \text{and} \quad \mathbf{h}_m = -c\Delta v - P^* \boldsymbol{\nabla}\phi + (1-\phi)\boldsymbol{\nabla}(\sigma\alpha) \tag{3.5}$$

where c is an interaction coefficient that can be related to the permeability law $k(\phi)$ by $c = \mu_f \phi^2 / k(\phi)$. P^* is the pressure at the interface between the two phases. σ is the surface tension and α is the interface area density. If surface tension is neglected, the combination of the two conservations of momentum leads to the following action-reaction equation:

$$\mathbf{v}_m = \frac{k(\phi)}{\mu_f} \left[-\boldsymbol{\nabla}[(1-\phi)\Delta P] + (1-\phi)\Delta\rho\mathbf{g} + \boldsymbol{\nabla} \cdot [(1-\phi)\boldsymbol{\tau}_m] \right] \tag{3.6}$$

where v_m is the matrix velocity, μ_f is the fluid viscosity. This equation describes the equilibrium force between a highly viscous solid matrix and a low viscosity fluid. Since there are five unknowns, $\mathbf{v}_f$, $\mathbf{v}_m$, P_m, P_f and ϕ, a closing relation is required. Bercovici *et al.* [2001] derive the relation between pressure difference and velocity from considering damage and surface tension in the energy equation:

$$\Delta P = -\frac{\mu_m + \mu_f}{\phi} \boldsymbol{\nabla} \cdot \mathbf{v}_m. \tag{3.7}$$

Replacing ΔP in equation 3.6 and assuming $\mu_m + \mu_f \simeq \mu_m$ enables recovering equation (20) from [Šrámek *et al.* , 2012]:

$$\mathbf{v_m} = \frac{k(\phi)}{\mu_f} \left(\boldsymbol{\nabla}[(1-\phi)\frac{\mu_m}{\phi} \boldsymbol{\nabla} \cdot \mathbf{v}_m] + (\overline{\rho} - \rho_f)\mathbf{g} + \boldsymbol{\nabla} \cdot [(1-\phi)\boldsymbol{\tau}_m] \right). \tag{3.8}$$

The full development of this equation in 1D spherical coordinates leads to:

$$v_m = \frac{k(\phi)\mu_m}{\mu_f}\left[\frac{\partial}{\partial r}(1-\phi)\left[\frac{1}{\phi}+\frac{4}{3}\right]\frac{1}{r^2}\frac{\partial r^2 v_m}{\partial r} + \frac{4v_m}{r}\frac{\partial \phi}{\partial r} - \frac{(\overline{\rho}-\rho_f)g}{\mu_m}\right]. \quad (3.9)$$

The permeability law is defined here as $k(\phi) = k_0 K$, where $K = \left(\frac{\phi}{\phi_0}\right)^2$, $k_0 = \frac{a^2\phi_0^2}{72\pi}$, where a is the grain size. $a^2\phi^2/(72\pi)$ is the classic permeability law considered and corresponds to the description of connected melt tubes. It is conserved in the following of this chapter. Note that other geometries may be considered, for instance, in the case of connected melt films, the permeability law becomes $a^3\phi^3/648$ [Schmeling, 2000, p9]. The compaction length is defined as $L_c = \sqrt{\mu_m k_0/\mu_f}$. Defining a variable $F = (1-\phi)\left[\frac{1}{\phi}+\frac{4}{3}\right]$, then using K and F to rearrange equation 3.9, one obtains:

$$KL_c^2\frac{\partial}{\partial r}\frac{F}{r^2}\frac{\partial r^2 v_m}{\partial r} + \left(KL_c^2\frac{4}{r}\frac{\partial \phi}{\partial r} - 1\right)v_m = KL_c^2\frac{(\overline{\rho}-\rho_l)g}{\mu_m}. \quad (3.10)$$

Non dimensional form of the action-reaction equation

Lengths can be normalized by the body radius R, such that the non-dimensional radius is $r' = r/R$. Two characteristic times are involved in the non-dimensionalization of the action-reaction equation. The first, the Darcy time, is the ratio of the length the fluid has to get through, to the filtration velocity. The latter is itself defined as $V_D = \delta\rho g k_0/\mu_f$. The second, τ_C, is the characteristic time of matrix deformation, defined as the time required to deform the matrix under the effect of the pressure gradient.

$$\tau_C = \frac{\mu_m}{\delta\rho g R} \quad \text{and} \quad \tau_D = \frac{R}{V_D} = \frac{\mu_f R}{\delta\rho g k_0}. \quad (3.11)$$

Of particular interest is that the ratio of the two characteristic times corresponds to the square of the ratio of the compaction length to the body radius $\tau_C/\tau_D = (L_c/R)^2$. Since gravity is proportional to the radius of the body, it is also worth noting that the Darcy time is independent of the size of the body, whereas the compaction time decreases as the square root of R. Thus, in the case of a porous flow dominated regime, the characteristic time for draining liquid will not be controlled by the radius of the body. However, if the deformation of the matrix is the dominant mechanism and all other parameters being equal, the draining time for small bodies will be much longer than for larger bodies.

The two possible forms of the non-dimensional matrix velocity are:

$$v'_m = \frac{KL_c^2}{R^2}\left[\frac{\partial}{\partial r'}\frac{F}{r'^2}\frac{\partial r'^2 v'_m}{\partial r'} + \frac{4v'_m}{r'}\frac{\partial \phi_l}{\partial r'}\right] - K\frac{\overline{\rho}-\rho_f}{\rho_0-\rho_f}\frac{g}{g_s}, \text{if } v_m = v'_m\frac{R}{\tau_D}, \quad (3.12)$$

and

$$v'_m = \frac{KL_c^2}{R^2}\left[\frac{\partial}{\partial r'}\frac{F}{r'^2}\frac{\partial r'^2 v'_m}{\partial r'} + \frac{4v'_m}{r'}\frac{\partial \phi_l}{\partial r'}\right] - K\frac{L_c^2}{R^2}\frac{\overline{\rho}-\rho_f}{\rho_0-\rho_f}\frac{g}{g_s}, \text{if } v_m = v'_m\frac{R}{\tau_C}. \quad (3.13)$$

This latter expression can be factorized and rearranged into:

$$\frac{\partial}{\partial r'}\frac{F}{r'^2}\frac{\partial r'^2 v'_m}{\partial r'} + \left(\frac{4}{r'}\frac{\partial \phi_l}{\partial r'} - \frac{1}{K}\frac{\tau_D}{\tau_C}\right)v'_m = \frac{\overline{\rho}-\rho_f}{\rho_0-\rho_f}\frac{g}{g_s}. \quad (3.14)$$

Solving equations 3.10 and 3.3 allows calculating the fraction of liquid and solid as a function of depth and time. The production/consumption of melt requires the consideration of the conservation of energy and as described later, the use of a phase diagram. Before considering the heat equation, one may want to check the following points:

1. checking the quality of the numerical solution of the velocity equation with an analytical solution.
2. comparing the computation of advection to numerical experiments presented in Ricard *et al.* [2001].
3. comparing the characteritic time and flow regime for magmatic liquids with previous studies.

Analytical solution for the velocity equation

The validity of the numerical resolution of equation 3.10 was controlled by comparing it to an analytical solution. This is done in the case of a constant porosity profile, for which the matrix velocity equation 3.10 reduces to:

$$-L_c^2 K F \frac{\partial}{\partial r}\frac{1}{r^2}\frac{\partial r^2 v_m}{\partial r} + v_m = -K\frac{k_0}{\mu_f}(\overline{\rho} - \rho_l)g, \tag{3.15}$$

whose analytical solution, considering an impermeable surface ($v_m(R) = 0$), is:

$$v_m(r) = C\frac{\exp\left(\frac{r}{A}\right)(-r + A) - \exp\left(-\frac{r}{A}\right)(r + A)}{r^2} - Br, \tag{3.16}$$

where

$$C = \frac{BR^3}{\exp\left(\frac{R}{A}\right)(-R + A) - \exp\left(-\frac{R}{A}\right)(R + A)}.$$

Equation 3.10 is solved numerically by a tridiagonal inversion method. The discretization scheme and the tridiagonal sets are presented in appendix B.2. As shown in figure 3.1, the numerical solution of the velocity equation is solved to a precision of $\sim 10^{-6}$.

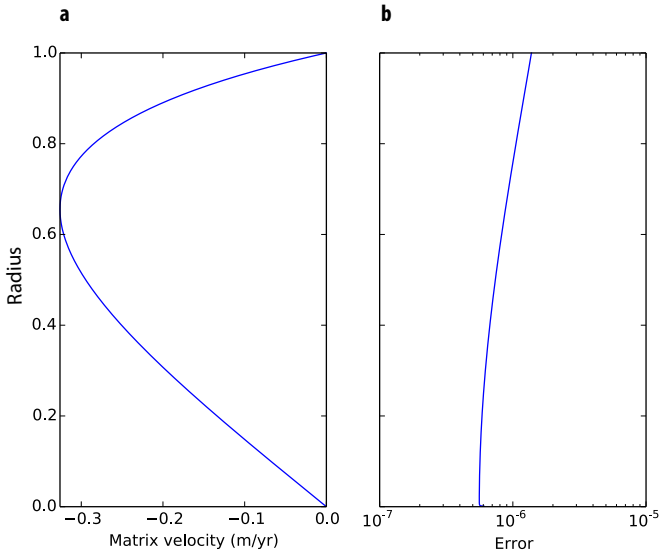

Figure 3.1: **a**: Analytical solution of the matrix velocity for a constant porosity profile (eqn 3.16), with parameters: $R = 263$ km, $\phi_l = 0.1$, $\overline{\rho}$ = 3260 kg/m^3, ρ_f = 2900 kg/m^3, $L_c = 17.3$ km and a number of radial levels $nr = 1000$. **b**: Relative error between the analytical solution and the numerical solution computed by a tridiagonal inversion using the finite difference scheme of Equation B.4.

3.3 Draining experiments

The numerical solution of liquid transport was benchmarked against two draining experiments described in [Ricard *et al.* , 2001]. The separation between a low viscosity fluid and a highly viscous matrix, under the effect of gravity, is computed for an imposed constant initial liquid fraction. The authors used a slightly different version of the action - reaction equation, taking the coefficient referred to as ω in [Bercovici & Ricard, 2003] to be equal to ϕ, changing the momentum equation to:

$$-(1-\phi)\boldsymbol{\nabla}\Delta P + (1-\phi)\Delta\rho\mathbf{g} + \boldsymbol{\nabla}\cdot[(1-\phi)\boldsymbol{\tau}_m] - \frac{c\Delta\mathbf{v}}{\phi} = 0. \tag{3.17}$$

In addition, the pressure drop between fluid and matrix is modified as:

$$\Delta P = -K_0\frac{\mu_m+\mu_f}{\phi(1-\phi)}\boldsymbol{\nabla}\cdot[(1-\phi)\mathbf{v}_m], \tag{3.18}$$

Equation 3.17 can be rearranged into:

$$\mathbf{v}_m = \frac{k(\phi)}{\mu_f}\left[-(1-\phi)\boldsymbol{\nabla}\Delta P + (1-\phi)\Delta\rho\mathbf{g} + \boldsymbol{\nabla}\cdot[(1-\phi)\boldsymbol{\tau}_m]\right]. \tag{3.19}$$

Replacing ΔP by 3.18 in 3.19 leads to:

$$\mathbf{v}_m = \frac{k(\phi)}{\mu_f}\left[(1-\phi)\boldsymbol{\nabla}\left[\frac{\mu_m}{\phi(1-\phi)}\boldsymbol{\nabla}\cdot[(1-\phi)\mathbf{v}_m]\right] + (\overline{\rho}-\rho_f)\mathbf{g} + \boldsymbol{\nabla}\cdot[(1-\phi)\boldsymbol{\tau}_m]\right] = 0, \tag{3.20}$$

whose 1D spherical developpement is:

$$\begin{aligned} v_m = \frac{k(\phi)}{\mu_f}\Bigg[\mu_m\Bigg((1-\phi)\frac{\partial}{\partial r}\frac{1}{\phi(1-\phi)}\frac{1}{r^2}\frac{\partial r^2(1-\phi)v_m}{\partial r} \\ +\frac{\partial}{\partial r}\frac{4}{3r^2}(1-\phi)\frac{\partial r^2 v_m}{\partial r} + \frac{4v_m}{r}\frac{\partial\phi}{\partial r}\Bigg) - (\overline{\rho}-\rho_f)g(r)\Bigg]. \end{aligned} \tag{3.21}$$

In [Ricard *et al.* , 2001], the compaction length L_c is defined as: $\sqrt{4\mu_m k_0/(3\mu_f)}$. Figure 3.2 shows experiments performed by [Ricard *et al.* , 2001] and the numerical solutions of equation 3.21 coupled to the solution of the advection equation computed using an explicit Runge-Kutta method presented in Appendix B.1.2. The profiles of liquid fractions and the time evolution calculated here appear coherent with the numerical simulation of Ricard *et al.* [2001]. The dependency of the flow regime on the R/L_c ratio is reproduced. When the size of the system is large compared to the compaction length, compaction waves are observed. However, when the size of the system is comparable to the compaction length, the liquid fraction is always a monotonically decreasing function of depth.

Draining time for isothermal small bodies of constant initial melt fraction

Draining experiments were performed for spherical bodies to investigate the dependencies of the time required for a liquid to reach the surface on the one hand, and to isolate the different possible migration regimes of this liquid on the other. Two characteristic times were proposed for the non-dimensional form of the matrix velocity equation 3.14, τ_D and τ_C. The compaction of a matrix of either a small body or a very viscous body would be difficult and would limit the separation of a liquid from a solid. On the other hand, the greater the permeability, or the lower the viscosity, the quicker a liquid can migrate. The

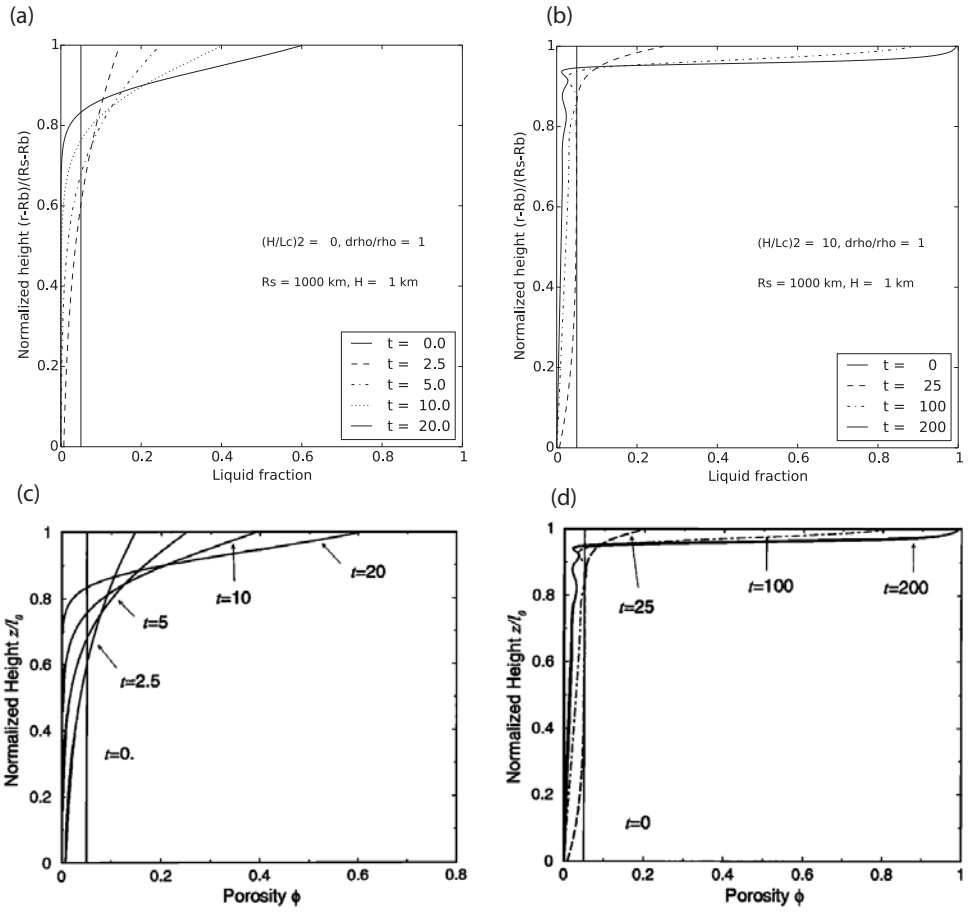

Figure 13. Porosity as a function of depth at different times for $\xi = 0$, $\lambda = 0$ and $\Delta\rho/\rho_m = 1$. The mixture is gravitationally unstable, and there is no surface tension. The matrix viscous term is dominant in the dynamics.

Figure 14. Porosity as a function of depth at different times for $\xi = 0$, $\lambda = 10$, and $\Delta\rho/\rho_m = 1$. The initial porosity is constant. The mixture is gravitationally unstable and without surface tension. Because of the presence of the Darcy term, porosity packets are generated.

Figure 3.2: (a) and (b) Draining experiments performed within an impermeable spherical shell of thickness $H = 1km$, for an external radius of 1000 km. This apect ratio is chosen in order to enable comparison with the cartesian solutions of [Ricard *et al.* , 2001]. $(H/L_c)^2 \sim 0$ (a) and $(H/L_c)^2 = 10$ (b). The initial liquid fraction is 10%. These are the numerical solution of equations 3.21 and 3.3 using the numerical methods presented in appendix B.1. Time is normalized by $4\mu_m/(3\rho 10H)$.

draining time is investigated by varying the body size, all other parameters being equal. Different initial fractions of liquid are tested, as illustrated in Figure 3.3.

When R/Lc is higher than ∼200 the draining time becomes dominated by the characteristic time for Darcy flow, and compaction waves develop. When $R/Lc < 10$ the migration of liquid is controlled by deformation of the matrix and in this case the liquid fraction is always a monotonically decreasing function of depth. For a body the size of Vesta with the parameters of table 3.1 $R/Lc \sim 125$, corresponds to the Darcy regime. For $\phi_0 = 0.1$ the draining time is ~ 6 Myr. The viscosity of the liquid silicates can be as low as 0.1 Pas as suggested by melting experiments carried out on peridotites [Dingwell *et al.* , 2004]. In this case, $R/Lc \sim 12$ and deformation becomes an important mechanism. Porosity waves do not develop in this case, the draining time for $\phi_0 = 0.1$ is ~ 0.3 Myr. Increasing the viscosity of the solid has an equivalent effect on the draining regime but the consequence on draining time is different. If $\mu_m = 10^{20}$ Pas the draining time is $\sim$

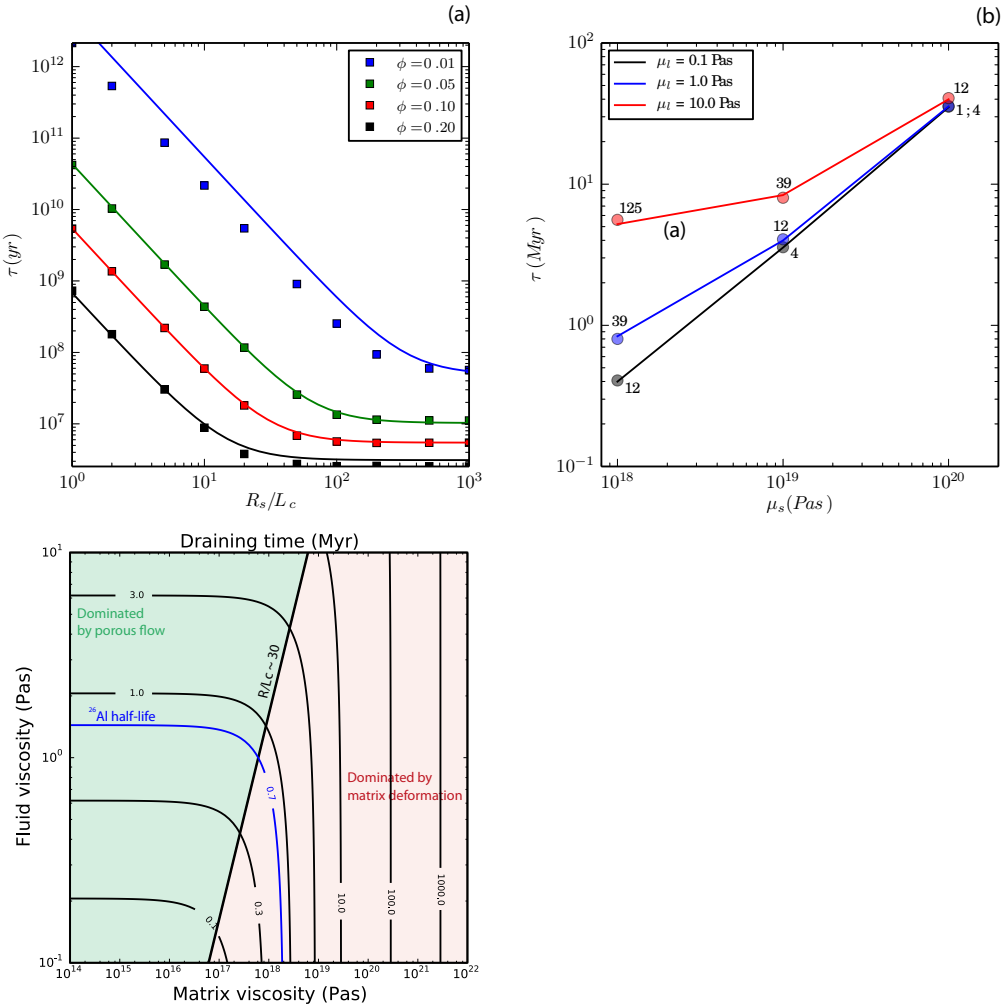

Figure 3.3: Time τ_{90} required for 90% of the volume of fluid initially homogeneously distributed inside the body to reach the surface. The initial volume of melt can be converted to a surface layer of equivalent volume, τ_{90} is the time required to fill this surface layer at 90%. Four initial fractions of melt ϕ_0 were tested, 1% (blue), 5% (green), 10% (black) and 20% (red). The solid lines correspond to $\tau \sim 28\tau_C/\phi_0 + 2.5\phi_0\tau_D$. Note that for small ratio R/L_c, the draining time is inversely proportional to $(R/L_c)^2$, the regime of migration is dominated by the deformation of the matrix and the melt fraction is always a monotonic function of depth. For larger R/L_c the draining time becomes independent on this ratio.

30 Myr. The time required to drain the body from a given fraction of liquid ϕ_0 at 90% is found to be $\tau \sim 28\tau_C/\phi_0 + 2.5\phi_0\tau_D$.

3.4 Melt production

The amount of liquid produced in a planetesimal is a function of the energy available. For small bodies with a radius less than a thousand kilometers, the energy is essentially provided by the decay of short-lived radionuclides such as ^{26}Al. Another potential heat source is ^{60}Fe which has a comparable decay energy, but the life time of this radioactive element is four times longer than that of ^{26}Al. [Castillo-Rogez *et al.* , 2009]. In addition, Quitté *et al.* [2010] show that there probably were important heterogeneities of iron isotopes in the early solar nebula and that the initial ^{60}Fe/^{56}Fe ratio of the reservoir from which angrites and eucrites originated could be as low as 2×10^{-8}, which is three orders of magnitude lower than the initial ^{26}Al/^{27}Al ratio. As a first order approximation the radiogenic heat produced by ^{60}Fe can be neglected.

The derivation of the conservation of energy of a multicomponent mixture is performed by a balance of energy exchanges across the surface of a control volume element, where the various terms consists in the sums of the contribution of each phase, and from which the expression for the temperature evolution is derived in [Ricard, 2007, p59-60]. Here the temperature evolution was derived from [Ricard, 2007, p60] by further neglecting pressure effects and viscous dissipation. Only radiogenic production ρQ, diffusion $\boldsymbol{\nabla} \cdot (k \boldsymbol{\nabla} T)$, advection and exchange of latent heat during melting/crystallisation are considered to be relevant in the energy budget:

$$\frac{DH}{Dt} = \boldsymbol{\nabla} \cdot (k \boldsymbol{\nabla} T) + \rho Q. \tag{3.22}$$

The enthalpy H is defined as $H = \rho(CT + \phi L)$, where C and L are respectively the specific and latent heats. The material derivative D is defined as: $\dfrac{D}{Dt} = \dfrac{\partial}{\partial t} + \overline{\mathbf{v}} \cdot \boldsymbol{\nabla}$.
k is the thermal conductivity and Q the heat production by radioactive decay. The ^{26}Al content of the solar nebula was reset during its condensation, but afterwards the abundance of this isotope has decayed exponentially with time, accretion time of planetesimals controlling the amount of energy available for internal heating:

$$Q(t) = C_{Al} Q_0 \exp[-\lambda_{26}(t + t_{acc})] \tag{3.23}$$

where t_{acc} is the time of accretion of the planetesimal, λ_{26} is the ^{26}Al decay constant and C_{Al} is the aluminium concentration (kg/m^3) of the material. Q_0 is the heating rate of 1 kg of aluminium when CAI formed:

$$Q_0 = \frac{\left[^{26}Al/^{27}Al\right]_0 \mathcal{A} \lambda_{26} E_d}{M_{26}}, \tag{3.24}$$

where $[^{26}Al/^{27}Al]_0$ is the initial isotopic ratio at CAI formation, $\mathcal{A}$ is Avogadro's number, E_d is the energy produced by the decay of one ^{26}Al atom and M_{26} is the molar mass of this radioactive isotope.

Note that since ρC is about the same for silicate and metal, one can expect that the term related to the advection of phases $\boldsymbol{\nabla} \cdot [\mathbf{v} \rho (CT + \phi L)]$ will be negligible, because the average velocity $\overline{\mathbf{v}}$ is null.

Correction at constant enthalpy

The latent heat term of the heat equation can be treated in an implicit fashion as implemented by [e.g. Ribe, 1985]. However, in the case of a complicated relation between temperature and melt fraction, it appears more convenient to solve the heat equation without considering latent heat first and to correct for this term when the thermodynamical

equilibrium state is computed [Katz, 2008; Šrámek *et al.* , 2012]. The latter consists in determining the fraction of the different chemical components in their liquid and solid form, and the equilibrium temperature as a function of the available energy $H = \rho(CT + \phi L)$, by using the geometry of a phase diagram.

Migration of ^{26}Al motivates the use of a binary phase diagram

As mentionned above, for small bodies heated by ^{26}Al decay, this heat source may rapidly leave the lower part of the body, which is therefore not able to significantly melt [Moskovitz & Gaidos, 2011]. As Al is a moderately incompatible element, Moskovitz & Gaidos [2011] and Neumann *et al.* [2012, 2014] use a partition coefficient to model the fact that Al preferentially integrates the liquid silicates during melting. However, Al is a major mineral forming element, which, in the case of the HEDs, is mostly contained in calcic plagioclase, i.e. anorthite, [e.g. McSween *et al.* , 2010]. This allows relating the amount of this component to the amount of aluminum,

$$C_{Al} = \rho\phi_{An}\frac{2M_{Al}}{M_{An}}. \tag{3.25}$$

which can be used to compute the heat source Q (see Equation 3.23). ρ is the silicate density, ϕ_{An} is the volume fraction of anorthite, and M_{An} is the molar mass of anorthite. A binary eutectic diagram seems appropriate to model the preferential melting of anorthite as this is the easiest phase to melt among the major minerals present in the HEDs. Toplis *et al.* [2013] derive a potential bulk composition for the HED parent body, i.e., Vesta, based on geochemical and geophysical constraints (see section 1.4.4 of the general introduction and the publication attached in appendix C. The authors use the thermodynamic calculator MELTS, [e.g. Ghiorso & Sack, 1995; Ghiorso, 2013] to show that it is possible to derive eucrite-like liquid from an H-chondrite precursor, as long as the source material is depleted in Na, consistently with former experimental studies [Jurewicz *et al.* , 1993, 1995].

The crystallization sequence of such precursor material is given in Figure 3.4**a**. The eutectic behaviour of the silicate mixture is supported by the fact that the temperature does not evolve much while the liquid fraction increases from 0 to $\sim$ 13 %, a melting degree which corresponds to the exhaustion of plagioclase from the solid. The binary eutectic phase diagram used to mimic this thermodynamic system is illustrated in Figure 3.4**b**. This binary phase diagram is made of a low temperature component, anorthite, and a more refractory component that would correspond to a mixture of pyroxene and olivine.

Technically, in the simulations presented below, the temperature is obtained by solving the heat equation 3.22. The correction at constant enthalpy is applied to compute the melt fraction. The calculation of composition at thermodynamical equilibrium, which is implemented by using the geometry of the phase diagram, is detailed in Appendix B.2. This appendix also treats the more general case of a ternary phase diagram.

3.5 Simulations of melt production - migration

The thermal evolution of a small body is sensitive to the migration of liquid silicates because they consist in a mixture of components with different melting temperatures. Of particular importance is the redistribution of plagioclase component, which carries the heat source, ^{26}Al.

Three kinds of 1D spherical simulations are performed to separate the effect of these mechanisms:

1. Melting is considered without any melt migration (see the first row of Figure 3.5).

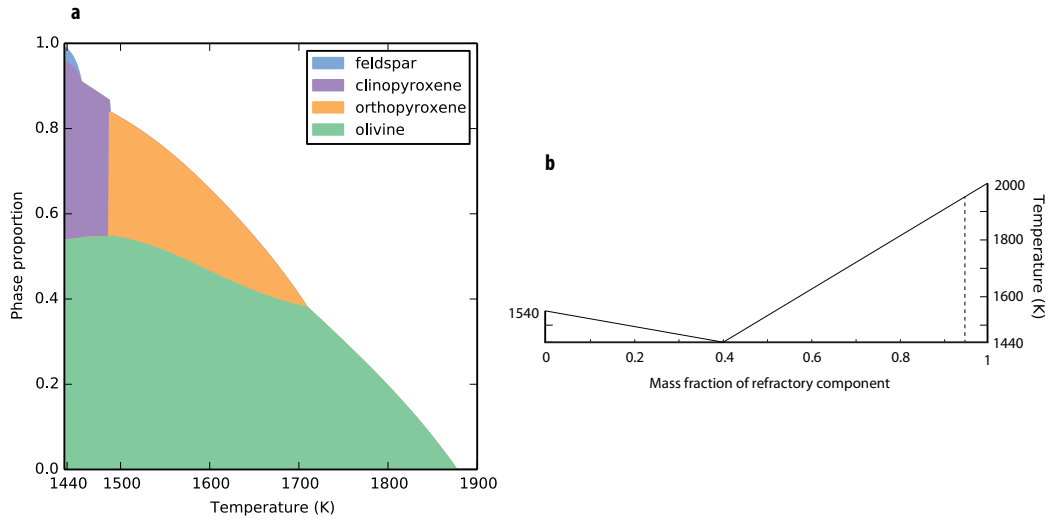

Figure 3.4: **a**: Fig. 11 from [Toplis *et al.* , 2013] "Phase proportions of liquid, olivine, pyroxene, and plagiocalse as a function of temperature prediced by MELTS for equilibrium melting/crystallization of the silicate portion of an Na-depleted H-chondrite bulk composition capable of producing Juvinas-like liquid". **b**: An anorthite - refractory component binary eutectic phase diagram proposed to implement melting in 3.5. The initial composition used is overplotted with a vertical dashed line.

2. Melting and melt migration are considered but the migration of ^{26}Al is not taken into account, i.e. the aluminium concentration, C_{Al}, is assumed to remain constant with depth (see the second row of Figure 3.5).
3. Melting, melt migration, and ^{26}Al migration are taken into account. In this case C_{Al} is obtained as a function of ϕ_{An} through Eqn. 3.25 (see the third row of Figure 3.5).

These three simulations were performed for a Vesta sized body and a time of accretion set to 1 Ma after CAI. Accretion is assumed to take place within a negligible time span. The initial amount of plagioclase was taken to be 6% [1] based on an average chondritic aluminium content [Wasson & Kallemeyn, 1988]. The presence of metal was neglected. The evolution of the temperature is given in the fourth row of Figure 3.5 for the three different model setups.

We focused on the first phases of melt migration to illustrate the consequences of the redistribution of components and sources of heat. Simulations were stopped when the global fraction of melt started to decrease (cooling phase). In the three cases, after the temperature reaches the eutectic (1440 K), liquid is produced with a composition of 60%An : 40%(Px+Ol) as dictated by the phase diagram. By mass balance, about 15% of melting is enough to remove the plagioclase from the solid. In the non static cases, an An-rich liquid migrates upward while a more refractory solid compacts downwards, altering the initial compositional profile. Anorthite is drained towards a near surface liquid layer, reaching the bottom of the thermal boundary layer. As melt migration is not instantaneous, the plagioclase component contained in the liquid remaining at depth leads to melting above the eutectic. Incidentally, the composition of the shallow liquid layer becomes less rich in anorthite than the eutectic composition. If the migration of ^{26}Al is taken into acount, the heat source ends up being concentrated within this top liquid layer. This is responsible for local overheating and thermal erosion of the conductive lid.

1. As there is no metal for these series of experiment, mass and volume fractions are equivalent.

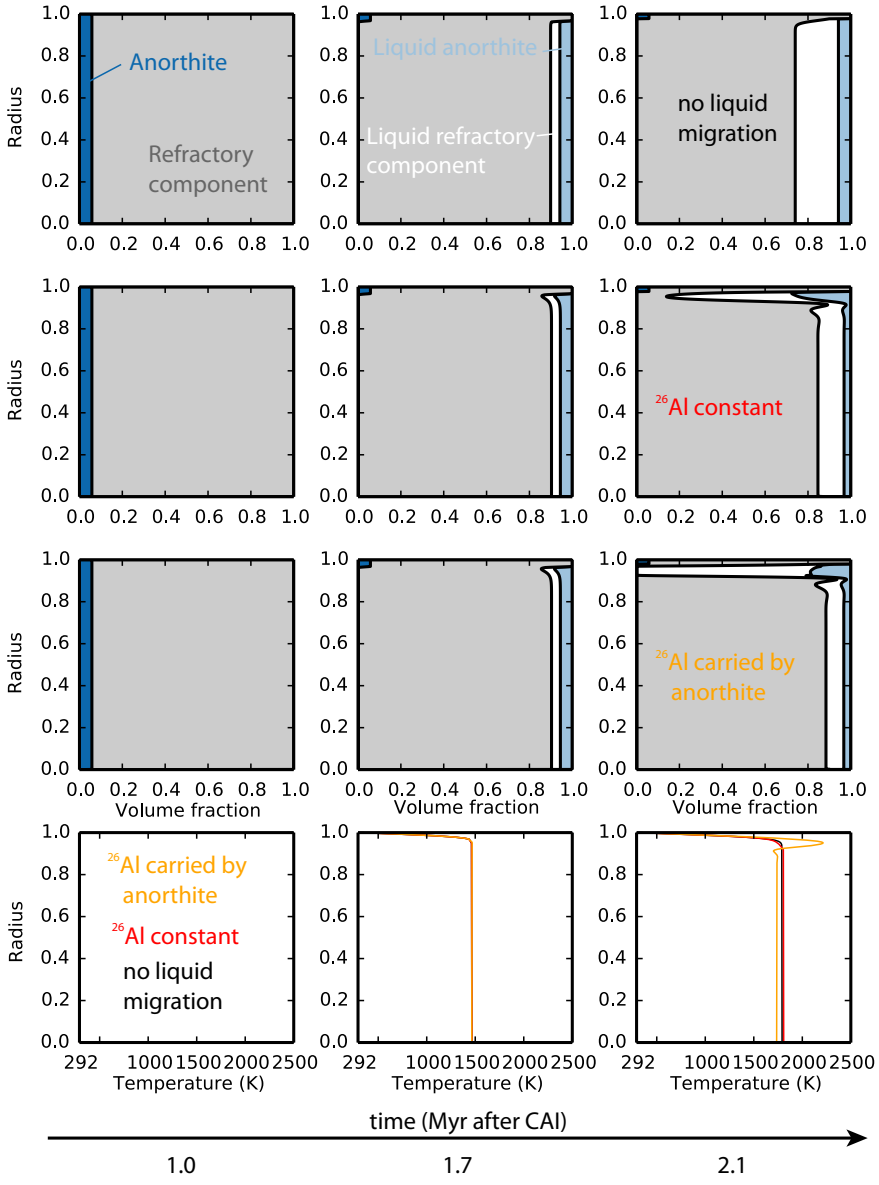

Figure 3.5: Composition and temperature as function of time for a Vesta sized body of homogeneous initial composition. The anorthite component is represented in blue (solid) and light blue (liquid). The refractory component is represented in grey and white (solid and liquid respectively). First row: Experiments without melt migration. The fraction of liquid increases with time, the anorthite is the first phase to be liquid, further melting increases the content in refractory component of the liquid. Second row: Experiment with melt migration but no redistribution of ^{26}Al. The anorthite component is rapidly concentrated in the layer where liquid accumulates. Third row: Experiment with melt migration and redistribution of ^{26}Al. Melting and melt migration are modelled and ^{26}Al migration is taken into account. In this case the concentration of the anorthite component near the surface causes local overheating as can be seen on the orange temperature profile: temperature at depth is lower than in the case of constant heat source term (black and red).

The same simulations were repeated for different times of accretion. Figure 3.6 illustrates the maximum volume of melt relative to the whole body reached during a simulation as a function of the accretion time. As expected, in all cases, the maximum melt fraction reached decreases with later accretion time because the energy available is itself a decreasing function of time. In the case of ^{26}Al migration, the removal of ^{26}Al has a dramatic effect, reducing the total melt fraction for early accretion. This result is consistent with the results of Moskovitz & Gaidos [2011].

However, the opposite is true for late accretion, the conductive surface lid which corresponds to relatively limited depth but represents an important volume fraction of the body would thicken without this concentrated supply of energy (orange curve). These simulations demonstrate that the redistribution with depth of components with different melting temperatures is much less important than the redistribution of the heat source. The fact that a refractory mantle is left behind by the migration of liquid accounts for a lower production of melt compared to the static case. The results of these simulations that take into account the migration of ^{26}Al lead to a conclusion which is similar to [Moskovitz & Gaidos, 2011; Neumann *et al.* , 2014], that is to say the migration of the heat source significantly reduces the maximum volume of silicate melting.

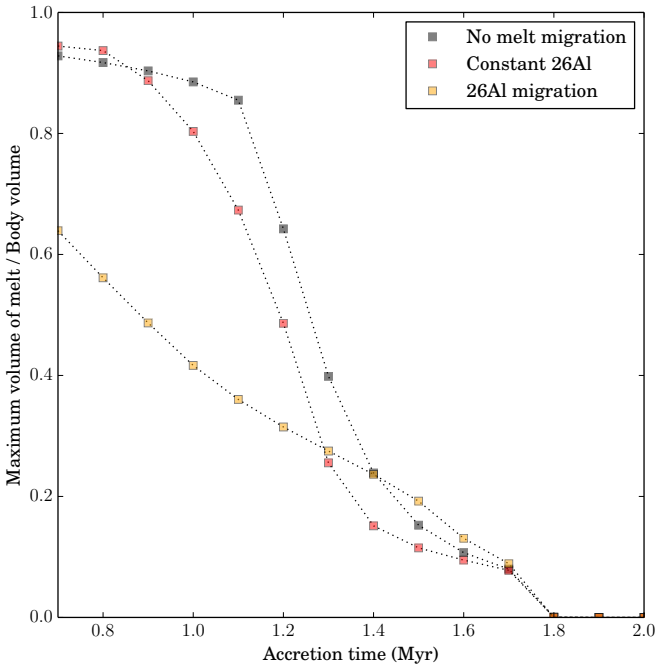

Figure 3.6: Maximum relative volume of melt produced during a simulation as a function of the time when the body accreted after the formation of CAIs. Three kinds of simulations are presented. In black the melt stayed where it was produced, in red the melt was mobile, but not the heat source, while in orange ^{26}Al migrated with the melt.

3.6 Magma ocean cooling

As just shown, when liquid moves up towards the surface, it may locally reach high concentrations and high ^{26}Al contents. The temperature calculated in the liquid rich layer (Figure 3.5) only takes into account heat transfer by conduction, but does not take into account the fact that convection is likely to occur within this low viscosity layer [Solomatov, 2007]. Convection is characterized by hot upwellings and cold downwellings that form spatially distinct features that obviously cannot be modelled in 1D. Neumann *et al.* [2014] propose to take account of the heat flux dissipated by convection, by replacing the conductivity in equation 3.22 by an effective one that accounts for this heat flux [Kraichnan, 1962; Solomatov, 2007]. The heat flux dissipated by a soft turbulent convective layer can be related to the Rayleigh number [Kraichnan, 1962] by:

$$F_{conv} = \frac{k\Delta T}{L} 0.089 Ra^{1/3}, \tag{3.26}$$

such that the effective conductivity accounting for this heat flux is:

$$k_{eff} = \frac{F_{conv} L}{\Delta T} = k 0.089 Ra^{1/3}, \text{where} \quad Ra = \frac{\alpha g \rho^2 C \Delta T L^3}{k \mu_f}. \tag{3.27}$$

α is the coefficient of thermal expansion, g the gravity, ρ density, C the specific heat, ΔT the temperature difference between the roof and the maximum temperature in the magma ocean, L the magma ocean thickness, and k the conductivity.

On the other hand, convection can maintain crystals in suspension. This is taken account of manually by assuming that the volume fractions of all components is homogeneized when the liquid fraction exceeds a critical value $\phi_l > MO_{thres}$, the latter taken at 60 % in the following.

Finally, it is likely that the solid surface loses its cohesion due to thermal expansion, impacts, or through the effect of the pressure exerted by the underlying magma ocean. This can lead to volcanism and rapid recycling of the surface [Wilson & Keil, 2012]. Here, it is proposed to make the assumption that the conductive lid is recycled into the magma ocean when the roof of the latter reaches a depth of h_{crit} = 3 km. The effect of changing the parameters h_{crit} and MO_{thres} is presented in section 3.9.

3.7 Numerical considerations

Two numerical schemes were tested to calculate the advection of liquid, an upwind scheme (see Appendix B.1.2) and a 5^{th} order WENO whose fortran implementation has been kindly provided by Henri Samuel and is described in [Samuel, 2014, A.1 p634]. Figure B.2 and B.3 in appendix B.1.2 shows the effect of increasing the number of points from 100 to 3000 for WENO and upwind schemes. WENO, which is constructed to limit the diffusive effects inherent to the upwind scheme, enables describing compaction waves. However, in 1D these waves tend to obstruct the ascent of liquid, which should not happen in 3D, due to the presence of lateral heterogenieties in permeability. The upwind scheme, which is numerically diffusive was conserved in order to avoid this effect. As far as this scheme is concerned, increasing the number of points above nr = 1000 does not seem necessary for the stability of the numerical solution, so this value is retained in the following.

3.8 Introduction of a ternary diagram

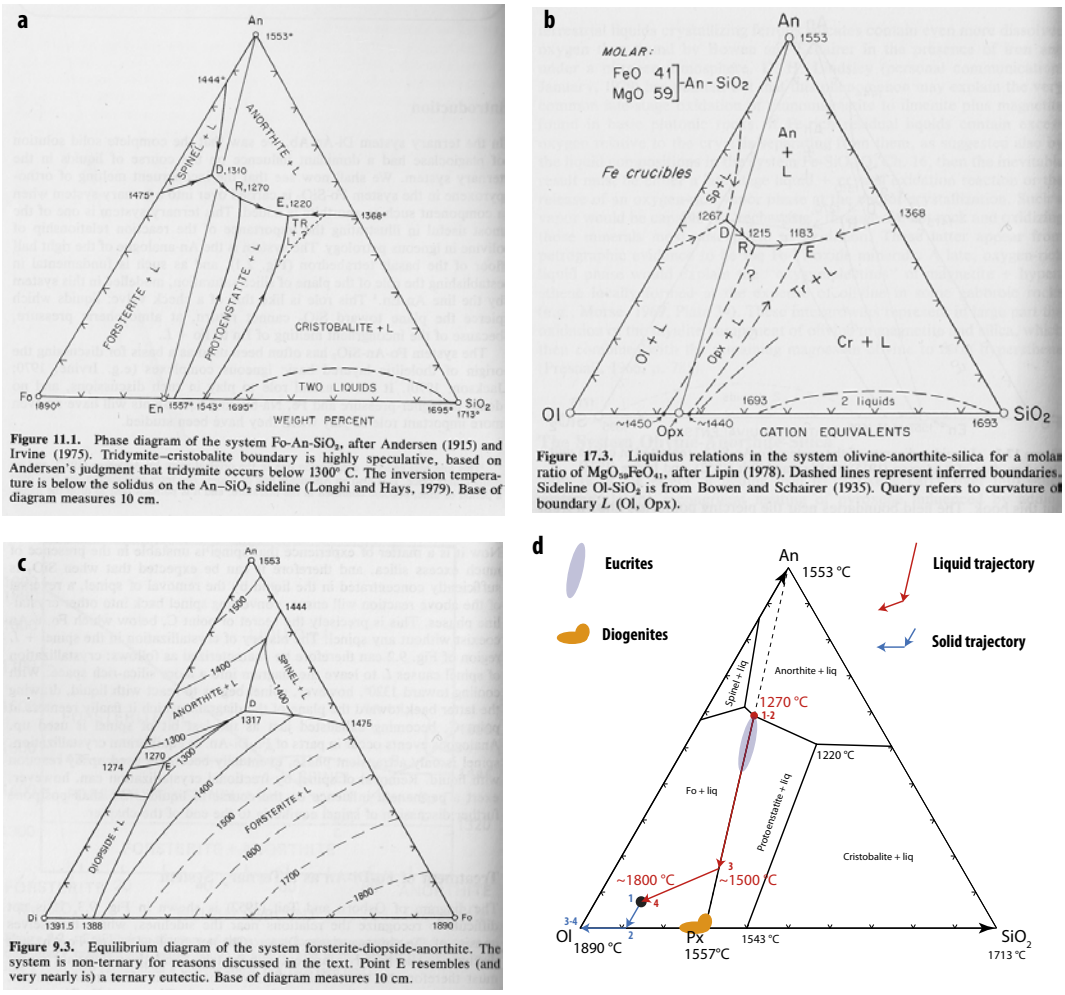

Figure 3.7: **a b c** are from Morse [1980] and references therein. **a** Forsterite-Anorthite-Silica system. **b** Olivine (Forsterite-Fayalite)-Pyroxene (Enstatite-Ferrosilite)-Silica system for a molar ratio of FeO0.41MgO0.59. **c** Forsterite-Diopside-Anorthite system. **d** Olivine-Pyroxene-Anorthite system used in this study. Eucrites and diogenites are plotted with respect to their content in olivine-pyroxene-plagioclase. The trajectory of liquid (red) and solid silicate (blue) compositions are shown for a bulk composition indicated by the black dots in the lower left corner ($\sim An_{10}Px_{40}Ol_{50}$). The first liquid produced has a eutectic composition (1) until complete exhaustion of plagioclase (2). The composition then evolves along the olivine-pyroxene cotectic line until complete exhaustion of pyroxene (3). Melting of olivine proceeds until F=100% (4).

Although the assumption of a binary diagram enables modelling the exhaustion of plagioclase and its consequences on the redistribution of ^{26}Al, it appears more than necessary to treat olivine and pyroxene as two separate phases because the presence / absence of olivine at the surface of Vesta is a matter of debate [e.g. Clenet *et al.* , 2014; Consolmagno *et al.* , 2015]. Diogenites are dominated by orthopyroxene with typical olivine content lower than 10 % and olivine bearing diogenites (harzbugite and dunites) are rare among the HED collection [Beck & McSween, 2010]. A large area of olivine rich rocks was expected in the Rheasilvia basin but it was not detected by the VIR instrument. Only small spots of olivine rich rocks of a few hundred meters across have been observed in the northern hemisphere [Ammannito *et al.* , 2013a], an observation which is not clearly understood on a petrogenetical point of view [McSween *et al.* , 2013].

The HED are marked by a strong volatile depletion notably in Na, possibly acquired by a degassing process during a magma ocean stage [Ikeda & Takeda, 1985]. Without going into the details this greatly simplifies the phase diagram for the HED, which can be described to first order within the Fo-An-Qz diagram (Figure 3.7**a**). However, the aforementionned simplification does not take into account the presence of iron in olivine and pyroxene, whereas in the HED, these phases have a molar $Fe/(Fe+Mg)$ of ~ 0.3.

Of particular interest is to note that, in the Fo-An-Qz diagram, the equilibrium line between olivine and enstatite corresponds to a peritectic, a configuration meaning that olivine melting takes place during crystallization ($Ol + liq <=> Px$). However this diagram does not take account of the presence of Fe in HED's pyroxene and olivine (see section 1.4). The addition of Fe in a Ol-An-Qz phase diagram brings the Ol-Px join closer to the An-Px join and causes a transformation of the Ol-Px reaction line into a cotectic relation ($Liq <=> Ol + Px$) (see Figure 3.7**a**). In addition, an increase in pressure to values corresponding to the internal pressure of Vesta (kbar) has a similar effect as shown by Bartels & Grove [1991]. This point is essential because it allows the possiblity that during partial melting of the mantle, after the exhaustion of plagioclase, the composition of the melt can evolve towards the Px pole thus allowing to produce significant amounts of orthopyroxenes. Furthermore, it can be seen in the Fo-Di-An phase diagram that the Px-Ol cotectic is also relatively close to the An-Px line a configuration consistent with the presence of Ca pyroxene in eucrites. Thus the simplified ternary diagram of Figure 3.7 is proposed to be used to take into account the presence of iron in eucrite and diogenite's olivine and pyroxene, the presence of Ca in eucrite pyroxene and of the effect of the internal pressure of Vesta. The liquidus surface was assumed to be linear. The correction at constant enthalpy is implemented as described in section 3.4. The method of calculation of the composition using this phase diagram is detailed in Appendix B.2.

3.9 Mineralogical models

Various series of experiments have been performed in order to assess the effect of parameters that potentially control the final mineralogy and trace element chemistry: the viscosities of the solid matrix and liquid silicates, the accretion time and the average composition. First, a reference experiment is described for a set of properties expected for Vesta. Figure 3.8 shows three snapshots of this simulation. The set of parameters used is given in Table 3.1. Vesta was assumed to be instantaneously accreted 1 Myr after the formation of CAIs. The initial composition is assumed to be an H type chondrite, as derived by mass balance [Toplis *et al.* , 2013]. The bulk composition was converted into proportions of olivine, pyroxene, anorthite, iron and iron sulfide. The influence of varying initial mineral proportions will be considered later.

During this simulation the first melt produced has a eutectic composition (58 wt%An, 42wt%Px), and reaches the surface within 1.2 Ma of CAI formation, a time at which the lower mantle experienced a melting degree of barely 10%. Eutectic melt is produced until the anorthite component is completely molten, i.e. after about 16% of melting. The migrating liquid accumulates below the conductive lid to form a liquid rich layer, which rapidly contains all the aluminum that was initially homogeneously distributed with depth inside the asteroid. In response to the depletion in heat source in the lower mantle, melt production stops at about 4.0 Myr after CAI in this particular simulation. At this point, the lower mantle olivine residue contains only a few percent of pyroxene.

In the meantime, near the surface a competition between heating by ^{26}Al and cooling by convection and melt extraction takes place. The liquid layer is fed both by the liquid coming from below and the melting of the lid due to ^{26}Al overheating. When the melt fraction reaches 60% (see section 3.6), the composition is stirred and homogenized in this convective layer, but more importantly, the surface lid is regularly recycled, which

significantly cools the magma ocean and makes it crystallize (see section 3.6). This process repeats itself until the energy provided by ^{26}Al cannot produce any further melt. When the magma ocean cools to the point where convection stops, the more refractory olivine and pyroxene crystallize at its base making the composition of the residual magma ocean evolves towards the eutectic.

The specificity of this model is that two modes of cooling take place:

1. The general conductive cooling, which is modulated by the concentration of ^{26}Al. This cooling then takes place within two conductive layers located at the top and at the bottom of the magma ocean.
2. Brutal cooling during crustal recycling of the surface lid into the magma ocean.

This last point is important because the surface preserves the composition of the last magma ocean which is able to recycle the subsurface. After the last recycling event the composition of the magma ocean evolves towards the eutectic, which is reflected by the increase in the plagioclase content as a function of depth within the uppermost basaltic layer, in the last snapshot of figure 3.8. Note that because ^{26}Al vanishes, recycling events stop at some point, which is why the composition of the magma ocean never reaches the eutectic composition.

The cooling history of the basaltic crust and pyroxenitic layer down to the harzburgitic transition with the residual dunite mantle, obtained in the reference simulation (Figure 3.8), is illustrated in Figure 3.9. In this model, basalts can be as old as 2.5 Ma after CAIs formation, which corresponds to the last recycling event. Crystallization of the base of the eucritic crust is complete by 15 Ma after CAIs formation. Rocks formed at the base of the basaltic layer ($\sim$14 km) cools below 800 °C by 25 Ma after CAI. The cooling age is a function of depth and it takes a much longer time for pyroxenitic and harzburgitic lithologies present at the base of the basaltic+pyroxenitic crust to crystallize (15 - 70 Myr after CAIs) and to cool below 800 °C (20 - $>$150 Ma after CAIs).

The use of the terms "crust" and "mantle" in the description of the simulation that was just presented, raises the question of how to employ these terms in the context of the HED's/Vesta. In the simulations presented here, the eucrites are basaltic, they are the product of liquid crystallization, and they occur at the surface. It is thus clearly appropriate to refer to them as "crustal rocks". The pyroxene-rich layer on the other hand occurs at depth and has an ultramafic mineralogy that on Earth might be associated with mantle provenance. However, in these models, this pyroxene-rich layer is also the result of precipitation from a liquid that was produced by mantle melting. If this vision of diogenite petrogenesis is correct, the diogenites are as much "crustal rocks" as the eucrites. In addition, significant proportions of olivine can be melted and crystallize at the bottom of the magma ocean. Therefore, the terms "crust" and "mantle" have to be used with caution for Vesta as these are ambiguous. The use of more specific terms such as "eucritic crust", "diogenitic crust" and "residual mantle" is proposed.

Viscosity

Classically a non dimensional approach reduces the number of parameters in the study of a phenomenon. The non dimensional number characteristic of compaction is the ratio of the compaction length to the length scale (L_c/R), which is also the ratio of two time scales: the Darcy time and the compaction time. However, a third time scale, the ^{26}Al half-life, plays a major role in the differentiation of small bodies so that the dimensionless approach loses a large part of its relevance especially as the length scale is fixed by the radius of Vesta. Since it remains important to assess independently the incidence of the variation of both former time scales compared to the ^{26}Al half-life, this requires explicit investigation of the effect of variations of the viscosities of the matrix and the fluid.

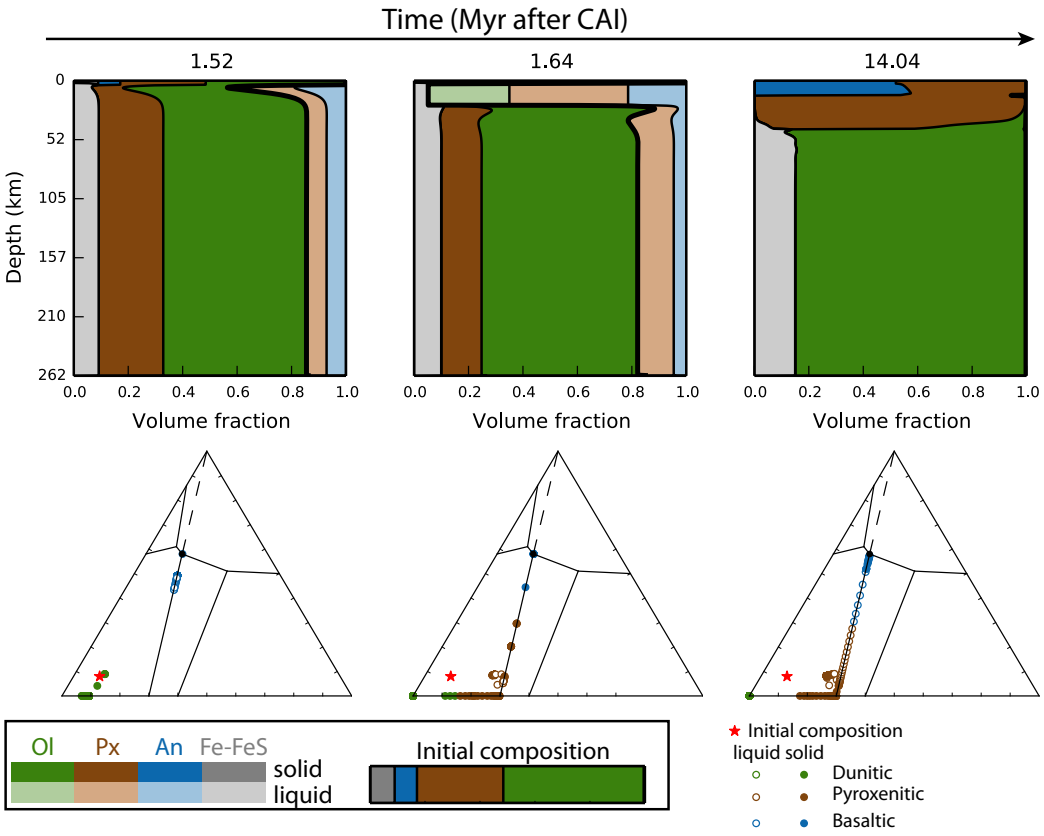

Figure 3.8: Predicted mineralogy inside Vesta as a function of depth and time. Vesta is assumed to be accreted instantaneously 1 Myr after the formation of CAIs, with an homogeneous composition. Soon after the onset of melting, a liquid rich in anorthite and pyroxene migrates upward, building a layer which accumulates below the conductive lid. Melt migration has the effect of concentrating fusible material in the subsurface region while the lower mantle enriches in refractory material. The subsurface liquid rich layer is modelled to homogenize when its liquid fraction exceeds 60% due to magma ocean convection. Overheating occurs in the subsurface region because it is enriched in anorthite which is the heat source carrier. This subsurface overheating leads to thermal erosion of the conductive lid, that is assumed to be recycled if it becomes thinner than 10 km. The competition between localized heating at ^{26}Al and cooling by surface recycling, takes place up to the decay of ^{26}Al. The more refractory olivine and pyroxene crystallize first and falls to the bottom of the magma ocean while rocks near the eutectic composition solidify in the uppermost layer (see text for details).

Dingwell *et al.* [2004] measured the viscosity of molten peridotites experimentally and showed that the viscosity at the liquidus can be as low as 0.1 Pas. Viscosities of basaltic liquids near the liquidus are typically 1 Pas [Chevrel *et al.* , 2013, 2014]. On the other hand, viscosities higher than 10 Pas are unlikely for basaltic liquids, but such viscosities are possible for more silicic melts [e.g. McKenzie, 1985]. On the other hand, the viscosity of the matrix is a strong function of temperature [Hirth & Kohlstedt, 2003; Ricard, 2007]. This important dependency is an important source of future work, that can be carried out only after investigating the already complex coupling between the dynamics of two phase flow and compositional evolution, including migration of the heat source. The nominal value of 10^{18} Pas was used here and the effect of a lower and greater viscosity on the compositional evolution was tested.

In Figure 3.10, the matrix viscosity is increased from 10^{17} to 10^{20} Pas in order to bring

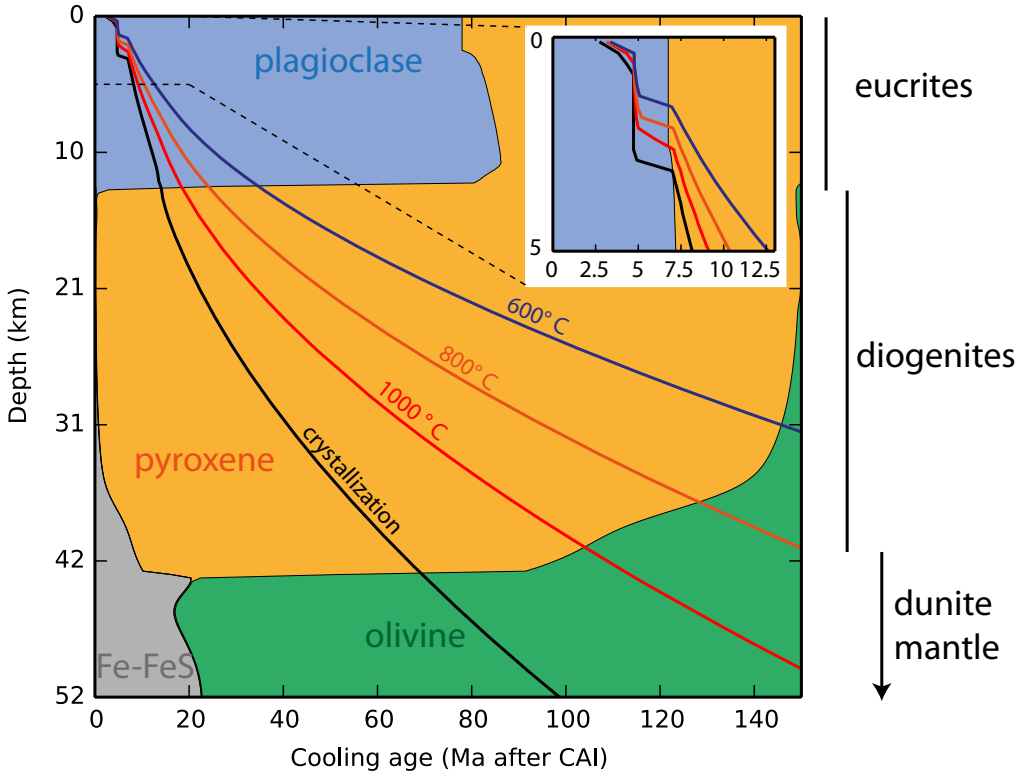

Figure 3.9: Cooling ages obtained in the crust of Vesta for the reference simulation of figure 3.8. The mineralogical structure is recalled in background with colors in terms of volume fractions of plagioclase (blue) pyroxene (orange) olivine (green) and metal (grey). The cooling age, indicated by the red profile corresponds to the last time at which the local liquid fraction becomes lower than 1 %. Oldest eucrites cool down 2.5 Ma after CAI. Diogenites crystallize for ages comprised between 15 and 50 Ma after CAIs formation.

the differentiation from the Darcy regime to the compaction regime (see Figure 3.3). This manifests itself as the loss of small compaction waves observed at low viscosity (10^{17} & 10^{18} Pas). The most important effect is an increase of the thickness of the magma ocean. This results from a longer draining time that keeps ^{26}Al in the deeper part of the body and allows more melting. In spite of the important change in the chemical composition of the magma ocean whose olivine content changes strongly, the final mineralogy is not dramatically affected.

On the other hand, the variation of the fluid viscosity does not lead to the same behaviour. In Figure 3.11, the viscosity has been varied from 10 (Darcy regime) to 0.1 (compaction regime). This leads to more rapid extraction of melt during the earliest stages of evolution. Given that Al is transferred to the first-formed eutectic liquids, this efficient removal of melt leads to greater fractions of unmolten pyroxenes in the lower mantle, but otherwise the final mineralogical stratification near the surface is the same.

In terms of compaction length, rows (b), (c), (d) of Figure 3.10 correspond to rows (a), (b) and (c) of Figure 3.11, so that increasing the matrix viscosity or decreasing the fluid viscosity brings the system from the Darcy regime to the compaction regime. However, the variations of the draining time are opposite. Furthermore in the second series of experiments the decrease of μ_f brings the draining time from more than three times to one third of the ^{26}Al half-time. These results illustrate the limit of the dimensionless approach as applied to systems involving short-lived radioactive heat sources.

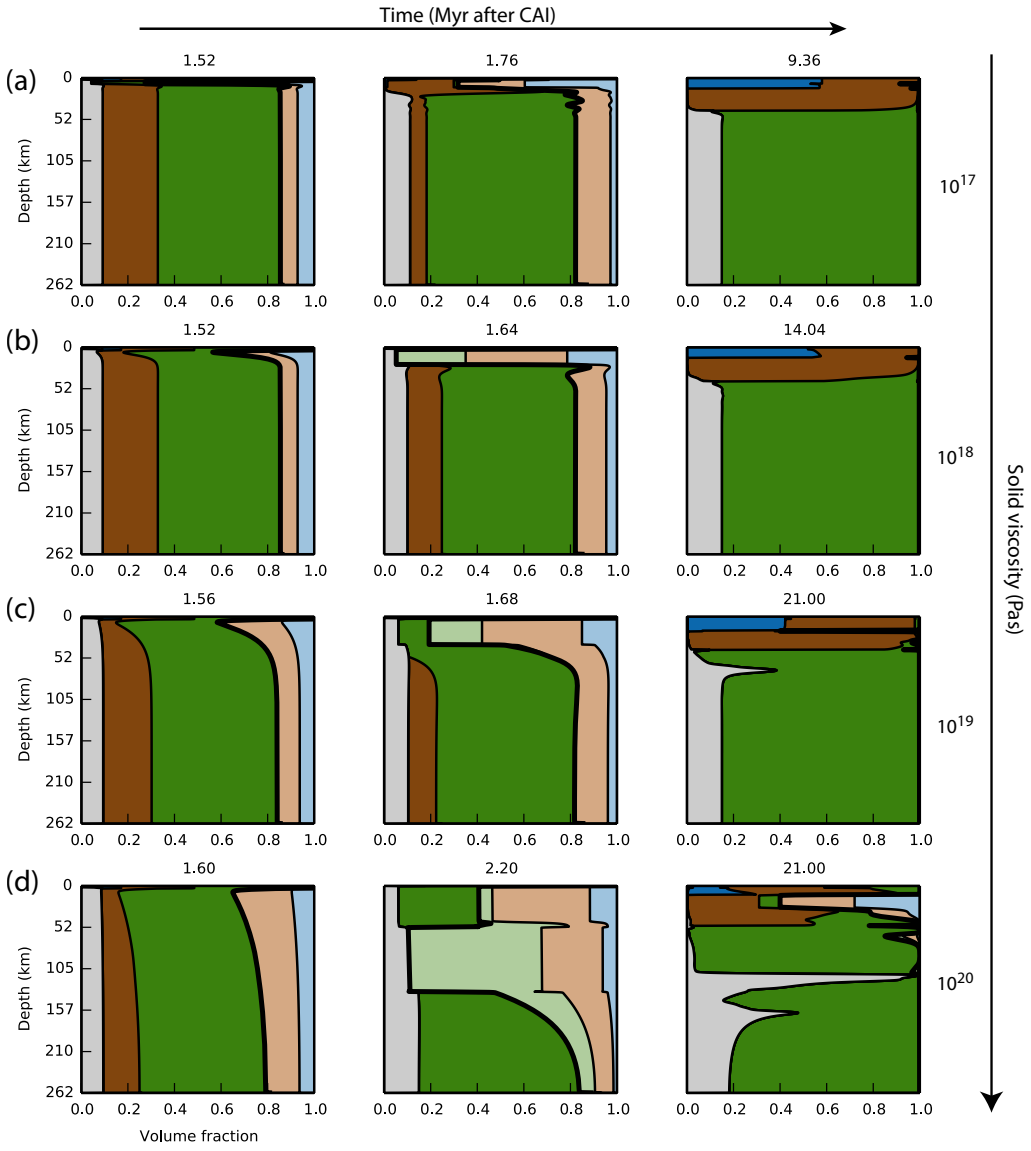

Figure 3.10: Effect of the matrix viscosity. (a) $\mu_m = 10^{17}$Pas, (b) $\mu_m = 10^{18}$Pas (c)$\mu_m = 10^{19}$Pas (d) $\mu_m = 10^{20}$Pas, ($\mu_f = 10$ Pas). Each quadrant represents the volume fractions of olivine (green), pyroxene (brown), plagioclase (blue) and metal (grey). Liquid components are represented in light colors. Time is represented from the left to the right. The first snapshot gives the state when the liquid fraction becomes greater than 0.3 near the surface. The second snapshot corresponds to the time at which maximum global melting is reached. The last snapshot gives the state when the liquid fraction becomes less than 0.05. The decrease of μ_m makes the migration time decrease, but it does not significantly affect the final mineralogical structure. However in the case of $\mu_m = 10^{20}$ Pas a thicker magma ocean form in reason of the difficult ascend of melt. This results in more fractionation and in a upper crust whose plagioclase content is lower compared to the cases where the solid is less viscous.

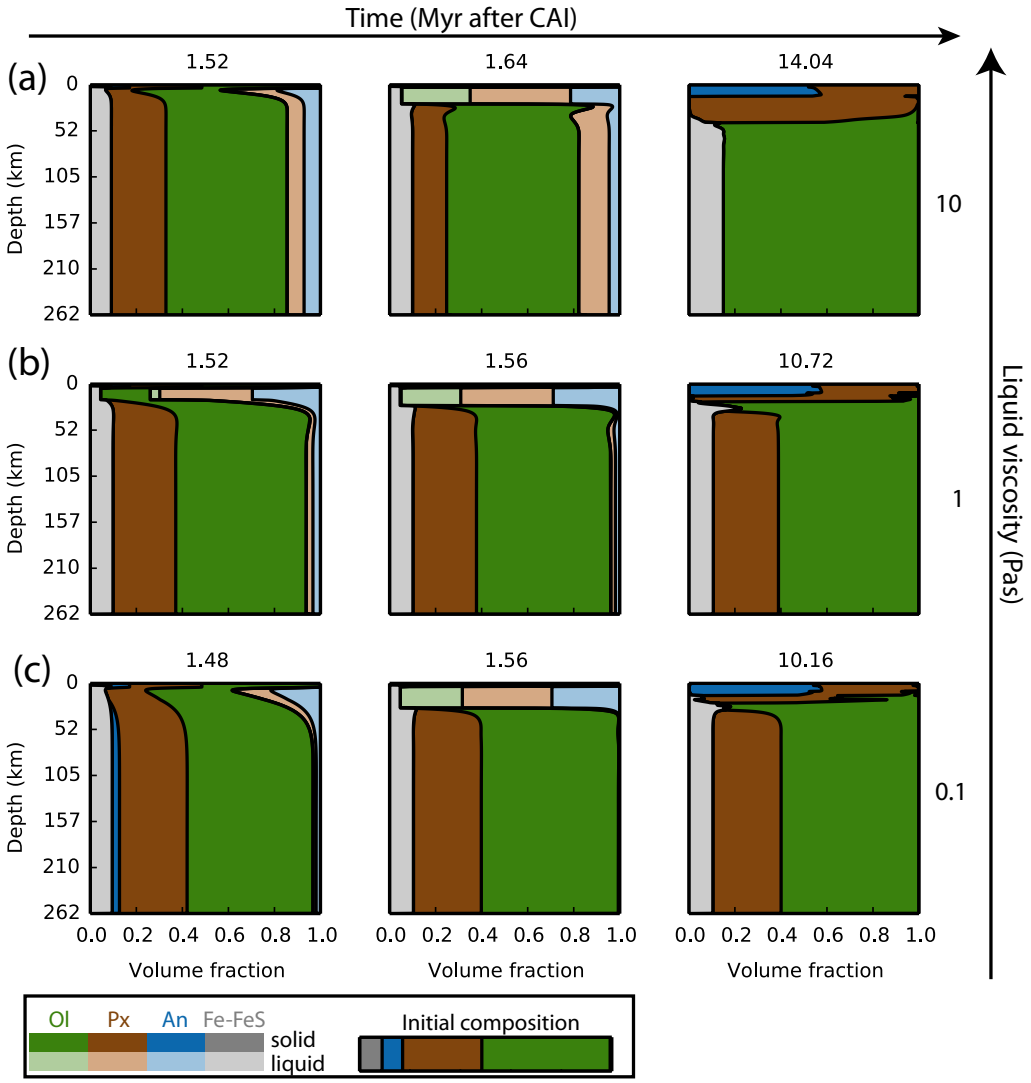

Figure 3.11: Effect of changing the liquid viscosity at $\mu_m = 10^{18}$ Pas. (a) $\mu_f = 10$ Pas, (b) $\mu_f = 1$ Pas (c) $\mu_f = 0.1$ Pas.The lower the viscosity of the liquid, the shorter is the characteristic time scale for Darcy flow, hence the faster migration of the liquid. ^{26}Al concentration near the surface is more efficient when the migration time is shorter. This limitates the melting degree in the lower mantle. The crust is thinner but the uppermost layer has always a basaltic composition.

Accretion time and composition

Another important parameter able to affect the final mineralogical distribution is of course the initial composition. Thus, two series of experiments are performed in which the initial composition is varied, one keeping the olivine content constant and a second where the anorthite content is kept constant. For each series, the accretion time is varied from 0.2 to 1.4 Ma after CAI formation. All the experiments are run with $\mu_f = 10$ Pas and $\mu_m = 10^{18}$ Pas. In all cases, the final state always consists in a superposition of three layers: a basaltic layer, a pyroxenitic layer and an olivine layer. This mineralogical structure is ilustrated in Figure 3.12 by three colors — blue where An $>$ 30 vol%, brown where Px $>$ 50 % and green where Ol $>$ 50% — as a function of accretion time for different bulk compositions.

The thickness of the eucritic part of the crust appears independent on the accretion time. The whole (eucritic+diogenitic) crust thickness which also includes a deep diogenite-like layer, follows the same behaviour, at least for accretion time less than 1 Myr after CAI formation. For later accretion, the thickness of the diogenite part decreases, because the amount of energy becomes insufficient to melt all the pyroxenes. This tendency persists whatever the composition tested, but the accretion date at which this threshold occurs, changes.

Indeed, changing the amount of plagioclase affects the amount of energy available and increasing the initial plagioclase content shifts the transition between thick to thin crust toward a later accretion time and results in a thicker eucrite-like layer. Of course, as the variations of plagioclase content are compensated for by variations in pyroxene content, the total thickness of the basaltic+pyroxenitic layer remains constant from one composition to the other. If the plagioclase content is kept constant the total crustal thickness increases with the amount of pyroxene available. However, the threshold decreases as the pyroxene increases because more energy is required to melt this quantity of silicates.

This model shows that whatever the accretion time and the global composition, the differentiation of a body of 200 km in size leads in a pile of eucritic and diogenitic crust atop an olivine rich mantle. Increasing further the global amount of pyroxene to 55% can theoretically lead to crust as thick as 80 km, as long as a high enough melting degree is reached to mobilize the entire pyroxene content up to the subsurface, but this requires an accretion time as early as $\sim$ 0.4 Ma after CAI formation.

Effect of convection threshold and thickness of recycled lid

Cooling by convection and volcanism was implemented using two thresholds to trigger these mechanisms. The values of these parameters were varied in the range of realistic values, corresponding on the one hand, to convective lockup [Solomatov, 2007] and on the other hand, to the lithosphere thickness through which magmatic liquid can be extracted [Wilson & Keil, 2012]. As shown on Figure 3.13 these parameters do not dramatically affect the final composition of the crust.

Arbitriraly imposing the convection threshold and the thickness of recycled lid does not reflect a correctly formulated physical problem and a more self-consistent approach should be implemented to treat the cooling of the magma ocean. In reality, recycling of the crust is probably continuous because even if volcanic eruptions take place in a non stationary fashion, in the form of dikes, sill like intrusions, and lava flows, recycling might be controlled by the subsidence of the lithosphere, its ability to deform, without which it is not capable of sinking. An adjustement of the boundary conditions that enable material to reach the surface and the surface to subside, i.e. a heat pipe cooling mechanism [OReilly & Davies, 1981], would be a different approach to cool down a magma ocean and is presented in the conclusive section as a perspective of future work.

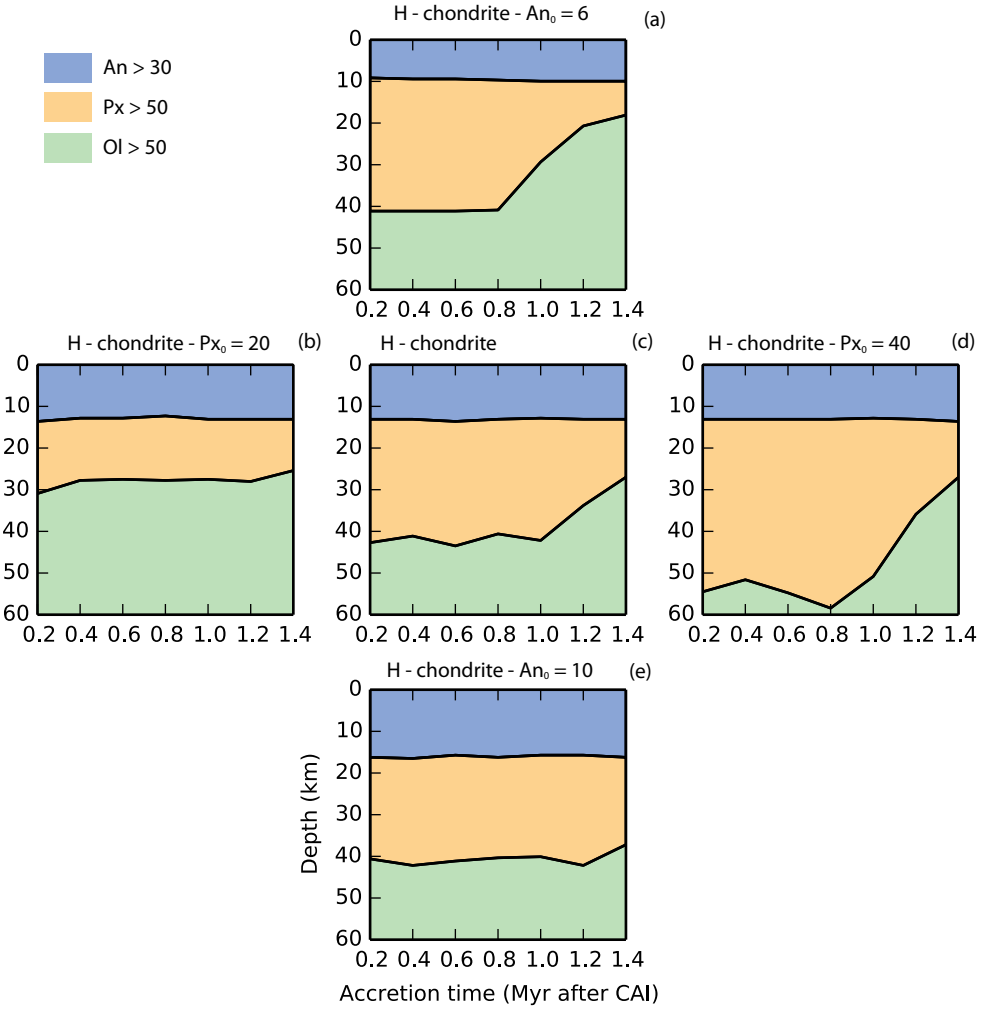

Figure 3.12: Mineralogy of the crust as a function of accretion time and composition. The central figure (c) corresponds to the composition derived from an H type chondrite from [Toplis *et al.* , 2013]. The amount of anorthite was decreased in figure (a) and increased in figure (e) at the expense of the pyroxene content. The amount of pyroxene was decreased (b) and increased (d) at the expense of the olivine content. Increasing the amount of anorthite enhances energy production, this has the consequence of delaying the accretion time after which it is not possible to mobilize all pyroxenes. Here increasing this content by 2% steps result in a shifting this transition by about 0.2 Myr. The thickness of the basaltic/gabbroic layer increases with the available amount of plagioclase. The thickness of the diogenite layer depends on the amount of pyroxene. However, obtaining a layer of pyroxenitic rocks which is thicker than in the H type case, also requires an earlier accretion time because a larger melting degree is required.

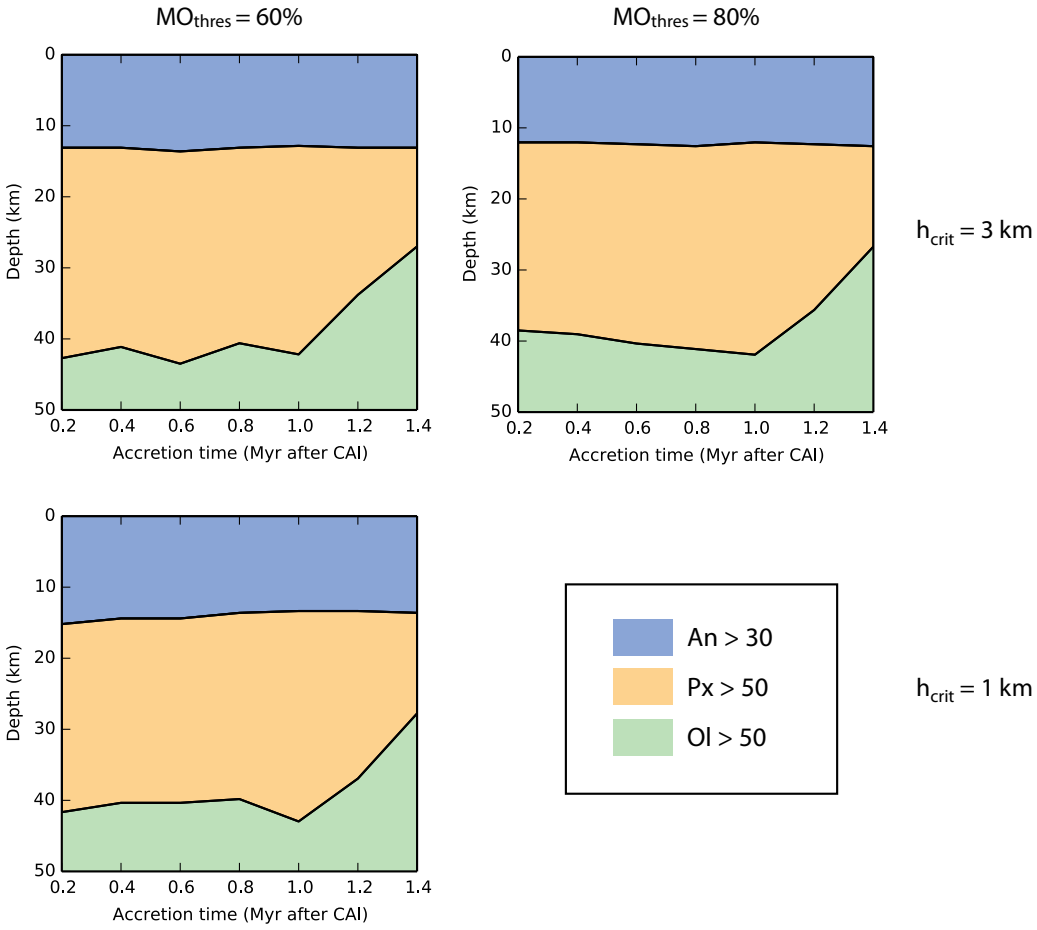

Figure 3.13: Effect of convection threshold MO_{thres} and the critical thickness of the recycled layer h_{crit} on the mineralogical structure obtained as a function of accretion time.

3.10 Rare Earth Elements

One advantage brought by the implementation of the ternary mineralogical model is the possibility of monitoring trace element concentrations. As shown in section 1.4 the decoupling between the major and trace element chemistries of diogenites is a specific characteristic of the HED meteorites that has been the subject of debate [Mittlefehldt *et al.* , 2011]. As discussed above, diogenites are dominated by orthopyroxenes and have a limited range in major element composition. In contrast to this apparent homogeniety, their trace element concentrations are highly variable from one sample to another as illustrated in Figure 1.10, which has led to a number of different interpretations, sometimes invoking the existence of different parental melts [Fowler *et al.* , 1995], hybrid melts [Barrat *et al.* , 2010] or fractional melting [Shearer *et al.* , 1997]. Monitoring trace element concentrations in the models shown above can be done using knowledge of partition coefficients between these highly incompatible elements and basaltic liquids [Schwandt & McKay, 1998]. This was done here to test the possibility that the observed diogenite variability is associated with an average vertical variability that stems from the processes modelled previously.

Trace element monitoring

The partition coefficient between a mineral i and a liquid silicate for a given incompatible trace element is defined as the ratio of the concentration of this element in the mineral to its concentration in the liquid:

$$D_{i-liq} = \frac{m_{s_i}}{M_{s_i}} \frac{M_l}{m_l} \tag{3.28}$$

m_{s_i} is the mass of the element present in mineral i, m_l is the mass of the element present in the liquid. M_{s_i} is the mass of mineral i, M_l is the mass of liquid silicate. Conservation of mass may be written as:

$$m = m_l + \sum_{i=1}^{N_{mineral}} m_{s_i} \tag{3.29}$$

Combining 3.28 and 3.29 leads to:

$$m_l = \frac{mM_l}{M_l + \sum D_{i-liq} M_{s_i}}. \tag{3.30}$$

3.11 Predicted REE concentrations

Reference simulation.

Figure 3.14 shows the evolution of REE concentrations as a function of depth for the reference simulation presented in Figure 3.8.

The first liquids produced are highly enriched in REE (with average enrichment $Er \sim$ 10 - 100) with respect to the source, the residual solid is depleted by an average factor of 10. As the magma ocean thickens, REE are diluted in this reservoir, while the lower mantle continues to deplete. The pyroxenitic layer that crystallizes from the magma ocean acquires mostly depleted concentrations ($Er \sim$ 0.01 - 0.1). The crystallization of these depleted phases make the REE concentrations increase in the residual magma ocean. Consequently, the surface lid also enriches in REEs, during successive recycling events. The

Initial volume fractions

Metal	Sulfide	Olivine	Pyroxene	Anorthite
0.05	0.04	0.52	0.31	0.08

Initial Rare Earth Element concentraions in silicates (ng/g)

La	Ce	Pr	Nd	Sm	Eu	Gd	Tb	Dy	Ho	Er	Yb	Lu
327	852	129	632	206	78	273	49	339	76	221	220	34

Partition Coefficients	**Olivine - Liquid**	**Pyroxene - Liquid**	**Anorthite - Liquid**
La	0.0001	0.0008	0.0360
Ce	0.0001	0.0022	0.0310
Pr	0.0001	0.0040	0.0280
Nd	0.0001	0.0078	0.0260
Sm	0.0006	0.0226	0.0200
Eu	0.0007	0.0084	1.1500
Gd	0.0010	0.0476	0.0160
Tb	0.0020	0.070	0.0140
Dy	0.0030	0.100	0.0130
Ho	0.0030	0.134	0.0110
Er	0.0080	0.180	0.0100
Yb	0.0190	0.206	0.0070
Lu	0.0300	0.214	0.0058

Table 3.2: Initial composition assumed for Vesta for this study derived from [Toplis *et al.* , 2013] and [Wasson & Kallemeyn, 1988]. Partition coefficients use to calculate REE concentrations are taken from [Barrat *et al.* , 2007] and reference therein.

end of the crystallization of the residual basaltic magma ocean is mostly controlled by plagioclase partition coefficients, with crystallization of high Eu anomaly eucrites at the bottom of the magma ocean and eucrites with higher enrichement toward the surface. Note that this model naturally reproduces the results obtained by Barrat *et al.* [2000] proposing in-situ crystallization as a mechanism to explain the different REE enrichments observed in basaltic and cumulate eucrites.

As illustrated in Figure 3.16, the pyroxene content has almost no impact on the final REE spectra for late accretion.

The gap observed between the spectra of diogenite-like and eucrite-like layers is filled by a range of different sloping spectra for pyroxene rich lithologies, in the case of earlier accretion (t_{acc} = 0.8 Ma / Px 20%) and the behavior of diogenite spectra becomes more chaotic for very early accretion (0.2 Ma after CAI formation). This behavior seems to be dependent on the randomness of the occurence of recycling events.

Increasing the amount of An does not significantly affect the average enrichment of the three lithological layers (eucritic in blue, pyroxenitic in brown and dunitic in green), although it makes the amplitude of the maximum Eu anomaly increase (Figure 3.15) but the details of this behaviour require further investigation.

A decrease either of the liquid or the solid viscosity results in more important fractionation within the basaltic layer (Figure 3.17). The range of REE concentrations within the pyroxenitic layer is much weaker in the case of lower liquid viscosity (1 Pas). In the case of a higher viscosity matrix (10^{19} Pas) the fractionation within the eucritic layer is limited while a range of different sloping REE spectra is obtained within the pyroxenitic layer.

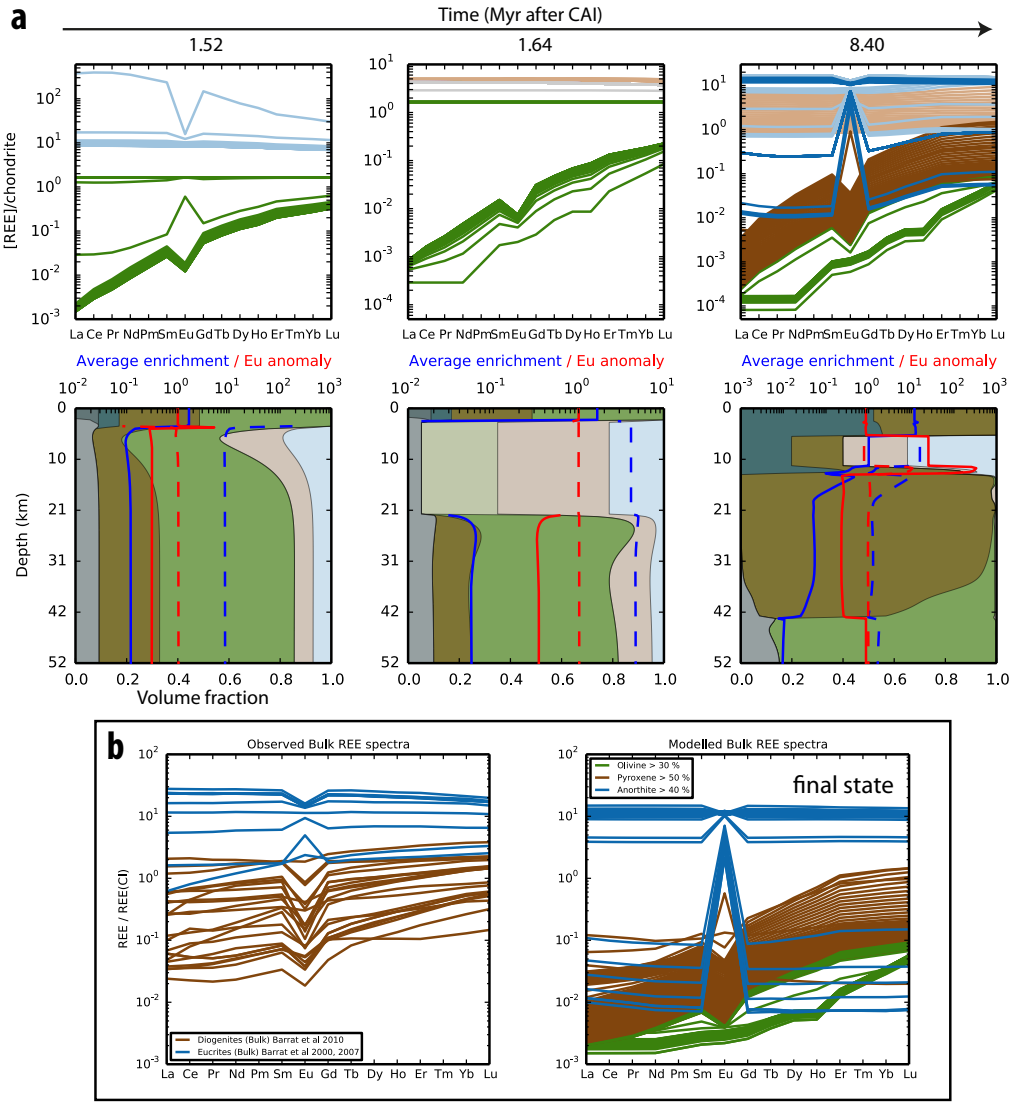

Figure 3.14: **a** REE enrichments (with resepct to CI chondrites) versus time for the reference simulation of Figure 3.8. The REE spectra shown on the first row are colored as a function of the mineralogy of the silicates (basaltic/gabbroic in blue, pyroxenitic in brown and dunitic in green), spectra shown in light colors correspond to the liquid silicates while spectra of the solid silicates are shown in dark colors. The lower row shows the mineralogical profile for the last 52 km, to concentrate on what happens to the basaltic and pyroxenitic part of the "crust". The blue line which is overplotted corresponds to the average REE enrichment of the solid silicates (solid line) and of the liquid (dashed line). Similarly the red solid and dashed lines represent the Eu anomaly in the solid and liquid silicates. For instance, this allows to highlight the important Eu anomaly of the gabbroic rocks that crystallize at the bottom of the final magma ocean (8.4 Myr after CAI). **b** Comparison between observed REE enrichments measured in basaltic and cumulate eucrites (blue data from [Barrat *et al.* , 2000, 2007] and diogenites (brown data from [Barrat *et al.* , 2010]) and the final state of REE enrichments for the reference simulation (right).

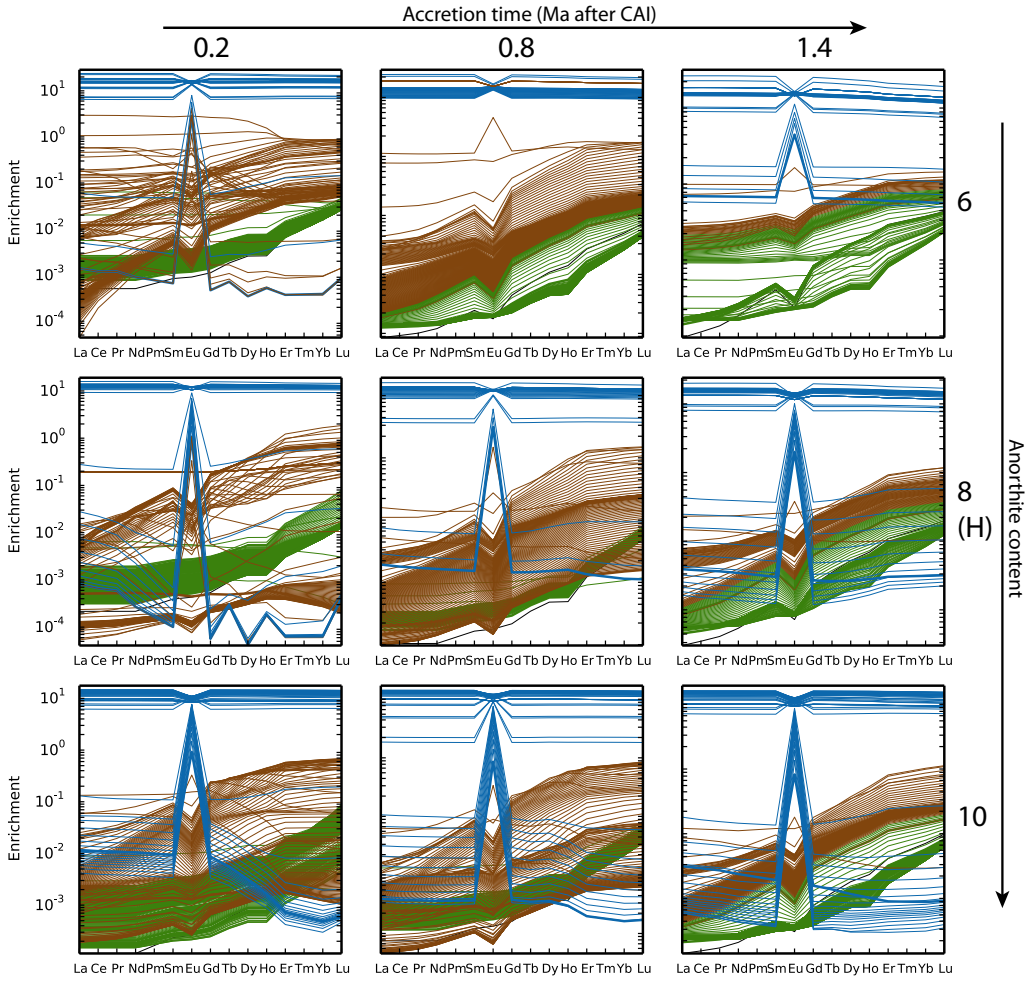

Figure 3.15: Effect of accretion time and An content on the predicted REE enrichments. Increasing the amount of An does not significantly affect the average enrichment of the three lithological layers (eucritic in blue, pyroxenitic in brown and dunitic in green), although it makes the amplitude maximum Eu anomaly increase.

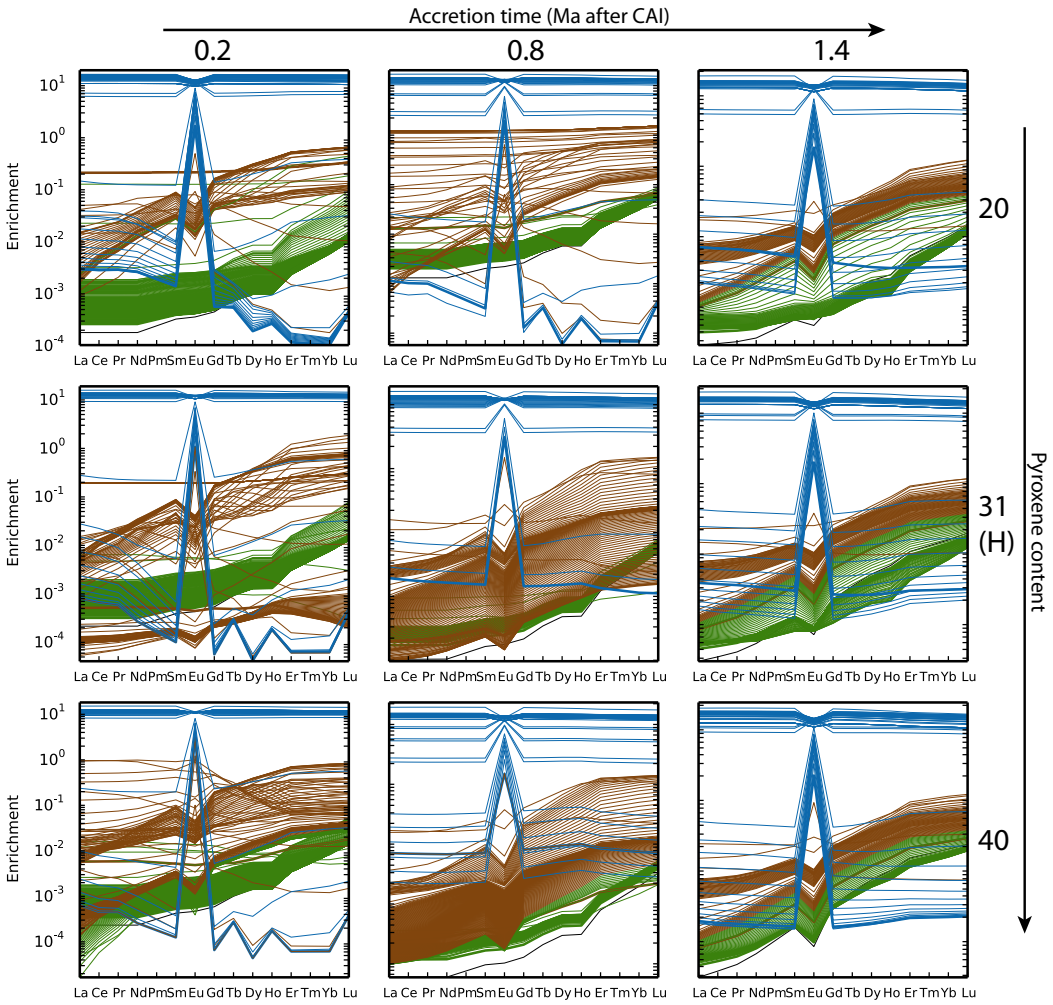

Figure 3.16: Effect of accretion time and Px content on the predicted REE enrichments. The pyroxene content has almost no impact on the final REE spectra for late accretion. The gap observed between the spectra of diogenite-like (brown) and eucrite-like (blue) layers (t_{acc} = 0.8, Px30%, Px40%) is filled by a range of different slopping spectra for pyroxene rich lithologies, which also show a range in Eu anomaly (t_{acc} = 0.8 Ma / Px 20%). The behavior of diogenite spectra is more chaotic for early accretion.

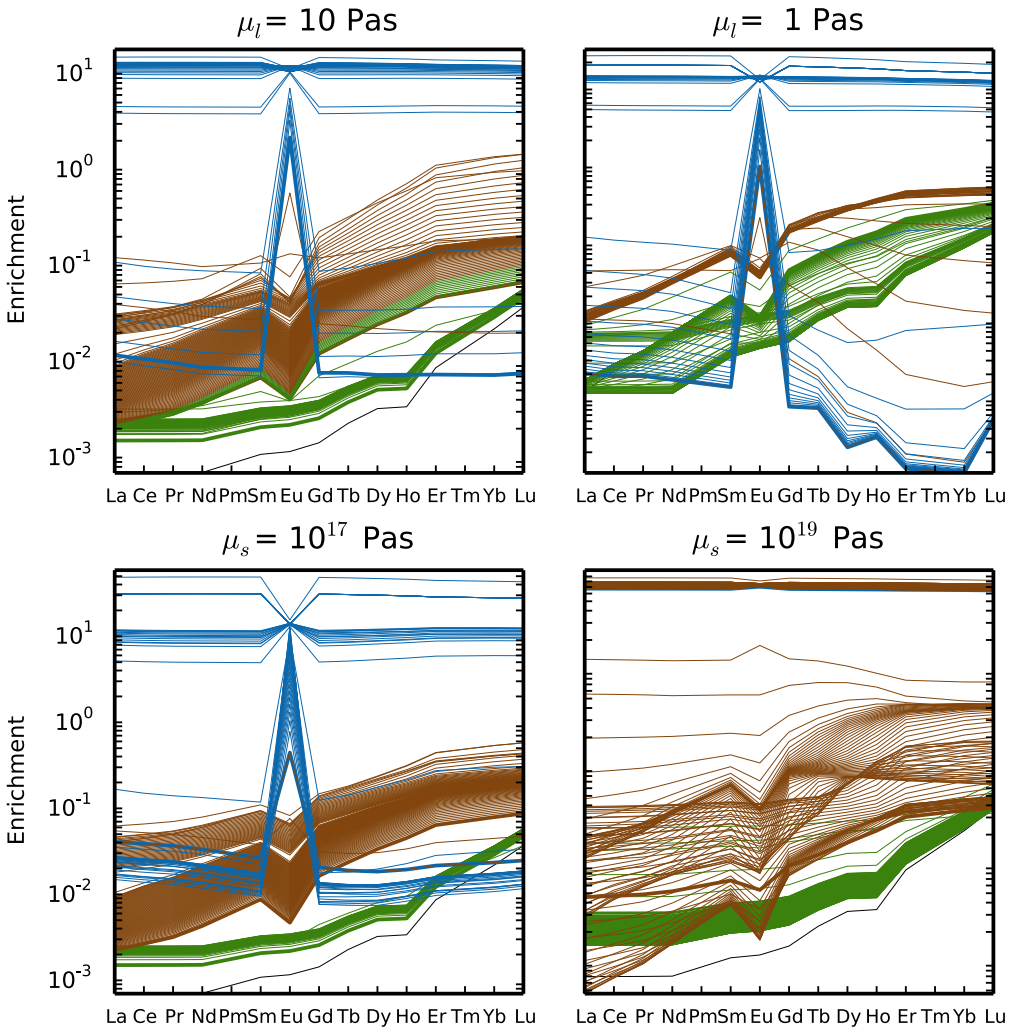

Figure 3.17: Effect of the liquid and solid viscosities on the modelled REE concentrations. A decrease either of the liquid or the solid viscosity results in more important fractionation within the basaltic layer (blue spectra). The range of REE concentrations within the pyroxenitic layer (brown) is much weaker in the case of lower liquid viscosity (1 Pas). In the case of a higher viscosity matrix (10^{19} Pas) the fractionation within the eucritic layer is limited while a range of different sloping REE spectra is obtained within the pyroxenitic layer.

3.12 Implications for Vesta and the HEDs

Among the HED meteorites, representing 5 % of the meteorite collection, some samples show anomalies with respect to the main features of the meteorite suite, notably because they differ in oxygen isotopic composition. A group of eucrites is thus interpreted to originate from a different parent body [Mittlefehldt *et al.* , 2015]. On the other hand, another group of meteorites, mesosiderites, described in chapter 1, shows basaltic components that are very similar on a petrological point of view to eucrites. This is sometimes interpreted as the fact that HED and mesosiderites may originate from the same parent body [e.g. McSween *et al.* , 2010]. High Fe abundance should be detected if Vesta was the parent body of such metal-silicate mixtures which is not the case according to analysis of GRaND's BGO spectra [Yamashita *et al.* , 2013]. Another possibility supported by this modelling is the fact that rocks that are mineralogically similar to eucrites and diogenites are a common feature of small bodies with sizes comparable to that of Vesta that accreted early in the early history of the solar system.

A global magma ocean?

According to the present study there are a range of possibilities to produce eucrites and diogenites, because the composition of the crust, i.e., the basaltic layer underlain by an orthopyroxenite layer, shows almost no dependency on the accretion time. For instance, even when the global melting degree is important and a significant amount of olivine is molten and migrates upward, olivine is fractionated first during the initial stages of crystallization of the magma ocean. The obtention of a full layering of eucrites and diogenites is only limited by the accretion time as shown in section 3.9.

This study confirms the results of previous works that invoke melt migration as a limiting factor for melt production in small bodies [Moskovitz & Gaidos, 2011; Wilson & Keil, 2012; Neumann *et al.* , 2014]. The effect of the distribution of ^{26}Al in this study can be considered as an upper bound because, in reality, chondritic plagioclase is not pure anorthite and because Al can also be present in pyroxenes. This would allow this phase to continue melting after the consumption of plagioclase. These factors may attenuate dampening of the melt production in the case of rapid melt migration (e.g. Figure 3.11), but probably not to the point that the whole lower mantle would reach global melting. On the other hand, bodies smaller than $\sim$ 100 km for which the matrix was harder to deform thus limiting two-phase flow are likelier to have completely melted.

The hypothesis of global melting, i.e. melting of all silicates to 100%, has often been supported by the homogeneity of HED O-isotopes [Greenwood *et al.* , 2014]. The shallow magma ocean predicted by Neumann *et al.* [2014] and in the present study is stirred by convection, which would also allow isotopic homogenization.

On the other hand, the global magma ocean stage is often devised as a mandatory stage to enable the formation of a metallic core which would not have been possible if a melting degree lower than 50% were not reached. Indeed, obtaining a connected network of liquid metal may require important degrees of silicate melting. This is because of the important wetting angle between droplets of liquid metal and silicates and the fact that liquid metal tends to form droplets remaining attached to olivine crystals. Here, of course the mobility of liquid metal was voluntarily not taken into account because the formalism only allows one liquid phase to be mobile. The consequences may not be important regarding the evolution of silicates as long as metal and silicates do not interact chemically. Still, the maximum melting degree reached in the lower mantle in the simulations presented here may provide some clues regarding the conditions of making a core for Vesta. Indeed, if 50 % of silicate melting is a necessary condition for the connectivity of metal, models presented here show that an accretion earlier than 0.3-0.4 Ma is required to obtain a metallic core.

The question of whether Vesta has a metallic core or not is a matter of discussion of the gravity data on the one hand, and on the constraints brought by the physics of three phase flow and silicate-metal segregation experiments on the other hand. Some gravity science is possible with Dawn by analyzing the doppler shifts that affect the signals used to communicate with the spacecraft. However, this analysis does not provide all coefficients of the gravity field of Vesta. The best constrained quantity appears to be Vesta's J2, a parameter related to the flattening of Vesta's gravity field which is mostly sensitive to the shallowest variations in density [Park *et al.* , 2014]. Dawn gravity data should be used to test if there cannot be any ambiguity between an internal structure including a fully differentiated core and a structure where metal/silicate separation is incomplete. This should be of particular relevance for future work concerning three-phase flow during planetesimal differentiation [Nishimura & Monnereau, 2015].

Chronology

The chronological inferences obtained from this modelling are broadly consistent with the data presented in section 1.4.3. The onset of Vesta's differentiation has to take place early ($<$1 Ma after CAI formation), otherwise it is not possible to make a thick diogenitic crust. Basaltic eucrites can be as old as a few Ma after CAI formation, magmatism can last for a further few tens of Ma. Even in the scenarios that were considered where the cooling is longer due to a difficult migration of the liquid, crystallization is always completed not later than 30 Myr after CAI. Modelled cumulate eucrites are younger than basaltic eucrites consistent with the ages inferred from radiochronology. Diogenites appear to be even younger, based on the fact that being emplaced at depth, they remain hot for a longer time ($\sim$100 Myr) [McSween *et al.* , 2010]. Schiller *et al.* [2011] based on ^{26}Mg-^{24}Mg data suggest that diogenite crystallization was much more rapid and complete within only a few Ma. However, another interpretation of the ^{26}Mg* ages is that they might be the consequence of Mg-Al separation after the onset of melting (because of the early exhaustion of plagioclase and migration of Al) rather than the crystallization age of the pyroxenes. As described above, early Mg-Al fractionation is a constant feature of the models presented which could thus explain the ^{26}Mg* ages. Finally, we note that the chronology of the HED's indicates that temperatures may have remained hot for up to 150 Ma after CAI formation even within the basaltic/gabbroic layer, corresponding to a slower cooling rate than in the models. The recycling mechanism implemented here may be too efficient and induce fast cooling. On the other hand, particularly low conductivity of the surface regolith could also result in slower cooling than modelled here. In any case, we stress the excellent first-order agreement between observed and modelled relative chronologies for the different HED lithologies.

In the light of Dawn

Why is olivine absent in Rheasilvia?

Ammannito *et al.* [2013a] demonstrate that olivine is not present in proportions greater than 30% in the Rheasilvia basin. On the other hand, this area should exhibit material coming from depth of 80 km based on impact simulations Jutzi *et al.* [2013]. Clenet *et al.* [2014] and Consolmagno *et al.* [2015] concluded that Vesta may not be chondritic in nautre

In the model presented here, it appers easy to extract components towards the surface and make compositions consistent with the mineralogy of eucrites and diogenites, and possibly with their trace element geochemistry. Indeed, it is not possible, simply by mass balance, to obtain a crust thicker than 40 km with an initial composition ressembling H-chondrite. Considering the effect of porosity, and/or taking into account the presence of

albite which would make plagioclase occupy a greater relative volume, cannot account for a crust that is twice as thick.

The only solution appears to be an increase of the average pyroxene content, up to 55 %. Obtaining such a thick crust would require either an early accretion time or a high aluminum content, as a higher melting degree has to be reached to mobilize more pyroxene to the surface.

It was shown that obtaining liquids that match primitive eucrite compositions, not only in terms of three mineralogical components but for a complete set of oxides, is possible from Na-depleted H-chondrite precursors [Jurewicz *et al.* , 1995; Toplis *et al.* , 2013]. A change in the initial pyroxene content might impact the ability to make eucritic like liquids, and this should be investigated.

Alternatively, Jutzi *et al.* [2013] have considered head-on impacts only. Assessing the effect of changing the incidence angle of the impactor might be interesting if it affects the excavation depth. Even if 80 km is the real excavation depth, the absence of large exposures of mantle olivine in Rheasilvia may not be enough to prove that the crust (eucrite + diogenite) was not excavated. Maybe gardening of the surface that occured after the giant impacts has covered the deepest ejecta, or has mixed the surface lithologies at a scale that does not allow VIR to detect them. Some large fragments (hundred meters scale) of olivine rich rocks occur on Vesta, but within the tongued shaped diogenite rich region (see Figure 1.17 in the introduction).

The small scale nature of plutons, according to [Clenet *et al.* , 2014] is one explanation for the appearance of olivine as local patches and not as a deep olivine rich layer. Some plutons would result from an olivine rich parent magma that rose through the crust and crystallized at shallow depth. If a significant amount of such olivine rich plutons is present, the crust can be thicker than if it is only the association of eucritic (an+px) and diogenitic (px) material, whether it be a layer of eucrites underlained by a diogenite layer, or a eucrite crust intruded by many diogenite intrusions. However, olivine spots detected at the surface of Vesta are hard to reconcile with a plutonic structure [Ammannito *et al.* , 2013a].

Finally, fragments of olivine that are related to the HED clan have recently been recovered and support the idea that the mantle of Vesta was indeed excavated [Lunning *et al.* , 2015].

Are there diogenite plutons?

Local olivine-rich spots are concentrated in a tongue shape region which extends from the Rheasilvia basin towards the North Pole of Vesta. This region could represent an ejecta blanket of diogenite rich material, stemming from the Rheasilvia impact [McSween *et al.* , 2013], or could be a region where the basaltic layer is thinner explaining why diogenites are more abundant there. This second interpretation is favoured by the correlation between positive Bouguer anomalies and diogenite concentration [Ermakov *et al.* , 2014; Park *et al.* , 2014; Raymond *et al.* , 2015].

The small scale variations of these crustal density anomalies are interpreted as the consequence of small scale intrusions, that have been proposed based upon the trace element geochemistry of diogenites [Mittlefehldt, 1994], [Fowler *et al.* , 1995], [Barrat *et al.* , 2010]. On the other hand gardening of the vestan surface may have randomly reorganized the structure of the crust down to a non negligible depth, an idea that is supported by the homogenity of the composition of the surface, which today is mostly howarditic.

The range of trace element concentrations observed in diogenites in particular their Rare Earth Element spectra, have often been interpreted as reflecting the existence of several parent magma for diogenites. As shown in section 3.11, modelled REE concentrations are broadly consistent with the main features of eucrites and diogenites although there is generally a "gap" in the REE spectra between highly enriched eucrites and more depleted

diogenites, although some simulations, (e.g. 20%Px, t_{acc} = 0.8 Ma after CAI formation, Figure 3.16) suggest that the diversity of Rare Earth element spectra in diogenites possibly stems from the complexity of the conditions of crystallization of the magma ocean, here controlled by the occurence of recycling events. This inferrence might join the interpretation from Barrat *et al.* [2010] that the diversity of diogenites REE may result from hybrid melt involving remelting of the primary eucritic crust. Furthermore, this 1D model cannot take account of the fact that recycling may not have been laterally uniform, which is another potential source of diversity.

This last point raises the question of what to expect in a real 3D world. Wiggins & Spiegelman [1995] show in 3D simulations, that 1D or 2D compaction waves are unstable and break up into sets of liquid-rich sub-spherical bulbs. Although the model presented in this study provides an average view of the composition as a function of depth. This does not exclude that plutons will develop in 3-D, especially since, given the size of Vesta, compaction waves are an important feature in the migration of liquid silicates.

3.13 Conclusion

Consistently with previous studies, heat source redistribution tends to prevent the complete melting of a Vesta sized body, even if the amount of melting is important due to very early accretion and leads to the formation of a shallow magma ocean, whose thickness is accretion-time dependent. Crustal recycling plays a crucial role during the cooling of the shallow magma ocean, which leads to the formation of an uppermost layer that tends toward the eutectic composition but never reaches it, a result which is consistent with eucrite mineralogy. The composition of the crust, which consists of a superposition of basaltic/gabbroic and pyroxenitic layer atop an olivine rich mantle is virtually independent of the accretion time.

A thick diogenite layer can be obtained only if accretion is earlier than 1 Ma after CAI in the case of an H chondrite bulk composition. The lack of broad dunitic regions in Rheasilvia basin and impact modelling suggest that the eucritic and diogenitic crust of Vesta is about 80 km thick. This would require a bulk pyroxene volume fraction of $\sim$ 55 %, and according to the presented models an accretion time earlier than $\sim$0.4 Ma after CAI.

The modelled thermal history of basaltic and cumulate eucrites and diogenites is broadly consistent with constraints brought by radiochronology, with an early onset of differentiation within 1 - 1.5 Ma after CAI, a rapid emplacement of basaltic eucrites within a few Ma after CAI, later crystallization of cumulate eucrites mostly complete by 10-20 Ma after CAI formation, diogenites crystallization complete by 10-50 Ma after CAI and a protracted thermal metamorphism lasting for a few tens up to 100 Ma after CAI. Although, the modelled thermal history of the upper crust may be fast compared to radiochronological records. This may be due to the cooling mechanism that is too efficient. For example, alternative ways to recycle the crust and/or the effects an insulating surface regolith should be considered.

The importance of crustal recycling also manifests in the success of the model to reproduce the main characteristics of the REE patterns in basaltic and cumulate eucrites. The group of diogenites with intermediate REE enrichments is not always reproduced. The conditions for obtaining a diversity in diogenites' REE seem related to the cooling conditions of the magma ocean and the detail of their behaviour requires further investigation.

Chapter 4

Conclusions and future work.

4.1 Blind source separation of BGO gamma ray spectra.

In the framework of the analysis of lunar and vestan gamma rays measured by a BGO detector, the performance of independent component analysis (ICA) and non-negative matrix factorization (NMF) was assessed, i.e. their ability to reconstruct elemental spectral shapes and the spatial distribution of elemental abundances. The association of ICA and NMF manages much better spectral and spatial reconstructions than ICA alone. The separation performance is degraded when the full set of relevant elemental spectra are mixed together because they are not all perfectly independent. For the same reason adding a background, which is strongly correlated with a number of elementary spectra, significantly reduces the performances of ICA-NMF. However, some of the elemental spectra have an strong enough 4^{th} order "contrast" that enables their separation. This explains the separation of K, Th and Fe contributions from the lunar data. The linear approximation, which is not entirely justified when compared to a physical model of gamma ray mixtures is found to be a minor problem compared to the lack of mutual independence of the source spectra. The viewing geometry does not seem to have a critical impact on source extraction as the same elements are recognized whether the analyzed synthetic datasets take account or not of the latitude dependent response function of the LPGRS instrument. The chemical variability of the observed surface is a much more critical factor. Synthetic lunar data show that if the dynamic range of element weight fractions is reduced a tenth to its real value, the separation of Fe, Th and K becomes more and more difficult and is impossible in the presence of a background if the variability is reduced only by a factor 5. This result is consistent with the fact that the vestan data show less spectral variability than the least variable lunar synthetic dataset analyzed and that no elemental signature can be clearly separated from the vestan data with the possible exception of iron. The surface of Ceres is potentially more chemically variable and possibly well suited for ICA-NMF due to the important concentrations of H at its surface and the expected variability of iron.

4.2 Future work for blind source separation on BGO spectra.

Lunar synthetic spectra provide an essential benchmark to test other BSS methods than independent component analysis. BGO datasets are neither sparse from one channel to the other because of the low spectral resolution and the presence of a Compton continuum, neither from one pixel to the other because of the spatial response function of the instrument and/or because of the characteristic size of geological units. One may want to look for representations of the signals where it is independent or sparse. Appropriate dictio-

naries (where signals are sparse) are essential parameters for the success of GMCA for blind source separation [Starck *et al.* , 2010]. The synthetic lunar data (spectra and maps) provide a guide to look for such dictionaries. A similar back and forth approach between synthetics and real data could be implemented to test and optimize the use of such tools on BGO spectra.

Two possibilities should be investigated: i) looking for the transformations where elementary spectra are sparse, using one or several appropriate transforms. If one is interested only in the spatial distribution of the sources, it is even not necessary to project sources back onto the real basis as long as the transformation does not affect the mixing process. ii) in the assumption that each channel (map of each channel to be more specific) is a linear combination of source maps, one can tranform each channel on a spherical wavelet basis and apply the separation algorithm to retrieve source maps that could match elemental maps.

4.3 Magmatism of Vesta.

This work has aimed to quantify the impact of melt migration on the composition and mineralogy of the rocks that finally crystallize, by coupling compaction equations similar to [Šrámek *et al.* , 2012] to a ternary phase diagram adapted for the HEDs, a method broadly inspired from previous studies concerning mid-ocean ridges [Katz, 2008]. In this way the fractions of liquid and solid can be calculated in space and time, the movement of the heat source ^{26}Al can be monitored, and the mineralogy of the final rocks once crystallization has taken place can be predicted. In addition, trace element concentrations can be computed using appropriate mineral - melt partition coefficients.

This model predicts that, during the heating phase, fractional melting driven by melt migration occurs while fractional crystallization takes place during cooling. Both these processes lead to vertical chemical fractionation, separating components with lower melting temperature from more refractory components. This manifests itself as a basaltic layer (eucrites) at the surface overlying a deeper and thicker orthopyroxenitic layer (diogenites), the latter displaying an important range in trace element patterns. The results of these simulations thus reproduce many of the first order features known for Vesta and/or the HEDs.

The independence of this result on the accretion time may be interpreted as the fact that eucrites and diogenites could be a general feature of early small bodies that had size comparble to Vesta. This interpretation offers an explanation to the existence of anomalous eucrites and similarities between the HEDs and baslatic components found in mesosiderites.

In addition, crust modelling is extremely relevant to the issue concerning the lack of olivine in the Rheasilvia basin of Vesta. This observation has been used to call into question simple petrological models of eucrites and diogenites based on chondritic compositions [Clenet *et al.* , 2014; Consolmagno *et al.* , 2015] despite the fact that a number of geochemical arguments support this idea [Toplis *et al.* , 2013]. The crystallization of the shallow magma ocean lead to the formation of an important volume of rocks that are dominated by pyroxenites, with an important range of REE concentrations. This offers an alternative explanation of diogenite trace element diversity that does not require multiple and hybrid parental melts [Barrat *et al.* , 2010], while it does not exclude the existence of different magma chambers.

Two notable aspects of this model are that: i) over regions where the predicted melt fraction exceeds a critical threshold (i.e. a local magma ocean), homogenization of the liquid was imposed, and ii) when such a liquid-rich layer was within a critical depth (3 km) of the surface, all the material above that depth was assumed to be instantaneously added to the melt-rich layer (i.e. the surface was recycled). This is an ad-hoc treatment for the cooling of a magma ocean. If it were not used, extreme ^{26}Al heating would take place in

the liquid rich layer leading to unrealistic temperatures. In addition, it is found that crustal recycling is an important mechanism for generating a crust with the characteristics of the HEDs in our model. This is also consistent with the involvement of metamorphism and remelting inferred from previous petrological models of the HED [Barrat *et al.* , 2010]. Following on from this study, the future work described below proposes to improve the chemical description of silicates and to implement more realistic boundary conditions for the treatment of magma ocean cooling.

4.4 Future work

4.4.1 A more self-consistent thermodynamic model

The physico-chemical model of Vesta presented here uses a ternary analogue system (forsterite-anorthite-enstatite), considered to be a first-order approximation that can provide useful insights into the behavior of the corresponding liquid-solid silicate system. In reality, however, the chemistry of eucrites and diogenites, as most rocks, is not limited to the simplified system forsterite-anorthite-enstatite and other compositional factors are likely to be important, in particular the presence of iron, leading to variable Mg#. Furthermore, the silica content of liquids produced by partial melting is very sensitive to minor concentrations of other components such as Na_2O, P_2O_5, K_2O and on the oxygen fugacity. A more consistent thermodynamic framework would help answering these questions and integrating the thermodynamic calculator MELTS developed by Ghiorso & Sack [1995]; Ghiorso [2013], to a melt migration code appears essential.

For instance, the HED meteorites are highly depleted in volatile elements such as Na and K. Eucrite plagioclase is mostly calcic, although some samples can be up to Ab_{19} [Mayne *et al.* , 2009]. Here, the assumption that Vesta was accreted from an originally Na-depleted material, allowed us to use a modified forsterite-anorthite-silica phase diagram. However, partial melting in the presence of Na leads to much more silicic melt than if this element is not present [Jurewicz *et al.* , 1995; Toplis *et al.* , 2013]. One solution to this problem is that during the magma ocean stage, i.e during the recycling events in this modelling, Na is progressively lost towards space [Ikeda & Takeda, 1985]. This idea could be tested by using a model that takes into account the presence of Na for the computation of thermodynamical equilibrium, and a surface condition which allows for loss of Na, according to the volatility of this element.

4.4.2 Modelling the end of a magma ocean

Basalts and gabbros forming the oceanic crust, as well as rhyolites or granites formed at subduction zones are some examples of the products of terrestrial magmatic differentiation. They can also be considered as the products of a permanent recycling process, which involves the cooling of the Earth, through mantle convection and plate tectonics. Alternatively, heat pipe cooling, i.e., dominated by volcanism and crustal subsidence, has been proposed as an alternative mode of cooling for the early Earth, possibly explaining some specificities of some of the oldest magmatic rocks on Earth, the Tonalite - Trondhjemite - Granodiorite suite [Moore & Webb, 2013]. Heat pipe cooling has also been proposed to dissipate Io's impressive tidal heating efficiently [Monnereau, 2002; Moore, 2003]. In that case, volcanism takes place at numerous places on the surface of the body. In return, the older crust moves progressively to deeper levels, eventually to be remelted in a region where partial melting takes place. This cooling mode may also be applicable to Vesta, because melt extraction is thought to be highly efficient on similar sized asteroids, [Wilson & Keil, 2012]. In addition, the concentration of ^{26}Al near the surface that results from melt transport [Neumann *et al.* , 2014], must have led to overheating, which probably required

an efficient cooling mechanism. For that matter, an interesting negative feedback between the viscous deformation of the sinking crust and heating by ^{26}Al of the magma ocean needs to be investigated. On the one hand, if the crust is easy to deform, recycling can take place rapidly, making heat pipe cooling efficient. This will tend to lower the temperature and to increase the viscosity, so the crust will have more difficulty to sink. On the other hand, if crustal subsidence is slowed down due to high viscosity, heat pipe cooling will be subdued, causing the magma ocean temperature to increase because of the presence of a concentrated heat source ^{26}Al. The viscosity will therefore decrease, which will make the crustal recycling easier once more. But at some point in the course of time, ^{26}Al will not be powerful enough to melt the subsiding crust again, which will stop being recycled, and the magma ocean crystallization will terminate. How many times can the crust of Vesta be recycled? What is the composition of the crust when magma ocean crystallization is complete? Study of this system would provide scaling laws between viscous deformation and radiogenic heating, improving our understanding of the differentiation of small bodies.

Chapter 5

Conclusions et perspectives

5.1 Séparation aveugle de sources de spectres gammas BGO.

Dans le cadre de spectres gamma acquis par un détecteur BGO, la performance de l'analyse en composantes indépendantes et de la factorisation en matrice non-négative a été mesurée, c'est-à-dire, leur capacité à reconstruire des formes spectrales élémentaires et les distributions spatiales des abondances élémentaires. L'association de l'ICA et de la NMF remplit mieux cet objectif que l'ICA seule. La performance de la séparation est dégradée lorsqu'on effectue le mélange de tous les spectres élémentaires, car ils ne sont pas parfaitement indépendants. De la même façon, l'ajout d'un background dégrade les performances de séparation car ce composant spectral est partiellement corrélé avec plusieurs spectres élémentaires. Cependant, certains spectres élémentaires ont des contrastes d'ordre quatre suffisamment élevés pour permettre leur séparation. Cela explique la séparation des contributions de K, Th et Fe pour les données lunaires. L'approximation de linéarité qui n'apparaît pas exacte au vu d'un modèle physique des données lunaires a un effet mineur comparé à celui des corrélations partielles entre les spectres sources. En revanche, la variabilité chimique de la surface joue un rôle majeur, comme on l'a montré à l'aide de spectres synthétiques. L'étude d'un jeu de données synthétiques pour la Lune montre que si la variabilité chimique de surface est diminuée d'un facteur dix, seule la contribution du fer peut-être reconstituée et ce, avec une faible qualité. Les données enregistrées autour de Vesta montrent moins de variabilité que le jeu synthétique lunaire le moins variable, ce qui semble expliquer le manque de séparation d'un signal clairement associable à la contribution d'un élément spécifique pour ces données à la possible exception du fer.

5.2 Différenciation magmatique de Vesta.

Le travail de modélisation présenté a eu pour but de quantifier l'impact de la migration du liquide magmatique sur la composition et la minéralogie des roches qui finalement cristallisent, en couplant des équations de compaction similaires à [Šrámek *et al.* , 2012] à l'équation de la chaleur en utilisant un diagramme de phase ternaire adapté aux HED. Cette méthode s'inspire de travaux précédents concernant les dorsales océaniques [Katz, 2008]. De cette façon les fractions de liquide et de solide peuvent être calculées en fonction de la profondeur et au cours du temps. La migration de la source de chaleur, l'^{26}Al, peut être prise en compte et la minéralogie des roches finales, une fois que la cristallisation a eu lieu, peut-être prédite. De plus, les concentrations en éléments en trace peuvent être calculées en utilisant les coefficients de partages appropriés.

Ce modèle montre qu'au cour de la phase de chauffage, la fusion fractionnée conduite

par la migration du liquide se produit alors que la cristallisation fractionnée a lieu lors de la phase de refroidissement. Ces deux processus conduisent à une stratification chimique verticale, qui sépare les composants fusibles des composants plus réfractaires. Cela se manifeste par une couche supérieure basaltique (eucritique) et d'une couche inférieur plus épaisse constituée principalement de pyroxènes (diogénitique).

La constance de ce résultat pourrait même être interprétée comme le fait que les eucrites et les diogénites sont l'expression naturelle du magmatisme sur les corps précoces de tailles comparables à Vesta. Cette interprétation offre la possibilité d'expliquer l'existence d'eucrites anormales et de certaines similitudes entre les HEDs et les composants basaltiques des mésosidérites [Mittlefehldt *et al.* , 2015].

La couche inférieure pyroxénitique modélisée peut montrer des variations importantes de concentrations en Terres Rares, en partie cohérentes avec les caractéristiques des diogénites. Cela offre une explication alternative à l'existence de réservoirs magmatiques distincts quoiqu'il n'exclut pas leur existence. Ces simulations reproduisent donc de nombreuses caractéristiques connues pour Vesta et les HED. Ces résultats sont particulièrement intéressant concernant l'absence d'olivine au niveau du bassin de Rheasilvia.

Deux aspects notables de ce modèle sont que: i) là où les fractions de liquides dépassent 60 %, l'homogénéisation du liquide était imposée et ii) quand le toit d'une telle couche atteint 3 km de la surface, tout le matériel sus-jacent est considéré comme étant recyclé dans la couche riche en liquide. Cette condition permet de modéliser le refroidissement de l'océan magmatique. S'il n'était pas mis en oeuvre un surchauffage non réaliste se produirait dans la couche riche en liquide. De plus, on trouve que le recyclage de la croûte est un mécanisme important dans l'obtention d'une croûte dont les caractéritiques correspondent à celles des HEDs. C'est peut être une nouvelle façon de voir le métamorphisme et la refusion prédite par des modèles pétrologiques [Barrat *et al.* , 2010].

Ce modèle présente des limitations, comme le fait de ne pas prendre en compte la migration du métal ou de considérer un densité constante pour les différents minéraux. Ici on propose de poursuivre le thème de la formation et de l'évolution de la croûte à travers deux possibles pistes de recherches, l'une concernant le modèle thermodynamique, l'autre le traitement de l'océan magmatique.

5.3 Perspectives

5.3.1 Vers une amélioration de l'aspect thermodynamique.

Le modèle physico-chimique de Vesta présenté ici utilise un diagramme ternaire comme analogue des HED. D'une part, en réalité, la chimie des eucrites et des diogénites, comme la plupart des roches ne se limite pas à ce système simplifié, d'autres facteurs compositionnels sont probablement importants, en particulier la présence de fer qui conduit à des Mg # variables. De plus, la teneur en silice des liquides produits par la fusion partielle est très sensible aux concentrations mineures d'autres composants comme Na_2O, P_2O_5, K_2O et la fugacité en oxygène. Un modèle thermodynamique plus complet permettrait de répondre à cette question. Pour ces raisons, intégrer le calculateur thermodynamique MELTS [Ghiorso, 2013] à un modèle dynamique comme celui développé ici apparaît comme une étape importante.

Par exemple, les météorites HED sont fortement appauvries en éléments volatiles comme Na et K. Les plagioclases des eucrites sont essentiellement calciques, même si certains échantillons peuvent atteindre 19 % d'albite [Mayne *et al.* , 2009]. Ici, l'hypothèse que Vesta a été accrété à partir d'un matériel initialement appauvri en sodium a permis d'utiliser un diagrame de phase forsterite-anorthite-quartz simplifié. Cependant, la fusion partielle en présence de sodium conduit a des magmas bien plus riches en silices qu'en l'absence de cet élément [Jurewicz *et al.* , 1995; Toplis *et al.* , 2013]. Une solution à ce

problème est qu'au cours de l'épisode de l'océan magmatique, plus précisément au cours du recyclage de la surface, le sodium est progressivement perdu vers l'espace [Ikeda & Takeda, 1985]. Cette idée pourrait être testée en utilisant un modèle qui prend en compte la présence du sodium dans le calcul de l'équilibre thermodynamique, et une condition de surface qui permet la perte de sodium selon le degrès de volatilité de cet élément.

5.3.2 Modéliser la fin d'un océan magmatique.

Les basaltes et les gabbros qui forment la croûte océanique, comme les rhyolites et les granites formés au niveau des zones de subduction, sont quelques examples des produits de la différenciation magmatique terrestre. Ils peuvent également être considérés comme les produits d'un processus de recyclage permanent qui implique le refroidissement de la Terre à tavers la convection mantellique et la tectonique des plaques. D'une façon alternative, le mode de refroidissement type "heat-pipe", c'est-à-dire dominé par le volcanisme et la subsidence crustale, a été proposé comme alternatif au mode de refroidissement de la Terre précoce, ce qui pourrait expliquer certaines spécificités des plus vieilles roches magmatique terrestres, la suite Tonalite-Trondjemite-Granodiorite [Moore & Webb, 2013]. Ce mode de refroidissement a également été proposé pour dissiper l'impressionnant chauffage par marée dont la lune de Jupiter, Io, fait l'expérience [Monnereau, 2002; Moore, 2003]. Dans ce cas, le volcanisme se produit en de nombreux endroits à la surface du corps. En retour, la croûte plus ancienne s'enfonce progressivement pour finalement être refondue dans une région où la fusion partielle a lieu. Un mode de refroidissement trés efficace, également dominé par le volcanisme a pu possiblement affecter Vesta [Wilson & Keil, 2012], étant donné l'importance de l'énergie délivrée par l'^{26}Al qui est concentré à la surface [Neumann *et al.* , 2014]. Ce refroidissement pourrait être implémenté à travers un ajustement des conditions aux limites.

Un important mécanisme de feedback négatif peut avoir lieu entre la déformation visqueuse de la croûte qui subside, et le chauffage par ^{26}Al. D'un côté, si la croûte est facile à déformer, le recyclage est facilité et le refroidissement est efficace. Ceci aura tendance à diminuer la température et donc à augmenter la viscosité, ce qui rendra la subsidence de la croûte plus difficile. D'un autre côté, si la subsidence crustale est ralentie en raison d'une forte viscosité, le refroidissement va ralentir, ce qui va conduire a l'augmentation de la température à cause de la présence d'^{26}Al. La viscosité pourra alors diminuer, ce qui rendra la croûte à nouveau plus facile à recycler. Mais à un certain point au cours du temps, l'^{26}Al ne sera plus suffisamment abondant pour continuer à fournir de l'énergie au système. Combien de fois la croûte peut-elle être recyclée? Quelle est la composition de la croûte quand la cristallisation de l'océan magmatique est terminée? D'un côté l'étude de ce système fournirait des lois d'échelles entre la déformation visqueuse et le chauffage radiogénique, en participant à améliorer la compréhension du processus de différenciation sur les petits corps. D'un autre côté, on peut comparer la composition et l'histoire thermique modélisé avec les données des HED, faisant de Vesta un cas test pour comprendre dans un cadre plus général les derniers instants d'un océan magmatique.

Appendix A

Supplementary information for blind source separation.

A.0.3 Correlation matrices

In section 2 an element recognition procedure is used to test the quality of source separation performed by ICA and ICA-NMF. This procedure is based on two correlation matrices: (1) one where the synthetic elementary spectra are compared to those reconstructed by blind source separation and (2) one where the elemental maps are compared to the maps reconstructed by BSS. An element is recognized when the spectral and spatial correlations are coherent, i.e. when the same element match the same output source both spatially and spectrally. If, in this way, an element is coherent with several output sources, the one that show the highest correlation coefficients is selected. This appendix gives the correlation matrices used for the various test realized on synthetic and real lunar data.

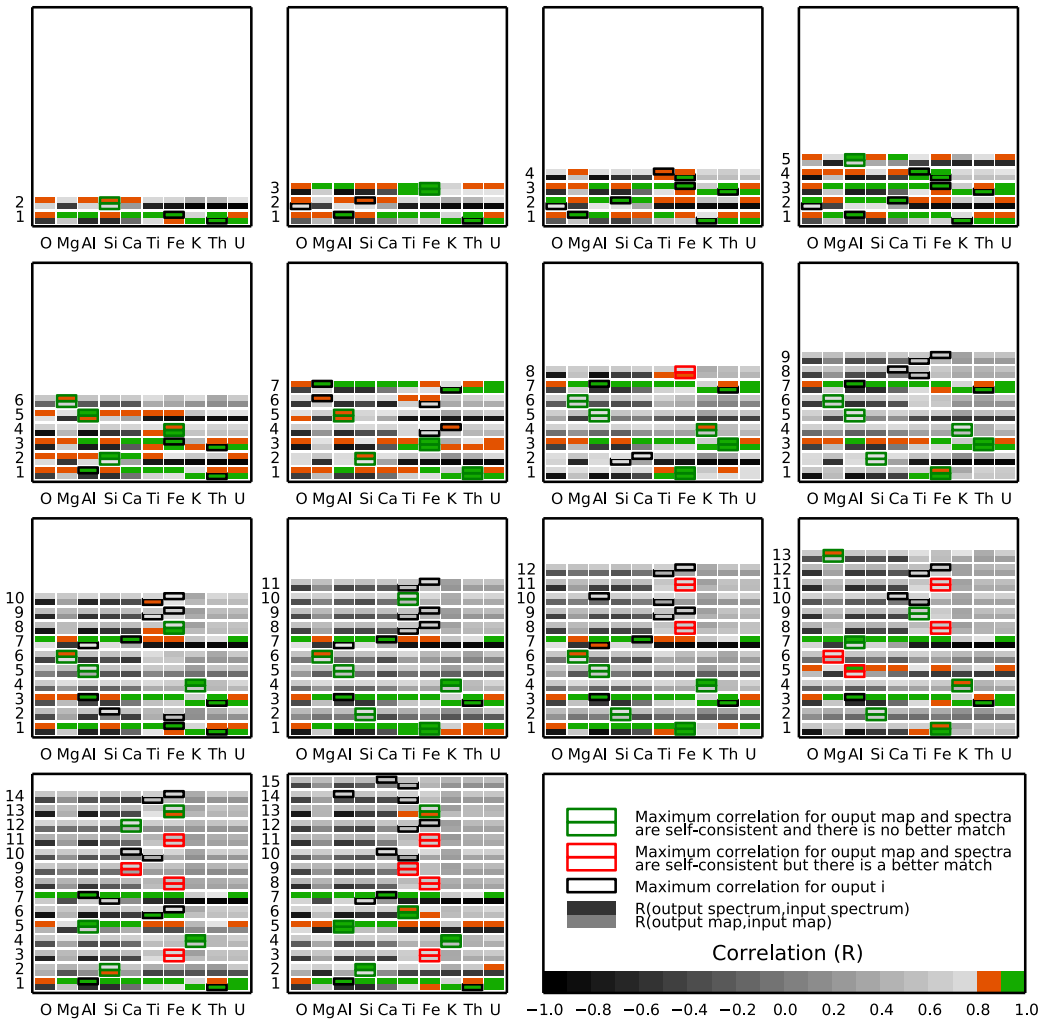

Figure A.1: **Correlation matrices between library data and ICA-NMF outputs from linear mixtures of ten elemental spectra.** The number of ouput sources was varied from 2 to 15. ICA-NMF was here applied to linear mixtures of ten elemental spectra that are indicated on each subplot x axis. For each output source, the lower rectangle gives the correlation of estimated source signals with library maps, the upper rectangle gives the correlation of mixing coefficients with library spectra. For each output, the best match is indicated by a black rectangle. Sometimes, the maximum correlation match the same element for the map and the spectrum. This is indicated either by two red or green rectangles. When the rectangle is red it indicates that there is a better match (for this element = in the same column). Two green rectangles indicate that there is no better match for the element considered. Note that when the maximum spatial correlation is reached for Th, the value for U is the same because these element abundances are correlated by construction [Prettyman *et al.* , 2006].

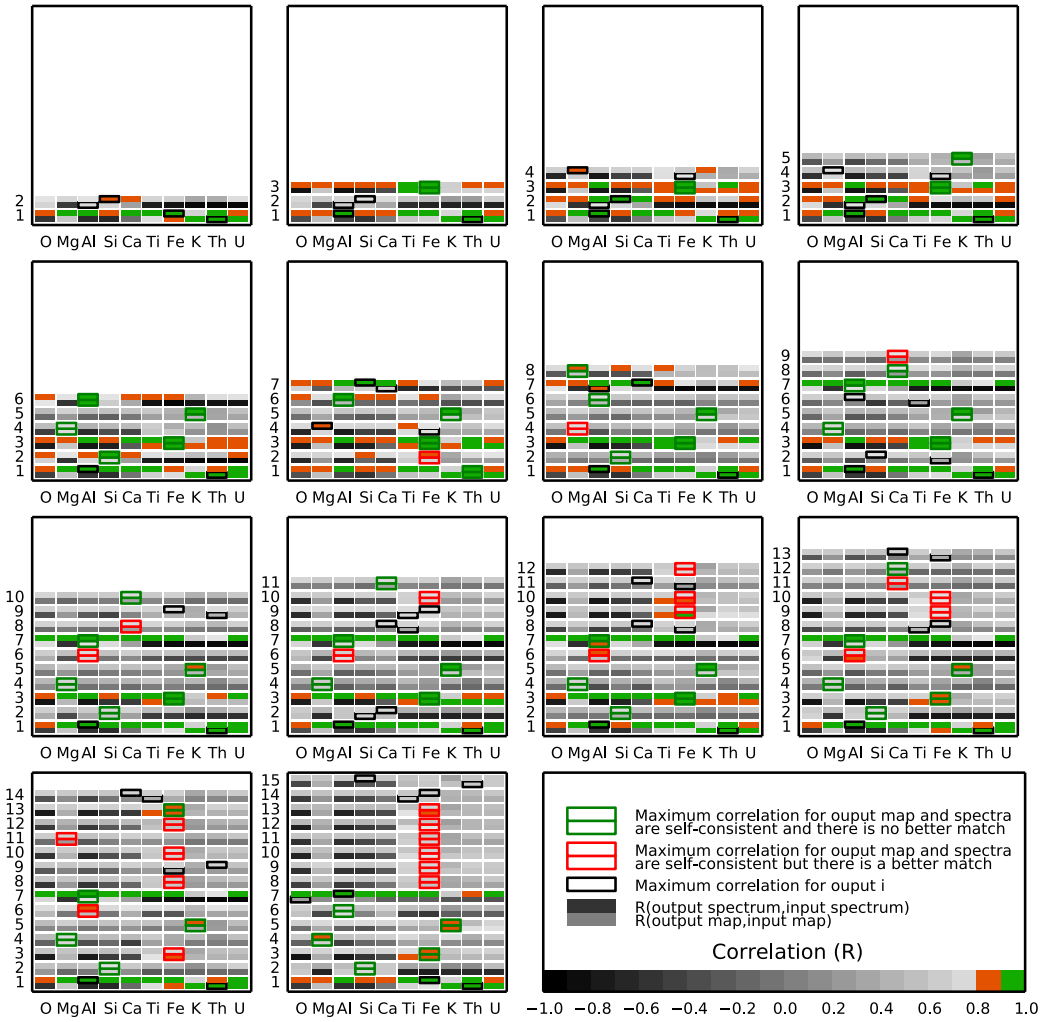

Figure A.2: **Correlation matrices between library data and ICA-NMF outputs.** The analyzed dataset was produced from the physical mixture model of equation 2.4, including all elements. The background gamma rays B_{pl} were not included.

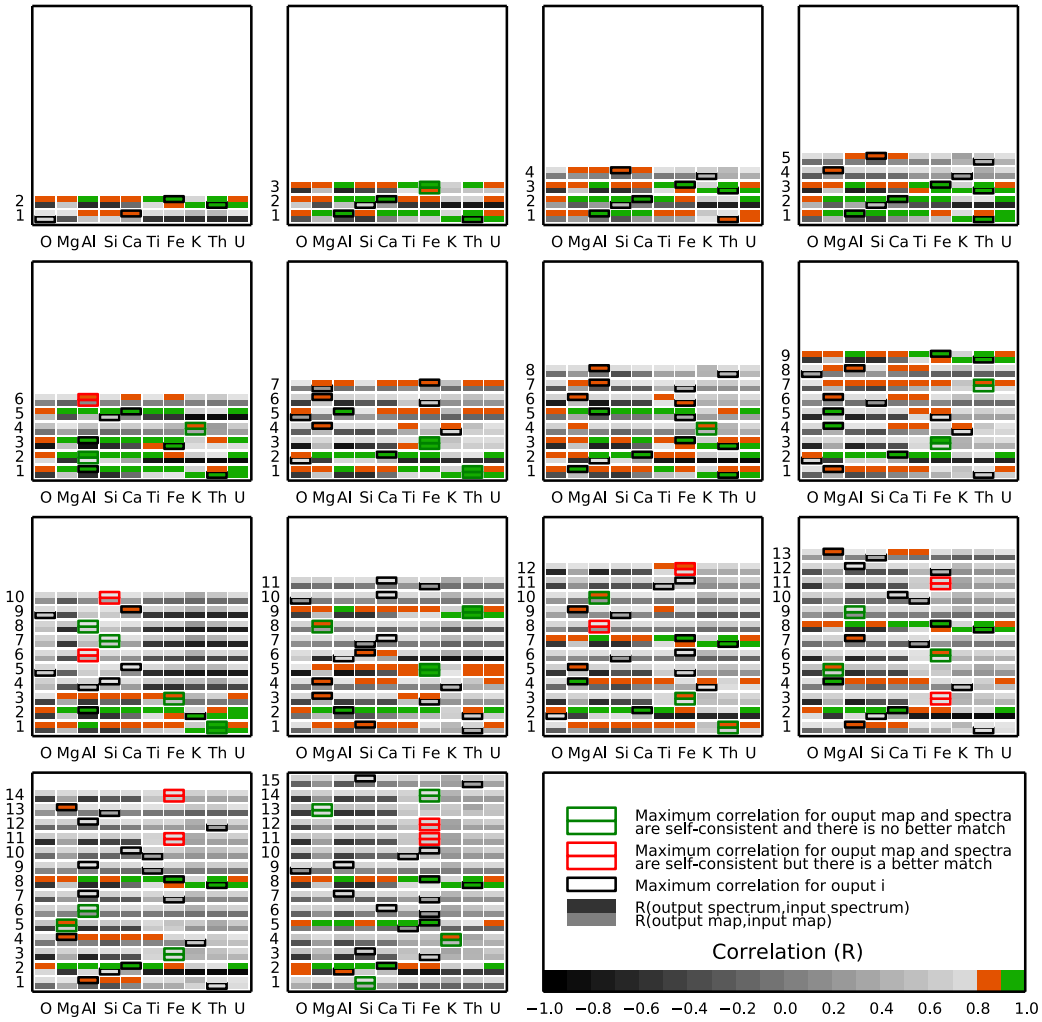

Figure A.3: Correlation matrices between library data and ICA-NMF outputs. The synthetic gamma ray spectra analyzed follow the physical mixture model of ten elemental spectra (Eqn. 2.4) including an additive background.

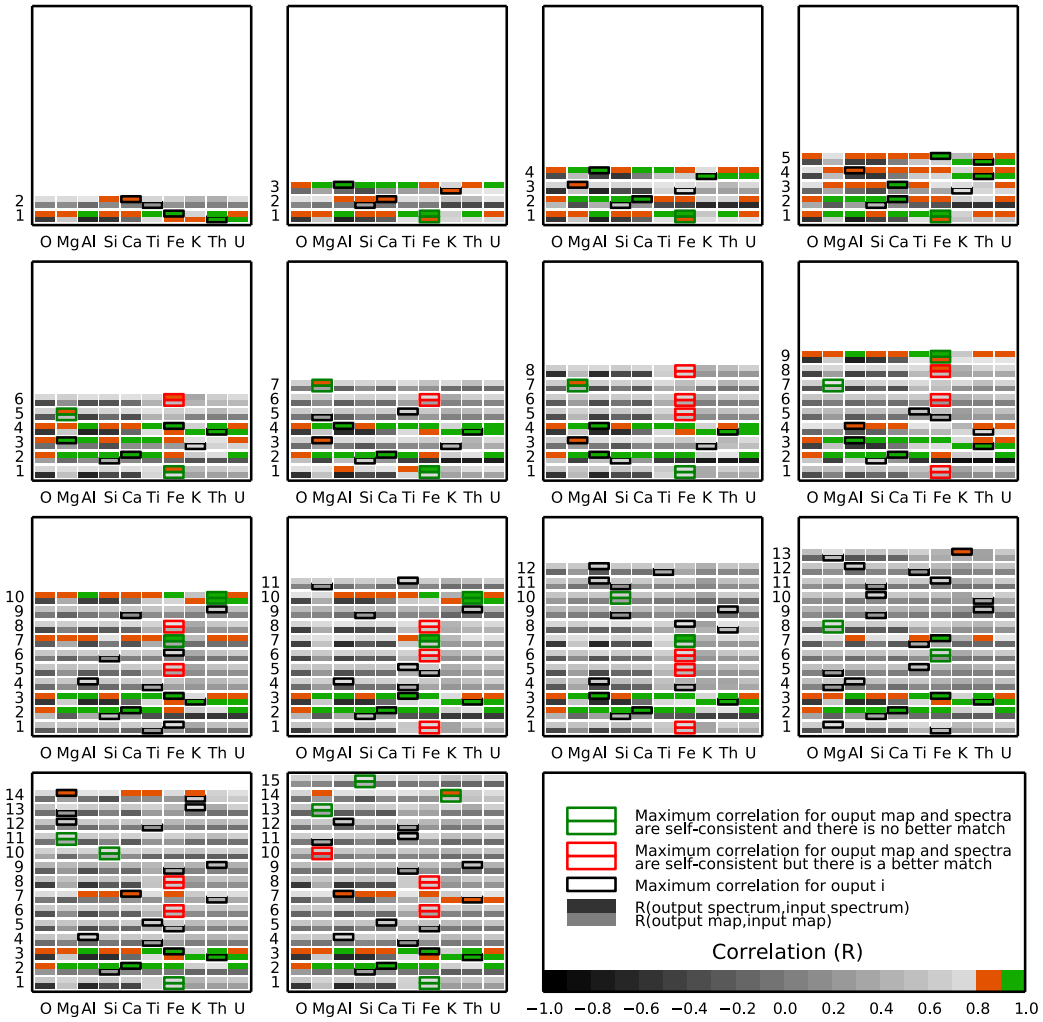

Figure A.4: Correlation matrices between library data and source extracted from the LP-GRS data by ICANMF as a function of the number of ouput sources from 2 to 15.

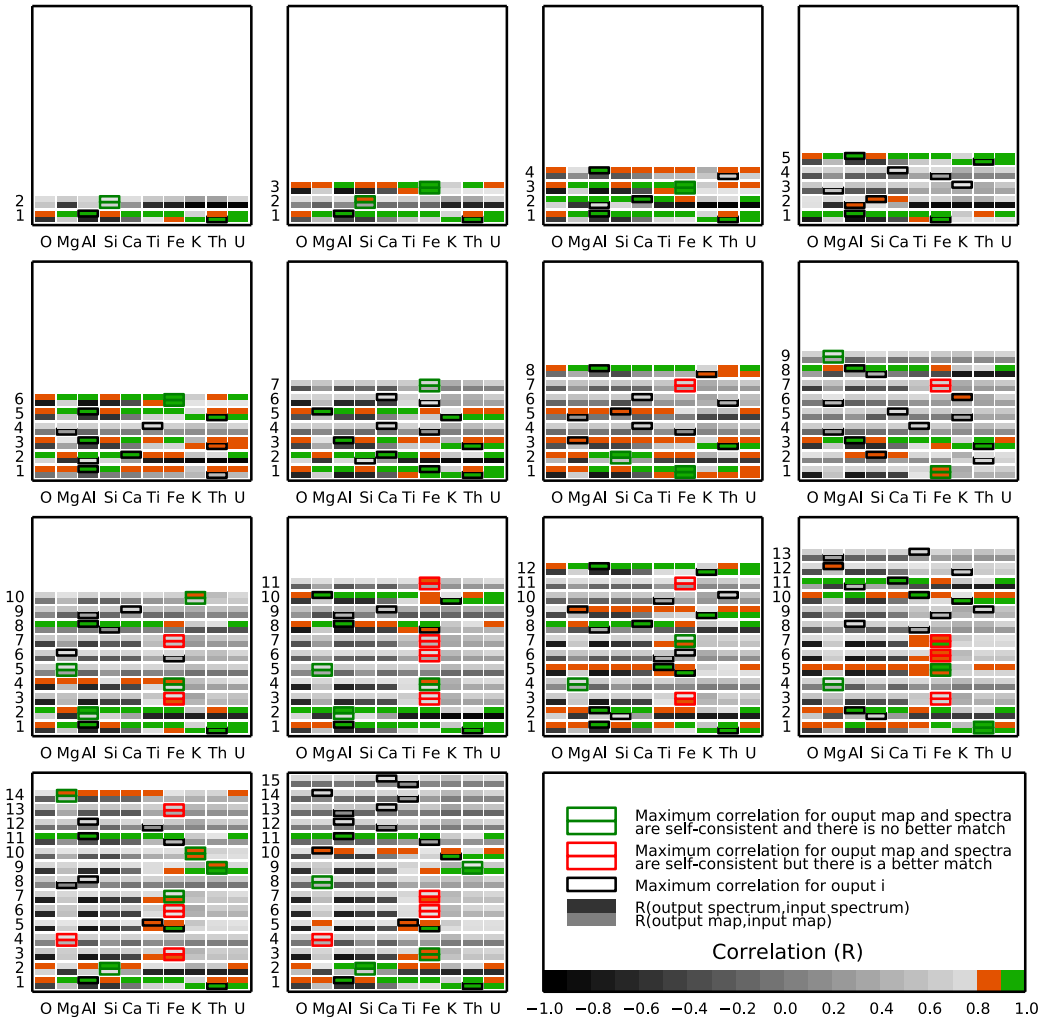

Figure A.5: Correlation matrices between library data and source extracted from LPGRS data by ICANMF, after removing the simulated background gamma rays.

Appendix B

Supplementary informations for numerical modelling.

B.1 Numerical methods.

B.1.1 Velocity of the matrix

Considering a finite volume V of surface S, one can write:

$$\int_V \boldsymbol{\nabla}[F\boldsymbol{\nabla}\cdot\mathbf{v}_m]dV = \int_S \boldsymbol{\nabla}[F(\mathbf{v}_m\cdot\mathbf{n}dS)], \tag{B.1}$$

where $\mathbf{n}$ is a vector normal to the surface and pointing outward. Equation 3.10 becomes for one computational cell:

$$\frac{\delta^2 K}{V_i}\int_S \frac{\partial}{\partial r}[F(\mathbf{v}\cdot\mathbf{n}dS)] + \left(K\delta^2\frac{4}{r}\frac{\partial\phi}{\partial r} - 1\right)v = K\delta^2\frac{(\overline{\rho}-\rho_f)g}{\mu_m}, \tag{B.2}$$

where the volume element $V_i = \int_r \frac{4\pi}{3}r^3dr$ and $dS = 4\pi r^2$. The discretization of this equation using the mesh of Figure B.1 is:

$$\begin{aligned} &K_i\frac{3\delta^2}{dr}\left(\frac{F_{i+\frac{1}{2}}(v_{i+1}r_{i+1}^2 - v_i r_i^2)}{r_{i+1}^3 - r_i^3} - \frac{F_{i-\frac{1}{2}}(v_i r_i^2 - v_{i-1}r_{i-1}^2)}{r_i^3 - r_{i-1}^3}\right) \\ &+\left(K_i\frac{4\delta^2}{r_i}\frac{\phi_{i+\frac{1}{2}} - \phi_{i-\frac{1}{2}}}{dr} - 1\right)v_i \\ &= K_i\frac{k_0}{\mu_l}(\overline{\rho}-\rho_f)g_i \end{aligned} \tag{B.3}$$

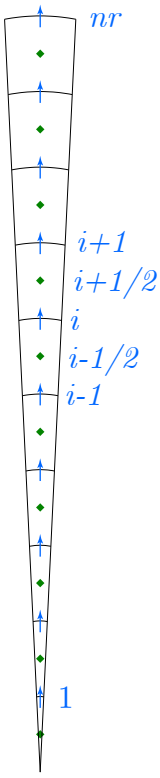

Figure B.1: Velocity mesh.

The ensemble of these descretized expressions for all radial levels lead to a tridiagonal

system of the form $a_i v_{i-1} + b_i v_i + c_i v_{i+1} = d_i$, whose coefficients are:

$$a_i = 3K_i F_{i-\frac{1}{2}} \frac{(r_{i-1}\delta)^2}{dr(r_i^3 - r_{i-1}^3)}$$

$$b_i = -1 + K_i \frac{4\delta^2}{r_i} \frac{\phi_{i+\frac{1}{2}} - \phi_{i-\frac{1}{2}}}{dr} - 3K_i F_{i+\frac{1}{2}} \frac{(r_i\delta)^2}{dr(r_{i+1}^3 - r_i^3)} - 3K_i F_{i-\frac{1}{2}} \frac{(r_i\delta)^2}{dr(r_i^3 - r_{i-1}^3)}$$

$$c_i = 3K_i F_{i+\frac{1}{2}} \frac{(r_{i+1}\delta)^2}{dr(r_{i+1}^3 - r_i^3)}$$

and

$$d_i = K_i \delta^2 \frac{(\overline{\rho}_i - \rho_f) g_i}{\mu_m}. \tag{B.4}$$

It is important to note that F has to be evaluated at the ϕ position $\left(i \pm \frac{1}{2}\right)$, whereas $K, \bar{\rho}$ and g are evaluated at the v position (i).

Boundary conditions

Any singularity at the center is avoided, if the first velocity point is located at $r = dr$. Thus no boundary equation is required for the center. At the surface $v_{nr} = 0$, then $c_{nr-1} = 0$.

B.1.2 Advection

The advection equations are solved using an explicit second order Runge-Kutta method, following:

$$\phi_i^{n+\frac{1}{2}} = \phi_i^n + \frac{dt}{2}(S^n - \boldsymbol{\nabla} \cdot (\phi_i^n v_i^n)), \tag{B.5}$$

the value of ϕ at iteration $n+1$ is obtained by:

$$\phi_i^{n+1} = \phi_i^n + dt(S_i^{n+1/2} - \boldsymbol{\nabla} \cdot (\phi_i^{n+1/2} v_i^{n+1/2})), \tag{B.6}$$

where the estimation of the divergence term follows an upwind scheme:

$$\boldsymbol{\nabla} \cdot (\phi_i v_i) = \frac{r_{i+\frac{1}{2}}^2 v_{i+\frac{1}{2}} \phi_{i+\frac{1}{2}} - r_{i-\frac{1}{2}}^2 v_{i-\frac{1}{2}} \phi_{i-\frac{1}{2}}}{dv_i}. \tag{B.7}$$

The upwind scheme tends to be very diffusive. In the case where the flow regime is concerned by the development of compaction waves, the use of this discretization scheme attenuate these waves. Samuel [2014] proposes to solve second order derivative form of the advection equation to avoid diffusion issues, but also present numerical schemes for solving the first order form of the advection equation that are less diffusive than an upwind scheme, such as the WENO scheme. Figure B.2 and B.3 shows the composition profiles computed for the reference simulation presented in section 3.9 by using WENO and upwind schemes. WENO allows to describe compaction waves of smaller scales, whose development is dampenned by numerical diffusion in the case of the upwind sceme. However, the development of small scale compaction waves can lock the liquid ascent and lead to the formation of several magma oceans (e.g., nr = 3000 in this case), an artifact inherent to 1D geometry. In order to avoid this effect and the associated non-linearities, the upwind scheme is conserved for the simulations presented in chapter 3.

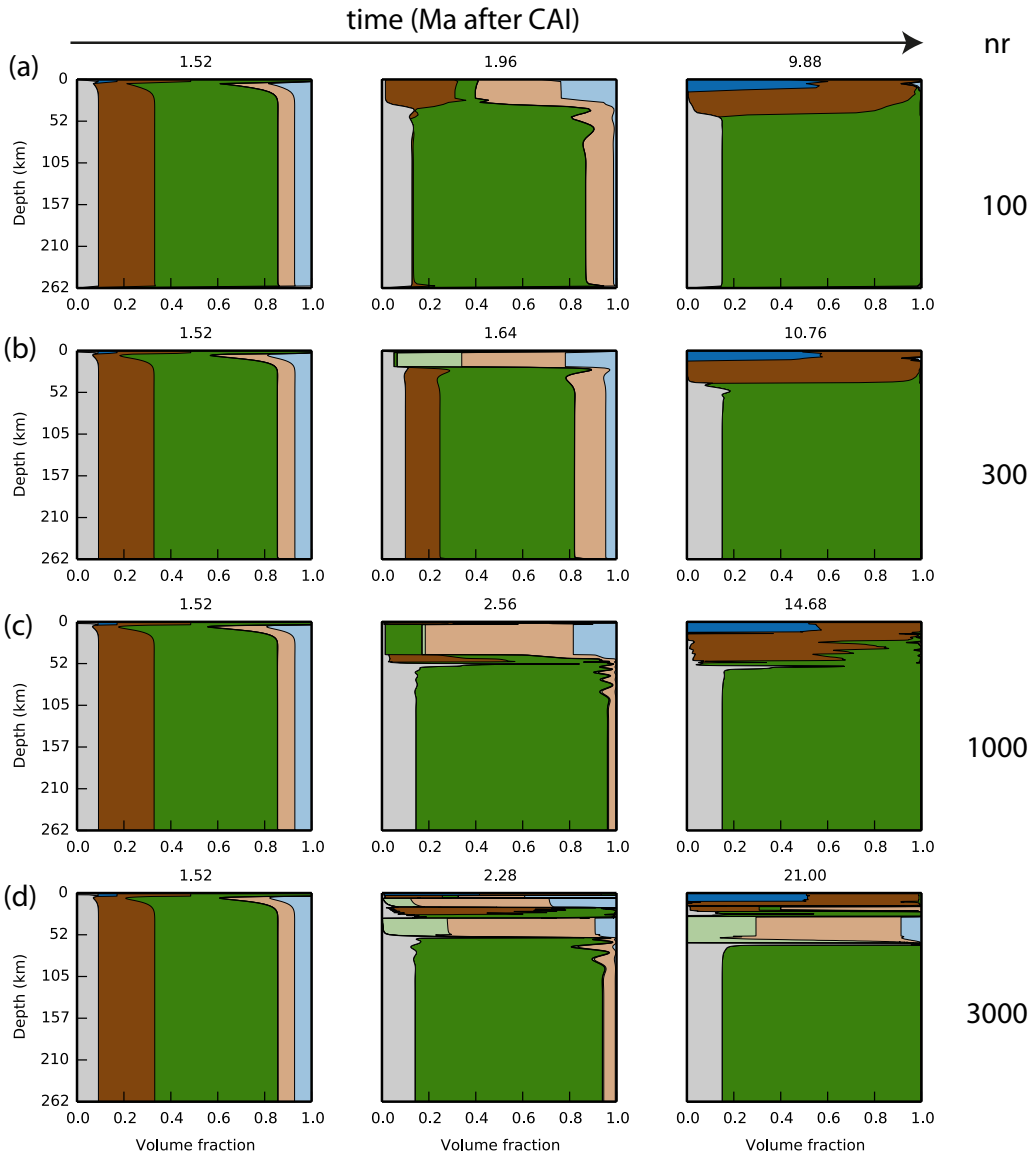

Figure B.2: Snapshots of a simulation of the differentiation of Vesta run for (a) $nr = 100$, (b) $nr = 300$ (c) $nr = 1000$ (d) $nr = 3000$. The advection is treated using a WENO term to discretize the divergence term. Although the development of small scale compaction waves has a physical meaning, the fact that these waves lock the liquid ascent and lead to the formation of several magma oceans (nr = 3000 in this case) is an artifact inherent to 1D geometry.

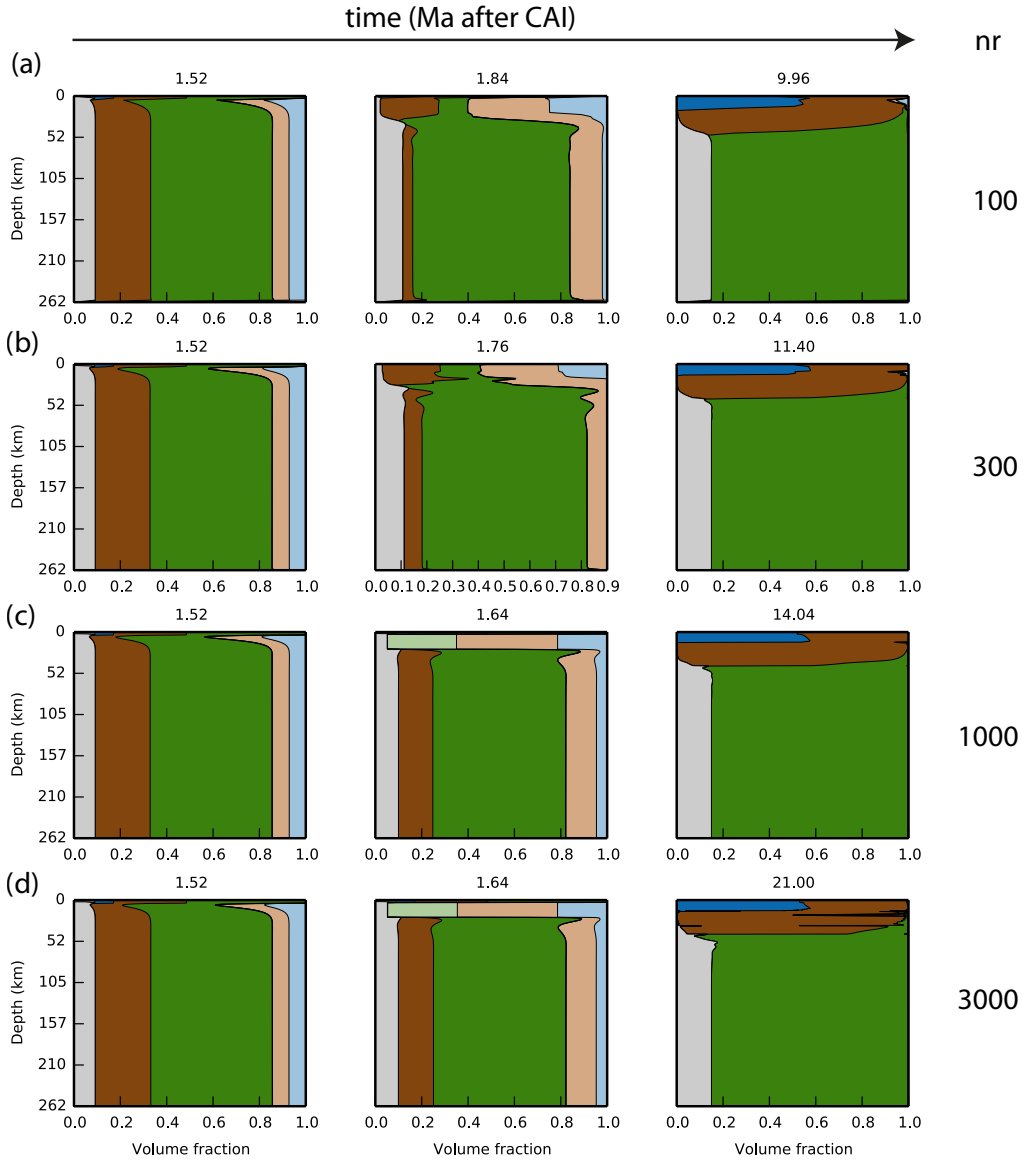

Figure B.3: Snapshots of a simulation of the differentiation of Vesta run for (a) $nr = 100$, (b) $nr = 300$ (c) $nr = 1000$ (d) $nr = 3000$. The advection is treated using an upwind scheme to discretize the divergence term. Increasing the number of points beyond 1000 has minor effects on the numerical solution, although compaction waves of relatively small wavelengths develop more in the case of $nr = 3000$ than for $nr = 1000$.

B.1.3 Temperature

Using a finite volume method, eqn 3.22 becomes:

$$\overline{\rho C}\frac{\partial T}{\partial t} + \frac{1}{V_i}\int_S (\overline{\mathbf{v}\rho C}T)\cdot \mathbf{n}dS = \frac{1}{V_i}\int_S (k\boldsymbol{\nabla}T)\cdot \mathbf{n}dS + \overline{\rho}Q. \tag{B.8}$$

A Euler implicite scheme is used to discretize this equation:

$$\begin{aligned}&\overline{\rho C}_i\frac{T_i^{n+1}-T_i^n}{dt} + Ad_{i+\frac{1}{2}}(T_{i+1}^{n+1}+T_i^{n+1}) - Ad_{i-\frac{1}{2}}(T_i^{n+1}+T_{i-1}^{n+1})\\ &= D_{i+\frac{1}{2}}(T_{i+1}^{n+1}-T_i^{n+1}) - D_{i-\frac{1}{2}}(T_i^{n+1}-T_{i-1}^{n+1}) + \overline{\rho}Q,\end{aligned} \tag{B.9}$$

where

$$D_{i+\frac{1}{2}} = k_{i+\frac{1}{2}}\frac{r_{i+\frac{1}{2}}^2}{drdv_i}, \quad D_{i-\frac{1}{2}} = k_{i-\frac{1}{2}}\frac{r_{i-\frac{1}{2}}^2}{drdv_i}, \tag{B.10}$$

and

$$Ad_{i+\frac{1}{2}} = \overline{v\rho C}_{i+\frac{1}{2}}\frac{r_{i+\frac{1}{2}}^2}{2dv_i}, \quad Ad_{i-\frac{1}{2}} = \overline{v\rho C}_{i-\frac{1}{2}}\frac{r_{i-\frac{1}{2}}^2}{2dv_i}. \tag{B.11}$$

It leads to the tridiagonal set:

$$\begin{aligned}a_i &= -D_{i-\frac{1}{2}} - Ad_{i-\frac{1}{2}}\\ b_i &= D_{i+\frac{1}{2}} + D_{i-\frac{1}{2}} + Ad_{i+\frac{1}{2}} - Ad_{i-\frac{1}{2}} + \frac{\overline{\rho C}_i}{dt} \qquad \forall\ 1<i<nr\\ c_i &= -D_{i+\frac{1}{2}} + Ad_{i+\frac{1}{2}}\\ d_i &= \frac{\overline{\rho C}_i}{dt}T_i^n + \overline{\rho}Q \qquad .\end{aligned} \tag{B.12}$$

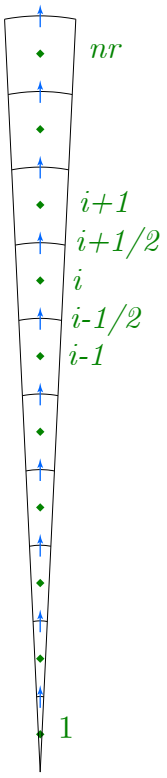

Figure B.4: Volume fractions and temperature meshing.

Boundary condition

A fixed surface temperature reflects as $T_e = \dfrac{T_{i+1}^{n+1}+T_i^{n+1}}{2}$ and results in a change of the top coefficients:

$$\begin{aligned}a_{nr} &\leftarrow a_{nr}\\ b_{nr} &\leftarrow b_{nr} - c_{nr}\\ d_{nr} &\leftarrow d_{nr} - 2c_{nr}T_e\\ c_{nr} &\leftarrow 0.\end{aligned} \tag{B.13}$$

B.2 Computation of the composition using the enthalpy method and the olivine - anorthite - silica phase diagram.

Depending on the energy available, the silicate material can be entirely solid, entirely liquids in which case determining the temperature is not dependent on the composition. Silicates are mixtures of minerals that have different melting temperatures individually, and whose mixture can lead to a complex composition - temperature path. For example in the olivine - anorthite silica system given a first solid silicate that is begin heated, the first liquid produced has a composition equivalent to a mixture of plagioclase and pyroxene called eutectic, plagioclase and pyroxenes are being molten, until the least refractory mineral is outconsummed. When plagioclase has been entirely molten, pyroxene continues melting but olivine stays solid. Finally, pyroxene is outconsummed and olivine starts to melt, olivine continues melting until everything is liquid. During these steps the composition of both liquid and solids has evolved along a path which are dependent on the intial composition. These paths are shown on Figure 3.7.

The liquidus temperature is given by:

$$T_l(X^l_{Px}, X^l_{An}) = T_{Fo}+(T_{Px}-T_{Fo})X^l_{Px}+\frac{X^l_{An}}{X^e_{An}}\left[(T_{Fo}-T_{Px})X^e_{Px}+T_e-T_{Fo}\right] \quad \text{(B.14)}$$

where, T_{Fo}, T_{Px} and T_e are the forsterite, pyroxene and eutectic melting temperatures. X^l_{Px}, X^l_{An} are the mass fractions of pyroxenes and anorthite in the liquid. X^e_{Px} and X^e_{An} correspond to the eutectic composition. We used $T_{Fo} = 2163K$, $T_{Px} = 1830K$ and $T_e = 1543K$.This equation relates temperature and composition in terms of mass fractions. In the case of different densities for the components of the silicate mixtures, volumes fractions need to be converted into mass fractions.

The following presents the algorithm that is used to perform the correction at constant enthalpy and satisfies the properties of the phase diagram to calculate composition. Depending on the composition, one may have :

- **A pure component**: forsterite for example. Composition will always be $X^l_{En} = 0$ and $X^l_{An} = 0$.

Depending on the total enthalpy one can be:

- below the onset of melting $H < H0 = CT_{Fo}$

In that case everything is solid $Xm_s = 1$, $Xm_l = 0$ the temperature is given by $T = H/C$.

- melting $H0 < H < H1 = CT_{Fo} + L$

The temperature is given by the pure component melting temperature, the melt fraction is given by $Xm_l = (H - H0)/L$.

- completely molten

$Xm_l = 1$ and $T = (H - L)/C$.

Pure pyroxene and pure anorthite would be treated similarly.

- **A binary mixture**, for example, an anorthite - enstatite mixture.

Depending on the total enthalpy one can be:

- below the onset of eutectic melting ($H < H0 = CT_e$)

$Xm_l = 0$, $T = H/C$, the composition of the solid correspond to the input composition $X^s_{En} = X^0_{En}$ and $X^s_{An} = X^0_{An}$.

- melting at the eutectic ($H0 < H < H1 = H0 + X^0_{An}/X^e_{An}L$), where $H1$ is enthalpy of the system when the least refractory component is outconsumed. $Xm_l = (H-H0)/L$, the liquid produced has the eutectic composition $X^l_{En} = X^e_{En}$ and $X^l_{An} = X^e_{An}$, the composition of the solid is determined by complementarity $X^s_{En} = (X^0_{En} - Xm_l X^e_{En})/(1-X_m l)$ and $X^s_{An} = 1. - X^s_{En}$, $T = T_e$.

- melting above the eutectic ($H1 < H < H2 = CT_l(X^0_{An}, X^0_{En}) + L$, where $H2$ is the

enthalpy of the system at the end of melting. Introducing the liquidus equation into the enthalpy leads to:

$$H/C = T_{Fo} + (T_{Px} - T_{Fo})X^l_{Px} + \frac{X^l_{An}}{X^e_{An}}\left[(T_{Fo} - T_{Px})X^e_{Px} + T_e - T_{Fo}\right] + Xm_l L/C \tag{B.15}$$

In addition, anorthite is completely molten here, $X^l_{An} = X^0_{An}/Xm_l$, $X^l_{En} = 1 - X^l_{An}$ and $X^e_{En} = 1 - X^e_{An}$ because it is a binary mixture, then:

$$H/C = T_{Px} + \frac{X^0_{An}}{Xm_l X^e_{An}}(T_e - T_{Px}) + Xm_l L/C \tag{B.16}$$

which can be rearranged into:

$$Xm_l^2 L/C + Xm_l(T_{Px} - H/C) + \frac{X^0_{An}}{X^e_{An}}(T_e - T_{Px}) = 0 \tag{B.17}$$

Since $L/C > 0$, $X^0_{An}/X^e_{An}(T_e - T_{Px}) < 0$ and $(T_{Px} - H/C)^2 + 4L(T_{Px} - T_e)CX^0_{An}/X^e_{An} > 0$, the only positive solution to Xm_l is:

$$Xm_l = \frac{H - CT_{Px} + \left[(CT_{Px} - H)^2 + 4L(T_{Px} - T_e)CX^0_{An}/X^e_{An}\right]^{\frac{1}{2}}}{2L} \tag{B.18}$$

from which stems $X^l_{Px} = X^0_{Px}/Xm_l + 1$, $X^l_{An} = 1. - X^l_{Px}$, $X^s_{Px} = 1$, $X^s_{An} = 0$
$T = T_l(X^l_{An}, X^l_{Px})$.
- completely molten ($H > H2$)
$X^l_{En} = X^0_{En}$, $Xm_l = 1$, $T = (H - L)/C$.
A forsterite - anorthite or a forsterite - pyroxene mixture would be treated similarly.

- **A ternary mixture** of forsterite, pyroxene and anorthite
- below the onset of eutectic melting $H < H0 = CT_e$ As previously, $Xm_l = 0$, $X^s_{An} = X^0_{An}$, $X^s_{Px} = X^0_{Px}$, $T = H/C$.
- melting at the eutectic ($H0 < H < H1 = H0 + X^0_{An}/X^e_{An}L$), where H1 is the enthalpy of the system when anorthite has been completely molten.
$Xm_l = (H - H0)/L$, $X^l_{An} = X^e_{An}$, $X^l_{Px} = X^e_{An}$, $X^s_{Px} = (X_{Px^0} - X^l_{Px}Xm_l)/(1 - Xm_l)$ $X^s_{An} = (X_{An^0} - X^l_{An}Xm_l)/(1 - Xm_l)$ and $T = T_e$.
- melting above the total melting of the least refractory component ($H1 < H < H2 = CT_l\left(\frac{X^0_{Px}}{X^0_{Px} + X^0_{An}}, \frac{X^0_{An}}{X^0_{Px} + X^0_{An}}\right) + (X^0_{Px} + X^0_{An})L$
H2 is the enthalpy of the system when both anorthite and pyroxene have been completely molten. Xm_l is obtained using equation B.18. $X^l_{An} = X^0_{An}/Xm_l$, $X^l_{Px} = 1. - X^l_{An}$, $T = T_l(X^l_{Px}, X^l_{An})$ $X^s_{An} = (X^0_{An} + X^0_{Px} - Xm_l)/(1 - X_m l)$ $X^s_{An} = 0$.
- melting above the total melting of the second least refractory component ($H2 < H < H3 = CT_l(X^0_{Px}, X^0_{An}) + L$)
$H3$ is the enthalpy of the system when melting of the three components is completed. Combination of enthalpy and liquidus equations using the fact that forsterite and anorthite are not present in solid leads to:

$$Xm_l^2 L + (CT_{Fo} - H)Xm_l + C\left[\left(\frac{X^0_{An}}{X^e_{An}}X^e_{Px} - X^0_{Px}\right)(T_{Fo} - T_{Px}) + \frac{X^0_{An}}{X^e_{An}}(T_e - T_{Fo})\right] \tag{B.19}$$

Since $(X^0_{An}/X^e_{An}X^e_{Px} - X^0_{Px})(T_{Fo} - T_{Px}) + (T_e - T_{Fo}) < 0$, the only positive solution to Xm_l is:

$$Xm_l = \frac{H - CT_{Fo} + \left[(CT_{Fo} - H)^2 + 4LC\left[\left(X^0_{Px} - \frac{X^0_{An}}{X^e_{An}}X^e_{Px}\right)(T_{Fo} - T_{Px}) + \frac{X^0_{An}}{X^e_{An}}(T_{Fo} - T_e)\right]\right]^{\frac{1}{2}}}{2L}$$

(B.20)

- completely molten ($H > H3$) $X^l_{En} = X^0_{En}$, $Xm_l = 1, T = (H - L)/C$.

B.3 Initial bulk composition.

The mineralogical composition used in chapter 3 was derived from table 2 and table 3 from [Toplis *et al.* , 2013]. We use the mass fraction of iron, sulfur and nickel in core: $\frac{m_{Fe}}{m_{met}}$, $\frac{m_S}{m_{met}}$, $\frac{m_{Ni}}{m_{met}}$ (table 3) the fraction of metal $\frac{m_{met}}{m_{tot}}$, the mass ratio $R = Fe0/(Fe0 + FeS)$ to derive the mass fractions of metallic iron, nickel, iron sulfide and nickel sulfide.

$$\begin{aligned}
\frac{m_{Fe0}}{m_{met}} &= \frac{m_{Fe} M_{FeS} R}{m_{met} M_{FeS} R + M_{Fe}(1 - R)} \\
\frac{m_{FeS}}{m_{met}} &= \frac{m_{Fe0}(1 - R)}{R m_{met}} \\
\frac{m_{NiS}}{m_{met}} &= \left(\frac{m_S}{m_{met} M_S} - \frac{m_{FeS}}{m_{met} M_{FeS}} \right) M_{NiS} \\
\frac{m_{Ni0}}{m_{met}} &= \left(\frac{m_{Ni}}{m_{met} M_{Ni}} - \frac{m_{NiS}}{M_{NiS} m_{met}} \right) M_{Ni}
\end{aligned} \tag{B.21}$$

On the other hand, the silicate composition provided in this paper can be converted into the mass fraction of anorthite, olivine and pyroxene by neglecting the contribution of $Na2O$ and $TiO2$: Using the equivalency between mineral formulae and oxides, $An <=> CaO + Al2O3 + 2SiO2$, $Di <=> MgO + CaO + 2SiO2$, $En <=> MgO + SiO2$, $Fs <=> FeO + SiO2$, $Fo <=> 2MgO + SiO2$ and $Fa <=> 2FeO + SiO2$. $Al2O3$ andCaO content are used to determine the Anorthite and Diopside contents. Using the fact that in Hyperstene (<=> En (MgSiO3) - Fs (FeSiO3) solid solution) the molar ratio $(MgO + FeO)/SiO2 = 1$ while it equals 2 in the Forsterite (Mg2SiO4) Fayalite (Fe2SiO4) solid solution, one can infer the equivalent Hypersthene and Olivine contents by complementarity. Using the Mg' of MgO' vs FeO (after formation of Di), the molar proportion of Forsterite, Fayalite, Enstatite and Ferrosilite can be computed. In summary:

$$\begin{aligned}
&n_{An} = n_{Al2O3} \\
&n_{Di} = n_{CaO} - n_{An} \\
&n_{Hy} = 2(n_{SiO2} - 2n_{An} - 2n_{Di}) - [(n_{MgO} - n_{Di}) + n_{FeO}] \\
&Mg' = (n_{MgO} - n_{Di})/(n_{MgO} - n_{Di} + n_{FeO}) \\
&n_{Ol} = n_{SiO2} - 2n_{An} - 2n_{Di} - n_{Hy} \\
&n_{Fo} = Mg' n_{Ol} \\
&n_{Fa} = (1 - Mg') n_{Ol} \\
&n_{En} = Mg' n_{Hy} \\
&n_{Fs} = (1 - mg') n_{Hy}
\end{aligned} \tag{B.22}$$

We then assimilate Di, En, Fs to pyroxene Px, Fo and Fs to olivine Ol, as we assimilate $FeNi$ to metal and $FeNiS$ to sulfide. Proportion of $Di\ En\ Fs$ are used to calculate the average density of pyroxenes, similarly the olivine density stems from Fo and Fa, the metal density results from FeM, NiM and the density of sulfide from FeS and NiS. A global average density ρ_{tot} a global average silicate density ρ_{sil} and a global average iron + sulfide density ρ_{met} are also calculated.

Average densities of mixtures (e.g. silicates, metal + sulfides, total) can be calculated as a function of mass fractions by:

$$\rho_{mix} = 1/\sum_{i=1}^{N} X_i/\rho_i \tag{B.23}$$

where X_i andρ_i are respectively the mass fractions and individual densities of the mixture components. Alternatively it can be defined as a function of volume fractions:

$$\rho_{mix} = \sum_{i=1}^{N} \phi_i \rho_i. \tag{B.24}$$

Volume fractions can be converted to mass fraction and vice versa using:

$$\phi_i = X_i \rho_{mix}/\rho_i. \tag{B.25}$$

The change in calcium, iron and magnesium content from a chondritic group to the other make carboneceous chondrites plausible olivine rich precursors, enstatite chondrites, the pyroxene dominated ones, ordinary chondrites forming an intermediate case.

Appendix C

Chondritic models of 4 Vesta: Implications for geochemical and geophysical properties.

The Meteoritical Society

Meteoritics & Planetary Science 48, Nr 11, 2300–2315 (2013)
doi: 10.1111/maps.12195

Chondritic models of 4 Vesta: Implications for geochemical and geophysical properties

M. J. TOPLIS[1*], H. MIZZON[1], M. MONNEREAU[1], O. FORNI[1], H. Y. McSWEEN[2], D. W. MITTLEFEHLDT[3], T. J. McCOY[4], T. H. PRETTYMAN[5], M. C. De SANCTIS[6], C. A. RAYMOND[7], and C. T. RUSSELL[8]

[1]IRAP (CNRS - UMR 5277), Observatoire Midi-Pyrénées, University of Toulouse, 14 Ave. E. Belin, Toulouse F-31400, France
[2]Department of Earth and Planetary Sciences, University of Tennessee, Knoxville, Tennessee 37996-1410, USA
[3]Astromaterials Research Office, NASA Johnson Space Center, Houston, Texas 77058, USA
[4]Department of Mineral Sciences, Smithsonian Institution, Washington, District of Columbia 20013-7012, USA
[5]Planetary Science Institute, Tucson, Arizona 85719-2395, USA
[6]Istituto di Astrofisica e Planetologia Spaziali INAF, Roma 00133, Italy
[7]Jet Propulsion Laboratory, California Institute of Technology, Pasadena, California 91109, USA
[8]Institute of Geophysics and Planetary Physics, University of California, Los Angeles, California 90095, USA
[*]Corresponding author: E-mail: mtoplis@irap.omp.eu

(Received 17 February 2013; revision accepted 04 August 2013)

Abstract–Simple mass-balance and thermodynamic constraints are used to illustrate the potential geochemical and geophysical diversity of a fully differentiated Vesta-sized parent body with a eucrite crust (e.g., core size and density, crustal thickness). The results of this analysis are then combined with data from the howardite–eucrite–diogenite (HED) meteorites and the Dawn mission to constrain Vesta's bulk composition. Twelve chondritic compositions are considered, comprising seven carbonaceous, three ordinary, and two enstatite chondrite groups. Our analysis excludes CI and LL compositions as plausible Vesta analogs, as these are predicted to have a negative metal fraction. Second, the MELTS thermodynamic calculator is used to show that the enstatite chondrites, the CV, CK and L-groups cannot produce Juvinas-like liquids, and that even for the other groups, depletion in sodium is necessary to produce liquids of appropriate silica content. This conclusion is consistent with the documented volatile-poor nature of eucrites. Furthermore, carbonaceous chondrites are predicted to have a mantle too rich in olivine to produce typical howardites and to have Fe/Mn ratios generally well in excess of those of the HEDs. On the other hand, an Na-depleted H-chondrite bulk composition is capable of producing Juvinas-like liquids, has a mantle rich enough in pyroxene to produce abundant howardite/diogenite, and has a Fe/Mn ratio compatible with eucrites. In addition, its predicted bulk-silicate density is within 100 kg m^{-3} of solutions constrained by data of the Dawn mission. However, oxidation state and oxygen isotopes are not perfectly reproduced and it is deduced that bulk Vesta may contain approximately 25% of a CM-like component. Values for the bulk-silicate composition of Vesta and a preliminary phase diagram are proposed.

INTRODUCTION

The vast majority of rocky and metallic objects delivered to Earth as meteorites are samples of proto-planetary bodies that escaped accretion into larger planets, providing a unique window into the history of the early solar system (e.g., McSween 1999). One of the principal findings of the meteorite record is that short-lived radioisotopes, in particular ^{26}Al, may have been abundant in the earliest solar system (e.g., MacPherson et al. 1995) providing a potent heat source capable of fueling internal differentiation of early-accreted bodies (e.g., Ghosh and McSween 1998; Hevey and Sanders 2006; Neumann et al. 2012).

Understanding the extent and nature of differentiation in such small bodies is of critical importance, as those bodies are in turn the building blocks of larger planets such as the Earth or Mars.

However, even within the simple conceptual framework of radiogenic heating, once temperature rises above the solidus of the silicate and/or metal fractions, physical, chemical, and thermal interactions are sufficiently complex that it is difficult to predict exactly how differentiation will proceed as a function of space and time within the body. For example, there is debate concerning the critical melt fraction necessary for efficient metal segregation, some authors arguing for the need for silicate melt fractions as high as 50% (e.g., Taylor 1992), others suggesting that even a negligible silicate melt fraction will suffice (e.g., McCoy et al. 1997; Terasaki et al. 2008). At the other end of the density spectrum, there is also debate concerning how silicate melt can rise to form a primitive crust, some authors believing that the time scales of melt extraction are low enough that protoplanetary interiors may retain large local melt fractions (e.g., Righter and Drake 1997; Moskovitz and Gaidos 2011; Neumann et al. 2012), others suggesting that pathways for rapid extraction to the surface may exist such that protoplanetary interiors never contained more than a few percent of interstitial liquid (e.g., Wilson and Keil 2012).

The study of achondrite and metallic meteorites confirms that internal differentiation occurred within the first few million years of the solar system and that ^{26}Al is a plausible heat source (e.g., Bizzarro et al. 2005; Kleine et al. 2005; Qin et al. 2008). However, despite important mineralogical and petrologic constraints, meteorite samples lack geological context (i.e., at the outcrop scale) and much of the information concerning their spatial distribution at the surface or within their original parent body must be inferred indirectly, complicating the use of these samples for unraveling the details of the differentiation process.

A viable alternative is to study remnant parent bodies in regions such as the main asteroid belt between Mars and Jupiter, where the planet-forming process is thought to have been arrested due to the presence of Jupiter. Of the objects in the Main Belt, the asteroid Vesta is of particular interest as it is large enough to have experienced internal differentiation (520 km diameter), and it is known to have a basaltic surface dominated by FeO-bearing pyroxenes as demonstrated by visible-IR spectra obtained by ground and space-based telescopes (e.g., McCord et al. 1970; Drake 2001). Furthermore, such spectra of Vesta and associated Vestoids are remarkably similar to laboratory spectra measured on meteorites of the howardite-eucrite-diogenite clan (HED), leading to the paradigm that the HEDs ultimately came from Vesta (e.g., Binzel and Xu 1993; Drake 2001). Geochemical and petrological studies of the HEDs confirm the differentiated nature of the near-surface region of their parent body, and imply that crust extraction occurred well within the first 10 Ma of solar system history (e.g., Nyquist et al. 2003; Trinquier et al. 2008; Kleine et al. 2009).

Vesta is therefore a prime target for studies that aim to constrain the earliest stages of planet building, and it is within this context that the NASA Dawn spacecraft (Russell and Raymond 2011) orbited Vesta from July 2011 to September 2012. The results of the Dawn mission so far have significantly reinforced the HED-Vesta connection, confirming a significant degree of internal differentiation of the asteroid (Russell et al. 2012), a surface mineralogy perfectly compatible with that of the HEDs (De Sanctis et al. 2012a; Reddy et al. 2012), and near-surface concentration ratios Fe/O and Fe/Si consistent with HED lithologies (Prettyman et al. 2012).

The combination of data from the HED meteorites and the Dawn mission thus presents an unprecedented opportunity to use Vesta as a natural laboratory of early differentiation processes in the early solar system. However, the bulk composition of Vesta remains a significant unknown parameter, but one that plays a key role on the physical and chemical properties of the internal and surface reservoirs (core, mantle, crust). Several attempts have been made over the years to constrain the bulk composition of the eucrite parent body, early endeavors relying on petrological or cosmochemical constraints (e.g., Consolmagno and Drake 1977; Dreibus et al. 1977; Morgan et al. 1978). More recently, individual chondrite-class compositions, or mixtures thereof, have been considered, constrained by considerations such as O-isotopes, trace element ratios and siderophile element concentrations of the eucrites (Boesenberg and Delaney 1997; Righter and Drake 1997; Ruzicka et al. 1997).

The work presented here builds upon these latter studies, with the primary aims of (1) illustrating the potential diversity of the geochemical and geophysical properties of a fully differentiated Vesta-sized parent body, and (2) assessing which, if any, of the known chondritic bulk compositions are plausible analogs for proto-Vesta.

METHODS

General Approach: Compositions and Chemical Elements Considered

There is consensus that the primitive building blocks of the solar system were "chondritic" in bulk

composition. However, diverse classes of chondrite exist, from the volatile-rich Ivuna-class (CI), to metal-poor varieties such as the LL ordinary chondrites (Wasson and Kallemeyn 1990). While there is no guarantee that Vesta accreted from known chondritic precursors, these compositions provide a convenient reference frame for exploring possible compositional variations of early solar system materials.

Twelve chondritic compositions are considered here, comprising seven carbonaceous groups (CI, CV, CO, CM, CK, CR, CH), the three ordinary chondrite groups (H, L, LL), and the two enstatite chondrite groups (EH, EL). Compositions of the CK, CR, and CH groups are taken from Lodders and Fegley (1998), all other compositions being taken from Wasson and Kallemeyn (1990). Significant differences in composition exist, in terms of Mg/Si, sulfur, and iron content, volatile depletion, oxidation state of iron, and the concentration of incompatible lithophiles such as the REE. The role of these factors on the mineralogy and internal structure of a fully differentiated parent body will be explored here.

The basis of our analysis consists of distributing each chemical element between one or more of the principal solid differentiated geochemical reservoirs (core, mantle, crust), assuming a distribution that is consistent with the thermodynamics of element partitioning at magmatic temperature, as detailed below. Because our aim is to quantify the first-order effects of differentiation, we focus on those chemical elements that dominate the mass of the bulk object (Si, Al, Mg, Ca, Ti, Na, Fe, Ni, S, O), minor or trace elements (e.g., Mn, REE) being considered only where they provide complementary constraints. The volatile elements (H, C, N, etc) are expected to be strongly partitioning into a vapor phase at magmatic temperature in the low-pressure and low-gravity conditions at Vesta. Traces of volatiles such as hydrogen exist both at the surface of Vesta and in certain HEDs (e.g., Treiman et al. 2004; Barrat et al. 2011; De Sanctis et al. 2012b; Prettyman et al. 2012), but an internal origin is generally considered unlikely. While we cannot exclude the survival of a fraction of the original volatile inventory, residual concentrations are not expected to be volumetrically or petrologically significant after magmatic processing, so these elements will not be considered further for the purposes of this study.

Core Materials and the Link to Bulk-Silicate Composition

The core of a fully differentiated protoplanet is expected to be dominated by Fe, S, and Ni. Of these three elements, the silicate-metal partition coefficients of S and Ni are very strongly in favor of the metallic melt phase at oxygen fugacities (fO_2) near the iron-wüstite buffer (e.g., O'Neill and Mavrogenes 2002; Holzheid and Palme 2007). We will therefore make the simplifying assumption that all available Ni and S are sequestered in the core. On the other hand, the case of iron is more complex, as the silicate-metal partition coefficient is close to 1 at relevant fO_2 (e.g., Holzheid and Palme 2007). In other words, the available iron in the bulk composition will be more or less evenly distributed between the core (where it occurs in reduced metallic form) and in the bulk silicate (where it occurs in oxidized form). As such, the mass of the core is not uniquely constrained by bulk composition, and a wide range of core mass is possible. A lower bound is provided by the mass of S and Ni, and an upper bound is provided by the case in which all available iron is in the core (i.e., the bulk silicate contains no iron). Despite the wide range of possible solutions, it is of note that there is a quantitative link between calculated core size and the Mg# (100 × molar Mg/(Mg + Fe)) of the bulk-silicate fraction of the body, as illustrated in Fig. 1a. For example, the minimum mass fraction of the core for a differentiated parent body of H-chondrite composition is on the order of 5%, in which case, the corresponding bulk silicate has a low Mg# of approximately 55, while the upper bound on core mass is approximately 30%, when the Mg# of the silicate fraction is 100. In detail, maximum core size and Mg# are also functions of assumed bulk composition, as illustrated in Fig. 1a where results for the H and L groups are compared. The question then becomes how to distinguish between these potential solutions and constrain the core size and composition of a given bulk composition, a step that requires consideration of the crustal rocks as detailed below.

Composition of the Crust and Its Implications

The crustal region of Vesta (as sampled by the HED meteorite suite) would appear to be a complex mixture of ultramafic Opx-rich cumulates (diogenite), gabbroic cumulates (cumulate eucrites), and various basaltic lithologies of diverse geochemistry (i.e., main-group eucrites, Stannern trend eucrites). Significant uncertainty surrounds the details of the petrogenesis of many of the HED lithologies, in particular, the diogenites and the Stannern-trend eucrites (e.g., Stolper 1977; Mittlefehldt 1994; Mittlefehldt and Lindstrom 2003; Barrat et al. 2007, 2008; Mittlefehldt et al. 2011). On the other hand, there is broad consensus that the main-group basaltic eucrites are samples of the magmatic crust of the parent asteroid (e.g., Stolper

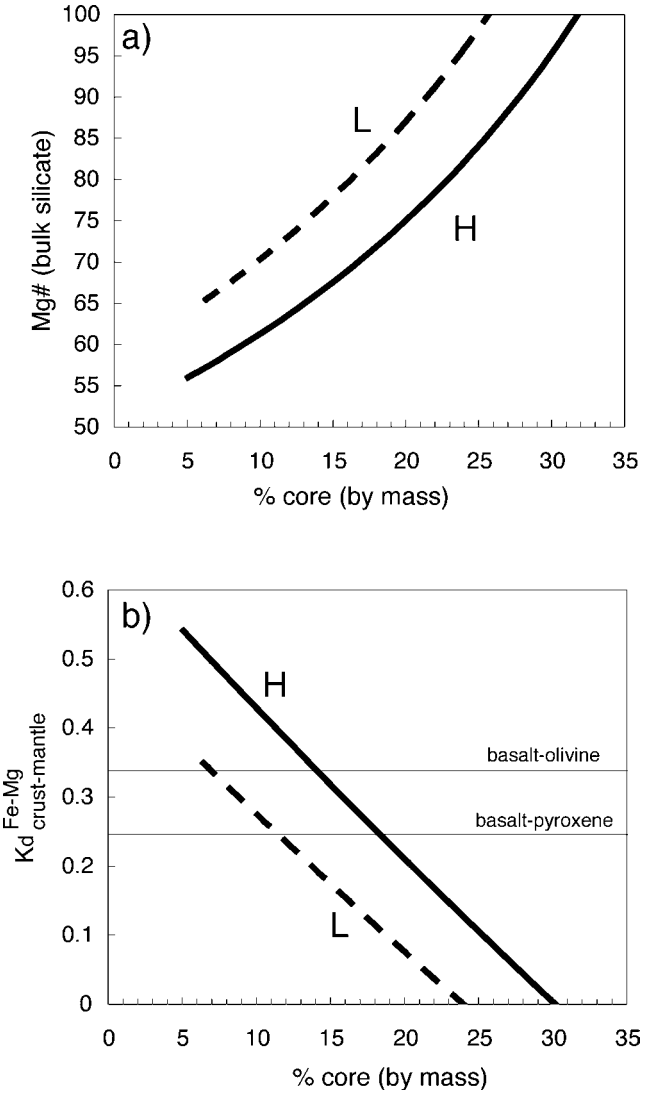

Fig. 1. a) Variation of the Mg# of the bulk mantle (defined as 100 × molar Mg/(Fe + Mg)) as a function of the mass of the core calculated for bulk compositions corresponding to H chondrite (continuous line) and L chondrite (dashed line). b) Variation of $K_{d_{mantle-Juvinas}}^{Mg-Fe}$ (defined as molar $(Mg/Fe^{2+})_{Juvinas}/(Mg/Fe^{2+})_{mantle}$) as a function of the mass of the core calculated for bulk compositions corresponding to H chondrite (continuous line) and L chondrite (dashed line). Values of K_d corresponding to pure olivine and pure pyroxene are shown for reference.

1977; Takeda 1997; McSween et al. 2011), as these samples show simple geochemical variations compatible with fractional crystallization of liquid in a near-surface environment. More importantly, as demonstrated by Stolper (1977), the most Mg-rich members of the main group are compatible with production by direct equilibrium melting of the primitive (i.e., chondritic) mantle (and/or equilibrium crystallization of a magma ocean; Righter and Drake 1997), a result that has far-reaching implications. For example, it implies that at least some preserved eucritic liquids were in chemical equilibrium with the Vestan interior, providing indirect constraints on the latter, as described below. Second, as samples of putative primary magma composition, the primitive main-group (PMG) eucrites may be used as a proxy for the composition of an average "geochemical" crust.

In light of these considerations, the "crust" of our differentiated parent bodies is assumed to have the composition of the primitive main-group eucrite Juvinas (Kitts and Lodders 1998). The link between this geochemical crust and the petrologically diverse near-surface region of the HED parent body will be discussed below, but, for the moment, we will consider what may be learned from the chemistry of Juvinas, assuming that it was in equilibrium with the vestan mantle. First of all, the REE content of Juvinas may be used to provide a direct estimate of the fraction of basaltic crust relative to the bulk silicate, assuming that the REE are perfectly incompatible during melting/crystallization. Given this relative mass fraction of basaltic crust and knowing its composition (i.e., Juvinas), the composition of the residual mantle may thus be calculated by mass balance if the bulk-silicate composition is known. For example, in this way, the FeO and MgO content of the residual mantle may be calculated. This is of significant interest, as the thermodynamics of Fe-Mg partitioning between olivine, pyroxene, and coexisting basaltic liquid are relatively simple and well known (e.g., Roeder and Emslie 1970; Beattie et al. 1991; Toplis 2005). In other words, the Mg/Fe ratio of the basaltic crust and that of the coexisting mantle are not independent, but are thermodynamically related through the Ol-liq and Px-liq exchange coefficients, $K_{d_{Ol-Liq}}^{Mg-Fe}$ and $K_{d_{Px-Liq}}^{Mg-Fe}$, defined as molar $(Mg/Fe^{2+})_{liq}/(Mg/Fe^{2+})_{\phi}$ where ϕ is olivine or pyroxene. For example, the model of Toplis (2005) may be used to calculate that $K_{d_{Ol-Liq}}^{Mg-Fe}$ has a value of approximately 0.35 for a liquid of Juvinas composition at 1170 °C (the liquidus temperature constrained experimentally by Stolper 1977), while experimental data in ferro-basaltic systems (e.g., Grove and Bryan 1983; Toplis and Carroll 1995) can be used to constrain the relevant $K_{d_{Px-Liq}}^{Mg-Fe}$ to be approximately 0.24.

A combined consideration of the distribution of iron between core, mantle, and crust may then be undertaken to constrain thermodynamically plausible solutions. For example, a given mass fraction of iron in the core results in an apparent $K_{d_{mantle-crust}}^{Mg-Fe}$, as illustrated in Fig. 1b. A cursory glance at this figure shows that of all the possible core mass fractions, only a restricted range is compatible with plausible Fe-Mg exchange coefficients. An even more stringent constraint

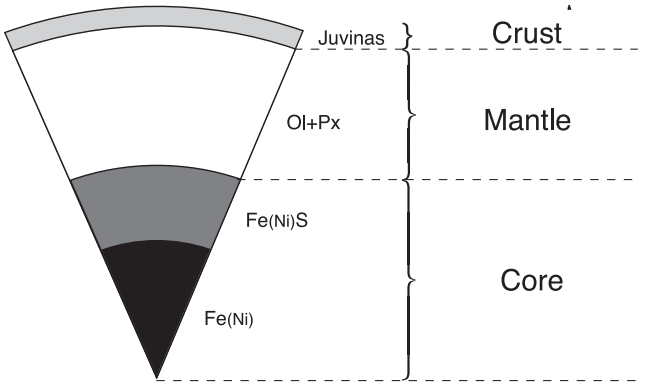

Fig. 2. Schematic section used to model fully differentiated chondritic parent bodies. The crust is assumed to have the composition of the primitive main-group eucrite Juvinas, the mantle is treated as a mixture of olivine and pyroxene, while both a metal component and sulfide component are considered for the core (see text for more details).

on core size can be made if the relative proportions of olivine and pyroxene in the mantle can be predicted. This is possible if the mantle contains negligible plagioclase (as suggested by a flat REE pattern and phase equilibria arguments: Stolper 1977). In this case, the molar ((Ca + Mg + Fe)/Si) ratio of the calculated mantle residue may be used as a crude indicator of the relative proportions of olivine and pyroxene, because $((Ca + Mg + Fe)/Si)_{Px} = 1$, while $((Ca + Mg + Fe)/Si)_{Ol} = 2$).

In summary, consideration of Fe-Mg partitioning constitutes the fundamental basis of our approach. An iterative process is applied to find the iron content of the core for a given bulk composition that results in a bulk $K_{d_{mantle-Juvinas}}^{Mg-Fe}$ that is the mean of the values for olivine and pyroxene weighted by their calculated relative fractions in the mantle.

Relative Masses, Volumes, and Thicknesses

The method described above provides estimates of the relative masses of the core (Fe-Ni-S), the mantle, and the basaltic crust, as shown schematically in Fig. 2. In detail, the core is divided into a sulfide component and a metal component of identical Fe/Ni ratio. While the latter assumption may not be correct in detail, available experimental data suggest that this is a reasonable first-order approximation at high temperature (Chabot et al. 2007). Relative masses are then converted into absolute masses using the mass of Vesta constrained by the Dawn mission (Russell et al. 2012). Masses are subsequently converted into volumes, using mineral densities. The values used are 1-bar room-temperature densities, as follows: Fe, 7874 kg m^{-3}; Ni, 8900 kg m^{-3}; FeS, 4840 kg m^{-3}; NiS, 5300 kg m^{-3}; mantle olivine, 3690 kg m^{-3} (employing the grain density of Chassigny—a dunite sample of equivalent Mg#—as an analog); mantle pyroxene, 3420 kg m^{-3} (employing the grain density of diogenite as an analog); crust (Juvinas), 3180 kg m^{-3} (Consolmagno et al. 2008). The total volume is calculated for each bulk composition and compared with the measured volume of Vesta (Russell et al. 2012). In all cases, the Dawn-derived volume is larger than that predicted by summing individual units. This difference may be related to uncertainties in the density values used, or may be the result of porosity on Vesta, caused either by thermal contraction from a high-temperature state and/or the role of impacts, some of which may have been large enough to cause body-wide disruption (e.g., Buczkowski et al. 2012; Schenk et al. 2012). Assigning this volume difference to porosity and assuming uniform distribution throughout the silicate portion of the theoretical parent bodies, the thickness of the core, mantle, and crust is calculated assuming spherical geometry (Fig. 2), and the average densities of each unit are calculated.

RESULTS

A summary of the calculated masses, thicknesses, densities, and other relevant compositions/mineralogies for each of the different bulk compositions can be found in Table 1. The principal differences concern the size and density of the core on the one hand, and the thickness of the crust and the mineralogy of the mantle on the other.

Core Size, Composition, and Density

All bulk compositions have a significant core, but the relative proportions of metal and sulfide can be widely different. Of note is that solutions corresponding to the CI and LL groups have a negative calculated metal fraction, implying that no satisfactory thermodynamic solution is possible in these cases. For the other groups, the metal fraction (relative to sulfide) is predicted to be as little as approximately 20% (in the case of a CM bulk composition), to almost 100% (in the case of a CH bulk composition). These highly variable metal/sulfide ratios lead to a wide range of predicted average core density, spanning values from approximately 5000 to almost 8000 kg m^{-3} (Table 1; Fig. 3). Furthermore, total core mass is predicted to vary from a little less than 10% by mass of the parent body (in the case of CV, CK, and L chondrites), to as much as approximately 30% in the case of CH and EH bulk compositions. However, core size (radius) is typically predicted to be in the range 100–120 km. Total

Table 1. Predicted characteristics of fully differentiated Vesta-sized parent bodies of chondritic composition.

	CI	CM	CO	CV	CK	CR	CH	LL	L	H	EL	EH	¾H + ¼CM
Mass (10^{19} kg)													
Mass FeNi	−1.03	0.63	1.26	0.46	0.82	1.65	7.31	−0.24	0.71	2.60	1.13	2.87	2.19
Mass FeNiS	5.84	2.85	1.45	1.60	1.26	1.47	0.26	1.66	1.56	1.41	2.37	4.22	1.71
Mass core	4.81	3.48	2.71	2.06	2.07	3.12	7.57	1.42	2.27	4.00	3.50	7.08	3.90
Mass mantle	17.77	18.49	19.17	18.96	19.92	19.85	15.75	21.12	20.18	18.68	21.14	16.38	18.63
Mass crust	3.33	3.94	4.02	4.89	3.92	2.94	2.59	3.37	3.46	3.22	1.27	2.45	3.38
%Mass core	18.6	13.4	10.5	8.0	8.0	12.0	29.2	5.5	8.8	15.5	13.5	27.3	15.1
%Mass mantle	68.6	71.4	74.0	73.2	76.9	76.6	60.8	81.5	77.9	72.1	81.6	63.2	71.9
%Mass crust	12.8	15.2	15.5	18.9	15.1	11.4	10.0	13.0	13.3	12.4	4.9	9.4	13.0
$\%Ni/(Ni + Fe)_{core}$	14.4	15.5	16.9	24.0	21.8	14.3	9.2	32.8	18.2	11.7	12.9	8.4	12.3
$\%Fe/(Fe + FeS)_{core}$	—	18	47	22	39	53	97	—	31	65	32	40	56
$\%Ol/(Ol + Px)_{mantle}$	93.7	95.0	95.9	116.7	100.0	82.3	65.4	54.6	55.4	62.0	30.7	11.1	68.2
Bulk porosity (%)	7	8	8	7	7	8	18	3	5	9	6	10	8
Thickness (km)[a]													
Crust	14.5	17.3	17.6	21.3	16.8	13.0	15.4	13.4	14.2	14.4	5.4	11.6	15.0
Mantle	110.6	128.0	141.5	143.5	150.1	142.2	113.8	158.4	148.5	133.7	142.0	107.0	132.4
Core	136.4	116.3	102.5	96.9	94.6	106.4	132.3	89.8	98.9	113.5	114.2	143.0	114.2
Density (kg m^{-3})[a]													
Crust	2909	2915	2924	2952	2952	2901	2533	3089	3026	2877	2981	2798	2885
Mantle	3358	3370	3382	3471	3425	3320	2861	3460	3392	3241	3279	3034	3266
Core	4529	5281	6005	5425	5838	6175	7802	4684	5607	6540	5600	5786	6259

[a]For calculations of thickness and density, bulk porosity was distributed uniformly throughout the silicate portion of the parent body.

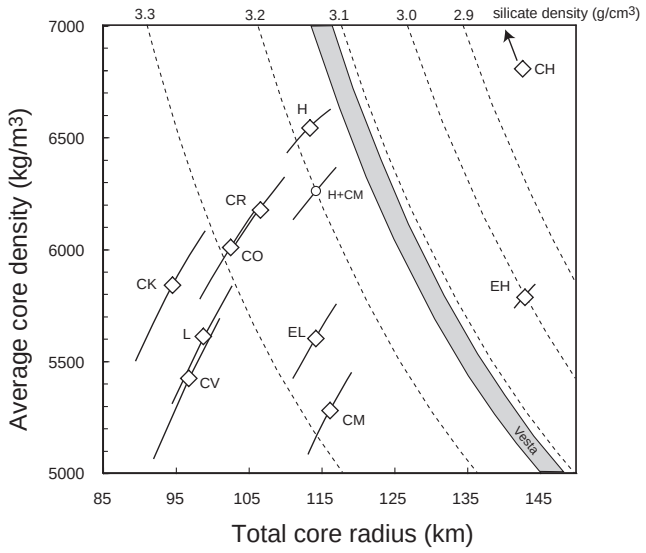

Fig. 3. Covariation of predicted core size (radius) and average core density. Open diamonds indicate the optimal solution calculated using the methods described in the text for each of the tested bulk chondrite compositions, as labeled. The open circle is a ¾ H: ¼ CM mixture, considered as a plausible analog of Vesta (see text for details). The solid lines around each point correspond to the range of acceptable solutions when the optimal value of K_d is varied by ±0.03. Thin dashed lines correspond to solutions of core size/density that are compatible with fixed values of bulk-silicate density in a simple two-layer model of Vesta (values of silicate density, as labeled). The gray region is the family of solutions that are consistent with gravity constraints from the Dawn mission.

core size (metal + sulfide) and average core densities nevertheless span a significant range, as illustrated in Fig. 3. This figure shows optimal values calculated using the methods described above (open symbols), as well as an indication of the range of possible solutions in each case (shown as solid lines), the latter calculated assuming a variation in $K_{d_{mantle-Juvinas}}^{Mg-Fe}$ of ±0.03 around the optimal value. The implications of these results in light of the geophysical/gravity data of the Dawn mission will be discussed below.

Mineralogy and Thickness of the Crust-Mantle System

The calculated mineralogy of the residual mantle is highly variable from one bulk composition to another, the mantle of carbonaceous chondrites being predicted to be almost pure olivine, while that of the enstatite chondrites is predicted to be dominated by pyroxene (Table 1). The ordinary chondrites are intermediate in this respect with 50–60% of the mantle being predicted to be olivine. An additional parameter of interest is the proportion of pyroxene relative to that of the eucrite crust, given that the howardites have a high proportion of diogenite mixed in with crustal eucrites (e.g., Warren 1985; Warren et al. 2009). As illustrated in Fig. 4, the mass of available pyroxene is typically well below that of the eucrite crust for the carbonaceous chondrites, but represents a mass at least equivalent to that of the crust for the ordinary and enstatite chondrites.

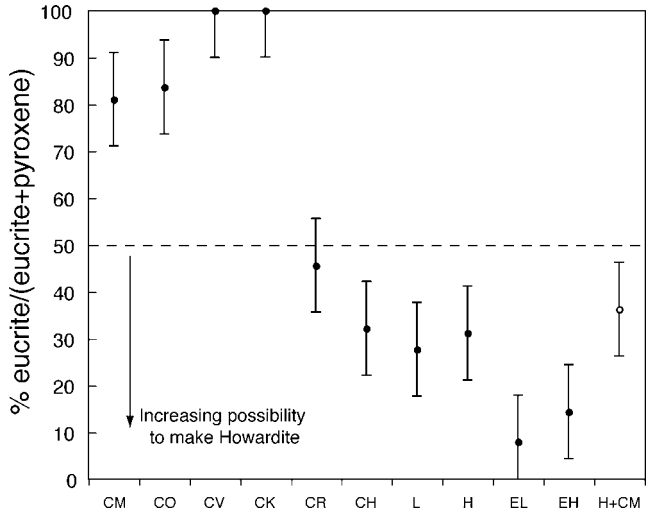

Fig. 4. Calculated proportion of eucrite (crust)/(eucrite+pyroxene) for each of the studied bulk compositions. Values of this parameter >50 (dashed line) make howardite formation unlikely due to a lack of pyroxene.

The degrees of partial melting necessary to reproduce the REE concentrations in Juvinas are in the range 5–9%, corresponding to a crustal thickness typically on the order of approximately 15 km, the total range covering 5–21 km, being thinnest for the EL composition and thickest for the CV composition (Table 1).

DISCUSSION

The thermodynamically constrained mass-balance calculations presented above highlight the important role of bulk composition, illustrating the potential variability in internal structure, mineralogy, and local composition of fully differentiated Vesta-sized parent bodies, even for the seemingly restricted compositional range of chondrites. In light of this variability, we will now assess which, if any, of these compositions provides the most satisfactory fit to known geochemical/geophysical properties of the HED meteorites/Vesta.

Making a Eucritic Crust

One of the principal limits of the approach employed above is that it arbitrarily assumes that the geochemical crust of each differentiated parent body has the major-element chemistry of Juvinas. While phase-equilibria constraints are consistent with the idea that Juvinas is a liquid in equilibrium with residual mantle (e.g., Stolper 1977), it is worth assessing to what extent partial melting of chondritic compositions really can produce Juvinas-like liquids or not.

Some experimental data relevant to this issue exist (e.g., Jurewicz et al. 1993, 1995a) and certain silicate inclusions in iron meteorites have been interpreted as the melting products of chondritic precursors (e.g., Takeda et al. 2000, 2003), but data are not available for all of the chondritic groups modeled here. For this reason, the MELTS thermodynamic calculator (Ghiorso and Sack 1995) has been used. The bulk-silicate composition (mantle + crust) calculated for each chondrite using the methods described above was used as an input to the MELTS model. Calculations were performed at oxygen fugacity conditions corresponding to the Fe-FeO buffer at 1 bar, assuming equilibrium melting/crystallization. Liquid compositions were calculated from the liquidus to close to the solidus typically in temperature steps of 10° in the range 1250–1600 °C and steps of 1° in the range 1100–1250 °C. The similarity of each liquid to Juvinas was quantified using the parameter:

$$\xi = \sqrt{\frac{1}{n}\Sigma_i\left(\frac{(c_i^{\mathrm{Liq}} - c_i^{\mathrm{Juv}})}{\sigma_{\mathrm{i}}^{\mathrm{Juv}}}\right)^2} \quad (1)$$

where c_{i} is the concentration of oxide i (in the liquid, or Juvinas), σ_{i} is the 2-sigma uncertainty in the concentration of oxide component i in Juvinas (derived from values given by Kitts and Lodders 1998), and n is the number of oxide components considered (seven in our case, SiO_2, Al_2O_3, TiO_2, MgO, FeO, CaO, Na_2O). If the calculated values for all oxide components are within the permitted bounds for Juvinas, then the value of ξ will be ≤ 1, increasing values of ξ indicating a calculated composition that is further and further away from that of Juvinas. For this exercise, the minimum value of ξ is not the only parameter of interest, as the temperature at which ξ reaches a minimum would ideally correspond to a degree of partial melting/crystallization consistent with that derived from analysis of the REE. In addition, the fact that the REE spectrum of Juvinas shows no europium anomaly would indicate that feldspar is not a stable crystalline phase in the temperature range corresponding to generation of Juvinas-like liquids, and that constraint too will be considered when assessing the results of the MELTS modeling.

The results of the detailed thermodynamic modeling show that none of the bulk chondritic compositions are capable of producing Juvinas-like liquids, the minimum values of ξ being typically >4. In particular, calculated silica contents are systematically well above that of Juvinas at relevant degrees of partial melting/crystallization. Furthermore, calculated values of Na_2O are also well in excess of those of Juvinas, consistent with the well-known depletion in alkalis of the HED suite in general relative to typical chondrites (e.g.,

Table 2. Characteristics of predicted parent bodies and their agreement with constraints from the howardite–eucrite–diogenite meteorites and/or Vesta.

	CM	CO	CV	CK	CR	CH	L	H	EL	EH	¾H+¼CM
Closest fit to Juvinas, ξ[b]	**1.1**[a]	**1.0**	3.7	1.8	**1.1**	**1.0**	1.2	**0.7**	2.5	3.4	**0.9**
Fe/Mn	68–85	87–109	107–133	101–127	76–96	99–123	50–63	**37–47**	64–81	**36–45**	**42–52**
Gravity data[c]	>−100	>−100	>−200	>−200	>−100	>200	>−200	**< −100**	>−100	>100	**< −100**
% eucrite/ (eucrite + Px)	81	84	100	100	46	**32**	**28**	**31**	**8**	**14**	**36**
Consistent with Righter	No	**Yes**	**Yes**	–	–	–	No	**Yes**	–	–	–
$\Delta^{17}O$	low	low	low	low	low	low	high	high	high	high	**OK**
Oxidation state	oxidized	**OK**	**OK**	–	reduced	reduced	reduced	reduced	reduced	reduced	**OK**

[a]Values indicated in bold show a satisfactory fit to constraints from the HED/Vesta. Others do not.
[b]See text for details concerning the definition of ξ.
[c]The values indicated are the minimum offset between the predicted density of the bulk-silicate mantle derived from the core size and density calculated here, and that constrained by the gravity data of the Dawn mission (in kg m^{-3}).

McSween et al. 2011). In light of this observation, and the fact that alkalis are known to strongly affect the silica content of olivine+pyroxene saturated liquids (e.g., Kushiro 1975; Jurewicz et al. 1995b; Hirschmann 2000), further simulations have been performed, modifying the initial Na_2O content of the bulk to a value of $0.43 \times F_{Juv}$ (where 0.43 corresponds to the wt% Na_2O in Juvinas, and F_{Juv} is the degree of partial melting predicted from the REE for the bulk composition of interest).

The results obtained are significantly different from those obtained in the alkali-rich case (Fig. 5). Ten bulk compositions were considered (CI and LL were not modeled in light of the negative metal core fractions) and of these, both of the enstatite chondrites and the CV group provided very poor fits to Juvinas for all degrees of partial melting/crystallization (see Table 2). The CK group and, to a lesser extent, the L-group also show poor agreement. On the other hand, minimum values of ξ for the CM, CO, CR, and CH groups are marginally consistent with production of Juvinas, while the simulations for the H-chondrite provide the best match of all tested compositions (Fig. 5). For all cases for which ξ falls to values close to 1, the fraction of liquid is generally consistent with values derived from the REE and to within a few Kelvin; all liquids are predicted to be unsaturated in plagioclase (Fig. 6). Furthermore, predicted temperatures for these groups (CM, CO, CR, CH, and H) are perfectly consistent with those measured experimentally by Stolper (1977) for the liquidus of Juvinas. The data shown in Figs. 5 and 6 thus indicate that certain bulk compositions are unlikely to have produced Juvinas-like liquids at any point during magmatic evolution, while for others, an excellent self-consistent scenario emerges.

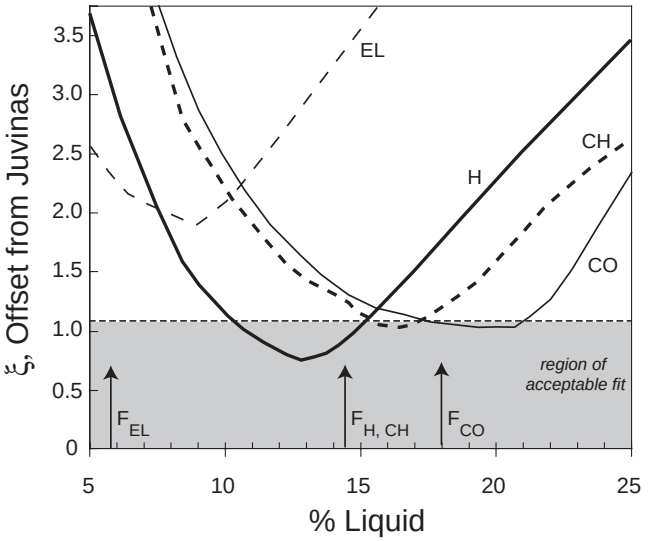

Fig. 5. Similarity of liquids predicted by MELTS to Juvinas, as a function of the fraction of liquid (see text for details), calculated for the silicate fraction of EL, H, CH, and CO groups. In all cases, the Na_2O content of the bulk composition was modified as described in the text. Values of ξ less than 1 indicate models that are indistinguishable from the composition of Juvinas at the 2 sigma level. Vertical arrows indicate the fraction of liquid expected for the EL, H, CH, and CO groups based upon analysis of their REE concentrations (see Table 1).

Fe/Mn Ratios of the Crust

An additional geochemical constraint of potential interest is the Fe/Mn ratio of the bulk silicate. Indeed, as discussed by Boesenberg and Delaney (1997), the HED parent body is known to have rather constant Fe/Mn, in the range 30–45. Assuming that Mn is not partitioned into the core, the Mn concentration of different chondrite groups can be combined with the

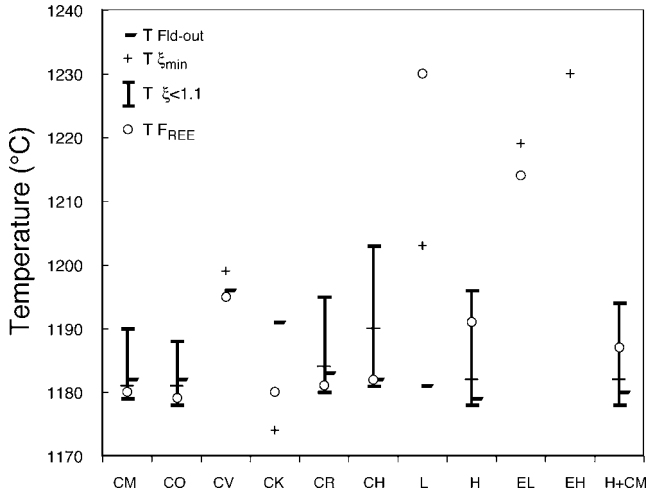

Fig. 6. Summary of MELTS results concerning the compositional similarity of predicted liquids and Juvinas. For each bulk composition, the small horizontal bars represent the temperature at which plagioclase is no longer a stable phase; the cross represents the temperature at which ξ is a minimum, while the open circle represents the temperature at which melt fraction is that derived from consideration of the REE. In addition, the temperature range over which ξ is ≤1 is shown by a solid bar, where applicable. Ideally, the cross and circle should be concordant, for a value of $\xi \leq 1$, at a temperature above the liquidus of plagioclase (see text for more details).

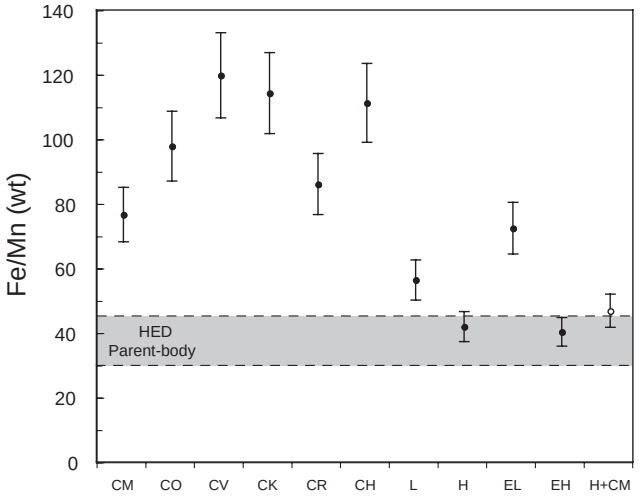

Fig. 7. Predicted Fe/Mn for the silicate portion of each bulk composition considered. In each case, the upper bound is calculated directly from mass balance calculations once Fe had been partitioned into the core, while the lower bound takes into account a possible effect of olivine/pyroxene crystallization (see text for more details). The range described for the howardite–eucrite–diogenite parent body is indicated in gray.

bulk-silicate Fe content calculated above to constrain bulk-silicate Fe/Mn. These values provide an upper bound as olivine and/or pyroxene crystallization may act to decrease the Fe/Mn of the liquid. A lower bound has thus been estimated using a value for $K_{d_{ol/px-liquid}}^{Mn-Fe}$ of approximately 1.3 (e.g., Snyder and Carmichael 1992), as illustrated in Fig. 7. This comparison shows that with the exception of the H and EH chondrites, the calculated values of Fe/Mn are typically well above the range observed in the HEDs.

Geophysical and Geochemical Properties of the Core

The calculated variations in core size/density (e.g., Fig. 3) also provide a potential means of constraining relevant bulk composition. For example, the measured bulk density of Vesta and its J2 gravity coefficient determined by the Dawn mission may be used to constrain internal mass concentration (Russell et al. 2012). Using simple 2-layer models, it may be shown that for reasonable values of oblateness, the density of the upper silicate layer is well constrained by J2 to have a value in the range 3050–3140 kg m^{-3} (Russell et al. 2012). This range of silicate density provides a stringent constraint on the size and density of the core, as illustrated in Fig. 3. Interestingly, none of the predicted cores provide a perfect match to the geophysically constrained range of acceptable values, although the closest approach is for the H-chondrite composition (Fig. 3).

On a related note, the concentrations of siderophile elements in eucrite basalts have been used to constrain estimates of core mass assuming a number of different bulk compositions (Righter and Drake 1997). Although not all chondrite groups were tested, it is of interest to compare the estimates of Righter and Drake (1997) with the values derived here, to assess to what extent the results of these two independent approaches are concordant. This comparison shows that for the CI, CV, CO, and H groups, the mass of the core predicted here and that predicted by Righter and Drake (1997) are in excellent first-order agreement, while values for the L, LL, and CM groups are not concordant (Fig. 8).

Oxidation State and Oxygen Isotopes

In the mass-balance calculations described above, the element oxygen was left unconstrained, its final concentration being ultimately fixed by the core-mantle redox equilibrium. As such, the final oxidation state of our differentiated chondrite parent bodies is not necessarily the same as that of bulk chondrite materials as they are found today. Indeed, with the exception of the EH-composition, all the other compositions studied here had a final calculated $Fe^{2+}/(Fe^{2+} + Fe^0)$ ratio of 0.6–0.8, whereas the starting materials have $Fe^{2+}/(Fe^{2+} + Fe^0)$ varying from 0 to 1, as illustrated in Fig. 9. Comparing the bulk oxidation state of natural chondrites with those predicted to be in equilibrium

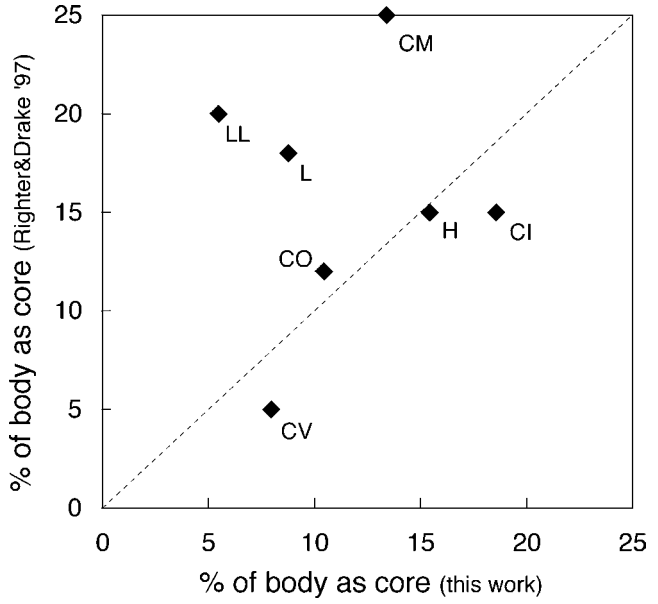

Fig. 8. Values of the % of parent body as core derived from this work, compared with values predicted by Righter and Drake (1997) from the concentrations of siderophile elements (Ni, Co) in eucrite basalts.

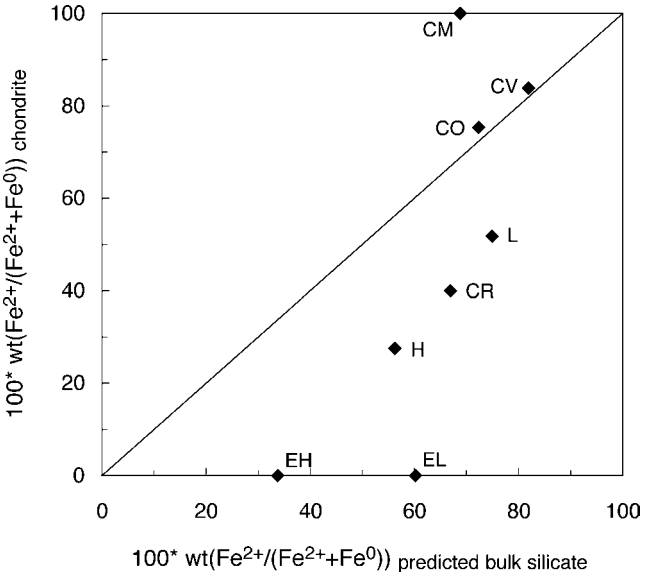

Fig. 9. Comparison of the bulk $Fe^{2+}/(Fe^{2+} + Fe^0)$ ratio required to satisfy the geochemical constraints of a eucrite crust (this work) with values of bulk $Fe^{2+}/(Fe^{2+} + Fe^0)$ for the different bulk chondrite groups as observed today.

with eucrite basalts, it is found that CV and CO groups require the least change in oxidation state, that EH, EL, H, L, CR, and CH groups require various amounts of oxidation, while the CM group requires reduction (Fig. 9). It is also of note that in light of the extremely reducing conditions recorded by the natural enstatite chondrite groups (e.g., McCoy et al. 1999; Berthet et al. 2009), the amount of oxidation required to reach the values of $Fe^{2+}/(Fe^{2+} + Fe^0)$ modeled here makes such a scenario unlikely.

Overview of the Constraints on Bulk Composition

Based upon our analysis, each of the predicted properties can be considered to constrain likely bulk composition (Table 2). First of all, simple mass-balance arguments would seem to exclude CI and LL bulk compositions, as these are predicted to have a negative metal fraction. Second, modeling of the production of Juvinas-like liquids using MELTS would likewise seem to exclude the enstatite chondrites, the carbonaceous groups CV and CK, and to a lesser extent, the L-ordinary chondrites. Of the five remaining groups, the carbonaceous chondrites CO and CM have a mantle that is far too rich in olivine to produce the volumes of pyroxene seen in typical howardites. Furthermore, CO, CM, CR, and CH chondrites all have predicted Fe/Mn well in excess of that of the HED parent body. On the other hand, the H-chondrite composition provides the closest fit to a Juvinas-like crustal composition (Fig. 5); it has a mantle relatively rich in pyroxene capable of producing abundant diogenite/howardite (Table 1; Fig. 4), and it is the only nonenstatite group with a Fe/Mn ratio compatible with eucrites (Fig. 7). In addition, the predicted bulk-silicate density (derived from predicted core size and density) is within 100 kg m^{-3} of solutions constrained by gravity and density data of the Dawn mission (Fig. 3). Taken together, a surprisingly coherent picture thus emerges, with an Na-depleted H-chondrite composition fulfilling almost all of the necessary criteria. Interestingly, this conclusion is perfectly consistent with the trace element chemistry of the HED suite, as described by Morgan et al. (1978) over 30 years ago.

However, the match is not perfect, in particular in terms of oxidation state, but more importantly in terms of oxygen isotopes, the latter providing a well-defined "fingerprint" for many different groups of meteorite (e.g., Clayton 1993). In this respect, it is of note that none of the chondrite groups provide a perfect match to the oxygen isotopic composition of the HED suite (see Fig. 10), leading several authors to propose a mixed origin (e.g., Boesenberg and Delaney 1997; Righter and Drake 1997). While it is possible that a body with a bulk composition similar to that of the H-chondrite, but with a different isotopic signature, may have existed, we briefly explore which mixture of known chondrite parent bodies provides the best fit to the available data. In light of the excellent first-order success of H-chondrite, we assume that this composition forms the dominant component by mass. Indeed, of all the chondrite groups

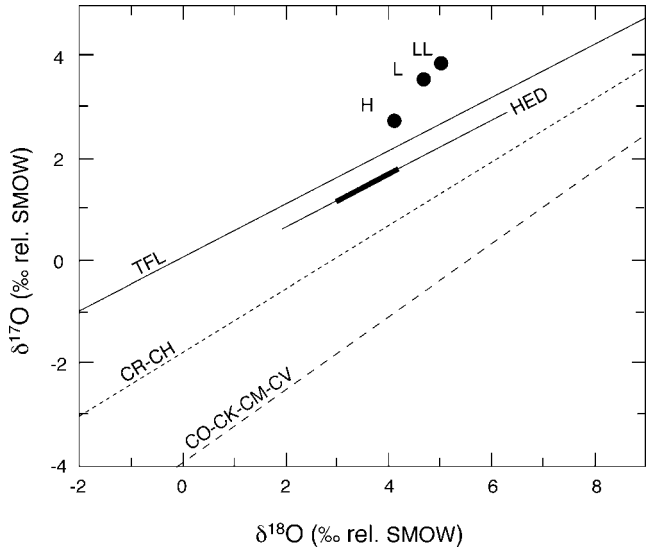

Fig. 10. Summary of the stable oxygen isotope composition of various materials of relevance to Vesta. H, L, and LL correspond to the ordinary chondrite groups. TFL is the terrestrial fractionation line. Howardite–eucrite–diogenite is the eucrite parent body and the thick section of this line is where the majority of samples concentrate (Boesenberg and Delaney 1997). The dashed lines, corresponding to the labeled carbonaceous chondrite groups, were drawn after Clayton and Mayeda (1999).

(with the exception of the enstatite chondrites), it is the H-chondrites that are closest to the HED in terms of O-isotopes. The choice of component to mix would appear to be limited to the carbonaceous groups, as these are the only ones with lower $\Delta^{17}O$ (e.g., Clayton and Mayeda 1999; see Fig. 10). However, to satisfy bulk oxygen isotopes, the calculated proportions of CR or CH material would be on the order of 50%, making such mixtures too rich in carbonaceous material. On the other hand, the relative proportion of CO, CV, CK, or CM would be approximately 25%. Of these possibilities, only addition of a CM component keeps Fe/Mn and core density relations within reasonable bounds of independently constrained values. Furthermore, addition of CM material would add a source of oxidized material, consistent with the bulk oxidation state calculated here that is intermediate between H and CM (Fig. 9). Detailed calculations have thus been performed for a ¾H:¼CM mixture (of reduced Na content), and this composition is found to satisfy all available constraints (see Tables 1 and 2, and Figs. 3, 4, 6, and 7).

A Preliminary Phase Diagram and Olivine in the Mantle

The analysis presented above thus provides estimates of bulk composition that are consistent with many geochemical and geophysical characteristics of the HEDs and/or Vesta. Two of these (H-chondrite and ¾H:¼CM) are summarized in Table 3. While the core composition is a little different in each case, the compositions of the silicate portions are very similar. Using this information, we have used MELTS to calculate a preliminary equilibrium phase diagram relevant to the high-temperature evolution of the vestan mantle (Fig. 11). The calculated differences between the two bulk compositions tested are negligible, both having olivine on the liquidus at a temperature close to 1600 °C. Pyroxene is the second phase to saturate upon cooling, at a temperature a little over 1350 °C for equilibrium crystallization, when the proportion of olivine is approximately 40% of the bulk silicate (and the fraction of melt approximately 60%). Pyroxene and olivine are then predicted to co-crystallize until saturation in plagioclase at 85% crystallization and a temperature a little below 1200 °C (Fig. 11). The solidus is predicted to be at approximately 1150 °C. Taken at face value, this phase diagram thus suggests that if the vestan mantle experienced perfect equilibrium crystallization of a magma ocean (e.g., Righter and Drake 1997) or direct equilibrium melting (e.g., Stolper 1977), then the rocks directly beneath the eucrite crust could contain on the order of approximately 65% olivine. On the other hand, if Vesta experienced a magma ocean, some fraction of the most refractory olivine may have sank to the bottom of the mantle, either because it never melted (due to insufficient ^{26}Al) and/or through crystal settling during cooling. Indeed, Righter and Drake (1997) suggested 20–40% of residual olivine in their analysis of Ni and Co partitioning. In this case, the rocks just below the eucrite crust may contain significantly less olivine than the value expected for perfect equilibrium crystallization. The exact proportion will be a function of the degree of fractional crystallization, and we note that the phase diagram suggests that in the range 1250–1200 °C, the cotectic proportion of olivine is very low (i.e., its proportion is not increasing significantly with decreasing temperature). Indeed, consideration of Fig. 11 shows that a natural consequence of this phase diagram is the generation of rocks with pyroxene as the sole crystallizing phase just prior to feldspar saturation. Although the trace element characteristics of diogenites suggest that their petrogenesis is not simple (e.g., Fowler et al. 1994; Barrat et al. 2008; Mittlefehldt et al. 2011), our analysis therefore implies that precipitation of Opx-rich cumulates does not seem unreasonable from a major-element phase equilibrium perspective (see also Warren 1997; Beck and McSween 2010).

Bulk Composition and Data from the Dawn Mission

One of the principal motivations for this study is to provide a framework for interpretation of data of the

Table 3. Bulk compositions of the silicate and metal fractions of plausible Vesta analogs.

	Bulk silicate[a]							Core[a]		
	wt% SiO_2	wt% TiO_2	wt% Al_2O_3	wt% FeO	wt% MgO	wt% CaO	wt% Na_2O	wt% S	wt% Fe	wt% Ni
H-chondrite	43.39	0.10	2.56	23.87	27.91	2.10	0.06	12.80	76.97	10.23
¾H+¼CM	42.59	0.10	2.70	24.42	27.92	2.20	0.07	16.01	73.67	10.32

[a]The relative mass fractions of bulk silicate and core can be found in Table 1.

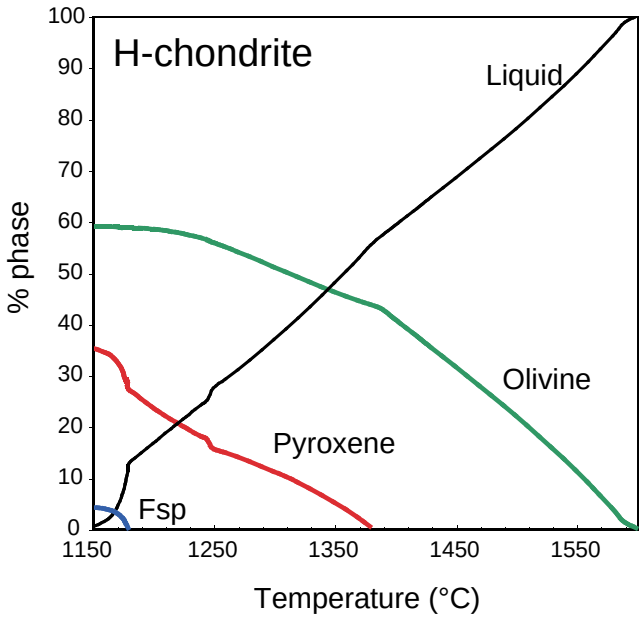

Fig. 11. Phase proportions of liquid, olivine, pyroxene, and plagioclase as a function of temperature predicted by MELTS for equilibrium melting/crystallization of the silicate portion of an Na-depleted H-chondrite bulk composition capable of producing a Juvinas-like liquid.

Dawn mission. For example, the results presented here may be used to predict that a pure eucrite crust on Vesta would have an average thickness on the order of 15 km (last column of Table 2), a value that could be larger if porosity is concentrated in the crust, but smaller if the Jovian Early Bombardment eroded the earliest crust (Turrini et al. 2012). This prediction would appear in first-order agreement with data from the Rheasilvia impact basin, where the depth to diogenite-rich lithologies was found to be on the order of 20 km (McSween et al. 2013). Furthermore, the predicted thickness and density of the principal geochemical reservoirs may also be a useful guide for interpretation of gravity data (e.g., Zuber et al. 2011). However, the stratigraphic section proposed here (e.g., Fig. 2) is clearly an oversimplification as it does not account for the petrologic complexity of the HED suite, nor does it necessarily represent the current configuration of the crust. For example, even if a simple interface between eucrite crust and underlying mafic lithologies once existed (e.g., Takeda 1979, 1997), that interface may have been erased by 4 billion years of impact. In addition, the original crustal structure may have been significantly more complex, with the possible presence of diogenite plutons emplaced throughout the crust (Barrat et al. 2010). Both of these possibilities will add a significant diogenite fraction to the near-surface region (e.g., Jutzi et al. 2013), increasing the thickness of the "crust" and its density relative to values shown in Table 1, and attenuating a sharp density contrast at the base of an eventual eucrite layer, conclusions consistent with analysis of the Dawn gravity data (e.g., Raymond et al. 2013).

Knowledge of the bulk composition is also of interest from a chemical point of view, as, although the HEDs provide an extremely useful basis for interpreting data from the Dawn mission, there is no guarantee that they provide a complete vision of all possible crustal (and mantle) lithologies that are exposed at the surface of Vesta (e.g., Barrat et al. 2009, 2012a). In this respect, our approach has the potential to extend predictions to thermodynamically plausible rock types that are not necessarily present in the HED collection. However, the fact that Juvinas-like liquids cannot be produced from bulk compositions with chondritic concentrations of alkalis (consistent with the depletion in alkalis that characterizes the HED suite) raises the question of whether the HED parent body was assembled from Na-depleted building blocks, or whether Na was lost during differentiation. In the former case, it is possible that other volatile elements were depleted too. In light of the possible loss of sulfur in this case, we have performed additional calculations with reduced concentrations of S. It is found that calculated bulk-silicate compositions are comparable to the full-S case. The core size is predicted to be smaller, but denser, such that average core properties lie along lines of constant bulk-silicate density (i.e., dashed lines of Fig. 3). Alternatively, the high temperatures and low oxygen fugacities during radiogenic heating may have resulted in significant loss of the alkalis (e.g., Tsuchiyma et al. 1981), either during surface volcanism under near vacuum conditions and/or through impact processes at the surface (e.g., Ikeda and Takeda 1985; Nyquist et al. 2003). In this case, severe redistribution of Na and K may have occurred (e.g.,

Mittlefehldt 1987), potentially explaining the existence of K-rich lithologies in certain howardite breccias (e.g., Barrat et al. 2009, 2012b). On the other hand, potassium isotopes do not show severe fractionations (Humayun and Clayton 1995), although the possibility of equilibration between gas and solid/liquid may act to attenuate isotopic fractionation (e.g., Yu et al. 2003; Alexander and Grossman 2005). Finally, it is also of note that many howardites contain a CM component (e.g., Herrin et al. 2011; McSween et al. 2011), and that certain regions of the Vestan surface are potentially rich in volatile-bearing carbonaceous chondrite material (De Sanctis et al. 2012b; Prettyman et al. 2012). In addition, simple models for the thermal evolution of radiogenically heated parent bodies predict the existence of a surface layer of primitive material that was never heated above the metal and/or silicate solidus (e.g., Neumann et al. 2012). In light of our results, the possibility thus arises that the observed CM material in howardites could be the remnants of primitive material. However, we consider this scenario highly unlikely because in that case, even greater fractions of H-chondrite material should be present, inconsistent with petrographic observations of the HED and inconsistent with the Fe/O ratio and neutron adsorption of the Vestan surface measured by GRaND, which would seem to exclude metal-rich materials (e.g., Mittlefehldt et al. 2012).

CONCLUDING REMARKS

The simple mass-balance and thermodynamic constraints employed here illustrate the potential diversity of the geochemical and geophysical properties of a fully differentiated Vesta-sized parent body with a geochemical crust of eucrite composition. However, detailed consideration of the results shows that important constraints on the bulk composition of Vesta are provided, and that the latter would appear to be dominated by a component similar to H-chondrite. Indeed, an Na-depleted H-chondrite bulk composition is capable of producing Juvinas-like liquids, has a mantle relatively rich in pyroxene capable of producing abundant diogenite/howardite, with a Fe/Mn ratio compatible with eucrites. In addition, its predicted bulk-silicate density (derived from calculated average core size and density) is within 100 kg m^{-3} of solutions constrained by gravity and density data of the Dawn mission. However, oxidation state and oxygen isotopes are not perfectly reproduced by this composition and it is deduced that bulk Vesta may contain approximately 25% of a CM-like component.

Identification of an acceptable bulk composition is an important step forward, as it opens the possibility of predicting the mineralogy and composition of solid and liquid products over wide ranges of partial melting and crystallization, provides a useful and self-consistent reference frame for interpretation of the Dawn data. Furthermore, knowledge of the bulk composition (core and bulk silicate) provides essential constraints for thermal and physical models of Vestan evolution at high temperature (e.g., Ghosh and McSween 1998; Gupta and Sahijpal 2010; Moskovitz and Gaidos 2011) that may ultimately lead to a better understanding of the differentiation process on protoplanetary bodies such as Vesta.

Acknowledgments—Enlightening discussions with J.-A. Barrat and formal reviews by H. Takeda and G. J. Taylor are gratefully acknowledged. MT thanks the Centre National d'Etudes Spatiales (CNES) for their financial support, which enabled participation in this work and the Dawn mission.

Editorial Handling—Dr. Carle Pieters

REFERENCES

Alexander C. M. O'D. and Grossman J. N. 2005. Alkali elemental and potassium isotopic compositions of Semarkona chondrules. *Meteoritics & Planetary Science* 40:541–556.

Barrat J.-A., Yamaguchi A., Greenwood R. C., Bohn M., Cotten J., Benoit M., and Franchi I. A. 2007. The Stannern trend eucrites: Contamination of main group eucritic magmas by crustal partial melts. *Geochimica et Cosmochimica Acta* 71:4108–4123.

Barrat J.-A., Yamaguchi A., Greenwood R. C., Benoit M., Cotton J., Bohn M., and Franchi I. A. 2008. Geochemistry of diogenites: Still more diversity in their parental melts. *Meteoritics & Planetary Science* 43:1759–1775.

Barrat J.-A., Bohn M., Gillet P., and Yamaguchi A. 2009. Evidence for K-rich terranes on Vesta from impact spherules. *Meteoritics & Planetary Science* 44:359–374.

Barrat J.-A., Yamaguchi A., Zanda B., Bollinger C., and Bohn M. 2010. Relative chronology of crust formation on asteroid Vesta: Insights from the geochemistry of diogenites. *Geochimica et Cosmochimica Acta* 74:6218–6231.

Barrat J.-A., Yamaguchi A., Bunch T. E., Bohn M., Bollinger C., and Ceuleneer G. 2011. Possible fluid-rock interactions on differentiated asteroids recorded in eucritic meteorites. *Geochimica et Cosmochimica Acta* 75:3839–3852.

Barrat J.-A., Yamaguchi A., Jambon A., Bollinger C., and Boudouma O. 2012a. Low-Mg rock debris in howardites: Evidence for KREEPy lithologies on Vesta? *Geochimica et Cosmochimica Acta* 99:193–205.

Barrat J.-A., Bodenan J. D., Yamaguchi A., Buchanan P. C., and Toplis M. 2012b. What can we learn on Vesta from the petrology of impact melts? (abstract #1438). 43rd Lunar and Planetary Science Conference. CD-ROM.

Beattie P., Ford C., and Russell D. 1991. Partition coefficients for olivine-melt and orthopyroxene-melt systems. *Contributions to Mineralogy and Petrology* 109:212–224.

Beck A. W. and McSween H. Y. 2010. Diogenites as polymict breccias composed of orthopyroxenite and harzburgite. *Meteoritics & Planetary Science* 45:850–872, doi:10.1111/j.1945-5100.2010.01061.x.

Berthet S., Malavergne V., and Righter K. 2009. Evolution of Indarch (EH4 chondrite) at 1 GPa and variable oxygen fugacity. Implications for early planetary differentiation processes. *Geochimica et Cosmochimica Acta* 63:6402–6420.

Binzel R. P. and Xu S. 1993. Chips off asteroid 4 Vesta: Evidence for the parent body of basaltic achondrite meteorites. *Science* 260:186–191.

Bizzarro M., Baker J. A., Haack H., and Lundgaard K. L. 2005. Rapid time-scales for accretion and melting of differentiated planetisimals inferred from ^{26}Al-^{26}Mg chronometry. *The Astrophysical Journal* 632:L41–L44.

Boesenberg J. S. and Delaney J. S. 1997. A model composition of the basaltic achondrite planetoid. *Geochimica et Cosmochimica Acta* 61:3205–3225.

Buczkowski D. L., Wyrick D. Y., Iyer K. A., Kahn E. G., Scully J. E. C., Nathues A., Gaskell R. W., Roatsch T., Preusker F., Schenk P. M., Le Corre L., Reddy V., Yingst R. A., Mest S., Williams D. A., Garry W. B., Barnouin O. S., Jaumann R., Raymond C. A., and Russell C. T. 2012. Large-scale troughs on Vesta: A signature of planetary tectonics. *Geophysical Research Letters* 39:L18205, doi:10.1029/2012GL052959.

Chabot N. L., Saslow S. A., McDonough W. F., and McCoy T. J. 2007. The effect of Ni on element partitioning during iron meteorite crystallization. *Meteoritics & Planetary Science* 42:1735–1750.

Clayton R. N. 1993. Oxygen isotopes in meteorites. *Annual Review of Earth and Planetary Sciences* 21:115–149.

Clayton R. N. and Mayeda T. K. 1999. Oxygen isotope studies of carbonaceous chondrites. *Geochimica et Cosmochimica Acta* 63:2089–2104.

Consolmagno G. J. and Drake M. J. 1977. Composition and evolution of eucrite parent body—Evidence from rare-earth elements. *Geochimica et Cosmochimica Acta* 41:1271–1282.

Consolmagno G. J., Britt D. T., and Macke R. J. 2008. The significance of meteorite density and porosity. *Chemie der Erde Geochemistry* 68:1–29.

De Sanctis M. C., Ammannito E., Capria M. T., Tosi F., Capaccioni F., Zambon F., Carraro F., Fonte S., Frigeri A., Jaumann R., Magni G., Marchi S., McCord T. B., McFadden L. A., McSween H. Y., Mittlefehldt D. W., Nathues A., Palomba E., Pieters C. M., Raymond C. A., Russell C. T., Toplis M. J., and Turrini D. 2012a. Spectroscopic characterization of mineralogy and its diversity across Vesta. *Science* 336:697–700, doi:10.1126/science.1219270.

De Sanctis M. C., Combe J. -Ph., Ammannito E., Palomba E., Longobardo A., McCord T. B., Marchi S., Capaccioni F., Capria M. T., Mittlefehldt D. W., Pieters C. M., Sunshine J., Tosi F., Zambon F., Carraro F., Fonte S., Frigeri A., Magni G., Raymond C. A., Russell C. T., and Turrini D. 2012b. Detection of widespread hydrated materials on Vesta by the VIR imaging spectrometer on board the Dawn mission. *The Astrophysical Journal Letters* 758:L36, doi:10.1088/2041-8205/758/2/L36.

Drake M. J. 2001. The eucrite/Vesta story. *Meteoritics & Planetary Science* 36:501–513.

Dreibus G., Kruse H., Spettel B., and Wänke H. 1977. The bulk composition of the moon and the eucrite parent body. Proceedings, 8th Lunar Science Conference. pp. 211–227.

Fowler G. W., Papike J. J., Spilde M. N., and Shearer C. K. 1994. Diogenites as asteroidal cumulates: Insights from orthopyroxene major and minor element chemistry. *Geochimica et Cosmochimica Acta* 58:3921–3929.

Ghiorso M. S. and Sack R. O. 1995. Chemical mass transfer in magmatic processes. IV. A revised and internally consistent thermodynamic model for the interpolation and extrapolation of liquid–solid equilibria in magmatic systems at elevated temperatures and pressures. *Contributions to Mineralogy and Petrology* 119:197–212.

Ghosh A. and McSween H. Y. 1998. A thermal model for the differentiation of asteroid 4 Vesta, based on radiogenic heating. *Icarus* 134:187–206.

Grove T. L. and Bryan W. B. 1983. Fractionation of pyroxene-phyric MORB at low pressure: An experimental study. *Contributions to Mineralogy and Petrology* 84:293–309.

Gupta G. and Sahijpal S. 2010. Differentiation of Vesta and the parent bodies of other achondrites. *Journal of Geophysical Research* 115:E08001, doi:10.1029/2009JE003525.

Herrin J. S., Zolensky M. E., Cartwright J. A., Mittlefehldt D. W., and Ross D. K. 2011. Carbonaceous chondrite-rich howardites: The potential for hydrous lithologies on the HED parent (abstract #2806). 42nd Lunar and Planetary Science Conference. CD-ROM.

Hevey P. J. and Sanders I. S. 2006. A model for planetesimal meltdown by ^{26}Al and its implications for meteorite parent bodies. *Meteoritics & Planetary Science* 41:95–106.

Hirschmann M. M. 2000. Mantle solidus: Experimental constraints and the effects of peridotite composition. *Geochemistry Geophysics Geosystems* 1, doi:10.1029/2000GC000070.

Holzheid A. and Palme H. 2007. The formation of eucrites: Constraints from metal-silicate partition coefficients. *Meteoritics & Planetary Science* 42:1817–1829.

Humayun M. and Clayton R. N. 1995. Potassium isotope cosmochemistry: Genetic implications of volatile element depletion. *Geochimica et Cosmochimica Acta* 59:2131–2148.

Ikeda Y. and Takeda H. 1985. A model for the origin of basaltic achondrites based on the Yamoto 7308 howardite. Proceedings, 15th Lunar and Planetary Science Conference. pp. C649–C663.

Jurewicz A. J. G., Mittlefehldt D. W., and Jones J. H. 1993. Experimental partial melting of the Allende (CV) and Murchison (CM) chondrites and the origin of asteroidal basalts. *Geochimica et Cosmochimica Acta* 57:2123–2139.

Jurewicz A. J. G., Mittlefehldt D. W., and Jones J. H. 1995a. Experimental partial melting of the St. Severin (LL) and Lost City (H) chondrites. *Geochimica et Cosmochimica Acta* 59:391–408.

Jurewicz A. J. G., Jones J. H., Mittlefehldt D. W., and Longhi J. 1995b. Making melts having 40%, 50%, or 60% SiO_2 from chondritic materials: A synopsis of low-pressure, low-volatile, equilibrium melting relations (abstract #1354). 26th Lunar and Planetary Science Conference. CD-ROM.

Jutzi M., Asphaug E., Gillet P., Barrat J.-A., and Benz W. 2013. The structure of the asteroid 4 Vesta as revealed by models of planet-scale collisions. *Nature* 494:207–210.

Kitts K. and Lodders K. 1998. Survey and evaluation of eucrite bulk compositions. *Meteoritics & Planetary Science* 33:A197–A213.

Kleine T., Mezger K., Palme H., Scherer E., and Munker C. 2005. Early core formation in asteroids and late accretion of chondrite parent bodies: Evidence from ^{182}Hf-^{182}W in CAIs, metal-rich chondrites, and iron meteorites. *Geochimica et Cosmochimica Acta* 69:5805–5818.

Kleine T., Touboul M., Bourdon B., Nimmo F., Mezger K., Palme H., Jacobsen S. B., Yin Q.-Z., and Halliday A. N. 2009. H-W chronology of the accretion and early evolution of asteroids and terrestrial planets. *Geochimica et Cosmochimica Acta* 73:5150–5188.

Kushiro I. 1975. On the nature of silicate melt and its significance in magma genesis: Regularities in the shift of the liquidus boundaries involving olivine, pyroxene, and silica minerals. *American Journal of Science* 275:411–431.

Lodders K. and Fegley B. J. 1998. *The planetary scientist's Companion*. New York: Oxford University Press.

MacPherson G. J., Davis A. M., and Zinner E. K. 1995. The distribution of ^{26}Al in the early solar system. A reappraisal. *Meteoritics* 30:365–386.

McCord T. B., Adams J. B., and Johnson T. V. 1970. Asteroid Vesta: Spectral reflectivity and compositional implications. *Science* 168:1445–1447.

McCoy T. J., Keil K., Muenow D. W., and Wilson L. 1997. Partial melting and melt migration in the Acapulcoite-lodranite parent body. *Geochimica et Cosmochimica Acta* 61:639–650.

McCoy T. J., Dickinson T. L., and Lofgren G. E. 1999. Partial melting of the Indarch (EH4) meteorite: A textural, chemical, and phase relations view of melting and melt migration. *Meteoritics & Planetary Science* 34:735–746.

McSween H. Y. 1999. *Meteorites and their parent planets*. Cambridge, UK: Cambridge University Press.

McSween H. Y., Mittlefehldt D. W., Beck A. W., Mayne R. G., and McCoy T. J. 2011. HED meteorites and their relationship to the geology of Vesta and the Dawn mission. *Space Science Reviews* 163:141–174.

McSween H.Y., Ammannito E., Reddy V., Prettyman T.H., Beck A. W., De Sanctis M. C., Nathues A., Le Corre L., O'Brien D. P., Yamashita Y., McCoy T. J., Mittlefehldt D. W., Toplis M. J., Schenk P., Palomba E., Turrini D., Tosi F., Zambon F., Longobardo A., Capaccioni F., Raymond C. A., and Russell C. T. 2013. Composition of the Rheasilvia basin, a window into Vesta's interior. *Journal of Geophysical Research* 118:335–346.

Mittlefehldt D. W. 1987. Volatile degassing of basaltic achondrite parent bodies: Evidence from alkali elements and phosphorus. *Geochimica et Cosmochimica Acta* 51:267–278.

Mittlefehldt D. W. 1994. The genesis of diogenites and HED parent body petrogenesis. *Geochimica et Cosmochimica Acta* 58:1537–1552.

Mittlefehldt D. W. and Lindstrom M. M. 2003. Geochemistry of eucrites: Genesis of basaltic eucrites, and Hf and Ta as petrogenetic indicators for altered antarctic eucrites. *Geochimica et Cosmochimica Acta* 67:1911–1934.

Mittlefehldt D. W., Beck A. W., Lee C.-T. A., McSween H. Y., and Buchanan P. C. 2011. Compositional constraints on the genesis of diogenites. *Meteoritics & Planetary Science* 47:72–98.

Mittlefehldt D. W., Prettyman T. H., Reedy R. C., Beck A. W., Blewett D. T., Lawrence D. J., McCoy T. J., McSween H. Y., and Toplis M. J. 2012. Do mesosiderites reside on Vesta? An assessment based on Dawn GRaND data (abstract #1655). 43rd Lunar and Planetary Science Conference. CD-ROM.

Morgan J. W., Higuchi H., Takahashi H., and Hertogen J. 1978. A "chondritic" eucrite parent body: Inference from trace elements. *Geochimica et Cosmochimica Acta* 42:27–38.

Moskovitz N. and Gaidos E. 2011. Differentiation of planetesimals and the thermal consequences of melt migration. *Meteoritics & Planetary Science* 46:903–918.

Neumann W., Breuer D., and Spohn T. 2012. Differentiation and core formation in accreting planetesimals. *Astronomy & Astrophysics* 543:A141, doi:10.1051/0004-6361/2012 19157.

Nyquist L. E., Reese Y., Wiesmann H., Shih C. Y., and Takeda H. 2003. Fossil ^{26}Al and ^{53}Mn in the Asuka 8813945 eucrite: Evidence of the earliest crust on asteroid 4 Vesta. *Earth and Planetary Science Letters* 214:11–25.

O'Neill H. S. C. and Mavrogenes J. A. 2002. The sulfide capacity and the sulfur content at sulfide saturation of silicate melts at 1400 degrees C and 1 bar. *Journal of Petrology* 43:1049–1087.

Prettyman T. H., Mittlefehldt D. W., Lawrence D. J., Yamashita N., Beck A. W., Feldman W. C., McCoy T. J., McSween H. Y., Toplis M. J., Titus T. N., Tricarico P., Reedy R. C., Hendricks J. S., Forni O., Le Corre L., Li J.-Y., Mizzon H., Reddy V., Raymond C. A., and Russell C. T. 2012. Elemental mapping by Dawn reveals exogenic H in Vesta's regolith. *Science* 308:242–246.

Qin L., Dauphas N., Wadhwa M., Masarik J., and Janney P. E. 2008. Rapid accretion and differentiation of iron meteorite parent bodies inferred from ^{182}Hf-^{182}W chronometry and thermal modeling. *Earth and Planetary Science Letters* 273:94–104.

Raymond C. A., Park R. S., Asmar S. W., Konopliv A. S., Buczkowski D. L., De Sanctis M. C., McSween H. Y., Russell C. T., Jaumann R., and Preusker F. 2013. Vestalia Terra: An ancient mascon in the southern hemisphere of Vesta (abstract #2882). 44th Lunar and Planetary Science Conference. CD-ROM.

Reddy V., Nathues A., Le Corre L., Sierks H., Li J.-Y., Gaskell R., McCoy T., Beck A. W., Schröder S. E., Pieters C. M., Becker K. J., Buratti B. J., Denevi B. W., Blewett D. T., Christensen U., Gaffey M. J., Gutiérrez Marqués P., Hicks M., Uwe Keller H., Maue T., Mottola S., McFadden L. A., McSween H. Y., Mittlefehldt D. W., O'Brien D. P., Raymond C., and Russell C. 2012. Color and albedo heterogeneity of Vesta from Dawn. *Science* 336:700–704.

Righter K. and Drake M. J. 1997. A magma ocean on Vesta: Core formation and petrogenesis of eucrites and diogenites. *Meteoritics & Planetary Science* 32:929–944.

Roeder P. L. and Emslie R. F. 1970. Olivine-liquid equilibrium. *Contributions to Mineralogy and Petrology* 29:275–289.

Russell C. T. and Raymond C. A. 2011. The Dawn mission to Vesta and Ceres. *Space Science Reviews* 163:3–23.

Russell C. T., Raymond C. A., Coradini A., McSween H. Y., Zuber M. T., Nathues A., De Sanctis M. C., Jaumann R., Konopliv A. S., Preusker F., Asmar S. W., Park R. S., Gaskell R., Keller H. U., Mottola S., Roatsch T., Scully J. E. C., Smith D. E., Tricarico P., Toplis M. J., Christensen U. R., Feldman W. C., Lawrence D. J., McCoy T. J., Prettyman T. H., Reedy R. C., Sykes M. E., and Titus T.

N. 2012. Dawn at Vesta: Testing the protoplanetary paradigm. *Science* 336:684–686.

Ruzicka A., Snyder G. A., and Taylor L. A. 1997. Vesta as the howardite, eucrite, and diogenite parent body: Implications for the size of a core and for large-scale differentiation. *Meteoritics & Planetary Science* 32:825–840.

Schenk P., O'Brien D. P., Marchi S., Gaskell R., Preusker F., Roatsch T., Jaumann R., Buczowski D., McCord T., McSween H. Y., Williams D., Yingst A., Raymond C., and Russell C. 2012. The geologically recent giant impact basins at Vesta's south pole. *Science* 336:694–697, doi:10.1126/science.1223272.

Snyder D. A. and Carmichael I. S. E. 1992. Olivine-liquid equilibria and the chelical activities of FeO, NiO, Fe_2O_3, and MgO in natural basic melts. *Geochimica et Cosmochimica Acta* 56:303–318.

Stolper E. 1977. Experimental petrology of eucritic meteorites. *Geochimica et Cosmochimica Acta* 41:587–611.

Takeda H. 1979. A layered-crust model of a howardite parent body. *Icarus* 40:455–470.

Takeda H. 1997. Mineralogical records of early planetary processes on the howardite, eucrite, diogenite parent body with reference to Vesta. *Meteoritics & Planetary Science* 32:841–853.

Takeda H., Bogard D. D., Mittlefehldt D. W., and Garrison D. H. 2000. Mineralogy, petrology chemistry and ^{39}Ar-^{40}Ar and exposure ages of the Caddo County 1AB iron: Evidence for early partial melt segregation of a gabbro area rich in plagioclase:diopside. *Geochimica et Cosmochimica Acta* 64:1311–1327.

Takeda H., Hsu W., and Huss G. R. 2003. Mineralogy of silicate inclusions of the Colomera IIE iron and crystallization of Cr-diopside and alkali feldspar from a partial melt. *Geochimica et Cosmochimica Acta* 67:2269–2288.

Taylor J. G. 1992. Core formation in asteroids. *Journal of Geophysical Research* 97: 14,717–14,726.

Terasaki H., Frost D. J., Rubie D. C., and Langenhorst F. 2008. Percolative core formation in planetisimals. *Earth and Planetary Science Letters* 273:132–137.

Toplis M. J. 2005. The thermodynamics of iron and magnesium partitioning between olivine and liquid: Criteria for assessing and predicting equilibrium in natural and experimental systems. *Contributions to Mineralogy and Petrology* 149:22–39.

Toplis M. J. and Carroll M. R. 1995. An experimental study of the influence of oxygen fugacity on Fe-Ti oxide stability, phase relations, and mineral-melt equilibria in ferro-basaltic systems. *Journal of Petrology* 36:1137–1170.

Treiman A. H., Lanzirotti A., and Xirouchakis D. 2004. Ancient water on asteroid 4 Vesta: Evidence from a quartz veinlet in the Serra de Mage eucrite meteorite. *Earth and Planetary Science Letters* 219:189–199.

Trinquier A., Birck J. L., Allegre C. J., Gopel C., and Ulfbeck D. 2008. ^{53}Mn-^{53}Cr systematics of the early solar system revisited. *Geochimica et Cosmochimica Acta* 72:5146–5163.

Tsuchiyma A., Nagahara H., and Kushiro I. 1981. Volatilization of sodium from silicate melt spheres and its application to the formation of chondrules. *Geochimica et Cosmochimica Acta* 45:1357–1367.

Turrini D., Coradini A., Federico C., Formisano M., and Magni G. 2012. The primordial history of Vesta and the Jovian early bombardment (abstract #2047). 43rd Lunar and Planetary Science Conference. CD-ROM.

Warren P. H. 1985. Origin of howardites, diogenites and eucrites—A mass balance constraint. *Geochimica et Cosmochimica Acta* 49:577–586.

Warren P. H. 1997. Magnesium oxide-iron oxide mass balance constraints and a more detailed model for the relationship between eucrites and diogenites. *Meteoritics & Planetary Science* 32:945–963.

Warren P. H., Kallemeyn G. W., Huber H., Ulff-Moller F., and Choe W. 2009. Siderophile and other geochemical constraints on mixing relationships among HED-meteorite breccias. *Geochimica et Cosmochimica Acta* 73:5918–5943.

Wasson J. T. and Kallemeyn G. W. 1990. Compositions of chondrites. *Philosophical Transactions of the Royal Society of London* 325:535–544.

Wilson L. and Keil K. 2012. Volcanic activity on differentiated asteroids: A review and analysis. *Chemie der Erde* 72:289–321, doi:10.1016/j.chemer.2012.09.002.

Yu Y., Hewins R. H., Alexander C. M. O'D., and Wang J. 2003. Experimental study of evaporation and isotopic mass fractionation of potassium in silicate melts. *Geochimica et Cosmochimica Acta* 67:773–786.

Zuber M. T., McSween H. Y., Binzel R. P., Elkins-Tanton L. T., Konopliv A. S., Pieters C. M., and Smith D. E. 2011. Origin, internal structure and evolution of 4 Vesta. *Space Science Reviews* 163:77–93.

Bibliography

Amelin, Yuri, & Ireland, Trevor R. 2013. Dating the oldest rocks and minerals in the solar system. *Elements*, **9**(1), 39–44.

Ammannito, E, De Sanctis, M C, Palomba, E, Longobardo, A, Mittlefehldt, D W, McSween, Harry Y, Marchi, S, Capria, M T, Capaccioni, F, Frigeri, A, Pieters, C M, Ruesch, O, Tosi, F, Zambon, F, Carraro, F, Fonte, S, Hiesinger, H, Magni, G, McFadden, L A, Raymond, C A, Russell, C T, & Sunshine, J M. 2013a. Olivine in an unexpected location on Vesta's surface. *Nature*, **504**(7478), 122–125.

Ammannito, Eleonora, De Sanctis, M Cristina, Capaccioni, Fabrizio, Teresa Capria, M, Carraro, F, Combe, Jean-Philippe, Fonte, Sergio, Frigeri, Alessandro, Joy, Steven P, Longobardo, Andrea, Magni, Gianfranco, Marchi, Simone, McCord, Thomas B, McFadden, Lucy A, McSween, Harry Y, Palomba, Ernesto, Pieters, Carli M, Polanskey, Carol A, Raymond, Carol A, Sunshine, Jessica M, Tosi, Federico, Zambon, Francesca, & Russell, Christopher T. 2013b. Vestan lithologies mapped by the visual and infrared spectrometer on Dawn. *Meteoritics & Planetary Science*, **48**(11), 2185–2198.

Asimow, P D, & Ghiorso, M S. 1998. Algorithmic modifications extending MELTS to calculate subsolidus phase relations. *American Mineralogist*, **83**(9-10), 1127–1132.

Barrat, Jean-Alix, & Yamaguchi, Akira. 2014. Comment on "The origin of eucrites, diogenites, and olivine diogenites: Magma ocean crystallization and shallow magma processes on Vesta" by B. E. Mandler and L. T. Elkins-Tanton. *Meteoritics & Planetary Science*, **49**(3), 468–472.

Barrat, Jean Alix, Blichert-Toft, Janne, Gillet, Philippe, & Keller, F. 2000. The differentiation of eucrites: The role of in situ crystallization. *Meteoritics & Planetary Science*, **35**, 1087–1100.

Barrat, Jean-Alix, Yamaguchi, Akira, Greenwood, Richard C, Bohn, Marcel, Cotten, J, Benoit, M, & Franchi, Ian A. 2007. The Stannern trend eucrites: Contamination of main group eucritic magmas by crustal partial melts. *Geochimica et Cosmochimica Acta*, **71**, 4108–4124.

Barrat, Jean Alix, Yamaguchi, A, Greenwood, R C, Benoit, M, Cotten, J, Bohn, A, & Franchi, I A. 2008. Geochemistry of diogenites: Still more diversity in their parental melts. *Meteoritics & Planetary Science*, **43**(11), 1759–1775.

Barrat, Jean-Alix, Bohn, Marcel, Gillet, Philippe, & Yamaguchi, Akira. 2009. Evidence for K-rich terranes on Vesta from impact spherules. *Meteoritics & Planetary Science*, **44**(3), 359–374.

Barrat, Jean-Alix, Yamaguchi, Akira, Zanda, Brigitte, Bollinger, Claire, & Bohn, Marcel. 2010. Relative chronology of crust formation on asteroid Vesta: Insights from the geochemistry of diogenites. *Geochimica et Cosmochimica Acta*, **74**(21), 6218–6231.

Bartels, K S, & Grove, T L. 1991. High-pressure experiments on magnesian eucrite compositions - constraints on magmatic processes in the eucrite parent body. *Proceedings of Lunar and Planetary Science*, **21**, 351–365.

Beck, A W, Lawrence, D J, Peplowski, P N, Prettyman, T H, McCoy, T J, McSween Jr, H Y, Toplis, M J, & Yamashita, N. 2015. Using HED meteorites to interupt neutron and gamma-ray data from asteroid 4-Vesta. *Meteoritics*, **50**(8), 1311–1337.

Beck, Andrew W, & McSween, Harry Y. 2010. Diogenites as polymict breccias composed of orthopyroxenite and harzburgite. *Meteoritics & Planetary Science*, **45**(5), 850–872.

Benachir, Djaouad, Hosseini, Shahram, Deville, Yannick, Karoui, Moussa Sofiane, & Hameurlain, Abdelkader. 2013. Modified independent component analysis for initializing non-negative matrix factorization. *IEEE th International Workshop of Electronics, Control, Measurement, Signals and their application to Mechatronics*, 1–6.

Bercovici, David, & Ricard, Yanick. 2003. Energetics of a two-phase model of lithospheric damage, shear localization and plate-boundary formation. *Geophysical Journal International*, **152**, 581–596.

Bercovici, David, Ricard, Yanick, & Schubert, Gerald. 2001. A two-phase model for compaction and damage: 1. General Theory. *Journal of Geophysical Research*, **106**(B5), 8887–8906.

Berry, Michael W, Browne, Murray, Langville, Amy N, Pauca, V Paul, & Plemmons, Robert J. 2007. Algorithms and applications for approximate nonnegative matrix factorization. *Computational Statistics & Data Analysis*, **52**, 155–173.

Bevington, P H, & Robinson, D K. 2003. *Data reduction and error analysis*. Third edition edn. for the physical sciences. Mc Graw Hill.

Binzel, R P, & XU, S. 1993. Chips off of asteroid 4-Vesta - Evidence for the parent body of basaltic achondrite meteorites. *Science*, **260**(5105), 186–191.

Binzel, R P, Gaffey, M J, Thomas, P C, Zellner, B H, Storrs, A D, & Wells, E N. 1997. Geologic mapping of Vesta from 1994 Hubble Space Telescope images. *Icarus*, **128**(1), 95–103.

Bobin, J, Moudden, Y, Starck, Jean-Luc, & Elad, M. 2006. Morphological diversity and source separation. *IEEE Signal Processing Letter*, **13**(7), 409–412.

Bobin, Jérôme, Starck, Jean-Luc, Fadili, Jalal, & Moudden, Yassir. 2007. Sparsity and Morphological Diversity in Blind Source Separation. *IEEE Transactions on Image Processing*, **16**(11), 2662–2674.

Boesenberg, J S, & Delaney, J S. 1997. A model composition of the basaltic achondrite planetoid. *Geochimica et Cosmochimica Acta*, **61**(15), 3205–3225.

Boyet, Maud, Carlson, Richard W, & Horan, Mary. 2010. Old Sm–Nd ages for cumulate eucrites and redetermination of the solar system initial 146Sm/144Sm ratio. *Earth and Planetary Science Letters*, **291**(1-4), 172–181.

Boynton, W V, Feldman, W C, Mitrofanov, I G, Evans, L G, Reedy, R C, Squyres, S W, Starr, R, Trombka, J I, Uston, Claude, Arnold, J R, Englert, PAJ, Metzger, A E, Wänke, H, Brückner, J, Drake, D M, Shinohara, C, Fellows, C, Hamara, D K, Harshman, K, Kerry, K, Turner, C, Ward, M, Barthe, H, Fuller, K R, Storms, S A, Thornton, G W, Longmire, J L, Litvak, M L, & Ton'chev, A K. 2004. The Mars Odyssey Gamma-Ray Spectrometer instrument suite. *Space Science Reviews*, **110**(1-2), 37–83.

Briesmeister, Judith F. 2000. MCNP^{TM} - A General Monte Carlo N-Particle Transport Code. *Diagnostics Applications Group Los Alamos National Laboratory*.

Buczkowski, D L, Wyrick, D Y, Iyer, K A, Kahn, E G, Scully, J E C, Nathues, A, Gaskell, R W, Roatsch, T, Preusker, F, Schenk, P M, Le Corre, L, Reddy, V, Yingst, R A, Mest, S, Williams, D A, Garry, W B, Barnouin, O S, Jaumann, R, Raymond, C A, & Russell, C T. 2012. Large-scale troughs on Vesta: A signature of planetary tectonics. *Geophysical Research Letters*, **39**(18), n/a–n/a.

Buczkowski, D L, Wyrick, D Y, Toplis, M, Yingst, R A, Williams, D A, Garry, W B, Mest, S, Kneissl, T, Scully, J E C, Nathues, A, De Sanctis, M C, LeCorre, L, Reddy, V, Hoffmann, M, Ammannito, E, Frigeri, A, Tosi, F, Preusker, F, Roatsch, T, Raymond, C A, Jaumann, R, Pieters, C M, & Russell, C T. 2014. The unique geomorphology and physical properties of the Vestalia Terra plateau. *Icarus*, **244**(C), 89–103.

Buono, Antonio S, & Walker, David. 2011. The Fe-rich liquidus in the Fe-FeS system from 1bar to 10GPa. *Geochimica et Cosmochimica Acta*, **75**(8), 2072–2087.

Burbine, Thomas H, Buchanan, Paul C, Binzel, Richard P, Bus, Schelte J, Hiroi, T, Hinrichs, J L, Meibom, A, & McCoy, Timothy J. 2001. Vesta, Vestoids, and the howardite, eucrite, diogenite group: Relationships and the origin of spectral differences. *Meteoritics & Planetary Science*, **36**(June), 761–781.

Bus, Schelte J, & Binzel, Richard P. 2002. Phase II of the Small Main-Belt Asteroid Spectroscopic Survey. *Icarus*, **158**, 146–177.

Cardoso, Jean-François. 1999. High-Order Contrasts for Independent Component Analysis. *Neural Computation*, **11**(Apr.), 157–192.

Cardoso, Jean-François, & Souloumiac, A. 1993. Blind beamforming for non-Gaussian signals. *IEE Proceedings-F*, **140**(6), 362–370.

Carrasco-González, Carlos, Rodríguez, Luis F, Anglada, Guillem, & Curiel, Salvador. 2009. High angular resolution radio observations of the HL/XZ Tau region: mapping the 50 AU protoplanetary disk around HL Tau and resolving XZ Tau s into a 13 AU binary. *The Astrophysical Journal*, **693**(2), L86–L90.

Castillo-Rogez, Julie, Johnson, Torrence V, Lee, Man Hoi, Turner, Neal J, Matson, Dennis L, & Lunine, Jonathan. 2009. 26Al decay: Heat production and a revised age for Iapetus. *Icarus*, **204**(2), 658–662.

Chevrel, M O, Platz, T, Hauber, E, Baratoux, D, Lavallée, Y, & Dingwell, D B. 2013. Lava flow rheology: A comparison of morphological and petrological methods. *Earth and Planetary Science Letters*, **384**(Dec.), 109–120.

Chevrel, Magdalena Oryaëlle, Baratoux, David, Hess, Kai-Uwe, & Dingwell, Donald B. 2014. Viscous flow behavior of tholeiitic and alkaline Fe-rich martian basalts. *Geochimica et Cosmochimica Acta*, **124**(Jan.), 348–365.

Cichocki, Andrzej, Zdunek, Rafal, Phan, Anh Huy, & Amari, Shun-ichi. 2009. *Nonnegative Matrix and Tensor Factorizations*. Applications to Exploratory Multi-way Data Analysis and Blind Source Separation. Chichester, UK: John Wiley & Sons.

Clenet, Harold, Jutzi, Martin, Barrat, Jean-Alix, Asphaug, Erik I, Benz, Willy, & Gillet, Philippe. 2014. A deep crust-mantle boundary in the asteroid 4 Vesta. *Nature*, **511**(7509), 303–306.

Cochran, Anita L, Vilas, Faith, Jarvis, Kandy S, & Kelley, Michael S. 2004. Investigating the Vesta–vestoid–HED connection. *Icarus*, **167**(2), 360–368.

Comon, Pierre. 1994. Independent component analysis: a new concept? *Signal Processing*, **36**(3), 287–314.

Consolmagno, G J, & Drake, M J. 1977. Composition and evolution of eucrite parent body - evidence from Rare Earth elements. *Geochimica et Cosmochimica Acta*, **41**(9), 1271–1282.

Consolmagno, G J, Golabek, G J, Turrini, D, Jutzi, M, Sirono, S, Svetsov, V, & Tsiganis, K. 2015. Is Vesta an intact and pristine protoplanet? *Icarus*, **254**(July), 190–201.

de Elia, G C, & Brunini, A. 2007. Collisional and dynamical evolution of the main belt and NEA population. *Astronomy and Astrophysics*, **466**, 1159–1177.

De Sanctis, M C, Ammannito, E, Capria, M T, Tosi, F, Capaccioni, F, Zambon, F, Carraro, F, Fonte, S, Frigeri, A, Jaumann, R, Magni, G, Marchi, S, McCord, T B, McFadden, L A, McSween Jr., Harry Y, Mittlefehldt, D W, Nathues, A, Palomba, E, Pieters, C M, Raymond, C A, Russell, C T, Toplis, M J, & Turrini, D. 2012. Spectroscopic Characterization of Mineralogy and Its Diversity Across Vesta. *Science*, **336**(6082), 697–700.

De Sanctis, Maria Cristina, Coradini, Angioletta, Ammannito, Eleonora, Capria, M Teresa, & Fonte, Sergio. 2009. VIR, the imaging spectrometer for the asteroid belt exploration. *Memorie della Società astronomica italiana*, **80**(June), 295–300.

Delaney, Jeremy S, Prinz, Martin, & Takeda, Hiroshi. 1984 (Nov.). The polymict eucrites. *Pages C251–C288 of: Proceedings of the fifteenth Lunar and Planetary Science Conference*.

DeMeo, F E, & Carry, B. 2014. Solar System evolution from compositional mapping of the asteroid belt. *Nature*, **505**(7485), 629–634.

DeMeo, F E, Alexander, C M OD, Walsh, K J, Chapman, C R, & Binzel, Richard P. 2015. The compositional structure of the main asteroid belt. *Arxiv*.

Denevi, B W, Blewett, D T, Buczkowski, D L, Capaccioni, F, Capria, M T, De Sanctis, M C, Garry, W B, Gaskell, R W, Le Corre, L, Li, J Y, Marchi, S, McCoy, T J, Nathues, A, O'Brien, D P, Petro, N E, Pieters, C M, Preusker, F, Raymond, C A, Reddy, V, Russell, C T, Schenk, P, Scully, J E C, Sunshine, J M, Tosi, F, Williams, D A, & Wyrick, D. 2012. Pitted Terrain on Vesta and Implications for the Presence of Volatiles. *Science*, **338**(6104), 246–249.

Deville, Yannick. 2011. *Traitement du signal: signaux temporels et spatiotemporels - Analyse des signaux, théorie de l'information, traitement d'antenne, séparation aveugle de source*. Paris: Ellipses Edition Marketing.

Deville, Yannick, & Puigt, Matthieu. 2007. Temporal and time-frequency correlation-based blind source separation methods. Part I: Determined and underdetermined linear instantaneous mixtures. *Signal Processing*, **87**(3), 374–407.

Dingwell, D B, Courtial, P, Giordano, D, & Nichols, A R L. 2004. Viscosity of peridotite liquid. *Earth and Planetary Science Letters*, **226**(1-2), 127–138.

Domeneghetti, M Chiara, Molin, G Mario, Stimpfl, Marinela, & Tribaudino, Mario. 1995. Orthopyroxene from Serra de Magé meteorite: Structure refinement and estimation of C2/c pyroxene contributions to apparent Pbca diffraction violations. *American Mineralogist*, **80**, 923–929.

Dreibus, G, & Wänke, H. 1980. THE BULK COMPOSITION OF THE EUCRITE PARENT ASTEROID AND ITS BEARING ON PLANETARY EVOLUTION. *ZEITSCHRIFT FUR NATURFORSCHUNG SECTION A-A JOURNAL OF PHYSICAL SCIENCES*, **35**(2), 204–216.

Drew, D A. 1971. Average equations for two-phase media. *Studies in Applied Mathematics*, **50**, 133–166.

Drew, D A, & Passman, S L. 1999. *Theory of Multicomponent Fluids*. Vol. 135. Applied Mathematical Science Springer.

Elkins-Tanton, Linda T. 2012. Magma Oceans in the Inner Solar System. *Annual Review of Earth and Planetary Sciences*, **40**(1), 113–139.

Elkins-Tanton, Linda T, Weiss, Benjamin P, & Zuber, Maria T. 2011. Chondrites as samples of differentiated planetesimals. *Earth and Planetary Science Letters*, **305**(1-2), 1–10.

Ermakov, Anton I, Zuber, Maria T, Smith, David E, Raymond, Carol A, Balmino, Georges, Fu, Roger R, & Ivanov, Boris A. 2014. Constraints on Vesta's interior structure using gravity and shape models from the Dawn mission. *Icarus*, **240**(C), 146–160.

Evans, L G, Reedy, Robert C, & Trombka, Jacob I. 1993. Introduction to planetary remote sensing gamma ray spectroscopy. *Pages 167–198 of:* Pieters, Carli M, & Englert, Peter A J (eds), *Remote Geochemical Analysis: Elemental and Mineralogical Composition*.

Evans, L G, Starr, R D, Brückner, J, Reedy, R C, Boynton, W V, Trombka, J I, Goldstein, J O, Masarik, J, Nittler, L R, & McCoy, T J. 2001. Elemental composition from gamma-ray spectroscopy of the NEAR-Shoemaker landing site on 433 Eros. *Meteoritics & Planetary Science*, **36**(12), 1639–1660.

Farinella, Paolo, Froeschlé, Claude, & Gonczi, Robert. 1994. Meteorite delivery and transport. *Asteroids, Comets, Meteors*, 205–222.

Feldman, W C. 2004. Gamma-Ray, Neutron, and Alpha-Particle Spectrometers for the Lunar Prospector mission. *Journal of Geophysical Research*, **109**(E7), E07S06–19.

Forni, Olivier, Gasnault, Olivier, Diez, B, Uston, Claude, Maurice, Sylvestre, Hasebe, N, Okudaira, O, Yamashita, N, Kobayashi, S, Karouji, Y, Hareyama, M, Reedy, R C, Kim, K J, & team, SELENE GRS. 2009. Independent Component Analysis of the Gamma Ray Spectrometer Data of Selene (Kaguya). *IEEE*, **978**(Apr.), 4244–4687.

Forni, Olivier, Gasnault, Olivier, Uston, Claude, Maurice, Sylvestre, Hasebe, N, Yamashita, Naoyuki, Kobayashi, S, Karouji, Y, Hareyama, M, Kobayashi, H, Reedy, R C, & Kim, K J. 2010. Large scale potassium-thorium fractionation around Imbrium. *Lunar and Planetary Science Conference 41st*, 1–2.

Fowler, G W, Shearer, C K, & Papike, James J. 1995. Diogenites as asteroidal cumulates: Insights from orthopyroxene trace element chemistry. *Geochimica et Cosmochimica Acta*, **59(14)**, 3071–3084.

Ganguly, Jibamitra, Ito, Motoo, & Zhang, Xiaoyu. 2007. Cr diffusion in orthopyroxene: Experimental determination, 53Mn–53Cr thermochronology, and planetary applications. *Geochimica et Cosmochimica Acta*, **71**(15), 3915–3925.

Ghiorso, M S, & Sack, R O. 1995. Chemical mass-transfer in magmatic processes a revised and internally consistent thermodynamic model for the interpolation and extrapolation of liquid-solid equilibria in magmatic systems at elevated temperatures and pressures. *Contributions to Mineralogy and Petrology*, **119**(2-3), 197–212.

Ghiorso, Mark S. 2013. A globally convergent saturation state algorithm applicable to thermodynamic systems with a stable or metastable omni-component phase. *Geochimica et Cosmochimica Acta*, **103**(C), 295–300.

Ghosh, Amitabha, & McSween, Harry Y. 1998. A Thermal Model for the Differentiation of Asteroid 4 Vesta, Based on Radiogenic Heating. *Icarus*, **134**(Aug.), 187–206.

Goldstein, J I, Scott, E R D, & Chabot, N L. 2009. Iron meteorites: Crystallization, thermal history, parent bodies, and origin. *Chemie der Erde - Geochemistry*, **69**(4), 293–325.

Golub, Gene H, & Van Loan, Charles F. 2013. *Matrix Computations*. 4th edn. Baltimore: Johns Hopkins University Press.

Gong, Pinghua, & Zhang, Changshui. 2012. Efficient Nonnegative Matrix Factorization via projected Newton method. *Pattern Recognition*, **45**(9), 3557–3565.

Gorski, K M, Hivon, E, Banday, A J, Wandelt, B D, Hansen, F K, Reinecke, M, & Bartelmann, M. 2005. HEALPix: A framework for high-resolution discretization and fast analysis of data distributed on the sphere. *The Astrophysical Journal*, **622**(Apr.), 759–771.

Gounelle, Matthieu, Meibom, Anders, Hennebelle, Patrick, & Inutsuka, Shu-ichiro. 2009. Supernova Propagation and Cloud Enrichment: A New Model for the Origin of 60Fe in the Early Solar System. *The Astrophysical Journal Letters*, **694**(1), L1–L5.

Gradie, J, & Tedesco, E F. 1982. Compositional structure of the asteroid belt. *Science*, **216**(4553), 1405–1407.

Greenwood, Richard C, Franchi, Ian A, Jambon, Albert, & Buchanan, Paul C. 2005. Widespread magma oceans on asteroidal bodies in the early Solar System. *Nature*, **435**(7044), 916–918.

Greenwood, Richard C, Barrat, Jean-Alix, Yamaguchi, Akira, Franchi, Ian A, Scott, Edward R D, Bottke, William F, & Gibson, Jenny M. 2014. The oxygen isotope composition of diogenites: Evidence for early global melting on a single, compositionally diverse, HED parent body. *Earth and Planetary Science Letters*, **390**(C), 165–174.

Gupta, G, & Sahijpal, S. 2010. Differentiation of Vesta and the parent bodies of other achondrites. *Journal of Geophysical Research*, **115**(E8), E08001.

Harland, W B, Armstrong, R L, Cox, A V, Craig, L E, Smith, A G, & Smith, D G. 1989. *A geologic time scale*. Cambridge University Press.

Harrington, Timothy M, Marshall, J Howard, Arnold, James R, Peterson, Laurence E, Trombka, Jacob I, & Metzger, Albert E. 1974. The Apollo gamma-ray spectrometer. *Nuclear Instruments and Methods in Physics Research Section B: Beam Interactions with Materials and Atoms*, **118**, 401–411.

Harriott, Theresa A, & Hewins, Roger H. 1984. Processes and subdivisions in diogenites, a multivariate statistical analysis. *Meteoritics*, **19**(1), 15–23.

Hasebe, N, Yamashita, Naoyuki, Karouji, Y, Kobayashi, S, Hareyama, M, Hatasu, K, Nemoto, S, Iwabuchi, K, Takeda, Y, Nagaoka, H, & Tsukada, K. 2009. Overview of Elemental Distributions on the Moon Observed by SELENE GRS. *TRANSACTIONS OF THE JAPAN SOCIETY FOR AERONAUTICAL AND SPACE SCIENCES, AEROSPACE TECHNOLOGY JAPAN*, 1–5.

Hérault, Jeanny, & Ans, Bernard. 1984. Neural network with modifiable synapses - decoding of composite sensory messages under unsupervised and permanent learning. *Comptes rendu de l'académie des sciences Série III - Sciences de la vie - Life Science*, 525–528.

Hirth, Greg, & Kohlstedt, David. 2003. Rheology of the upper mantle and the mantle wedge: a view from the experimentalists. *Inside the subduction factory*, 83–105.

Hotelling, H. 1933. Analysis of a complex of statistical variables into principal components. *Journal Of EducationaL Psychology*, **24**, 417–441.

Hyvärinen, A, & Oja, E. 2000. Independent component analysis: algorithms and applications. *Neural Networks, IEEE Transactions on*, **13**(July), 411–430.

Iizuka, Tsuyoshi, Yamaguchi, Akira, Haba, Makiko K, Amelin, Yuri, Holden, Peter, Zink, Sonja, Huyskens, Magdalena H, & Ireland, Trevor R. 2015. Timing of global crustal metamorphism on Vesta as revealed by high-precision U–Pb dating and trace element chemistry of eucrite zircon. *Earth and Planetary Science Letters*, **409**(C), 182–192.

Ikeda, Y, & Takeda, Hiroshi. 1985. A model for the origin of baslatic achondrites based on the Yamato 7308 Howardite. *Proceedings of the fifteenth Lunar and Planetary Science Conference*, **90**, C649–C663.

Ito, M, & Ganguly, J. 2006. Diffusion kinetics of Cr in olivine and Mn-53-Cr-53 thermochronology of early solar system objects. *Geochimica et Cosmochimica Acta*, **70**(3), 799–809.

Jambon, Albert, Barrat, Jean-Alix, Boudouma, O, Fonteilles, M, Badia, D, Göpel, C, & Bohn, M. 2005. Mineralogy and petrology of the angrite Northwest Africa 1296. *Meteoritics & Planetary Science*, **40**(3), 361–375.

Jaumann, R, Williams, D A, Buczkowski, D L, Yingst, R A, Preusker, F, Hiesinger, H, Schmedemann, N, Kneissl, T, Vincent, J B, Blewett, D T, Buratti, B J, Carsenty, U, Denevi, B W, De Sanctis, M C, Garry, W B, Keller, H U, Kersten, E, Krohn, K, Li, J Y, Marchi, S, Matz, K D, McCord, T B, McSween, Harry Y, Mest, S C, Mittlefehldt, D W, Mottola, S, Nathues, A, Neukum, G, O'Brien, D P, Pieters, C M, Prettyman, T H, Raymond, C A, Roatsch, T, Russell, C T, Schenk, P, Schmidt, B E, Scholten, F, Stephan, K, Sykes, M V, Tricarico, P, Wagner, R, Zuber, M T, & Sierks, H. 2012. Vesta's Shape and Morphology. *Science*, **336**(6082), 687–690.

Jolliffe, I T. 2002. *Principal Component Analysis, Second Edition*. New York: Springer-Verlag.

Jurewicz, A J G, Mittlefehldt, David W, & Jones, J H. 1993. Experimental partial melting of the Allende (CV) and Murchison (CM) chondrites and the origin of asteroidal basalts. *Geochimica et Cosmochimica Acta*, **57**(9), 2123–2139.

Jurewicz, A J G, Mittlefehldt, David W, & Jones, J H. 1995. Experimental partial melting of the St. Severin (LL) and Lost City (H) chondrites. *Geochimica et Cosmochimica Acta*, **59**(2), 391–408.

Jutten, Christian, & Taleb, Anisse. 2000. Source separation: From dusk till dawn ICA 2000. *Proc. Int. Workshop on Independent Component Analysis and Blind Signal Separation*, 15–26.

Jutzi, M, Asphaug, E, Gillet, P, Barrat, Jean Alix, & Benz, W. 2013. The structure of the asteroid 4 Vesta as revealed by models of planet-scale collisions. *Nature*, **494**(7436), 207–210.

Katz, R F. 2008. Magma Dynamics with the Enthalpy Method: Benchmark Solutions and Magmatic Focusing at Mid-ocean Ridges. *Journal of Petrology*, **49**(12), 2099–2121.

Keil, Klaus. 2002. Geological History of Asteroid 4 Vesta: The "Smallest Terrestrial Planet". *Asteroids III*, Oct., 573–584.

Kleine, T, Mezger, K, Münker, C, Palme, H, & Bischoff, A. 2004. 182Hf-182W isotope systematics of chondrites, eucrites, and martian meteorites: Chronology of core formation and early mantle differentiation in Vesta and Mars. *Geochimica et Cosmochimica Acta*, **68**(13), 2935–2946.

Kleine, Thorsten, Touboul, Mathieu, Bourdon, Bernard, Nimmo, Francis, Mezger, Klaus, Palme, Herbert, Jacobsen, Stein B, Yin, Qing-Zhu, & Halliday, Alexander N. 2009. Hf–W chronology of the accretion and early evolution of asteroids and terrestrial planets. *Geochimica et Cosmochimica Acta*, **73**(17), 5150–5188.

Konopliv, A S, Asmar, S W, Bills, B G, Mastrodemos, N, Park, R S, Raymond, C A, Smith, D E, & Zuber, M T. 2011. The Dawn Gravity Investigation at Vesta and Ceres. *Space Science Reviews*, **163**(1-4), 461–486.

Korotev, Randy L, Jolliff, Bradley L, Zeigler, Ryan A, Gillis, Jeffrey J, & Haskin, Larry A. 2003. Feldspathic lunar meteorites and their implications for compositional remote sensing of the lunar surface and the composition of the lunar crust. *Geochimica et Cosmochimica Acta*, **67**(24), 4895–4923.

Kraichnan, Robert H. 1962. Turbulent Thermal Convection at Arbitrary Prandtl Number. *Physics of Fluids*, **5**(11), 1374.

Krot, A N, Amelin, Y, Bland, P, Ciesla, F J, Connelly, J, Davis, A M, Huss, G R, Hutcheon, I D, Makide, K, Nagashima, K, Nyquist, L E, Russell, S S, Scott, E R D, Thrane, K, Yurimoto, H, & Yin, Q Z. 2009. Origin and chronology of chondritic components: A review. *Geochimica et Cosmochimica Acta*, **73**(17), 4963–4997.

Krot, A N, Keil, K, Scott, E R D, Goodrich, C A, & Weisberg, M K. 2014. 1.1 - Classification of Meteorites and Their Genetic Relationships. *Pages 1–63 of:* Turekian, Heinrich D HollandKarl K (ed), *Treatise on Geochemistry (Second Edition)*. Oxford: Elsevier.

Lacoume, Jean-Louis, Amblard, Pierre-Olivier, & Comon, Pierre. 1997. Statistiques d'ordre supérieur pour le traitement du signal. *MASSON*, 290.

Langville, Amy N, Meyer, Carl D, & Albright, Russell. 2006. Initializations for the Nonnegative Matrix Factorization. 1–8.

Lawrence, D J. 2004. Gamma-ray measurements from Lunar Prospector: Time series data reduction for the Gamma-Ray Spectrometer. *Journal of Geophysical Research*, **109**(E7), E07S05.

Lee, Daniel D, & Seung, H Sebastian. 2001. Algorithms for Non-negative Matrix Factorization. *Pages 556–562 of:* Leen, T K, Dietterich, T G, & Tresp, V (eds), *Advances in Neural Information Processing Systems 13*. MIT Press.

Lee, Typhoon, Papanastassiou, D A, & Wasserburg, G J. 1977. Aluminum 26 in the early solar system: fossil or fuel? *The Astrophysical Journal*, **211**, L107–L110.

Li, Jian-Yang, McFadden, Lucy A, Thomas, Peter C, Mutchler, Max J, Parker, Joel Wm, Young, Eliot F, Russell, Christopher T, Sykes, Mark V, & Schmidt, Britney E. 2010. Photometric mapping of Asteroid (4) Vesta's southern hemisphere with Hubble Space Telescope. *Icarus*, **208**(1), 238–251.

Lin, Chih-Jen. 2007a. On the Convergence of Multiplicative Update Algorithms for Non-negative Matrix Factorization. *Neural Networks, IEEE Transactions on*, **18**, 1589–1596.

Lin, Chin-Jen. 2007b. Projected Gradient Methods for Non-negative Matrix Factorization. *Neural Computation*, **19**(10), 2756–2779.

Lodders, K. 2003. Solar system abundances and condensation temperatures of the elements. *ASTROPHYSICAL JOURNAL*, **591**(2, 1), 1220–1247.

Lorenz, C A, Nazarov, M A, Brandstaetter, F, & Ntaflos, Th. 2010. Metasomatic alterations of olivine inclusions in the Budulan mesosiderite. *Petrology*, **18**(5), 461–470.

Lugmair, G W, & Shukolyukov, A. 1998. Early solar system timescales according to ^{53}Mn-^{53}Cr systematics. *Geochimica et Cosmochimica Acta*, **62**(16), 2863–2886.

Lunning, Nicole G, McSween, Harry Y, Tenner, Travis J, Kita, Noriko T, & Bodnar, Robert J. 2015. Olivine and pyroxene from the mantle of asteroid 4 Vesta. *Earth and Planetary Science Letters*, **418**(May), 126–135.

MacPherson, Glenn J, Davis, Andrew M, & Zinner, E K. 1995. The distribution of aluminium-26 in the early solar system - A reappraisal. *Meteoritics*, **30**, 365–386.

Mandler, Ben E, & Elkins-Tanton, Linda T. 2013. The origin of eucrites, diogenites, and olivine diogenites: Magma ocean crystallization and shallow magma chamber processes on Vesta. *Meteoritics & Planetary Science*, **48**(11), 2333–2349.

Marchi, S, McSween, Harry Y, O'Brien, D P, Schenk, Paul, De Sanctis, Maria Cristina, Gaskell, R, Jaumann, Ralf, Mottola, S, Preusker, F, Raymond, Carol A, Roatsch, T, & Russell, Christopher T. 2012. The violent collisional history of asteroid 4 Vesta. *Science*, **336**(6082), 690–694.

Mayne, R G, McSween Jr., Harry Y, McCoy, T J, & Gale, A. 2009. Petrology of the unbrecciated eucrites. *Geochimica et Cosmochimica Acta*, **73**(3), 794–819.

McCord, Thomas B, Johnson, Torrence V, & Adams, J B. 1970. Asteroid Vesta - Spectral Reflectivity And Compositional Implications. *Science*, **168**(3938), 1445.

McCoy, Timothy J, Keil, Klaus, Clayton, Robert N, Mayeda, Toshiko K, Bogard, Donald D, Garrison, Daniel H, Huss, Gary R, Hutcheon, I D, & Wieler, Rainer. 1996. A petrologic, chemical, and isotopic study of Monument Draw and comparison with other acapulcoites: Evidence for formation by incipient partial melting. *Geochimica et Cosmochimica Acta*, **60**(14), 2681–2708.

McFadden, Lucy A, McCord, Thomas B, & Pieters, Carli M. 1977. Vesta - 1st Pyroxene Band From New Spectroscopic Measurements. *Icarus*, **31**(4), 439–446.

McKenzie, Dan. 1984. The Generation and Compaction of Partially Molten Rock. *Journal of Petrology*, **25**(Mar.), 713–765.

McKenzie, Dan. 1985. The extraction of magma from the crust and mantle Dan McKenzie. *Earth and Planetary Science Letters*, **74**, 81–91.

McSween, Harry Y, Mittlefehldt, David W, Beck, Andrew W, Mayne, Rhiannon G, & McCoy, Timothy J. 2010. HED Meteorites and Their Relationship to the Geology of Vesta and the Dawn Mission. *Space Science Reviews*, **163**(1-4), 141–174.

McSween, Harry Y, Ammannito, Eleonora, Reddy, Vishnu, Prettyman, Thomas H, Beck, Andrew W, Cristina De Sanctis, M, Nathues, Andreas, Corre, Lucille Le, O'Brien, David P, Yamashita, Naoyuki, McCoy, Timothy J, Mittlefehldt, David W, Toplis, Michael J, Schenk, Paul, Palomba, Ernesto, Turrini, Diego, Tosi, Federico, Zambon, Francesca, Longobardo, Andrea, Capaccioni, Fabrizio, Raymond, Carol A, & Russell, Christopher T. 2013. Composition of the Rheasilvia basin, a window into Vesta's interior. *Journal of Geophysical Research: Planets*, **118**(2), 335–346.

Mittlefehldt, D W. 1987. Volatile degassing of basaltic achondrite parent bodies - evidence from alkali elements and phosphorus. *Geochimica et Cosmochimica Acta*, **51**(2), 267–278.

Mittlefehldt, D W, McCoy, T J, Goodrich, C A, & Kracher, A. 1998. Non-chondritic meteorites from asteroidal bodies. *Pages D1–D195 of:* Papike, James J (ed), *Remote Geochemical Analysis: Elemental and Mineralogical Composition*. MINERALOGICAL SOC AMER.

Mittlefehldt, David W. 1994. The genesis of diogenites and HED parent body petrogenesis. *Geochimica et Cosmochimica Acta*, **58**(5), 1537–1552.

Mittlefehldt, David W. 2005. Ibitira: A basaltic achondrite from a distinct parent asteroid and implications for the Dawn mission. *Meteoritics & Planetary Science*, **40**(5), 665–677.

Mittlefehldt, David W. 2008. Meteorite dunite breccia MIL03443: A probable crustal cumulate closely related to diogenites from the HED parent asteroid. *Lunar Planetary Science Conference ,39th.*

Mittlefehldt, David W, Beck, Andrew W, LEE, Cin-Ty A, McSween, Harry Y, & Buchanan, Paul C. 2011. Compositional constraints on the genesis of diogenites. *Meteoritics & Planetary Science*, **47**(1), 72–98.

Mittlefehldt, David W, Peng, Z X, & Ross, D K. 2015. Petrology of anomalous eucrites. *Lunar and Planetary Science Conference 46th*.

Monnereau, M. 2002. Is Io's Mantle Really Molten? *Icarus*, **158**(2), 450–459.

Monnereau, Marc, Toplis, Michael J, Baratoux, David, & Guignard, Jérémy. 2013. Thermal history of the H-chondrite parent body: Implications for metamorphic grade and accretionary time-scales. *Geochimica et Cosmochimica Acta*, **119**(C), 302–321.

Moore, W B. 2003. Tidal heating and convection in Io. *Journal of Geophysical Research*, **108**(E8), 1–6.

Moore, William B, & Webb, A Alexander G. 2013. Heat-pipe Earth. *Nature*, **501**(7468), 501–505.

Morse, S A. 1980. *Basalts and Phase Diagrams*. An Introduction to the Quantitative Use of Phase Diagrams in Igneous Petrology. New York Heidelberg Berlin: Spinger-Verlag.

Moskovitz, Nicholas, & Gaidos, Eric. 2011. Differentiation of planetesimals and the thermal consequences of melt migration. *Meteoritics & Planetary Science*, **46**(6), 903–918.

Moskovitz, Nicholas A. 2009. *Spectroscopic and theoretical constraints on the differentiation of planetesimals*. Ph.D. thesis, University of Hawaii.

Moudden, Y, & Bobin, J. 2011. Hyperspectral BSS Using GMCA With Spatio-Spectral Sparsity Constraints. *IEEE Transactions on Image Processing*, **20**(3), 872–879.

Moussaoui, S, Hauksdóttir, H, Schmidt, F, Jutten, C, Chanussot, J, Brie, D, Douté, S, & Benediktsson, J A. 2008. On the decomposition of Mars hyperspectral data by ICA and Bayesian positive source separation. *Neurocomputing*, **71**(10-12), 2194–2208.

Neumann, W, Breuer, D, & Spohn, T. 2012. Differentiation and core formation in accreting planetesimals. *Astronomy and Astrophysics*, **543**(July), A141.

Neumann, Wladimir, Breuer, Doris, & Spohn, Tilman. 2014. Differentiation of Vesta: Implications for a shallow magma ocean. *Earth and Planetary Science Letters*, **395**(C), 267–280.

Nishimura, Yo, & Monnereau, Marc. 2015. Silicate-metal segregation in small bodies of the Early Solar System: a three-phase 1-D spherical model. *Stage de Master - Recherce, ASEP, Université Paul Sabatier*.

Nyquist, L E, Takeda, Hiroshi, Bansal, B M, Shih, C Y, Wiesmann, H, & Wooden, J L. 1986. Rb-Sr and Sm-Nd Internal Isochron Ages of a Subophitic Basalt Clast and Matrix Sample from the Y75011 Eucrite. *Journal of Geophysical Research*, **91**(B8), 8137–8150.

O Brien, David P, Marchi, Simone, Morbidelli, Alessandro, Bottke, William F, Schenk, Paul M, Russell, Christopher T, & Raymond, Carol A. 2014. Constraining the cratering chronology of Vesta. *Planetary and Space Science*, **103**(Nov.), 131–142.

OReilly, Thomas C, & Davies, Geoffrey F. 1981. Magma Transport of Heat on Io: A Mechanism Allowing a Thick Lithosphere. *Geophysical Research Letters*, **8**(4), 313–316.

Paatero, Pentti, & Tapper, Unto. 1994. Positive matrix factorization: a non-negative factor model with optimal utilization of error estimates of data values. *Environmetrics*, **5**(2), 111–126.

Pal, Madhab, Roy, Rajib, Basu, Joyanta, & Bepari, Milton S. 2013. Blind Source Separation: A Review and Analysis. *In: 2013 International Conference Orientak Coscoda heldjointly with 2013 Conference On Asian Spoken Language Research and Evaluation (O-COCOSDA/CASLRE)*. IEEE.

Park, R S, Konopliv, A S, Asmar, S W, Bills, B G, Gaskell, R W, Raymond, C A, Smith, D E, Toplis, M J, & Zuber, M T. 2014. Gravity field expansion in ellipsoidal harmonic and polyhedral internal representations applied to Vesta. *Icarus*, **240**, 118–132.

Pearson, K. 1901. On lines and planes of closest fit to systems of points in space. *Philosophical Magazine*, **2**, 559–572.

Peplowski, Patrick N, Lawrence, David J, Rhodes, Edgar A, Sprague, Ann L, McCoy, Timothy J, Denevi, Brett W, Evans, Larry G, Head, James W, Nittler, Larry R, Solomon, Sean C, Stockstill-Cahill, Karen R, & Weider, Shoshana Z. 2012. Variations in the abundances of potassium and thorium on the surface of Mercury: Results from the

MESSENGER Gamma-Ray Spectrometer. *Journal of Geophysical Research*, **117**(E12), n/a–n/a.

Petit, Jean-Marc, Morbidelli, Alessandro, & Chambers, John E. 2001. The primordial excitation and clearing of the asteroid belt. *Icarus*, **153**(2), 338–347.

Prettyman, T H. 2014. Remote sensing of Chemical Elements Using Nuclear Spectroscopy. *Pages 1161–1183 of: Encyclopedia of the Solar System*. Elsevier.

Prettyman, T H, Hagerty, J J, Elphic, R C, Feldman, W C, Lawrence, D J, McKinney, G W, & Vaniman, D T. 2006. Elemental composition of the lunar surface: Analysis of gamma ray spectroscopy data from Lunar Prospector. *Journal of Geophysical Research*, **111**(E12), E12007.

Prettyman, T H, Mittlefehldt, D W, Yamashita, N, Lawrence, D J, Beck, A W, Feldman, W C, McCoy, T J, McSween Jr., Harry Y, Toplis, M J, Titus, T N, Tricarico, P, Reedy, R C, Hendricks, J S, Forni, O, Le Corre, L, Li, J Y, Mizzon, H, Reddy, V, Raymond, C A, & Russell, C T. 2012. Elemental Mapping by Dawn Reveals Exogenic H in Vesta's Regolith. *Science*, **338**(6104), 242–246.

Prettyman, T H, Yamashita, N, Reedy, R C, McSween Jr, H Y, Mittlefehldt, D W, Hendricks, J S, & Toplis, M J. 2015a. Concentrations of Potassium and Thorium within Vesta's Regolith. *Icarus*, **259**, 39–52.

Prettyman, T H, Burger, A, Lambert, J L, Castillo-Rogez, Julie, & Yamashita, Naoyuki. 2015b. Strontium-Iodide: An ultra-gright scintillator for planetary gamma-ray spectroscopy. *Lunar and Planetary Science Conference 46th*.

Prettyman, Thomas H. 2006. Remote Chemical Sensing Using Nuclear Spectroscopy. *Pages 1–22 of: Encyclopedia of the Solar System*. Elsevier.

Prettyman, Thomas H, Feldman, William C, McSween, Harry Y, Dingler, Robert D, Enemark, Donald C, Patrick, Douglas E, Storms, Steven A, Hendricks, John S, Morgenthaler, Jeffery P, Pitman, Karly M, & Reedy, Robert C. 2011. Dawn's Gamma Ray and Neutron Detector. *Space Science Reviews*, **163**(1-4), 371–459.

Prettyman, Thomas H, Mittlefehldt, David W, Yamashita, Naoyuki, Beck, Andrew W, Feldman, William C, Hendricks, John S, Lawrence, David J, McCoy, Timothy J, McSween, Harry Y, Peplowski, Patrick N, Reedy, Robert C, Toplis, Michael J, Le Corre, Lucille, Mizzon, Hugau, Reddy, Vishnu, Titus, Timothy N, Raymond, Carol A, & Russell, Christopher T. 2013. Neutron absorption constraints on the composition of 4 Vesta. *Meteoritics & Planetary Science*, **48**(11), 2211–2236.

Quitté, Ghylaine, Markowski, A, Latkoczy, C, Gabriel, A, & Pack, A. 2010. Iron-60 heterogeneity and incomplete isotope mixing in the early Solar System. *The Astrophysical Journal*, **720**(2).

Raymond, Carol A, McSween, Harry Y, Park, Ryan S, Konopliv, Alexander S, Asmar, Sami W, Ammannito, Eleonora, De Sanctis, Maria Cristina, Prettyman, Thomas H, Buczkowski, D L, Jaumann, Ralf, Russell, Christopher T, Toplis, Michael J, & Zuber, Maria T. 2015. Gravity evidence for post-magma ocean serial magmatism on protoplanet Vesta. *Lunar and Planetary Science Conference 46th*.

Reedy, Robert C. 1978. Planetary gamma-ray spectroscopy. *Proceedings of the 9th Lunar and Planetary Science Conference*, 2961–2984.

Ribe, Neil M. 1985. The generation and composition of partial melts in the earth's mantle. *Earth and Planetary Science Letters*, **73**, 361–376.

Ricard, Yanick. 2007. Physics of mantle convection. *Pages 31–87 of:* Schubert, Gerald, & Bercovici, David (eds), *Treatise on Geophysics*.

Ricard, Yanick, Bercovici, David, & Schubert, Gerald. 2001. A two-phase model for compaction and damage: 2. Applications to compaction, deformation, and the role of interfacial surface tension. *Journal of Geophysical Research*, **106**(B5), 8907–8924.

Rice, John. 1995. *Mathematical Statistics and Data Analysis*. Second edition. Duxbury Press.

Righter, Kevin, & Drake, Michael J. 1997. A magma ocean on Vesta: Core formation and petrogenesis of eucrites and diogenites. *Meteoritics & Planetary Science*, **32**, 929–944.

Rubin, Alan E. 2007. Petrogenesis of acapulcoites and lodranites: A shock-melting model. *Geochimica et Cosmochimica Acta*, **71**(9), 2383–2401.

Rudge, John F, Bercovici, David, & Spiegelman, Marc. 2010. Disequilibrium melting of a two phase multicomponent mantle. *Geophysical Journal International*, **184**(2), 699–718.

Russell, C T, Capaccioni, F, Coradini, A, De Sanctis, M C, Feldman, W C, Jaumann, R, Keller, H U, McCord, T B, McFadden, L A, Mottola, S, Pieters, C M, Prettyman, T H, Raymond, C A, Sykes, M V, Smith, D E, & Zuber, M T. 2007. Dawn Mission to Vesta and Ceres. *Earth, Moon, and Planets*, **101**(1-2), 65–91.

Russell, C T, Raymond, C A, Coradini, A, McSween Jr., Harry Y, Zuber, M T, Nathues, A, De Sanctis, M C, Jaumann, R, Konopliv, A S, Preusker, F, Asmar, S W, Park, R S, Gaskell, R, Keller, H U, Mottola, S, Roatsch, T, Scully, J E C, Smith, D E, Tricarico, P, Toplis, M J, Christensen, U R, Feldman, W C, Lawrence, D J, McCoy, T J, Prettyman, T H, Reedy, R C, Sykes, M E, & Titus, T N. 2012. Dawn at Vesta: Testing the Protoplanetary Paradigm. *Science*, **336**(6082), 684–686.

Russell, C T, Raymond, C A, Jaumann, R, McSween, Harry Y, De Sanctis, M C, Nathues, A, Prettyman, T H, Ammannito, E, Reddy, V, Preusker, F, O'Brien, D P, Marchi, S, Denevi, B W, Buczkowski, D L, Pieters, C M, McCord, T B, Li, J Y, Mittlefehldt, D W, Combe, J P, Williams, D A, Hiesinger, H, Yingst, R A, Polanskey, C A, & Joy, S P. 2013. Dawn completes its mission at 4 Vesta. *Meteoritics & Planetary Science*, **48**(11), 2076–2089.

Ruzicka, Alex, Snyder, Gregory A, & Taylor, Lawrence A. 1997. Vesta as the howardite, eucrite and diogenite parent body: Implications for the size of a core and for large-scale differentiation. *Meteoritics & Planetary Science*, **32**, 825–840.

Sack, Richard O, Azeredo, William J, & Lipschutz, Michael E. 1991. Olivine diogenites: The mantle of the eucrite parent body. *Geochimica et Cosmochimica Acta*, **55**, 1111–1120.

Sahijpal, S, Soni, P, & Gupta, G. 2007. Numerical simulations of the differentiation of accreting planetesimals with 26Al and 60Fe as the heat sources. *Meteoritics & Planetary Science*, **42**(9), 1529–1548.

Samuel, Henri. 2014. A level set two-way wave equation approach for Eulerian interface tracking. *Journal of Computational Physics*, **259**(C), 617–635.

Schenk, Paul, O'Brien, D P, Marchi, Simone, Gaskell, Robert W, Preusker, F, Roatsch, T, Jaumann, Ralf, Buczkowski, D L, McCord, Thomas B, McSween, Harry Y, Williams, D A, Yingst, Aileen, Raymond, Carol A, & Russell, Christopher T. 2012. The geologically recent giant impact basins at Vesta's South pole. *Science*, **336**(6082), 694–697.

Schiller, Martin, Baker, Joel, Creech, John, Paton, Chad, Millet, Marc-Alban, Irving, Anthony J, & Bizzarro, Martin. 2011. Rapid Timescales For Magma Ocean Crystallization On The Howardites-Eucrite-Diogenite Parent Body. *The Astrophysical Journal*, **740**(1), L22.

Schmeling, Harro. 2000. Partial melting and melt segregation in a convecting mantle. *Pages 1–35 of:* Bagdassarov, N, Laporte, D, & Thompson, A B (eds), *Remote Geochemical Analysis: Elemental and Mineralogical Composition*. Dordrecht: Kluwer academic publisher.

Schwandt, Craig S, & McKay, Gordon A. 1998. Rare earth element partition coefficients from enstatite/melt synthesis experiments. *Geochimica et Cosmochimica Acta*, **62(16)**, 1–4.

Shearer, C K, Fowler, G W, & Papike, James J. 1997. Petrogenetic models for magmatism on the eucrite parent body: evidence from orthopyroxene in diogenites. *Meteoritics & Planetary Science*, **32**, 877–889.

Shukolyukov, A, & Lugmair, G W. 1993. Fe-60 in eucrites. *Earth and Planetary Science Letters*, **119**(1-2), 159–166.

Smoliar, M I. 1993. A survey of Rb-Sr systematics of eucrites. *Meteoritics*, **28**(1), 105–113.

Solomatov, V. 2007. Magma oceans and primordial mantle differentiation. *Pages 91–119 of:* Schubert, Gerald, & Stevenson, David (eds), *Treatise on Geophysics*.

Solomon, Sean C. 1980. Differentiation of crusts and cores of the terrestrial planets: lessons for the early Earth? *Precambrian Research*, **10**, 177–194.

Spiegelman, Marc. 1993. Physics of Melt Extraction: Theory, Implications and Applications. *Philosophical Transactions of the Royal Society*, **342**, 23–41.

Šrámek, Ondřej, Milelli, Laura, Ricard, Yanick, & Labrosse, Stéphane. 2012. Thermal evolution and differentiation of planetesimals and planetary embryos. *Icarus*, **217**(1), 339–354.

Srinivasan, G, Goswami, J N, & Bhandari, N. 1999. Al-26 in eucrite Piplia Kalan: Plausible heat source and formation chronology. *Science*, **284**(5418), 1348–1350.

Starck, Jean-Luc, & Murtagh, Fionn. 2006. *Astromical Image and Data Analysis*. Springer.

Starck, Jean-Luc, Murtagh, Fionn, & Fadili, Jalal M. 2010. *Sparse Image and Signal Processing: Wavelets, Curvelets, Morphological Diversity*.

Stolper, Edward. 1975. Petrogenesis of eucrite, howardite and diogenite meteorites. *Nature*, **258**, 220–222.

Stolper, Edward. 1977. Experimental petrology of eucritic meteorites. *Geochimica et Cosmochimica Acta*, **41**, 587–611.

Swedenborg, Emanuel. 1734. *Opera Philosophica et Mineralia*.

Takahashi, Kazuya, & Masudat, Akimasa. 1990. Young ages of two diogenites and their genetic implications. *Nature*, **343**(6258), 540–542.

Taylor, Jeffrey G, Keil, Klaus, McCoy, Timothy J, Haack, Henning, & Scott, Edward R D. 1993. Asteroid differentiation: pyroclastic volcanism to magma oceans. *Meteoritics*, **28**(1), 34–52.

Toplis, M J, Mizzon, H, Monnereau, M, Forni, O, McSween Jr., Harry Y, Mittlefehldt, D W, McCoy, T J, Prettyman, T H, De Sanctis, M C, Raymond, C A, & Russell, C T. 2013. Chondritic models of 4 Vesta: Implications for geochemical and geophysical properties. *Meteoritics & Planetary Science*, **48**(11), 2300–2315.

Touboul, Mathieu, Sprung, Peter, Aciego, Sarah M, Bourdon, Bernard, & Kleine, Thorsten. 2015. Hf-W chronology of the eucrite parent body. *Geochimica et Cosmochimica Acta*, **156**(C), 106–121.

Trinquier, A, Birck, J L, Allegre, C J, Göpel, C, & Ulfbeck, D. 2008. (53)Mn-(53)Cr systematics of the early Solar System revisited. *Geochimica et Cosmochimica Acta*, **72**(20), 5146–5163.

Trombka, Jacob I, Arnold, James R, Adler, I, Metzger, Albert E, & Reedy, Robert C. 1974. Lunar elemental analysis obtained from the Apollo gamma-ray and X-ray remote sensing experiment. *The proceedings of the soviet-american conference on the cosmochemistry of the Moon and planets*, 1–75.

Usui, Tomohiro, & McSween, Harry Y. 2007. Geochemistry of 4 Vesta based on HED meteorites: Prospective study for interpretation of gamma ray and neutron spectra for the Dawn mission. *Meteoritics & Planetary Science*, **42**(2), 255–269.

Usui, Tomohiro, McSween, Harry Y, Mittlefehldt, David W, & Prettyman, Thomas H. 2010. K-Th-Ti systematics and new three-component mixing model of HED meteorites: Prospective study for interpretation of gamma-ray and neutron spectra for the Dawn mission. *Meteoritics & Planetary Science*, **45**(7), 1170–1190.

Wadhwa, M, & Lugmair, G W. 1995. Samarium-neodymium and manganese-chromium systematics in the eucrite caldera. *Meteoritics*, **30**(5), 592.

Walsh, Kevin J, Morbidelli, Alessandro, Raymond, S N, O'Brien, D P, & Mandell, A M. 2011. A low mass for Mars from Jupiter's early gas-driven migration. *Nature*, **475**, 206–209.

Walsh, Kevin J, Morbidelli, Alessandro, Raymond, S N, O'Brien, D P, & Mandell, A M. 2012. Populating the asteroid belt from two parent source regions due to the migration of giant planets-"The Grand Tack". *Meteoritics & Planetary Science*, **47**(12), 1941–1947.

Wasson, John T, & Kallemeyn, Gregory W. 1988. Compositions of Chondrites. *Philosophical Transactions of the Royal Society of London. Series A, Mathematical and Physical Sciences*, **325**(1587), 535–544.

Weidenschilling, S J. 2011. Initial sizes of planetesimals and accretion of the asteroids. *Icarus*, **214**(2), 671–684.

Wiggins, Chris, & Spiegelman, Marc. 1995. Magma migration and magmatic solitary waves in 3-D. *Geophysical Research Letters*, **22**(10), 1289–1292.

Williams, Jonathan P, & Cieza, Lucas A. 2011. Protoplanetary Disks and Their Evolution. *Pages 67–117 of:* Faber, S M, & VanDishoeck, E (eds), *Remote Geochemical Analysis: Elemental and Mineralogical Composition*. ANNUAL REVIEWS.

Wilson, Lionel, & Keil, Klaus. 2012. Volcanic activity on differentiated asteroids: A review and analysis. *Chemie der Erde - Geochemistry*, **72**(4), 289–321.

Yamaguchi, A, Barrat, Jean Alix, Greenwood, R C, Shirai, N, Okamoto, C, Setoyanagi, T, Ebihara, M, Franchi, I A, & Bohn, M. 2009. Crustal partial melting on Vesta: Evidence from highly metamorphosed eucrites. *Geochimica et Cosmochimica Acta*, **73**(23), 7162–7182.

Yamaguchi, Akira, Taylor, Jeffrey G, & Keil, Klaus. 1996. Global Crustal Metamorphism of the Eucrite Parent Body. *Icarus*, **124**(Nov.), 97–112.

Yamaguchi, Akira, Taylor, Jeffrey G, & Keil, Klaus. 1997. Metamorphic history of the eucritic crust of 4 Vesta. *Journal of Geophysical Research*, **102**(E6), 13–381–13–386.

Yamaguchi, Akira, Taylor, Jeffrey G, Keil, Klaus, & Floss, Christine. 2001. **Post-crystallization reheating and partial melting of eucrite EET90020 by impact into the hot crust of asteroid 4Vesta** ~4.50 **Ga ago**. *Geochimica et Cosmochimica Acta*, **65**(20), 3577–3599.

Yamashita, N, Gasnault, O, Forni, O, Uston, Claude, Reedy, R C, Karouji, Y, Kobayashi, S, Hareyama, M, Nagaoka, H, Hasebe, N, & Kim, K J. 2012. The global distribution of calcium on the Moon Implications for high-Ca pyroxene in the eastern mare region. *Earth and Planetary Science Letters*, **353-354**(C), 93–98.

Yamashita, N, Prettyman, T H, Mittlefehldt, D W, Toplis, M J, McCoy, T J, Beck, A W, Reedy, R C, Feldman, W C, Lawrence, D J, Peplowski, P N, Forni, O, Mizzon, H, Raymond, C A, & Russell, C T. 2013. Distribution of iron on Vesta. *Meteoritics & Planetary Science*, **48**(11), 2237–2251.

Yang, Jijin, Goldstein, Joseph I, & Scott, Edward R D. 2010. Main-group pallasites: Thermal history, relationship to IIIAB irons, and origin. *Geochimica et Cosmochimica Acta*, **74**(15), 4471–4492.

Zellner, N E B, Gibbard, S, de Pater, I, Marchis, F, & Gaffey, M J. 2005. Near-IR imaging of Asteroid 4 Vesta. *Icarus*, **177**(1), 190–195.

Zema, Michele, Domeneghetti, M Chiara, Molin, G Mario, & Tazzoli, Vittorio. 1997. Cooling rates of diogenites: A study of Fe2+-Mg ordering in orthopyroxene by single-crystal x-ray diffraction. *Meteoritics & Planetary Science*, **32**, 855–862.

Zhou, Qin, Yin, Qing-Zhu, Young, Edward D, Li, Xian-Hua, Wu, Fu-Yuan, Li, Qiu-Li, Liu, Yu, & Tang, Guo-Qiang. 2013. SIMS Pb-Pb and U-Pb age determination of eucrite zircons at<5um scale and the first 50Ma of the thermal history of Vesta. *Geochimica et Cosmochimica Acta*, **110**(C), 152–175.

Zhu, Meng-Hua, Ma, Tao, & Chang, Jin. 2010. Chang'E-1 gamma ray spectrometer and preliminary radioactive results on the lunar surface. *Planetary and Space Science*, **58**(12), 1547–1554.

Zhu, Meng-Hua, Chang, Jin, Ma, Tao, Ip, Wing-Huen, Fa, WenZhe, Wu, Jian, Cai, Ming-Sheng, Gong, YiZhong, Hu, YiMing, Xu, AoAo, & Tang, ZeSheng. 2013. Potassium Map from Chang'E-2 Constraints the Impact of Crisium and Orientale Basin on the Moon. *Scientific Reports*, **3**(Apr.), 1–6.

Zibulevsky, Michael, & Pearlmutter, Barak A. 2001. Blind source separation by sparse decomposition in a signal dictionnary. *Neural Computation*, **13**, 863–882.

Zolotov, Mikhail Yu. 2009. On the composition and differentiation of Ceres. *Icarus*, **204**(1), 183–193.

Abstract

Asteroids Vesta and Ceres motivated the space mission Dawn because they represent two different planetary embryos that remained relatively intact since their formation. Vesta is broadly considered as the parent body of the HED meteorites suite that are witnesses of a magmatic activity probably due to the presence of the radioactive isotope ^{26}Al, which was present in significant amount to cause internal melting of primitive rocky bodies. The composition of a planetary surface can be quantified through the analysis of the gamma rays it produces. This is made possible for the Dawn spacecraft by the instrument GRaND and the scintillation of a BGO crystal. This thesis presents the analysis of gamma ray spectra from Vesta by two blind source separation methods: the independent component analysis and the non negative matrix factorization. These methods are also applied to an equivalent lunar dataset already well interpreted. Lunar synthetic spectra are used to test ICA and NMF. The separation of elementary spectra is delicate although K, Th and Fe can be discriminated due to the more favorable statistical properties of their source signals. The sensitivity of separation to the chemical variability is assessed based on artificial lunar spectra, which allows to explain the lack of separation of a clear elemental signal in the case of Vesta. Despite the observations of Dawn and the important collection of HED data, there is no consensus on the conditions of the vestan magmatism. A global magma ocean is often put forward, whereas the migration of the heat source, contained in the easiest mineral to melt, plagioclase, does not allow it. A model of melt migration is implemented, based on two-phase flow equations. This model is combined with the olivine-anorthite-quartz equilibrium phase diagram. This allows to predict the mineralogy as a function of depth and time. Results obtained show that eucrites and diogenites may be a common feature of large bodies accreted early in solar system history.

Résumé

Les astéroïdes Cérès et Vesta ont motivé la mission spatiale Dawn parce qu'ils représentent deux embryons planétaires différents restés relativement intacts depuis leur formation. Vesta est largement considéré comme le corps parent des météorites HED témoins d'une activité magmatique probablement due à la présence de l'isotope radioactif ^{26}Al qui était suffisamment abondant pour permettre la fusion interne des corps rocheux primitifs. La composition d'une surface planétaire peut être mesurée grâce à l'analyse des rayons gammas qu'elle produit. Pour la sonde Dawn cela est rendu possible par l'instrument GRaND et la scintillation d'un cristal de BGO. Cette thèse présente l'analyse des spectres gammas de Vesta par deux outils de séparation aveugle de source: l'analyse en composantes indépendantes (ICA) et la factorisation en matrice non-négative (NMF). Ces méthodes sont aussi appliquées à un jeu de données lunaire comparable et déjà bien interprété. Des spectres synthétiques lunaires permettent de tester ICA et NMF. La séparation de spectres élémentaires s'avère délicate même si on peut distinguer les éléments K, Th et Fe en raison des propriétés statistiques de leur signaux sources plus favorables. On mesure la sensibilité d'ICA-NMF à la variabilité chimique de la surface pour des Lunes artificielles, ce qui permet d'expliquer l'absence de séparation d'un signal élémentaire clair dans le cas de Vesta. Malgré les observations de la sonde Dawn et le nombre important d'informations fournies par les HED, il n'y a pas de consensus sur la formation des HED. On met souvent en avant l'existence d'un océan magmatique global sur Vesta, alors que la migration de la principale source chaleur, contenue dans le premier minéral fondu, le plagioclase, ne permet pas la fusion totale. On met en oeuvre un modèle de migration des magmas, basé sur les équations de la compaction. On adapte ce modèle en utilisant un diagramme d'équilibre de phase olivine-anorthite-quartz. Cela permet de calculer l'évolution de la minéralogie en fonction du temps et de la profondeur. Les résultats montrent que les eucrites et les diogénites pourraient être une caractéristique commune des gros corps accrétés tôt dans l'histoire du système solaire.